



BRUNEL UNIVERSITY

# Novel FFAG Gantry and Transport Line Designs for Charged Particle Therapy

by

Richard Fenning

A thesis submitted in partial fulfillment for the  
degree of Doctor of Philosophy

in the  
School of Engineering and Design

December 2011

# Declaration of Authorship

I, Richard Fenning, declare that this thesis titled, ‘Novel FFAG Gantry and Transport Line Designs for Charged Particle Therapy’ and the work presented in it are my own. I confirm that:

- This work was done wholly while in candidature for a research degree at Brunel University.
- Where I have consulted the published work of others, this is always clearly attributed.
- I have acknowledged all main sources of help.
- Where the thesis is based on work done by myself jointly with others, I have made clear exactly what was done by others and what I have contributed myself.

Signed:

A handwritten signature in black ink, appearing to read 'Richard Fenning', written in a cursive style.

Date: 30/6/2011

# *Abstract*

This thesis describes the design of novel magnetic lattices for the transport line and gantry of a charged particle therapy complex. The designs use non-scaling Fixed Field Alternating Gradient (ns-FFAG) magnets and were made as part of the PAMELA project. The main contributions in this thesis are the near-perfect FFAG dispersion suppression design process and the designs of the transport line and the gantry lattices.

The primary challenge when designing an FFAG gantry is that particles with different momenta take up different lateral positions within the magnets. This is called dispersion and causes problems at three points: the entrance to the gantry, which must be rotated without distortion of the beam; at the end of the gantry where reduced dispersion is required for entry to the scanning system; and a third of the way through the gantry, where a switch in curvature of the magnets is required. Due to their non-linear fields, dispersion suppression in conventional FFAGs is never perfect. However, as this thesis shows, a solution can be found through manipulation of the field components, meaning near-perfect dispersion suppression can be achieved using ns-FFAG magnets (although at a cost of irregular optics). The design process for an FFAG dispersion suppressor shown in this thesis is a novel solution to a previously unsolved problem. Other challenges in the gantry lattice design, such as height and the control of the optics, are tackled and a final gantry design presented and discussed.

The starting point for the transport line is a straight FFAG lattice design. This is optimised and matched to a  $45^\circ$  bend. Fixed field solutions to the problem of extracting to the treatment room are discussed, but a time variable field solution is decided on for practical and patient safety reasons. A matching scheme into the gantry room is then designed and presented.

## *Acknowledgements*

My first thanks go to my supervisor, Akram Khan, for all your help, support and corrections; and to Rob Edgecock for the same.

Shinji Machida and David Kelliher at the Rutherford Appleton Labs gave me a lot of essential mentoring in the art of lattice design, for which I cannot thank them enough, while the advice and support of Ken Peach, Holger Witte and Takeichiro Yokoi at Oxford was invaluable. I would also like to thank Suzie Sheehy and all the other members of the PAMELA and EMMA teams who have helped greatly. Thank you too to everyone at Brunel University who helped me to get started and set out in the right direction.

Thank you to Mum and Dad for everything (literally), to Kate and Al and the rest of my brilliant family.

The main thanks and gratitude are to Haley. You encouraged me to start this when we hardly knew each other and you have given me all I needed every day since. Thank you.

# Contents

<b>Declaration of Authorship</b>	<b>i</b>
<b>Abstract</b>	<b>ii</b>
<b>Acknowledgements</b>	<b>iii</b>
<b>List of Figures</b>	<b>viii</b>
<b>List of Tables</b>	<b>xiii</b>
<b>1 Introduction</b>	<b>1</b>
1.1 History of Particle Accelerators . . . . .	2
1.1.1 Electrostatic Accelerators . . . . .	4
1.1.2 Resonating Accelerators . . . . .	6
1.1.3 Betatron Accelerators . . . . .	8
1.1.4 Synchrotrons . . . . .	9
1.1.5 Fixed Field Alternating Gradient Accelerators . . . . .	10
1.2 Introduction to Radiotherapy and Charged Particle Therapy . . . . .	11
1.2.1 The Molecular Effects of Ionising Radiation . . . . .	12
1.2.2 Dose Response Curves . . . . .	12
1.2.3 Dose Distributions . . . . .	14
1.2.4 Other Benefits of Charged Particle Therapy . . . . .	16
1.2.5 Caveats to the Superiority of Charged Particle Therapy . . . . .	19
1.3 Chapter Summary . . . . .	20
<b>2 Basic Particle Accelerator Physics</b>	<b>21</b>
2.1 Introduction . . . . .	21
2.2 Coordinate System . . . . .	22
2.3 Accelerator Types . . . . .	22
2.4 Circular Motion and Magnetic Rigidity . . . . .	23
2.4.1 Aperture . . . . .	24
2.4.2 Closed Orbits . . . . .	24
2.4.3 Focusing . . . . .	25
2.4.4 Betatron Oscillations and the Effective Gradient . . . . .	27

2.4.5	Tune . . . . .	29
2.4.6	Resonances . . . . .	30
2.4.7	Bunches and the Phase Space Ellipse . . . . .	31
2.4.8	Acceptance and Smear . . . . .	36
2.4.9	Dispersion . . . . .	39
2.4.10	Dispersion Suppression . . . . .	40
2.5	Fixed Field Alternating Gradient Accelerators . . . . .	41
2.5.1	Scaling Law . . . . .	42
2.5.2	Focusing is Tied to Bending . . . . .	43
2.5.3	Negative k . . . . .	44
2.5.4	Non-Scaling Fixed Field Alternating Gradient Accelerators . . . . .	44
2.6	Simulation Code . . . . .	46
2.7	Parameter Searches and Downhill Fitting . . . . .	47
2.8	Chapter Summary . . . . .	49
<b>3</b>	<b>Immediate Context</b>	<b>50</b>
3.1	The CONFORM Project and EMMA . . . . .	50
3.2	PAMELA . . . . .	52
3.2.1	Clinical Requirements . . . . .	54
3.2.2	Spot Scanning Issues . . . . .	54
3.2.3	The PAMELA Lattice . . . . .	55
3.2.4	Magnet Design . . . . .	59
3.2.5	Extraction . . . . .	59
3.2.6	Acceleration . . . . .	61
3.2.7	Pre-Acceleration . . . . .	61
3.3	Existing Gantries . . . . .	62
3.3.1	Designs for Matching into a Rotating Gantry . . . . .	65
3.4	FFAG History and Relevant Literature . . . . .	67
3.4.1	Early FFAGs . . . . .	67
3.4.2	Revival of the Fixed Field Alternating Gradient Accelerator . . . . .	70
3.4.3	The First Non Scaling FFAG Design . . . . .	70
3.4.4	The Keil, Sessler, Trbojevic Lattice . . . . .	72
3.4.5	Edge Focusing ns-FFAG . . . . .	73
3.4.6	Grahame Rees Pumplet Design . . . . .	74
3.4.7	Gantry Design Developed from the KST Lattice . . . . .	74
3.4.8	Gantry Design by Grahame Rees . . . . .	76
3.4.9	Transport Line Design by Shinji Machida . . . . .	76
3.5	Motivation for a New Gantry and Transport Line . . . . .	79
3.6	Chapter Summary . . . . .	79
<b>4</b>	<b>Specifications and Challenges</b>	<b>80</b>
4.1	Specifications . . . . .	81
4.1.1	Summary of Specifications . . . . .	84
4.2	Design Challenges and Possible Solutions . . . . .	85
4.2.1	The Design of the Gantry . . . . .	85
4.2.1.1	Switch of Curvature . . . . .	85
4.2.1.2	Rotation . . . . .	86

4.2.1.3	The End of the Gantry . . . . .	87
4.2.2	Transport Line . . . . .	88
4.2.2.1	Transporting the beam in a straight line . . . . .	88
4.2.2.2	Bending . . . . .	88
4.2.2.3	Switching into Treatment Rooms . . . . .	89
4.2.3	Matching to PAMELA . . . . .	89
4.2.4	Matching from Transport line into the Gantry . . . . .	90
4.2.5	Dispersion Suppression with Scaling Magnets . . . . .	90
4.3	Chapter Summary . . . . .	91
<b>5</b>	<b>Gantry Design Studies</b> . . . . .	<b>92</b>
5.1	Introduction . . . . .	92
5.2	Basic Magnet Design . . . . .	93
5.3	Basic Cell Design . . . . .	95
5.4	Proof of Principle Gantry Design . . . . .	95
5.4.1	Results and Discussion . . . . .	97
5.5	Near Perfect Dispersion Suppression . . . . .	100
5.5.1	Cell Description . . . . .	100
5.5.2	Non-Linearity . . . . .	101
5.5.3	Fitting Method . . . . .	104
5.5.4	Results . . . . .	107
5.5.5	Error Study of A Dispersion Suppression Point . . . . .	109
5.5.5.1	Method and Results . . . . .	112
5.5.5.2	Discussion of the Results of the Error Study . . . . .	114
5.5.6	Discussion of the Dispersion Suppression Study . . . . .	115
5.6	Properties of the Non-Scaling Gantry . . . . .	115
5.6.1	Discussion . . . . .	115
5.7	Flattened Gantry Design . . . . .	118
5.7.1	Design strategy . . . . .	118
5.7.2	The 90° Bending Section . . . . .	119
5.7.2.1	Parameter Search . . . . .	120
5.7.2.2	Parameter Search Results . . . . .	122
5.7.2.3	Optimisation . . . . .	123
5.7.2.4	Triplet alternative in section 4 . . . . .	125
5.7.2.5	Parameter Search for Alternative Design to the End of the Gantry . . . . .	126
5.7.2.6	Alternative parameter search results . . . . .	127
5.7.2.7	The Defocusing Magnet . . . . .	128
5.7.3	The Design of Gantry Sections 1 and 2 . . . . .	129
5.7.3.1	Parameter Search . . . . .	131
5.7.3.2	Matching Sections 2 and 3 using intermediate $k$ values . . . . .	134
5.7.4	Joining Up the Whole Gantry . . . . .	135
5.8	Characteristics of the Whole Gantry . . . . .	137
5.9	Testing Rotation of the Gantry and Tolerance of Positional Errors at the Entrance . . . . .	140
5.10	Ideas for Further Study . . . . .	144
5.11	Chapter Summary . . . . .	147

<b>6</b>	<b>Transport Line Design Studies</b>	<b>149</b>
6.1	Introduction . . . . .	149
6.2	Basic Cell Design . . . . .	149
6.3	Optimisation of Straight FFAG Beam Transport Line . . . . .	150
6.3.1	Parameters of Study and Method of Optimisation . . . . .	151
6.3.2	Straight Transport Line Optimisation Results . . . . .	152
6.4	Transport Cell for Carbon . . . . .	156
6.5	Adding a Bending Section to the Transport Line . . . . .	159
6.5.1	Parameter Search for the Bending Section . . . . .	160
6.5.2	Bending Section Result and Final Straight Cell Design . . . . .	161
6.5.3	Discussion of the Matched Bending Section . . . . .	161
6.6	Extraction from the Transport Line . . . . .	163
6.6.1	Purpose of Study . . . . .	163
6.6.2	Ideas for Fixed Field Extraction from the Transport Line . . . . .	164
6.6.2.1	Switching One Magnet Off . . . . .	164
6.6.2.2	Switchable Dipoles . . . . .	168
6.6.2.3	Dispersion Suppression . . . . .	169
6.6.2.4	Curved Transport Line . . . . .	170
6.6.3	Justification for a Variable Field Switching Dipole . . . . .	173
6.7	Design for 45° bend and Matching into Treatment Room . . . . .	175
6.7.1	Dispersion Suppression and bending . . . . .	176
6.7.1.1	Results . . . . .	177
6.7.1.2	Discussion of The 45° Bend and Matched Dispersion Suppressor . . . . .	179
6.7.2	Design for a Variable Field Switching Dipole . . . . .	180
6.7.3	Matching of Beta Functions . . . . .	181
6.7.4	The Whole Transport Line . . . . .	183
6.8	Conclusion . . . . .	185
<b>7</b>	<b>Conclusion</b>	<b>187</b>
7.1	Assessment of Final Designs . . . . .	187
7.2	Further Study . . . . .	189
<b>A</b>	<b>Miscellaneous Tables</b>	<b>192</b>
	<b>Bibliography</b>	<b>194</b>

# List of Figures

1.1	William Crookes with cathode tube in Vanity Fair, 1902. . . . .	2
1.2	The exponential rise of energies achieved by accelerators in the twentieth century. . . . .	3
1.3	Map showing the sites of all 150 particle accelerators in the UK. . . . .	4
1.4	Cockroft and Walton’s accelerator and voltage generator . . . . .	5
1.5	A schematic of Widerøe’s linac. . . . .	6
1.6	A schematic of Lawrence’s cyclotron. . . . .	7
1.7	Direct and indirect effects of radiation on DNA . . . . .	13
1.8	Example of dose response curves. . . . .	13
1.9	Comparison of the dose depositions in water of X-rays and protons as a function of depth . . . . .	14
1.10	Comparison of tomotherapy and multi-beam proton therapy . . . . .	16
1.11	RBE and OER for a variety of radiation types . . . . .	17
1.12	Comparison of the effect of fractionation in X-ray therapy and charged particle therapy . . . . .	18
2.1	Co-ordinate System . . . . .	22
2.2	Circular Motion in a Magnetic Field . . . . .	24
2.3	Directions of Force in Fields With Horizontal and Vertical Gradients . . . . .	26
2.4	Betatron Oscillations Vary With $S$ . . . . .	30
2.5	Betatron Oscillations Vary Within a Bunch . . . . .	32
2.6	Phase Space Ellipse at Single $s$ . . . . .	34
2.7	Comparison of Different Values of Smear . . . . .	37
2.8	Example of a Smear of 0.1 . . . . .	38
2.9	Dispersion Suppression Using Half a Betatron Oscillation . . . . .	40
2.10	Radial sector FFAG . . . . .	41
2.11	Scaling Fields . . . . .	43
2.12	Fields with Positive and Negative $k$ . . . . .	45
2.13	Multipole Components of a Scaling Field . . . . .	46
2.14	The difference between a scaling field and its Taylor expansion . . . . .	47
2.15	Zgoubi Magnet Map . . . . .	48
3.1	The EMMA accelerator at the Daresbury Laboratory. . . . .	51
3.2	Four EMMA cells. . . . .	52
3.3	The layout of the PAMELA accelerator. . . . .	53
3.4	Conversion from FFAG sector shaped magnets to ns-FFAG rectangular magnets. . . . .	56
3.5	The PAMELA proton lattice. . . . .	58

3.6	A ‘tilted solenoid’ dipole magnet. . . . .	60
3.7	PAMELA magnet winding trial. . . . .	60
3.8	Extraction set-up in the PAMELA ring. . . . .	61
3.9	The final section of the Heidelberg Gantry. . . . .	63
3.10	Examples of isocentric and exocentric gantries . . . . .	64
3.11	An example variable field gantry design. . . . .	65
3.12	Rotator schematic. . . . .	66
3.13	spiral sector FFAG section. . . . .	68
3.14	A radial slice through the field of a spiral sector FFAG . . . . .	69
3.15	Comparison of FFAG and ns-FFAG orbit positions . . . . .	71
3.16	The three rings of the KST lattice. . . . .	72
3.17	A cell of the KST lattice. . . . .	73
3.18	A ‘pumpet’ cell. . . . .	74
3.19	A gantry developed from the KST lattice. . . . .	75
3.20	A proposed gantry layout without a reverse bend. . . . .	77
3.21	Tracks thorough a quadruplet straight transport line cell. . . . .	78
3.22	Beta functions thorough a quadruplet straight transport line cell. . . . .	78
4.1	Scanning schematic . . . . .	83
4.2	Gantry schematic using PAMELA ring . . . . .	86
4.3	Schematic of the transport line and treatment rooms. . . . .	88
5.1	An example Enge function . . . . .	94
5.2	Example of a triplet cell . . . . .	96
5.3	Schematic of Scaling Gantry Design . . . . .	98
5.4	Scaling Gantry: Particle Tracks . . . . .	99
5.5	Scaling Gantry: Final particle positions . . . . .	99
5.6	Scaling Gantry: Final particle angles . . . . .	100
5.7	Dispersion Suppressor Cell Schematic . . . . .	101
5.8	The equations of motion for a linear field and a scaling field . . . . .	102
5.9	Comparison of linear and scaling field profiles . . . . .	103
5.10	Sketch of dispersion suppression in a scaling field . . . . .	104
5.11	Tracks through a scaling dispersion suppressor . . . . .	105
5.12	Horizontal position vs momentum at the end of a scaling dispersion sup- pressor . . . . .	105
5.13	Horizontal deflection vs momentum at the end of a scaling dispersion suppressor . . . . .	106
5.14	Tracks through a non-scaling FFAG dispersion suppressor . . . . .	108
5.15	Horizontal position vs momentum at the end of a non-scaling dispersion suppressor . . . . .	108
5.16	Horizontal deflection vs momentum at the end of a non-scaling dispersion suppressor . . . . .	109
5.17	Beta functions thorough the non-scaling dispersion suppressor . . . . .	110
5.18	Phase advance through the non-scaling dispersion suppressor . . . . .	110
5.19	Sensitivity of particle position to errors in the magnet positions in an FFAG dispersion suppressor. . . . .	113
5.20	Sensitivity of particle deflection to errors in the magnet positions in an FFAG dispersion suppressor. . . . .	113

5.21	Tracks through the non-scaling gantry . . . . .	116
5.22	Horizontal position vs momentum at the end of a non-scaling gantry . . . . .	116
5.23	Horizontal deflection vs momentum at the end of the non-scaling gantry . . . . .	117
5.24	Beta functions through the non-scaling gantry . . . . .	117
5.25	Gantry Sections . . . . .	118
5.26	Schematic of the last two sections of the gantry. . . . .	120
5.27	Bend Angle of Section 3 vs Total Gantry Height . . . . .	121
5.28	Tracks through result of parameter search. . . . .	122
5.29	Fields through result of parameter search. . . . .	123
5.30	Beta functions through result of parameter search. . . . .	123
5.31	Particle tracks through result of parameter search and section 4 optimi- sation. . . . .	124
5.32	Beta functions through result of parameter search and section 4 optimi- sation. . . . .	124
5.33	Schematic of the alternative section 4. . . . .	125
5.34	Particle tracks through result of parameter search for alternative gantry end. . . . .	127
5.35	Fields through result of parameter search for alternative gantry end. . . . .	128
5.36	Beta functions through result of parameter search for alternative gantry end. . . . .	128
5.37	Tracks through initial design of final defocusing magnet . . . . .	129
5.38	Fields through initial design of final defocusing magnet. . . . .	130
5.39	Tunes for 4 cell solution to sections 1 and 2 . . . . .	132
5.40	Tunes for 6 cell solution to sections 1 and 2 . . . . .	132
5.41	Tunes for 8 cell solution to sections 1 and 2 . . . . .	133
5.42	Tunes for 10 cell solution to sections 1 and 2 . . . . .	133
5.43	Dispersion matching solution for section 2. . . . .	135
5.44	Tunes for 8 cell solution to sections 1 and 2, with $k$ values. . . . .	136
5.45	Beta functions through joined up gantry. . . . .	136
5.46	Tracks through the whole gantry. . . . .	139
5.47	Fields through the whole gantry. . . . .	139
5.48	Beta functions through the whole gantry. . . . .	140
5.49	Gantry rotation deflection errors with 0.369 GeV/c particles. . . . .	141
5.50	Gantry rotation deflection errors with 0.549 GeV/c particles. . . . .	141
5.51	Gantry rotation deflection errors with 0.729 GeV/c particles. . . . .	142
5.52	Gantry position errors with 0.369 GeV/c particles. . . . .	142
5.53	Gantry position errors with 0.549 GeV/c particles. . . . .	143
5.54	Gantry position errors with 0.729 GeV/c particles. . . . .	143
5.55	Tracks through sections 1 and 2 if scanning is integrated into sections 3 and 4. . . . .	145
5.56	Beta functions through sections 1 and 2 if scanning is integrated into sections 3 and 4. . . . .	146
5.57	Initial schematic design for a lattice to create elevation in the gantry. . . . .	148
5.58	Tracks through initial design for a simple lattice to create elevation in the gantry. . . . .	148
6.1	Example of a quadruplet cell . . . . .	150

6.2	Acceptances for a non-scaling cell in a DFFD configuration . . . . .	152
6.3	Acceptances for a non-scaling cell in a FDDF configuration . . . . .	153
6.4	Dispersion in the long drift for all cell configurations . . . . .	153
6.5	Acceptances of working points with $k$ close to 12 for a non-scaling cell in a DFFD configuration . . . . .	154
6.6	Tracks through cell with $k = 11$ and a DF ratio of 1.17. . . . .	154
6.7	Fields through cell with $k = 11$ and a DF ratio of 1.17. . . . .	155
6.8	Beta functions through cell with $k = 11$ and a DF ratio of 1.17. . . . .	155
6.9	Horizontal phase space ellipses through 6 cells with $k = 11$ and a DF ratio of 1.17. . . . .	156
6.10	Vertical phase space ellipses through 6 cells with $k = 11$ and a DF ratio of 1.17. . . . .	157
6.11	Tracks through a possible straight transport line for both protons and carbon. . . . .	157
6.12	Fields through a possible straight transport line for both protons and carbon. . . . .	158
6.13	Beta Functions through a possible straight transport line for both protons and carbon. . . . .	158
6.14	Tracks through a $45^\circ$ bending section between two straight transport cells. . . . .	162
6.15	Beta functions through a $45^\circ$ bending section between two straight transport cells. . . . .	163
6.16	Tracks through a straight transport cell with the second D magnet switched off. . . . .	165
6.17	Tracks through a straight transport cell with the second F magnet switched off. . . . .	165
6.18	Tracks through a straight transport cell with the first F magnet switched off. . . . .	166
6.19	Tracks through a straight transport cell with the first D magnet switched off. . . . .	166
6.20	Beta functions through a straight transport cell with the second F magnet switched off. . . . .	167
6.21	Example of an ejection system using two dipoles of opposite field strength. . . . .	168
6.22	Comparison of particle positions at the exit of the fixed dipole ejection system and the equilibrium positions in a scaling FFAG cell. . . . .	169
6.23	How a curved transport line might switch to treatment rooms. . . . .	171
6.24	Possible layouts of a curved transport line. . . . .	171
6.25	Tracks through ‘snake’ type curved transport line. . . . .	172
6.26	Betas through ‘snake’ type curved transport line. . . . .	172
6.27	Schematic of an energy selecting ejection system for the transport line, using variable field dipoles and movable collimator. . . . .	174
6.28	Tracks through best design of $45^\circ$ extraction bend and dispersion suppressor. . . . .	178
6.29	Beta functions through best design of $45^\circ$ extraction bend and dispersion suppressor. . . . .	179
6.30	Final positions of particles through the $45^\circ$ extraction bend and dispersion suppressor with ideal initial positions. . . . .	179
6.31	Final angles of particles through the $45^\circ$ extraction bend and dispersion suppressor with ideal initial positions. . . . .	180
6.32	Tracks through the variable field transport extraction dipoles. . . . .	181

---

6.33	Beta functions through the five matching quadrupoles at the end of the transport line. . . . .	182
6.34	Tracks through the entire transport line. . . . .	184
6.35	Beta functions through the whole transport line. . . . .	184
6.36	Final positions at the end of the transport line. . . . .	185
6.37	Final deflections at the end of the transport line. . . . .	185

# List of Tables

3.1	Summary of the clinical requirements of PAMELA . . . . .	54
3.2	Lattice parameters for the PAMELA proton ring . . . . .	57
3.3	Lattice parameters for the PAMELA carbon ring. . . . .	58
3.4	Parameters of existing gantries . . . . .	63
5.1	Cell Parameters . . . . .	97
5.2	Scaling Gantry Design . . . . .	98
5.3	Non-scaling FFAG dispersion suppressor multipole values . . . . .	108
5.4	Final 90° bend parameter search . . . . .	121
5.5	Result of parameter search . . . . .	122
5.6	Final 90° bend with alternative section 4 parameter search . . . . .	126
5.7	Result of parameter search . . . . .	127
5.8	Flattened Gantry Design . . . . .	138
5.9	Values of the $b_n$ constants for the final gantry design. . . . .	138
5.10	Optimal initial beta values for the gantry. . . . .	139
6.1	Transport Cell Geometry . . . . .	151
6.2	Transport Line Straight Cell for carbon and protons Specifications. . . . .	159
6.3	Bending Section Parameter Search. . . . .	161
6.4	Transport Line Bending Cell Specifications. . . . .	162
6.5	Transport Line Straight Cell Specifications. . . . .	162
6.6	Parameter Search for 45° Bend and Dispersion Suppression into Treatment Room. . . . .	177
6.7	Designs of 45° Bend and Dispersion Suppression into Treatment Room. . . . .	178
6.8	Field strengths for variable field switching dipole. . . . .	181
6.9	Quadrupole strengths for matching Twiss functions from the transport line to the gantry. . . . .	183
A.1	Optimal initial betas values for the gantry. . . . .	192
A.2	Field strengths for the dipole transport line extraction scheme. . . . .	193

*Dedicated to my Grandparents and their battles with cancer*

# Chapter 1

## Introduction

In 1838, investigations into why electric sparks travelled further in the ‘rarified air’ of partially evacuated glass tubes than in normal air, led Michael Faraday to notice a coherent arc of light emerging from the negative spark generating terminal. By 1870 William Crookes had invented a tube with a vacuum good enough to produce an invisible beam which travelled from the cathode, all the way passed the anode, and fluoresced against the glass at the end (figure 1.1 shows Crookes holding one such tube). The term ‘cathode ray’ was coined to describe it.

Nearly thirty years later, in 1897, J.J. Thomson showed, by observation of the lack of diffraction patterns around the silhouettes of objects, that these cathode rays were in fact made up of particles (called electrons) [3]. Soon after, Wilhelm Roentgen discovered the X-ray using a Crookes type tube when he noticed radiation coming from the point where the cathode ray hit a target and causing fluorescence on the other side of the room [4]. It is difficult to overstate the importance of both discoveries. They were a vital step on the way for a whole swathe of technologies and areas of knowledge from welding to the study of cosmology. The two intellectual descendants of this work that are of interest



FIGURE 1.1: William Crookes with cathode tube in *Vanity Fair*, 1902 [1]. The caption read ‘ubi Crookes ibi lux’ which translates to ‘Where there is Crookes there is light’ [2].

to this thesis, however, are particle accelerators and radiotherapy. The first section of this chapter gives an overview of the history of particle accelerators while the second gives an introduction to radiotherapy and, more specifically, Charged Particle Therapy (CPT).

## 1.1 History of Particle Accelerators

The increase in energies reached by particle accelerators has been phenomenal over the last century and the Large Hadron Collider continues to grab headlines as it achieves energies closer and closer to those at the Big Bang. The rise of maximum energy can be seen in figure 1.2 and this section will give an overview of its history. However, the number of accelerators with more earthly purposes has also expanded dramatically as new applications from isotope dating to food preservation and virus crystallography continue to be found [6]. There are now more than 30,000 accelerators around the world [7, p.82] and over 150 of those are in the UK (see figure 1.3) [8].

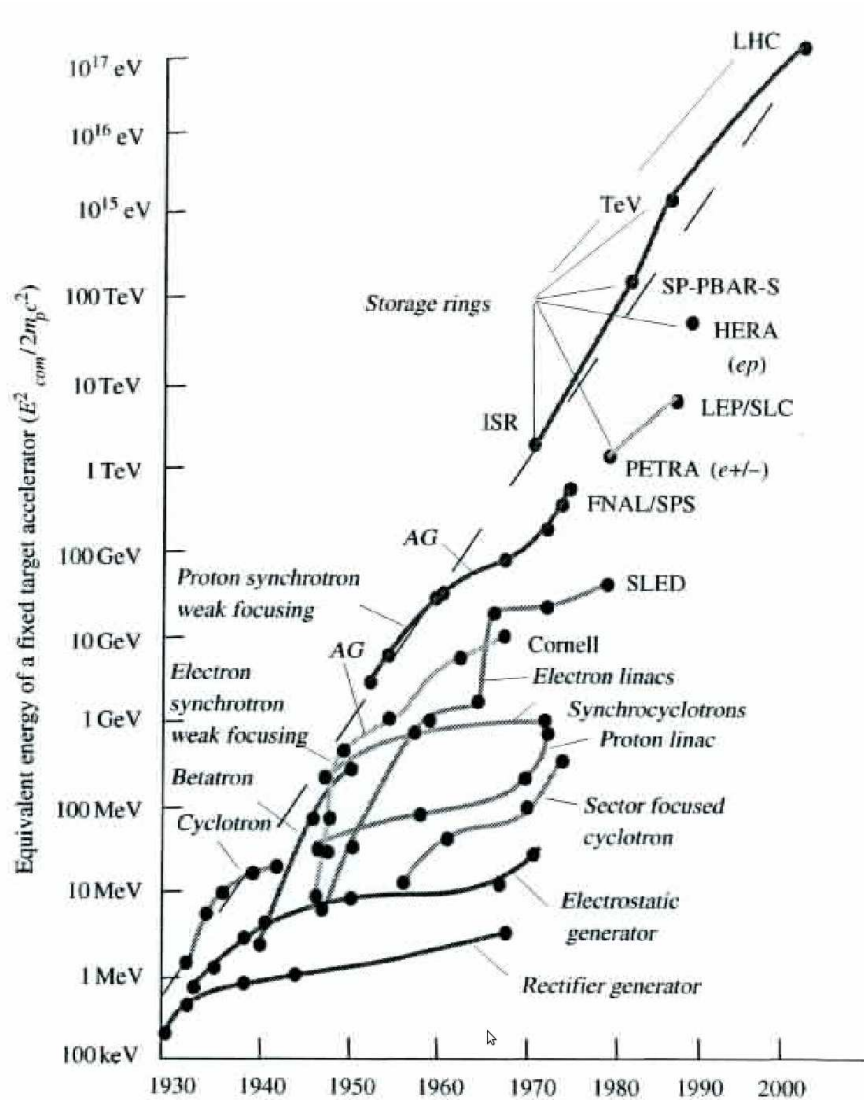


FIGURE 1.2: The exponential rise of energies achieved by accelerators in the twentieth century. The lines join up the type of technology used. [5, p.2]

The study of particle accelerators really got going in the 1930s. The Crookes type machines suffered electrical breakdown at anything over a few tens of kV [5], so radioactive sources had been used to study the nature of particles. However, with the discovery of quantum mechanics, higher energies were required to study the realm of the very small, while Einstein's famous energy equation  $E = mc^2$  gave good reason to reach energies high enough to create new particles.

In their early development, accelerators could be split up into three distinct groups, based on their method of acceleration [9]: electrostatic, resonant and betatron acceleration.



FIGURE 1.3: Map showing the sites of all 150 particle accelerators in the UK. Created using Google Maps at [8].

### 1.1.1 Electrostatic Accelerators

An electrostatic accelerator is, in principle, the most straight forward method of acceleration. A large potential difference is built up and a charged particle is accelerated over it.

Some of the first big leaps away from the limitations of the early Crookes style tubes were achieved by Cockroft and Walton. Their accelerator, as shown in figure 1.4, has a straight forward potential difference with a source at the top and a target at the base. Their great technological advance, however, was their ‘cascade’ type generator which could be used to accelerate to energies approaching 1MeV (that is the energy an electron gains when it is accelerated with a potential difference of  $1 \times 10^6$  Volts) [10]. This generator, shown in figure 1.4(b) charged up capacitors connected with diodes to prevent immediate discharge. The first half cycle of the AC source would charge the first capacitor to its peak voltage and the second half-cycle loads the second and so on

until the large potential difference is created. In 1932 they became the first people to trigger a nuclear reaction using a particle accelerator when they transmuted Lithium into Helium with 700 keV protons [10].



FIGURE 1.4: Cockroft and Walton's accelerator and voltage generator. The accelerator has large potential difference built up between the terminal at the top and the earth. The particles are fired downwards through the evacuated drift tube to a target at the bottom. The generator has large capacitors, encased in the vertical pipes, and diodes, in the diagonal pipes, to prevent them discharging. Image from [11]

A different approach to creating large voltages was invented by R. van de Graaff [12] in 1931. The van de Graaff generator carries charge from the low to the high voltage terminal on a belt and can reach  $\approx 10$  MV.

The problem all electrostatic accelerators encounter is voltage breakdown due to coronal discharge [13, p.9]. A charged particle will only be accelerated to the energy created by the potential difference built between two terminals, so as the voltage increases, the limitation becomes how well the space between the terminals, or the earth, can be

insulated. To overcome these limitations, it was found that much higher energies could be reached if the particle was accelerated with small pushes, rather than in one go.

### 1.1.2 Resonating Accelerators

The limitations of the electrostatic accelerators were overcome using the pulsed nature of alternating current electricity, which allows acceleration to be built up in a series of smaller kicks, rather than stacks of higher and higher voltages.

The first design to use this technique was that of the linear accelerator (linac). A design was proposed by Ising in 1924 [14] in which particles were accelerated in the gaps between copper drift tubes, which all alternated between positive and negative potential at the same time. In this set-up, the charged particles are shielded within the copper tubes when they would be decelerated and are in the gaps when accelerated.

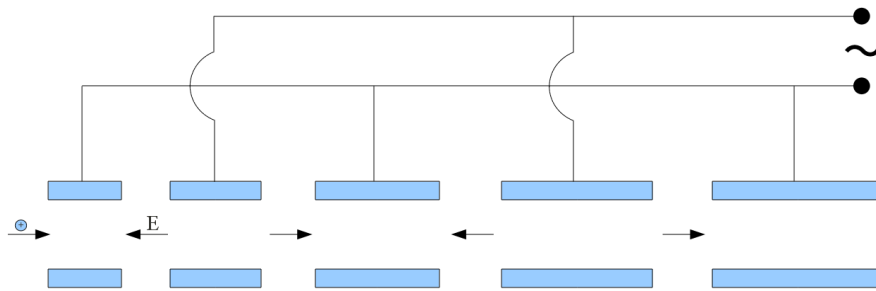


FIGURE 1.5: A schematic of Widerøe's linac. The alternating current means that the electron will be accelerated at each gap.

This idea was improved by a young Norwegian student Rolf Widerøe, into what became the standard design for a linear accelerator. He saw that ions (he used sodium ions) could be accelerated in both phases of the AC cycle if every other drift tube was connected to earth. Figure 1.5 shows this in principle. The timing must be such that the gap in which the ion is in should always have an accelerating field; so as the particle accelerates, larger distances have to be made between gaps. A three tube model of this device was

accepted as his thesis in 1928 and although he saw that it could be extended indefinitely, he abandoned research to take up a job designing circuit breakers [5].

Shortly after Widerøe's linac, Lawrence realised the acceleration idea could be used in a circular accelerator, which was called the cyclotron [15]. Figure 1.6 shows how this works. The particles are again accelerated in the gap between points of alternating potential, however, now they are bent in a circle by a large magnet so that the same two accelerating gaps can be reused. The acceleration increases the radius of the particle's motion until it eventually has enough energy to be ejected.

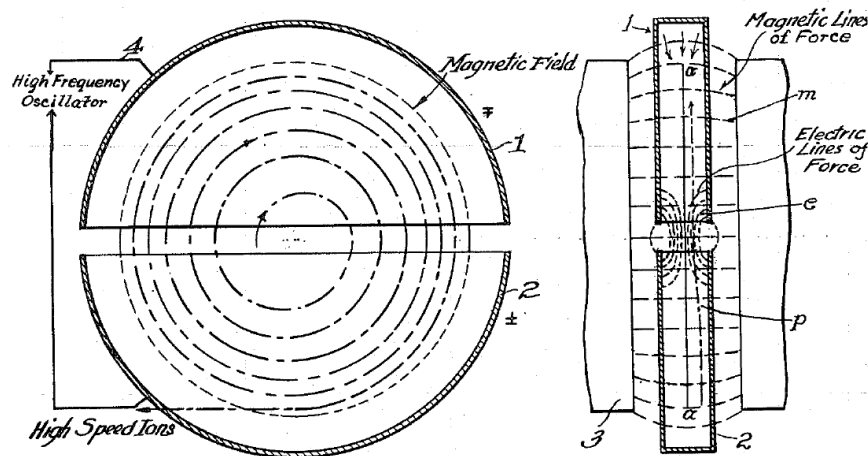


FIGURE 1.6: A schematic of Lawrence's cyclotron. [15].

Timing is again important as the voltage over the gap has to be of the correct sign at the arrival of the particle. However, this is a situation where the laws of physics lend a helping hand. Because of the increased path length caused by a particle's increasing radius, the bending field strength can be chosen so that the frequency of a particle's rotation does not change as it accelerates, meaning a constant stream of particles can be accelerated all at the same time.

This useful balance of effects breaks down as the particles approach the speed of light and energy put in by the accelerator increases their velocity less and less. The radius of their

orbits still increase, however, so the frequency of rotation is reduced and acceleration will stop.

Developments in cyclotrons have tried to overcome this limitation using variable field strengths and more complicated acceleration schemes but they are also limited by the size of the magnets required for larger energies and the difficulties in evacuating such large spaces. However, cyclotrons remain one of the most prevalent type of accelerator because of their compact size and simplicity at non-relativistic energies.

### 1.1.3 Betatron Accelerators

The first design for a circular accelerator came as early as 1923 from the notebooks of Rolf Widerøe, even before he had built the first linac. Although it was unfortunately never built due to some unfounded criticisms from the inventor's professor [5], his design of the 'Ray Transformer', laid the groundwork for later work into the betatron accelerator.

The ray transformer was reinvented in 1940 by Kerst and Serber in the United States and renamed the 'betatron' [5, p.11]. Uniquely among accelerator designs, it uses magnetic fields to accelerate the beam, but it was also the first design to increase the strength of the magnetic bending field to keep the radius of rotation fixed during acceleration.

In a betatron, the particles are contained in a doughnut shaped vacuum chamber. A magnetic flux through its centre provides the acceleration in the ring in a similar way to how current is induced in a loop encircling a current carrying wire. A guide field to hold the particles in orbit is placed over the tube and its strength increased with acceleration [16, p.10].

### 1.1.4 Synchrotrons

The Second World War saw advances in technology requiring radio frequency (RF) signals, with inventions such as the klystron (which uses rapidly oscillating electrons to amplify the power of high frequency signals) benefiting the study of particle accelerators [17].

After the war, as the energy requirements of the study of fundamental physics grew, a new type of accelerator was conceived by Mark Oliphant [18], pulling together the ideas of resonating cavities and of varying magnetic fields to keep a fixed radius during acceleration. This was called the synchrotron, because the frequency of the RF increases in synchronisation with the strength of the magnetic field in the bending magnets.

The development of synchrotron technology has been the driving force in the continued exponential rise in particle energies from about 1950 onward. There are a few reasons why synchrotrons can reach such high energies including: the splitting up of the single bending magnet into smaller elements, the strength of focusing and the space freed up for extra accelerating elements (called RF cavities).

Instead of a single bending magnet, as in the betatron and cyclotron, the synchrotron is made up of many smaller magnets. This means the radius can be orders of magnitude greater while the increase in the sum of magnet size for the whole accelerator will increase with its circumference, not its area, requiring much less magnet material and volume covered by the vacuum system.

A consequence of having bending split up in this way is that space can be made between the bending magnets to place many more RF cavities. This means that much more energy can be given to a circulating particle.

One necessary development for the circulation of such high energy beams was the development of ‘strong’ or ‘alternate gradient’ (AG) focusing by Christofilos [19] and Courant, Snyder and Livingston [20] at the Brookhaven National Laboratory in the United States. This will be explained in section 2.4.3, but it keeps the particle beam very small, which further decreases the size of the magnets, but also makes the design of RF cavities much easier, meaning more powerful ones could be built.

Technically speaking, the current accelerator reaching the highest energies, the Large Hadron Collider (LHC) at CERN, is called a ‘storage ring’. This refers to an accelerator in which beams can circulate for very long periods (e.g. around 20 hours at the Diamond Light Source [21]). The LHC is also, as the name suggests, a collider because it has two beams travelling in opposite directions, to maximise the kinetic energy available, and collision points where detectors are placed to analyse the debris. Storage rings (a translation of the Italian ‘Anello di Accumulazione’) and colliders have been developed from the ideas of Bruno Touschek and Rolf Widerøe, working together in the early 1960s at Frascati National Laboratories, Italy [22].

The energies being reached at the LHC make this a very exciting time, with the promise of the possibility a deeper understanding of physics within the next few years [23].

### 1.1.5 Fixed Field Alternating Gradient Accelerators

One type of accelerator has so far been left out of this history: the Fixed Field Alternating Gradient (FFAG) accelerator. As the name suggests, these use alternating gradient focusing, but with fixed magnetic fields. FFAGs are usually reduced to footnote status in the history of particle accelerators as their development was abandoned in the fifties because they were deemed too complicated. However, there has recently been a revival

in interest based around the requirements of muon generation [24] (where high currents of high energy protons are needed), muon acceleration [25] (where a large acceleration is needed in the small time these ephemeral particles exist before they decay) and the treatment of some cancers [26] (where high currents of charged particles need to be accelerated reliably to a range of moderate energies).

This thesis will be mainly concerned with this type of accelerator, so their details and history will be more fully explained in sections 2.5 and 3.4 after some of the basic physics has been explored.

## 1.2 Introduction to Radiotherapy and Charged Particle Therapy

In the months following Roentgen's discovery of X-rays in 1895, doctors had already started using them to locate bullets in patients and photograph broken bones [27]. While only two years later, the first radiotherapy treatment took place of a young woman with a sarcoma.

Since then, after a tragic naivety about the dangers of radiation in the early years was overcome, the use of ionising radiation to treat some cancers has gone on to save millions of lives and relieve pain in many more with palliative treatments.

Mainly this has been done with X-rays, however in 1946, Wilson proposed the use of protons [28] as a more precise alternative. This was the beginning of Charged Particle Therapy (CPT), which as the name suggests is radiotherapy with electrons, protons or any ion.

This section will give an overview of radiotherapy with particular attention paid to the relative benefits of X-rays, protons and carbon ions.

### **1.2.1 The Molecular Effects of Ionising Radiation**

Radiotherapy works by damaging the DNA of cancer stem cells in the developmental stages of their life-cycle, destroying their ability to reproduce. Figure 1.7 shows that this can be done by two mechanisms: either when the incident radiation directly ionises the DNA, or indirectly when it creates chemically active molecules with missing electrons (free-radicals) from the surrounding tissue [29].

The damage to DNA is in the form of broken bonds in the individual strands of the double helix. An isolated break can usually be repaired easily as part of the DNA's normal function, however increased exposure to radiation will force errors in the recombination mechanism. This can happen in two ways: if two strands of DNA are broken in close proximity, the loose ends of one strand can recombine with the ends of the other strand, or a single break can connect to a free-radical.

Radiation damage can also occur, via the creation of free-radicals, to cell membranes and other important cell organelles.

### **1.2.2 Dose Response Curves**

Ionising radiation can damage any living cell, so it is unavoidable that healthy tissue will be damaged during radiotherapy, however this damage must be minimised, especially where vital organs are at risk. Cancer tumours are caused by over active, or unrestrained, stem cells giving them a seemingly improvised and haphazard physiology, which can

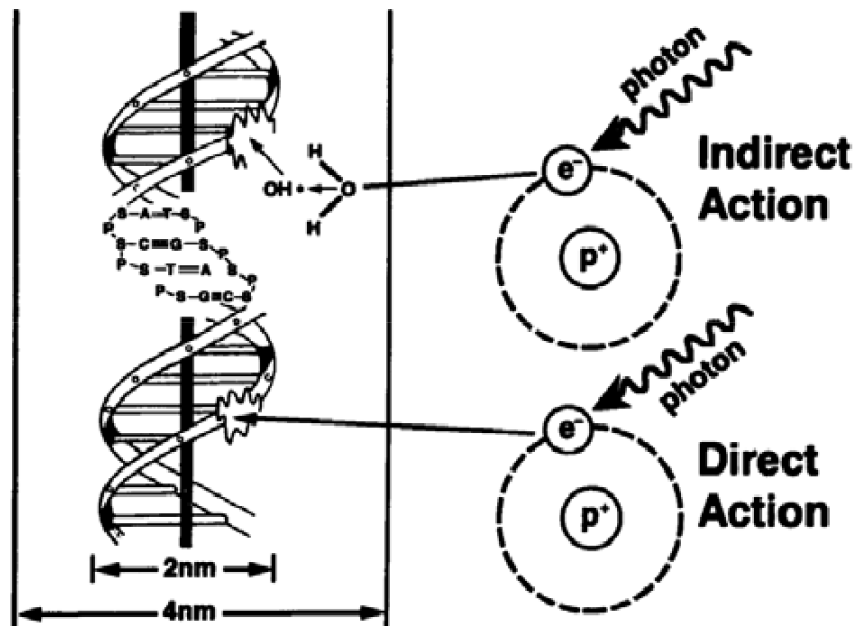


FIGURE 1.7: Direct and indirect effects of radiation on DNA [29].

make them more responsive to radiation damage and less efficient at repairing it than healthy tissue. This can go some way towards minimising the iatrogenic effects.

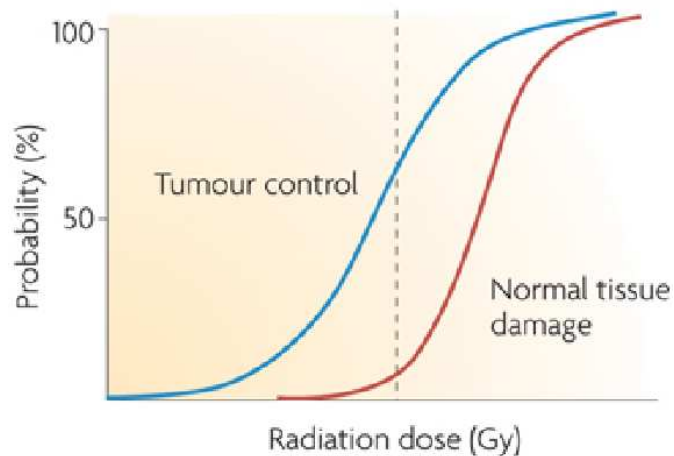


FIGURE 1.8: Examples of dose response curves for normal tissue and a tumour[30]. The more the overlap, the more precise the delivery of dose to the tumour needs to be.

The relative responses to radiation dose is plotted as 'dose response curves'. An example of this is shown in figure 1.8. The ideal situation would be one in which there is no overlap between the two curves and the tumour responds to a significantly lower dose than the surrounding healthy tissue. In this case an equal dose could be given to all the tissue

and the tumour will be destroyed, however, very often there is overlap and significant damage can be done to healthy tissue when controlling the tumour. When the radiation affects healthy and cancerous tissue equally, it is very important to be precise about where the dose is delivered. This is where the main benefit of CPT can be found.

### 1.2.3 Dose Distributions

Figure 1.9 compares the dose deposition in water of X-rays and protons as a function of depth. When X-rays travel through water, they bounce off the water molecules very frequently in almost random directions. At each interaction they will deposit a small amount of energy, which, on average, will be the same until it is absorbed. The random nature of this behaviour creates the exponential decay part of the dose deposition curve and the very long tail. The peak at start of the curve is caused by backscatter from the point where, on average, the X-rays undergo their first interaction.

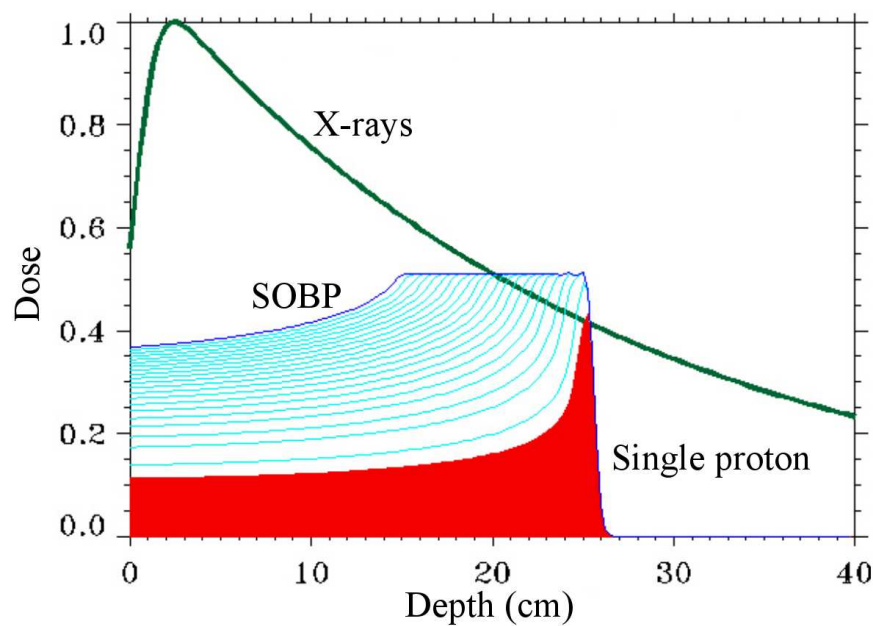


FIGURE 1.9: Comparison of dose depositions in water of X-rays and protons as a function of depth and normalised to the peak dose of the X-rays. The spread out Bragg peak (blue lines) is made up of many smaller doses, shown here as the space between the blue lines, with the red area showing the first dose [31].

Protons interact with water molecules in a different way to X-rays. At high kinetic energies, the probability a proton will collide is fairly low compared to an X-ray and the result of the interaction will mainly be a small amount of energy transmitted from the proton to the water. As the kinetic energy of the proton decreases, the probability of an interaction will increase, slowing it down even further, until all the energy is deposited. This creates the sharp ‘Bragg Peak’ (named after William Bragg who discovered it in 1903), which can be seen at the end of the curve and the very sharp fall off in dose afterwards. The small tail visible after the Bragg peak is because of freed electrons which deposit dose. However, even with the tail, the dose deposited before and after the Bragg peak is small compared to X-rays.

In practice, the Bragg peak is too small to treat the full volume of a tumour, so a spread out Bragg peak is used (SOBP). This uses the energy dependence of the Bragg peak to build up a uniform dose over a range of depths with lots of smaller doses of less energetic protons. A negative side effect of this is to increase the dose in front of the tumour, but the advantage over X-rays is still apparent, especially behind the tumour.

The Bragg peak, with its reduced dose before the tumour and very small dose behind, makes it possible to side-step some of the problem caused by overlapping dose distribution curves as well as increase the dose given to the tumour at any one time. This is especially true where vital organs are adjacent to the target tumour.

Dose given outside the tumour can also be reduced by delivering it from a number of different angles, and this is of great benefit to X-ray therapy, where state of the art ‘Tomotherapy’ techniques deliver dose in very small amounts from a source spiralling around the patient [33]. However, in some cases at least, the well defined maximum range of protons can be used to deliver a much better defined dose distribution, which

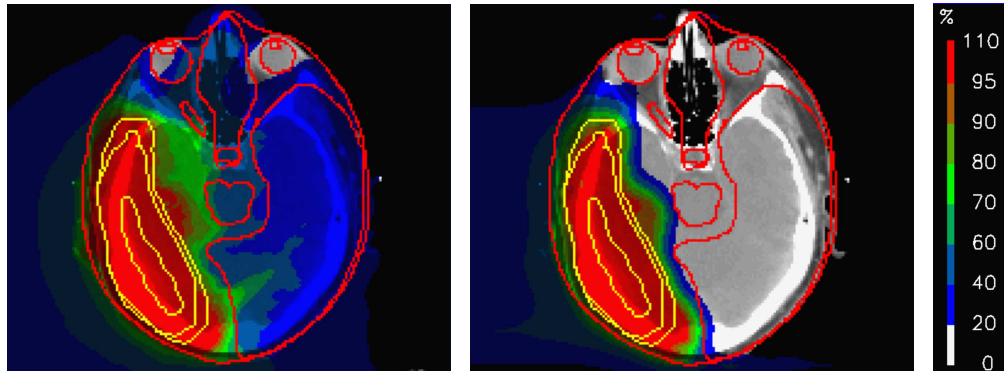


FIGURE 1.10: Comparison of tomotherapy and multi-beam proton therapy [32]. The colours represent percentage dose normalised to the prescribed dose within the tumour. The red lines demarcate areas of interest. The especially sensitive organs are the ocular nerves at the top of the image and the brain stem in the middle.

is especially useful when sensitive organs such as the brain are at risk. Figure 1.10 demonstrates this with treatment plans for a large tumour at the side of a brain. Figure 1.10(a) shows the dose distribution in a treatment plan using tomotherapy and 1.10(b) shows the distribution using protons. The tomotherapy plan manages to avoid depositing dose in the sensitive ocular nerves (outlined in red at the top of the image), where blindness can be caused by 50 Gy [34], and limiting the dose to the brain stem (at the centre of the image). However using only three beams, the proton plan manages to entirely avoid the ocular nerves, the brain stem and over half of the rest of the brain [32].

#### 1.2.4 Other Benefits of Charged Particle Therapy

The benefits of using charged particles over photons for radiotherapy do not stop there. It has already been noted that X-rays and charged particles deposit their energy differently. Another way of talking about this is the Linear Energy Transfer (LET). This is the amount of energy deposited per unit length and depends on the material as well as the type of radiation, but it tends to be higher when using charged particles [29].

The Radio-Biological Effectiveness (RBE) of a radiation gives a measure of how much damage a given dose will do. Heavier particles tend to do more direct damage to the DNA of tumour stem cells than X-rays, which combines with their higher LET to give them an increased RBE. This effect is increased even further between protons and ions such as carbon [29].

Many of the chemical reactions that make up the indirect effects of radiation involve oxygen and the degree to which oxygen is required is encapsulated in the ‘oxygen enhancement ratio’ (OER). Because the effects of X-ray radiation are about two thirds indirect, it means X-rays have a high OER, however, it also means they lose effectiveness in hypoxic tissue. This is of particular concern because the peculiar physiology of cancer tumours mean they can have large volumes, especially at their centres, where blood vessels carrying oxygen do not reach. Ions like carbon create more direct effects which do not need the presence of oxygen, so this problem is reduced.

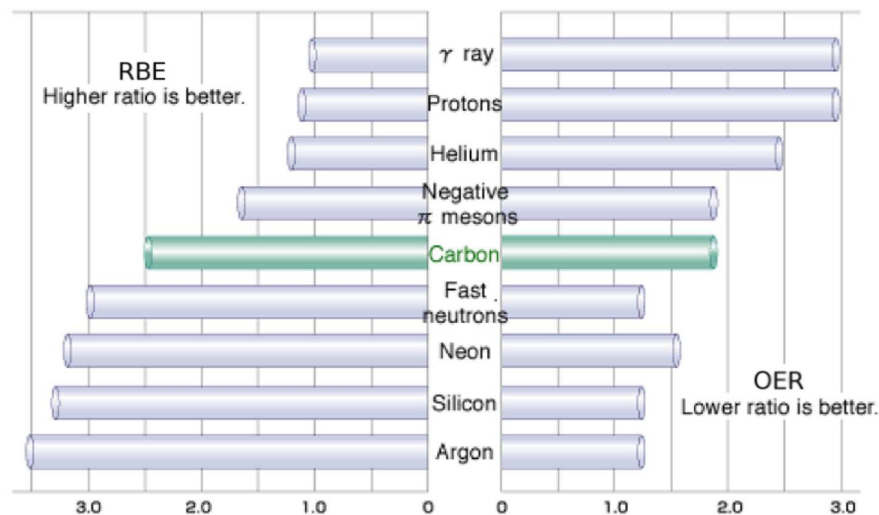


FIGURE 1.11: Radio biological effectiveness (RBE) and oxygen enhancement ratio (OER) for a variety of radiation types. A low OER is desirable because it means the radiation can be effective in hypoxic regions of a tumour [35]

Figure 1.11 shows the relative RBEs and OERs for a number of different radiation types. From this it can be seen that the advantage protons have over X-rays in their

dose distributions is not matched by an advantage here. However, carbon ions represent a major improvement over both protons and X-rays for RBE and OER.

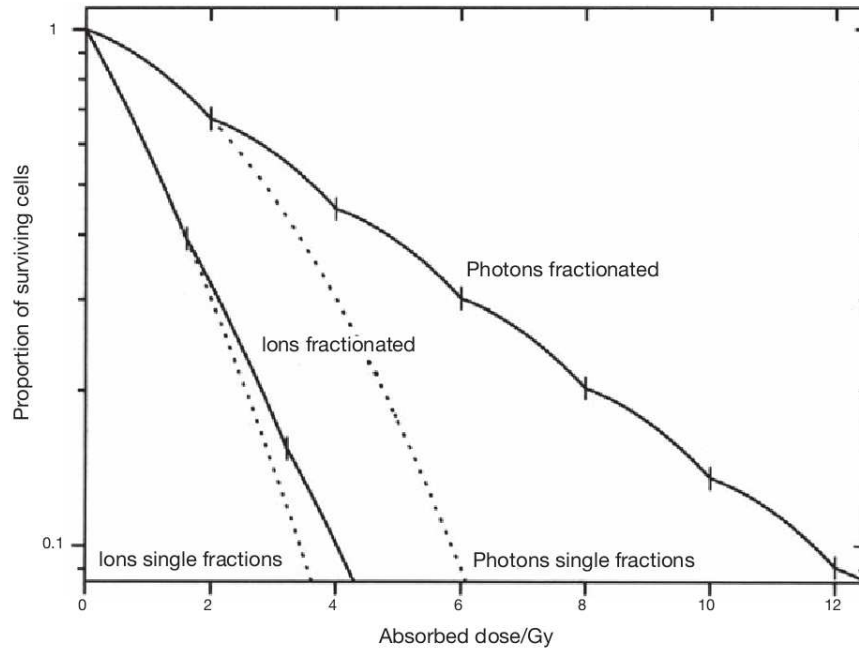


FIGURE 1.12: Comparison of the effect of fractionation in X-ray therapy and charged particle therapy [36, p.43]. The dotted lines show the response to a single dose and the solid lines show the response to fractions. There is a dramatic difference in the number of fractions required and the total dose.

The reason LET, RBE and OER are of practical importance is to do with the amount of time a patient spends being treated. Because of the effects to healthy tissue, the complete dose is given to a patient in a series of smaller doses called ‘fractions’. Figure 1.12 shows the difference in the number of fractions required when using X-rays and ions. This does not just save time; because tumour cells will recover between fractions, reducing the number of fractions can reduce the total dose required to control a tumour by a factor of 2  $\rightarrow$  10 depending on the clinical application [26]. This reduces the side effects to the patient, reduces the probability of secondary cancers caused by the treatment radiation and the reduced time it takes to control a tumour can increase the amount of people treated at a facility.

### 1.2.5 Caveats to the Superiority of Charged Particle Therapy

Although the benefits of CPT (especially carbon) are overwhelming in principle, they must be qualified by some of the problems with their practical application.

CPT will not take over X-rays as the main form of cancer therapy in the foreseeable future mainly because of the relative costs and space requirements. X-rays are usually produced by compact electron linacs using readily available and cheap technology ( $\approx$  £1 → 2 million [37]). Whereas, even though it can be bought almost ‘off the shelf’ at present, the technology for delivering protons is still around 20 times more expensive than conventional X-ray radiotherapy [38, p.342]. Carbon therapy is even more difficult to achieve as the technology is still largely experimental and requires very large amounts of space.

There is also a practical problem with determining the exact location of dose delivery within a patient. If CPT is going to be used to deliver much larger doses than at present, the clinical practitioners have to be completely certain that this dose is being deposited completely within the tumour. Unfortunately, due to the limitations of current imaging as well as the effects of organ motion and tumour shrinkage during treatment, this cannot always be done. This can result in practitioners either reducing the dose or adding safety margins to the treatment area, which can eat away at the advantage CPT has over X-ray therapy [39]. However, an effort to produce good quality real time imaging is ongoing [40], so this may not be a problem forever.

The final caveat is the proof of the biological benefits of CPT, especially using carbon ions, is not entirely there. This section has shown that in principle CPT should be a much better treatment than conventional radiotherapy in both tumour control and cancer recurrence rates, however, according to the US Agency for Healthcare Research

and Quality there is not enough *clinical* data to say this for sure [41]. This may be true, but the only way to discover if CPT really is better than X-ray therapy is to do long term studies, which means many more CPT centres will be required and new ways of delivering therapeutic protons and carbon ions must be found.

### 1.3 Chapter Summary

This chapter demonstrated the author's understanding of the general history of particle accelerators (section 1.1) and Charged Particle Therapy (section 1.2). The history of particle accelerators could be said to have started with the discovery of the electron, but the roots of modern accelerators are in three types of accelerator technology: the electrostatic accelerator, the resonating accelerator and the betatron (sections 1.1.1, 1.1.2 and 1.1.3). In modern high energy physics the synchrotron is dominant (section 1.1.4), but cyclotrons and linacs are used more generally for industrial and medical applications. Charged particle therapy has two main advantages over X-ray therapy: it is more precise (section 1.2.3) and requires fewer dose fractions (section 1.2.4). X-ray therapy is, for the foreseeable future, cheaper and uses much less space (section 1.2.5).

## Chapter 2

# Basic Particle Accelerator Physics

### 2.1 Introduction

In the broadest sense, a particle accelerator is a series of electromagnetic elements which increase the momentum of a beam of particles, direct it and keep it focused. Electric fields [13, p.19] are generally used to accelerate the particles, while the focusing and bending is done by a configuration of magnets [42, p.38]. This configuration is called the magnetic lattice and is the part of accelerator physics that this thesis mainly considers.

Beyond this simple premise lies a very complicated and detailed field of science that has developed from J.J Thompson discovering electrons in 1897 to the Large Hadron Collider probing the nature of mass in 2010; while splitting the atom, the invention of the television set and the discovery of quarks and much more were achieved along the way. More complete descriptions can be found in a variety of text books ([13], [5] and [42] for example) however, this section aims to give a brief introduction to the concepts required to understand the area of accelerator physics that this thesis deals with as well as its wider context.

## 2.2 Coordinate System

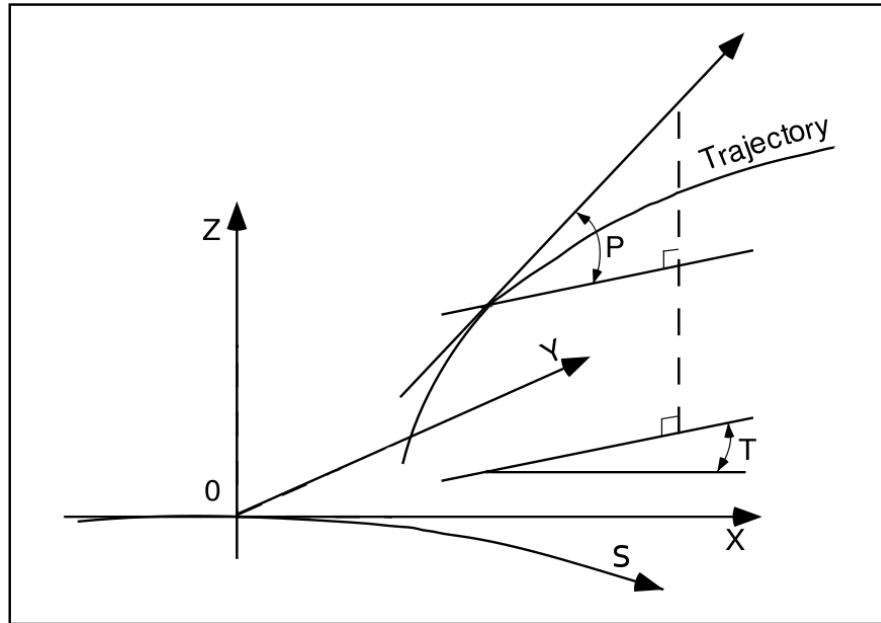


FIGURE 2.1: The co-ordinate system.

The coordinate system this thesis uses is that used by the particle accelerator simulation code Zgoubi [43, p.13] and is shown in figure 2.1. The coordinate  $s$  is the distance along an ideal path through the accelerator called the reference orbit,  $y$  is the horizontal axis which runs from the centre of the accelerator through  $s$  and outwards,  $z$  is the vertical axis, perpendicular to both  $y$  and  $s$ ,  $t$  is the angle the direction of the particle makes with  $s$  in the horizontal plane and  $p$  is the equivalent in the vertical plane (alternately, these may be referred to as  $y'$  and  $z'$ ).

## 2.3 Accelerator Types

There are four main types of particle accelerator: linear accelerators (linacs), cyclotrons, synchrotrons and Fixed Field Alternating Gradient accelerators (FFAGs). Linacs are linear accelerators and are the most common. Cyclotrons are the simplest of the circular accelerators and generally use fixed magnetic fields while accelerating high currents of

particles over a limited energy range. Synchrotrons achieve the highest energy (the LHC at CERN is a synchrotron), but are more complicated than Cyclotrons and require magnets with fields that vary over time. Fixed Field Alternating Gradient accelerators take aspects from Cyclotrons and Synchrotrons, but their development was abandoned in the 1950s because they were deemed too complicated. They have been recently revived, however, and may offer solutions to problems in which very fast acceleration of a high current of particles to moderate energies is required [44].

## 2.4 Circular Motion and Magnetic Rigidity

A charged particle moving in a magnetic field,  $B$ , experiences a force,  $F$ , perpendicular to the direction of the field and the direction of motion:

$$F = qv \times B \quad (2.1)$$

where  $q$  is the charge of the particle and  $v$  is its velocity. If the field is uniform, this results in circular motion in the plane of the force and the direction of  $v$  (figure 2.2), with the radius dependent on the strength of the field, the particle's momentum and charge. This is characterised by the magnetic rigidity:

$$B\rho = \frac{p}{q} \quad (2.2)$$

where  $\rho$  is the radius of curvature and  $p$  is the momentum of the particle. This is an interesting equation to help understand the differences between the types of circular accelerators. In all three, momentum will increase as the particle accelerates. In most cases the charge will remain constant, so the increase in momentum must be compensated

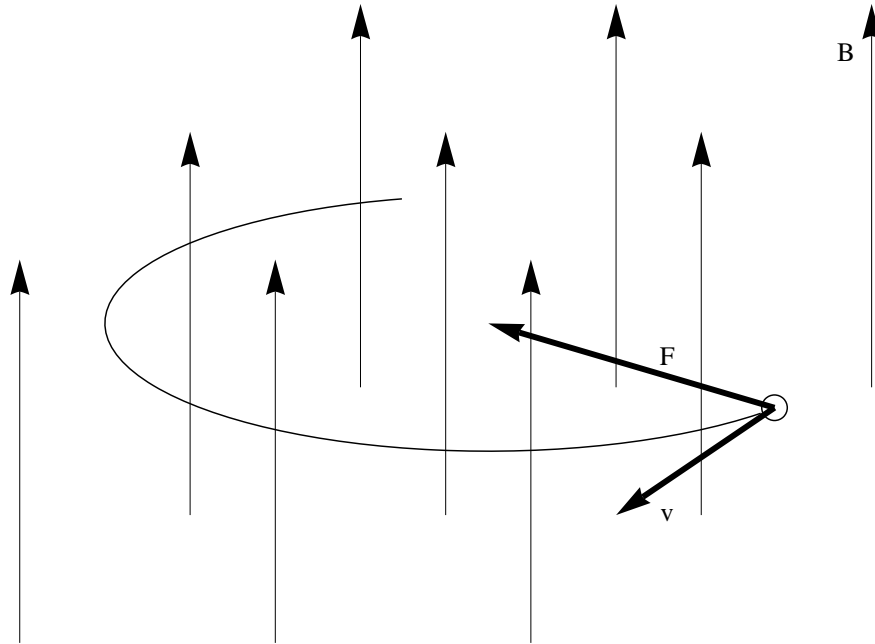


FIGURE 2.2: A particle travelling in a uniform magnetic field will move in a circle

for by an increase in  $B$ ,  $\rho$  or both. Generally speaking, in a Cyclotron,  $B$  is kept constant and  $\rho$  increases; in a Synchrotron,  $\rho$  is kept constant and  $B$  is increased; and in an FFAG, a combination of  $\rho$  and  $B$  is varied.

### 2.4.1 Aperture

The change in  $\rho$  also has an impact on the ‘aperture’ of each type of machine. The aperture is defined as the space required in a magnet to fit the beam over the whole of the energy range. So the Cyclotron has the highest aperture, because  $\rho$  is allowed to grow as the particle accelerates; the Synchrotron has the smallest aperture, because  $\rho$  does not change; and the FFAG is somewhere in between.

### 2.4.2 Closed Orbits

A closed orbit is a path through a periodic structure in which the start point and the end point are the same. In a non periodic structure, this thesis may refer to an

equilibrium orbit or reference orbit instead, which is the ideal path of a particle with a given momentum. In reality, most particles will not be exactly on the closed orbit. They may have slightly different starting positions or angles, which if left unchecked could result in them being lost from the accelerator. This is where focusing is required.

### 2.4.3 Focusing

The simplest form of focusing happens in a completely uniform field. If a particle starts at a position slightly removed from the desired closed orbit, it will simply shift its centre of rotation. From the point of view of the reference orbit, the particle will be oscillating around it. This is called ‘weak focusing’ and is only important in basic Cyclotrons. The more important ‘strong focusing’ uses fields that are not uniform, but have a gradient.

Consider the rigidity equation (equation 2.2). If a particle is displaced horizontally from its closed orbit away from the centre of the accelerator, it could be angled back by increasing the field strength. Conversely, if the particle were inside the closed orbit, the field could be reduced and the particle moved outwards. For this reason, adding a gradient to the field where  $\frac{dB_z}{dy} > 0$  will force off orbit particles towards their closed orbit and stop them from being lost; this is called strong focusing. However, there is a problem. From Maxwell’s equations, it follows that [45, p.29-5]:

$$\frac{dB_z}{dy} = \frac{dB_y}{dz} \quad (2.3)$$

Unfortunately for accelerator physicists, a positive gradient in the vertical plane will force particles away from the closed orbit; defocusing the beam. To understand this, consider a particle immediately above the closed orbit in a field with positive horizontal and vertical field gradient. Assuming the horizontal field is zero at the closed orbit,



FIGURE 2.3: A particle just above the reference orbit will experience a force upwards if  $B_y$  is positive.

a positive gradient means the particle will feel a positive field. As shown in figure 2.3, a positive  $B_z$  gives the particle a force towards the centre of the accelerator, but the corresponding  $B_y$  field will result in an upward force being applied to the particle. A particle below the closed orbit will feel a negative field and a downward force. A negative gradient will produce focusing in the vertical plane, however, it will also produce defocusing in the horizontal plane.

As already mentioned, Cyclotrons have weak focusing in the horizontal plane. However, in a completely uniform field, any particle with a deflection in the vertical plane will spiral away until it is lost. Luckily only a small amount of focusing in the vertical plane is required to prevent this, and the defocusing it causes in the horizontal plane is tolerated [5, p.15].

The focusing in the Cyclotron is not sufficient for higher energy machines involving many revolutions. To increase focusing and solve the problem created by equation 2.3, ‘alternate gradient focusing’ is employed [45, p.29-6]. This is where elements with horizontally focusing and defocusing fields (simply referred to as focusing and defocusing) are used in combination to bring about overall focusing in both the vertical and horizontal planes [5, p.30].

#### 2.4.4 Betatron Oscillations and the Effective Gradient

The behaviour of off-orbit particles is important to the design of particle accelerators because the focusing gradient will not make all the particles move neatly along the closed orbit. In fact, the field gradient causes the off-orbit particles to oscillate around the closed orbit, this motion is called a betatron oscillation. Consider a field where:

$$\frac{dB_z}{dy} \propto c \cdot y \quad (2.4)$$

where  $c$  is an arbitrary constant. This is called a linear field because the gradient is proportional to the linear term;  $y$ . If the field gradient is related to  $y$  in any other way, it would be a non-linear field.

We are interested in the motion of the particle along the coordinate  $s$ , so consider the deflection given by this field over the short distance;  $ds$ . The force is proportional to the field (equation 2.1) which we have set as proportional to  $y$ , so we can see that:

$$\frac{dy}{ds} = k_e \cdot y \quad ds \quad (2.5)$$

where  $k_e$  is a constant of proportionality. To understand the characteristics of  $k_e$ , consider that the deflection in  $y$ , will be proportional to the field gradient, and inversely proportional to the rigidity of the particle. This is expressed as the effective gradient [5, p.32]:

$$k_e = \frac{1}{B\rho} \frac{dB_z}{dy} \quad (2.6)$$

Particle accelerators do not have uniform fields all the way round the ring, so  $k_e$  is a function of  $s$ . Equation 2.6 differentiated is [5, p.33]:

$$y'' + \left[ \frac{1}{\rho(s)^2} - k_e(s) \right] y = 0 \quad (2.7)$$

which is similar in form to a simple harmonic oscillator, except here we use  $s$  instead of time. In the vertical plane, where there is no bending and so no rigidity term, the equation of motion is even simpler:

$$z'' + k_e(s)z = 0 \quad (2.8)$$

These are forms of Hill's equation [42, p.250] and the solution gives us more insight into how the motion of a particle around the accelerator can be described [5, p.33].

$$y = \sqrt{\beta(s)\varepsilon} \cos[\phi(s) + \phi_0] \quad (2.9)$$

$\phi$  is called the phase and  $\sqrt{\beta(s)\varepsilon}$  is the amplitude modifier, which is made up of what are called the beta function ( $\beta(s)$ ) and the emittance ( $\varepsilon$ ). The phase of an oscillation is a measure of the point the oscillation has reached, so a phase of  $\pi$  radians, would be half way through and a  $2\pi$  phase would be a complete oscillation. The amplitude modifier in an oscillator describes the maximum and minimum points in the oscillation, since the cos or sin part will always have the range  $-1 \leq \cos(\phi) \leq 1$ .

Equation 2.9 is, again, analogous to simple harmonic motion, with a phase  $\phi$  and an amplitude modifier  $\sqrt{\beta(s)\varepsilon}$ . However, there are some important differences. Firstly, part of the amplitude modifier is a function of  $s$ , but also, the phase is not dependent on  $s$  in a simple way, as it would be with time in, for example, a pendulum.

The beta function's dependence on  $s$  comes from the fact that it is a property of the magnetic lattice, and describes the shape of the envelope of possible particle positions, relative to the closed orbit, through the lattice. The emittance, on the other hand, has no  $s$  dependence and its precise meaning will be explained shortly, but for now it is sufficient to know it limits the size of a particle's betatron oscillation.

The relation of  $\phi$  to  $s$  depends on how the effective gradient changes with  $s$ ; which will have been constructed by the designer along with bending elements and drift spaces. However,  $\phi$  and  $\beta$  have to have the same periodicity in a closed ring and are linked by [5, p.33]:

$$\phi' = \frac{1}{\beta} \quad \text{and} \quad \phi = \int \frac{ds}{\beta} \quad (2.10)$$

So the higher  $\beta$  the smaller  $\phi$  (referred to as the phase advance) and vice-versa. This holds for any length of lattice, so it gives the lattice designer their control over the beta function. Qualitatively, it is straight forward to see that the effective gradient will control the amplitude of the oscillation and its phase advance: The higher the gradient, the more quickly the field strength will diverge from its value at the equilibrium orbit, so the shorter a distance the particle will travel before being forced back. Figure 2.4 is a visualisation of the path a particle might take through a circular accelerator. The amplitude and frequency of the betatron oscillation will vary depending on the field the particle is travelling through.

### 2.4.5 Tune

The tune is defined as the number of betatron oscillations over some length of  $s$ . So the 'machine tune' will be the number of oscillations in one turn of the accelerator. Accelerators are commonly split up into 'cells', which are sections of lattice that have

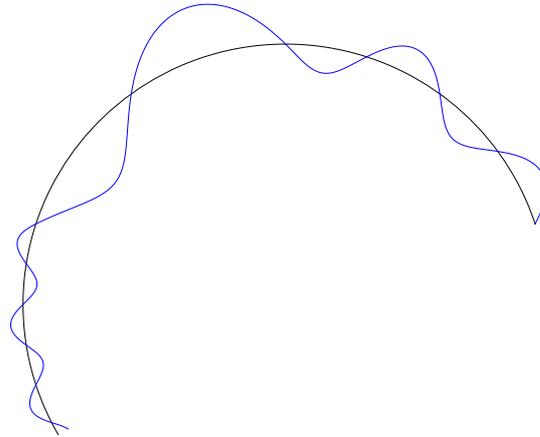


FIGURE 2.4: Possible path of a particle through a section of a circular accelerator The black line is the closed orbit and the blue line is the particle path.

some periodicity about them. For example, an accelerator might be made up of cells which have one focusing and one defocusing magnet separated by lengths with spaces in between (called FODO cells). A ‘cell tune’ will be the number of oscillations per cell.

#### 2.4.6 Resonances

The tune is important because under the right circumstances in accelerators in which particles circulate many times, betatron oscillations can resonate and destroy the beam. This subject is not immediately relevant to this thesis, however, it is worth touching upon to help explain some of the characteristics of Synchrotrons and FFAGs. There are two ways in which this can happen. One way is the horizontal and vertical betatron oscillations constructively interfering with each other if the sum or the difference of their tune is an integer [13, p.188]. The other is for a betatron tune to resonate with an imperfection in the lattice [5, p.87]. If there is an imperfection at any point in the ring, the particle may receive a small kick; and if a particle has an integer number of betatron oscillations per turn, the particle will come to exactly the same point every time it completes a revolution and will receive the same kick over and over again until the particle is thrown out of the ring. The same will happen with a tune that is an exact

fraction,  $\frac{m}{n}$  (where  $m$  and  $n$  are integers), because the particle will receive the kick every  $n$  turns. If the tune is not an integer or exact fraction, the particle will receive the kick at different phases of its oscillation each time and the effect of the kick will average to zero.

This is why controlling the tune, and the effective gradient, is such an important part of Synchrotron and FFAG design. In Synchrotrons, the field gradient (as well as the dipole strength and, at low energies, RF frequency) is varied over time in synchronisation with the accelerating particles, and in the FFAG, the gradient is varied over position to match the closed orbits (this will be discussed in greater depth in 2.5). This thesis deals with lattices through which particles will only travel once, so resonances will not always be as important as in a recirculating lattice, however, if the resonance is large enough it could effect the emittance of the beam, which will be explained in the next section.

#### 2.4.7 Bunches and the Phase Space Ellipse

At this point, it is important to recognise that particles do not travel through real accelerators one at a time. Instead, particles travel as part of ‘bunches’, which are a large number of particles having a distribution of slightly different starting angles and positions, as well as different starting phases;  $\phi_0$ . The bunching is an artefact of the acceleration process [5, p.59] and the distribution is determined by how the particles are sourced.

The tracks of a bunch of five particles may look something like figure 2.5 (in reality, the number of particles in a bunch would likely be nearer  $\approx 10^9$ ). Note that the different particle oscillations have different maximum amplitudes; some particles stay close to the closed orbit, while others stray further away. This might not, at first, seem possible,

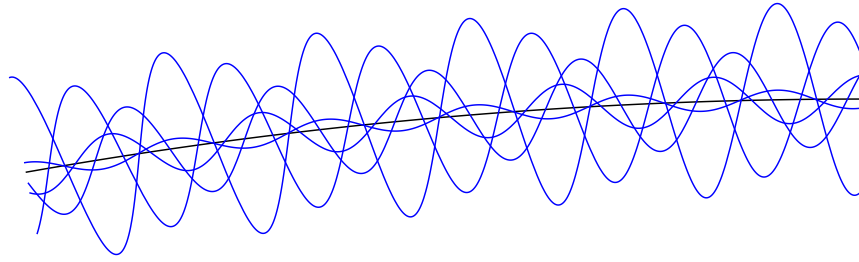


FIGURE 2.5: A number of particle oscillations with differing  $\phi_0$ s and amplitudes.  $\phi$  is the same for each particle, however.

because all these particles are described by the same equation of motion (equation 2.9). However, the factors of the amplitude modifier,  $\varepsilon$  and  $\beta(s)$  have not yet been properly defined because we have not been using  $\varepsilon$  and  $\beta$  in relation to bunches of particles. The emittance and the beta function do describe the amplitude of the oscillations of the particles, but it is done in a statistical way, as would be expected when dealing with such large numbers of particles. Both these terms are defined by the particles with the highest amplitudes in the bunch, (or more precisely, at some number of standard deviations away from the particle with the mean amplitude [5, p.50], but for simplicity, they will be referred to as having the maximum amplitude).

So when we plot the beta function, we are showing how the maximum amplitude changes through the accelerator. However as we have a bunch of particles, all with different  $\phi_0$ s, at any one point there will probably always be a particle at that maximum amplitude. This means that the shape of the  $\beta$  function (or more precisely its square root) is the shape that the bunch makes as it travels along the closed orbit. The  $\beta$  function can also be described as the ‘betatron envelope’: the shape of the space to which a particle travelling around the accelerator is restricted.

It is important to be careful to refer to the ‘shape’ of the  $\beta$  function, rather than its absolute size, because although it is measured in metres, in equation 2.9,  $\beta$  is modified

by the emittance. As has been said, the  $\beta$  function is a property of the specific lattice design, but we can now see that the emittance is purely a property of the particle bunch.

To understand its physical significance, consider the motion of one of the maximum amplitude particles in a two dimensional space made up of its horizontal distance from the closed orbit and the angle it makes with it, which is called the ‘phase space’. If the equation of motion were simply:

$$y = \cos(\phi + \phi_0) \quad (2.11)$$

the shape of the motion in phase space would describe a simple circle: as the particle increases in  $y$ , it decreases in  $y'$ . However as equation 2.9 has an  $s$  dependent amplitude, the situation becomes much more complicated. By differentiating equation 2.9 we find that:

$$y' = -\sqrt{\frac{\varepsilon}{\beta(s)}} \sin[\phi(s) + \phi_0] + \sqrt{\frac{\varepsilon}{\beta(s)}} \frac{\beta'(s)}{2} \cos[\phi(s) + \phi_0] \quad (2.12)$$

and the phase space diagram for a single particle travelling around the ring would be very complicated and not very instructive. However, at a single  $s$ ,  $\beta$  and  $\phi$  will be fixed, but a bunch of particles will have a full range of  $\phi_0$ s and there will be a large number with the maximum amplitude. Plotting the maximum amplitude particles together will give a simple ellipse, such as that in figure 2.6.

The emittance is the area of this ellipse, and through simple magnetic lattices, with no acceleration, collimation or other forms of beam loss, it will remain constant [5, p.45]. Collimation can bring down the emittance because, if you take away the maximum amplitude particle in figure 2.5, the new emittance will be defined by the second highest amplitude particle, and so on.

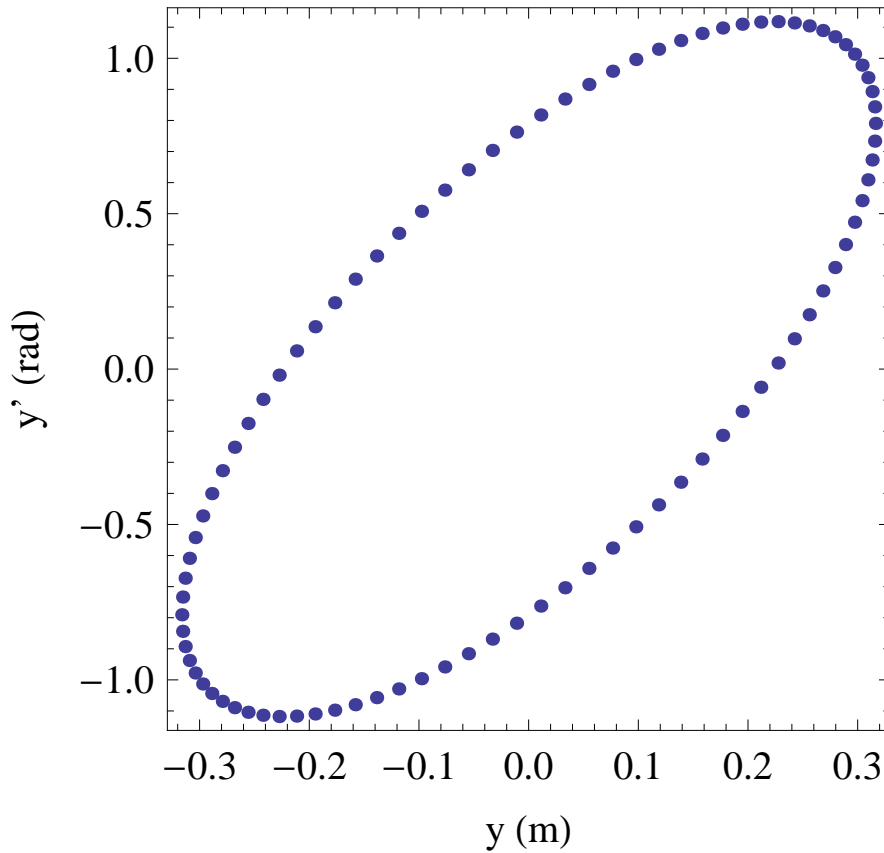


FIGURE 2.6: At a single  $s$ , there are enough particles with the maximum amplitude to have a full range of  $\phi_{0s}$  and describe an ellipse.

The decrease and increase of emittance with acceleration and deceleration is called ‘adiabatic damping’ and is caused by the effects of relativity. ‘Adiabatic damping’ is a bit of a misnomer because just by using a different reference frame, it can be seen that emittance *is* constant when accelerating into relativistic speeds. Emittance will shrink in the lab frame as the particles accelerate if we use Classical mechanics, however, an emittance defined using Hamiltonian mechanics will not be affected [5, p.48] [42, p.292].

While discussing adiabatic damping,  $\gamma$  and  $\beta$  take on their relativistic definitions, rather than the Twiss definitions used elsewhere.

With Hamiltonian mechanics, coordinates in phase space would not be  $(y, y')$ , but instead be the ‘canonical coordinates’  $(q, p)$ , where:

$$q = y, \quad p = \gamma m y' \quad (2.13)$$

where  $m$  is the mass and  $\gamma$  is the relativistic definition

$$\gamma = \sqrt{1 - \beta^2} \quad (2.14)$$

and  $\beta$  is the relativistic definition

$$\beta = \frac{v}{c} \quad (2.15)$$

not the  $\beta$  function described above in equation 2.9 and the  $\gamma$  defined later in equation 2.18.  $v$  and  $c$  are the velocity of the particle and the speed of light respectively. Using these coordinates, we find a ‘normalised emittance’ which is defined as

$$\varepsilon^* = (\beta\gamma)\varepsilon \quad (2.16)$$

and remains constant throughout acceleration[5]. Again,  $\gamma$  and  $\beta$  are their relativistic definitions, however, from this point on, they revert back to their definitions as Twiss parameters.

The phase space ellipse can tell us the value of the  $\beta$  function (from equation 2.9, not the relativistic version) by taking the highest amplitude particle: i.e. when  $\cos[\phi + \phi_0] = 1$ ,  $y = \sqrt{\varepsilon\beta(s)}$ . There are also two other functions related to  $\beta$  that are used to describe the beam and can be calculated from the phase space ellipse.  $\alpha$  is a measure of the rate of change of  $\beta$  and is defined as:

$$\alpha = \frac{\beta'}{2} \quad (2.17)$$

$\gamma$  is the equivalent of  $\beta$  in  $y'$  in that  $y'_{max} = \sqrt{\varepsilon\gamma}$ . It is defined as:

$$\gamma = \frac{1 + \alpha^2}{\beta} \quad (2.18)$$

with  $\beta$ ,  $\alpha$  and  $\gamma$  defined, we can calculate the emittance thus:

$$\varepsilon = \beta y'^2 + 2\alpha y y' + \gamma y^2 \quad (2.19)$$

where  $y$  and  $y'$  are taken as the highest value in the ellipse. This is also known as the ‘Courant Snyder Invariant’ [5, p.46] and collectively,  $\beta$ ,  $\alpha$  and  $\gamma$  are referred to as the Twiss parameters<sup>1</sup>.

### 2.4.8 Acceptance and Smear

Acceptance is usually defined as the largest emittance the beam can have before it grazes an obstacle, usually a collimator, divided by  $\pi$  [5, p.51]. This thesis, however, is looking at short lengths of transport line as opposed to thousands of turns of accelerator rings, so a more sensitive definition is perhaps more useful. For this, the concept of ‘Smear’ is useful.

‘Smear’ is a measure of the distortion of the beam, or more precisely, the deviation of a circle of particles from their initial configuration and is defined as:

$$smear = \sqrt{\frac{\langle (\varepsilon_i - \langle \varepsilon_i \rangle)^2 \rangle}{\langle \varepsilon_i \rangle}} \quad (2.20)$$

---

<sup>1</sup>By rights these should be also be named after Courant and Snyder, as they developed them. However this thesis will use the more widely accepted name for clarity.

where  $\varepsilon_i$  is calculated using equation 2.19, but is not exactly the same as the emittance. It is calculated for each individual particle with  $y$  and  $y'$  in the place of  $y_{max}$  and  $y'_{max}$ . Vertical phase space ( $z, z'$ ) smear is calculated in the same way.

So the smear is the mean deviation from the average individual particle emittance, divided by the average individual particle emittance, but to get a visual idea of what it means, consider figure 2.7. The blue dots represent the particles at the start of a section of lattice, and the red dots represent the same particles at the end. The different rings of particles have been given different emittances and result in different values of Smear. As you can see, the central ring with the smallest emittance has a very small smear (the blue ring is obscured by the red, they are that closely matched); while the outer ring has become very distorted and has a smear a factor of ten larger.

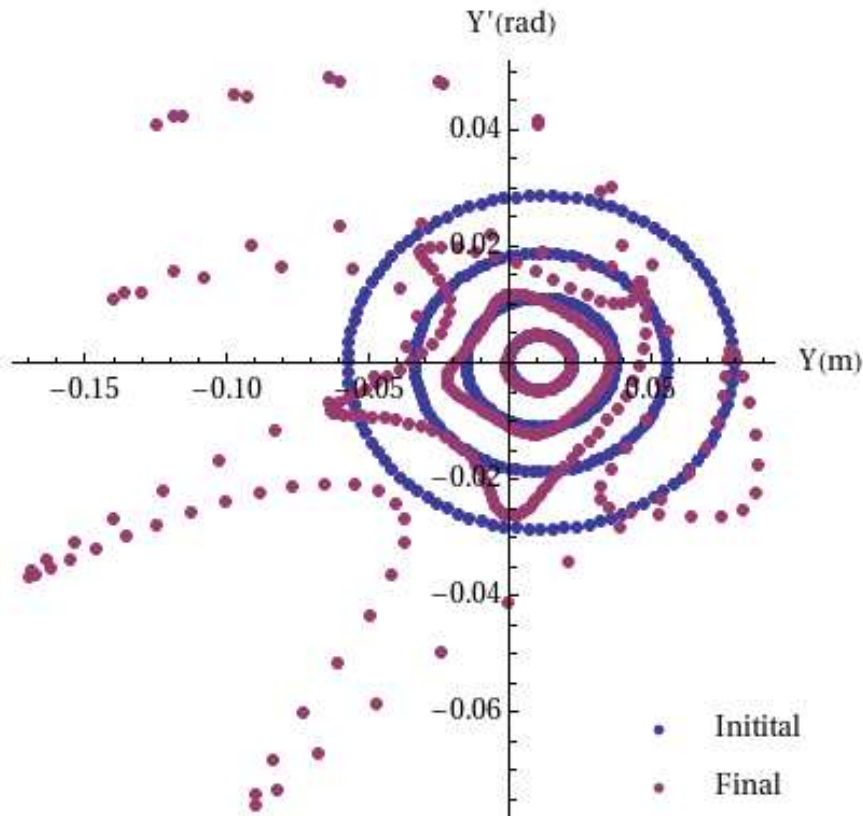


FIGURE 2.7: Phase space ellipses with smears of (from centre) 0.1, 0.25, 0.5 and 1.

The acceptance, then, is defined as the initial emittance given to particles which results in an arbitrarily defined smear at the end. A smear of 0.1 was chosen to be acceptable initially, however this may change as the studies develop. A smear of 0.1 means the average deviation from the average particle emittance is 10% when the particles reach the end. The initial emittance is equal in both planes and the acceptance is found when the smear reaches the limit in either plane.

Figures 2.7 and 2.8 give an illustration of why a smear limit of 0.1 was chosen. In figure 2.7 phase space ellipses with smears of 0.25 upwards show noticeable distortion, so a significant change to the properties to the beam over the full range of the transport line is likely to occur; whereas the ellipse with a 0.1 smear is much less effected. The  $10\pi$  (mm mrad) emittance shown in figure 2.8 appears only slightly affected through a lattice with an acceptance of  $54\pi$  (mm mrad) and has a smear of just 0.004.

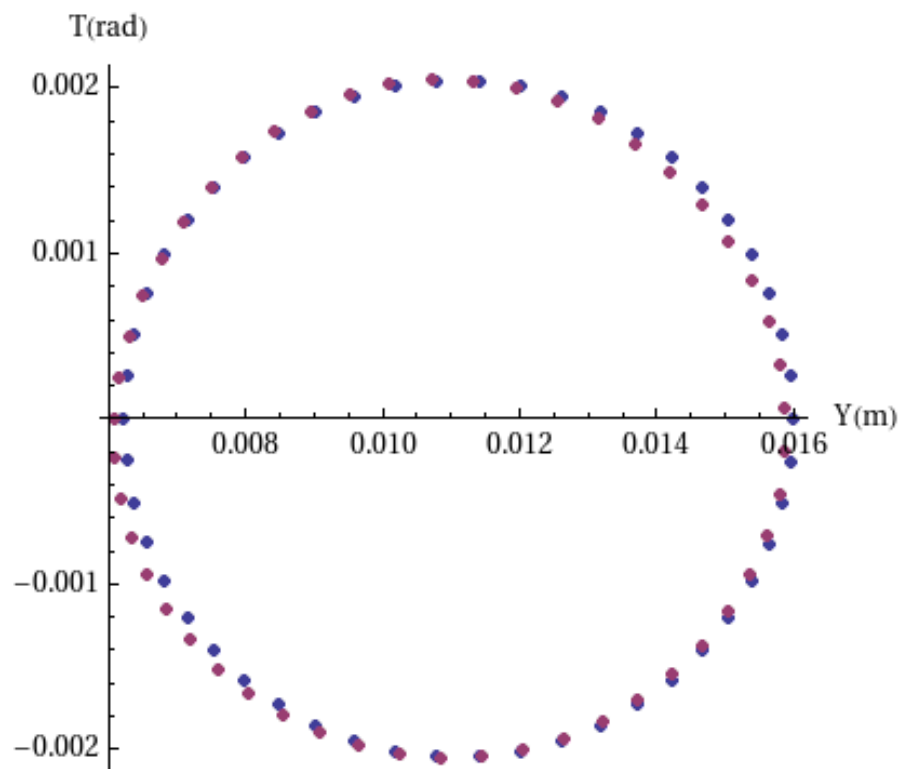


FIGURE 2.8: A  $10\pi$  (mm mrad) emittance in a lattice with a  $54\pi$  (mm mrad) acceptance defined using a smear of 0.1.

### 2.4.9 Dispersion

Just as a bunch of particles will have a distribution of  $y$  and  $y'$  within it, it will also have a distribution of momenta. Most acceleration schemes deal with this by giving more of an accelerating kick to particles travelling slower than an ideal particle and less of a kick to those travelling quicker. In a similar way to off-orbit particles oscillating around the closed orbit, this leads to particles oscillating around the ideal momentum, without precisely joining it [5, p.60]. The details of this is not immediately relevant to this thesis because we will be studying non-circulating sections of lattice and will not need to design an acceleration scheme. However, the dispersion itself is relevant because it will be important to control it through certain sections of the lattice.

For a particle with momentum  $p$  travelling in a bunch where  $p_0$  is the ideal momentum, the deviation is defined as:

$$\delta = \frac{\Delta p}{p} \quad (2.21)$$

where:

$$\Delta p = p - p_0 \quad (2.22)$$

In practice, the different momenta of the particles will result in slightly different closed orbits given by:

$$y(s) = \delta D(s) \quad (2.23)$$

The dispersion function  $D(s)$  is derived from the equation of motion (equation 2.7), but with a driving term.  $D(s)$  can be obtained experimentally by observing the difference in the positions of two particles with different  $\delta$ s at any given  $s$ . Using equation 2.22.

$$D(s) = \frac{\Delta u}{\delta_2 - \delta_1} \quad (2.24)$$

Where  $\Delta u$  is the difference in energy between the two particles [42, p.177].

### 2.4.10 Dispersion Suppression

In order to reduce this dispersion, one can use betatron oscillations to our advantage. Consider figure 2.9. A particle with a momentum deviation  $\delta$  has the closed orbit position  $\delta D(s)_1$  in Cell 1 and  $\delta D(s)_2$  in Cell 2. If the particle is exactly on the closed orbit in Cell 1, it will start to oscillate around the new closed orbit in cell 2. Now, if Cell 2 is designed so that  $\delta D(s)_2$  is half way between  $\delta D(s)_1$  and the ideal orbit, half a betatron oscillation will bring the particle to the ideal orbit [16, p.77]. This idea can be applied to a distribution of  $\delta$ s if a field can be designed in which the  $\delta D(s)_2$  positions are half the  $\delta D(s)_1$  positions for all particles.

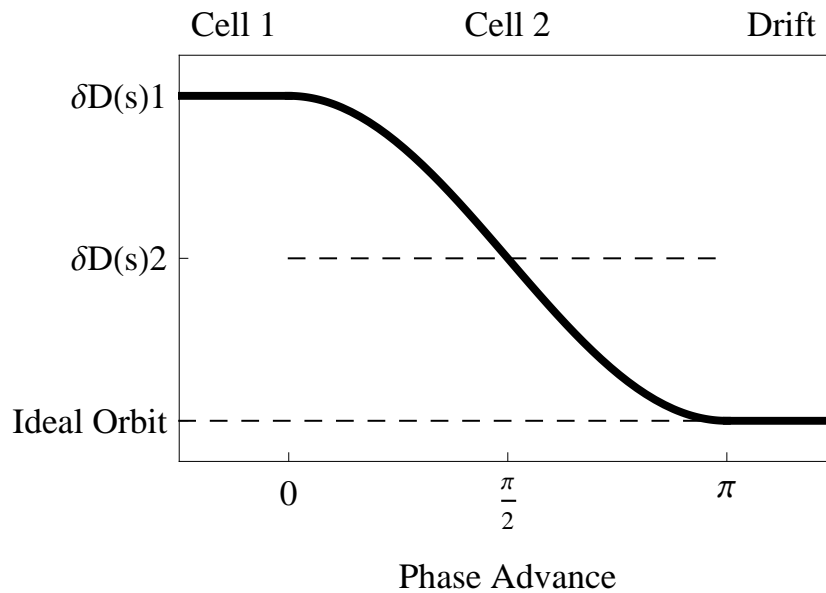


FIGURE 2.9: Half of a betatron oscillation can be used to move a particle from one orbit to another. This is the principle behind dispersion suppression.

## 2.5 Fixed Field Alternating Gradient Accelerators

Fixed Field Alternating Gradient accelerators were conceived of in the early 1950s as a way to reduce the radius relative to existing circular accelerators. However, their development was stalled due to the complexity of their magnets compared to the developing Synchrotron. A useful, and classic, paper on this subject is [46]. The simplest of the designs presented, and one most relevant to this thesis, is the ‘Radial-Sector FFAg’ [46, p.1838]. (See section 3.4 for further discussion.)

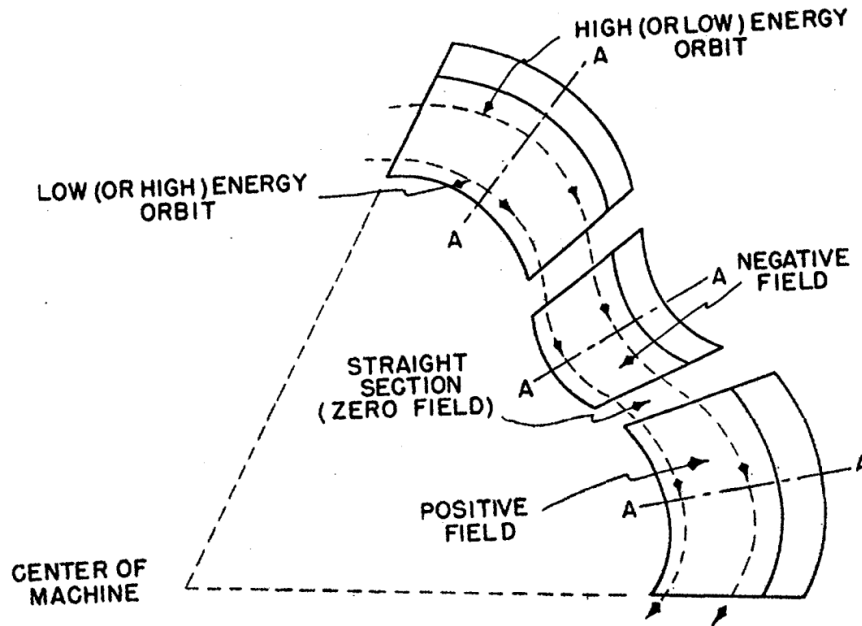


FIGURE 2.10: A drawing of a section of a radial sector FFAg taken from [46].

Consider a simple dipole field as one would find in a basic Cyclotron. To reduce the aperture, a gradient can be added to the field. This will increase the field strength,  $B$ , with radius meaning that the equilibrium orbits will have a smaller  $\rho$  at any given momentum than in the dipole case (equation 2.2). However, as discussed in sec.2.4.3, this will result in vertical defocusing and loss of the beam. To deal with this, ‘alternate gradient focusing’ is introduced. Now, rather than a continuous field, the magnet can be split up into focusing and defocusing elements (see figure 2.10) and create spaces to fit

accelerating cavities and all the other elements required to inject, extract and monitor the beam.

### 2.5.1 Scaling Law

The simple model described so far has fixed magnetic fields and alternating gradient, so is an FFAG by definition. However, there is an important problem that arises. As shown in equation 2.6, if the gradient,  $\frac{dBz}{dy}$  remains constant, the effective gradient,  $k_e$  will decrease as the momentum of the particle increases. This will cause the tune to vary, which is called ‘chromaticity’, which may cause a loss of the beam due to resonances, and will at least will distort the Twiss functions.

There are a few strategies for dealing with this, but in a radial-sector FFAG the ‘zero chromaticity condition’ is strived for, where the tune does not vary with momentum. More specifically, at any point around the accelerator:

$$\frac{\delta\rho}{\delta p} = 0 \quad (2.25)$$

and

$$\frac{\delta k_e}{\delta p} = 0 \quad (2.26)$$

which means that the shape of the orbits must remain the same with momentum, but the gradient must change so that  $k_e$  in equation 2.6 remains constant. The field which allows this is described by the Scaling Law [46, p.1838]:

$$Bz = Bz_0 \left( \frac{y}{y_0} \right)^k \quad (2.27)$$

where  $Bz = Bz_0$  when  $y = y_0$  and  $k$  is called the field index and is a measure of the ‘momentum compaction’: the higher  $k$ , the closer together the equilibrium orbits of particles with different momentum. Figure 2.11 shows the profile of a scaling field in a focusing and a defocusing magnet.

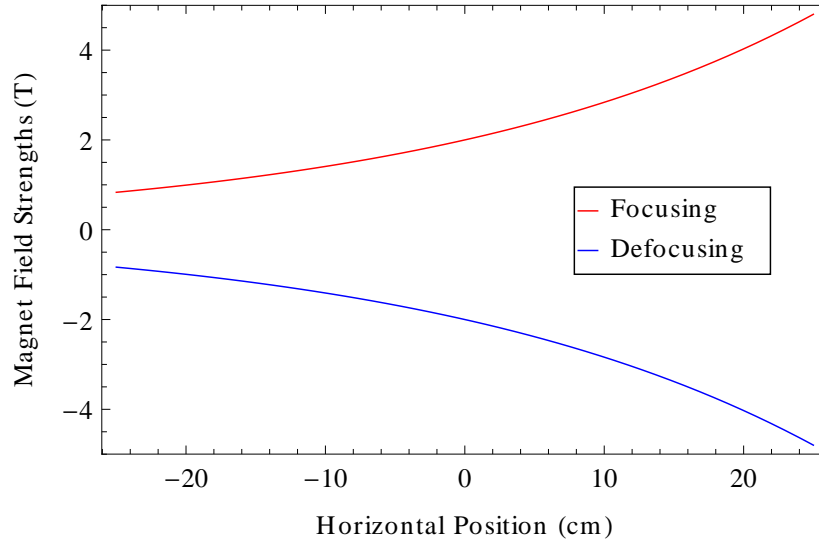


FIGURE 2.11: An example of focusing and defocusing fields that obey the scaling law.

The equilibrium positions of the different momentum particles in such a field can be derived from the similar equation [46, p.1838]:

$$p = p_0 \left( \frac{y}{y_0} \right)^{k+1} \quad (2.28)$$

### 2.5.2 Focusing is Tied to Bending

Alternate gradient focusing in a radial sector FFAG is different than in a Synchrotron. In a Synchrotron, the bending and focusing elements are usually split up into different magnets, so focusing and defocusing will have no effect on bending.

In a radial sector FFAG, however, focusing and bending are done in the same magnet.

In a scaling magnet which obeys equation 2.27, the gradient is given by:

$$\frac{dBz}{dy} = k \frac{Bz_0}{y_0} \left( \frac{y}{y_0} \right)^{k-1} \quad (2.29)$$

So to swap the sign of the gradient, we can change the sign of  $Bz_0$ , however, this will also change the direction of bending in the magnet. For this reason, alternate gradient focusing in FFAGs also gives rise to alternate curvature bending, which increases the radius of the FFAG beyond a Cyclotron for a similar energy range.

### 2.5.3 Negative $k$

Of course, the sign of the gradient in equation 2.29 can also be changed by swapping the sign of  $k$ . This can indeed produce a lattice in which the focusing and defocusing elements bend in the opposite way to a positive  $k$  lattice, and it might be tempting to think that alternating  $k$  rather than  $Bz$  would be a way of eliminating the negative bend of the FFAG. However, as figure 2.12 shows, a negative  $k$  field not only swaps the gradient of the field, it also flips the magnitude of the field around  $y_0$ , which swaps the equilibrium positions of the particles. This results in the higher energy particles travelling on the inside of the curve and the lower energy particles travelling on the outside of the curve. This will be discussed further in section 4.2.1.1

### 2.5.4 Non-Scaling Fixed Field Alternating Gradient Accelerators

The first Non-Scaling FFAG was proposed in 1997 [47] for a rapid cycling muon collider, but the first to be built is called the Electron Model of Many Applications (EMMA) and is just nearing completion [48]. In these designs, the zero chromaticity condition is

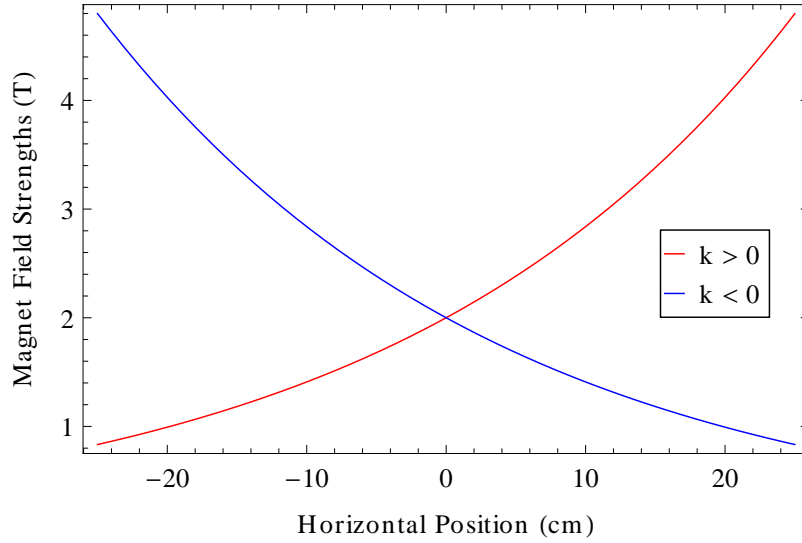


FIGURE 2.12: Swapping the sign of  $k$  in a scaling field results in the equilibrium positions being flipped around  $y_0$ .

abandoned, so the shapes of the orbits vary with energy (figure 3.15), as does the effective gradient and tune. The problem of resonances is sidestepped, in theory, by accelerating so fast that they do not have time to build up. The advantages of these designs are that they use simple magnets with linear fields, and the variation of orbit shape can create a smaller aperture, meaning the magnets are relatively easy to manufacture.

This approach runs into a problem when trying to accelerate anything more massive than an electron because acceleration systems that can accelerate them fast enough to avoid resonances do not yet exist [49].

Another form of ns-FFAG uses the scaling FFAG as a starting point, but approximates the scaling law using a Taylor expansion, which can be written as:

$$Bz = Bz_0 \left[ 1 + b_1 \frac{y}{y_0} + b_2 \left( \frac{y}{y_0} \right)^2 + b_3 \left( \frac{y}{y_0} \right)^3 \right] \quad (2.30)$$

where

$$b_1 = k \quad b_2 = \frac{(k-1)k}{2!} \quad b_3 = \frac{(k-2)(k-1)k}{3!} \quad (2.31)$$

Each term represents a different multipole field which can then be tuned by varying  $b_n$ . Figure 2.13 shows the first five multipole components that sum to the fit of a scaling field. Notice that the dominant terms are the dipole, quadrupole and sextupole terms, but the higher order terms become more important the larger the distance from  $y_0$ . Figure 2.14 shows the magnitude of the scaling field minus the magnitude of the sum of the first four terms of the Taylor expansion. The difference becomes much larger the further away from  $y_0$  you go because this is where the missing terms would have had an effect.

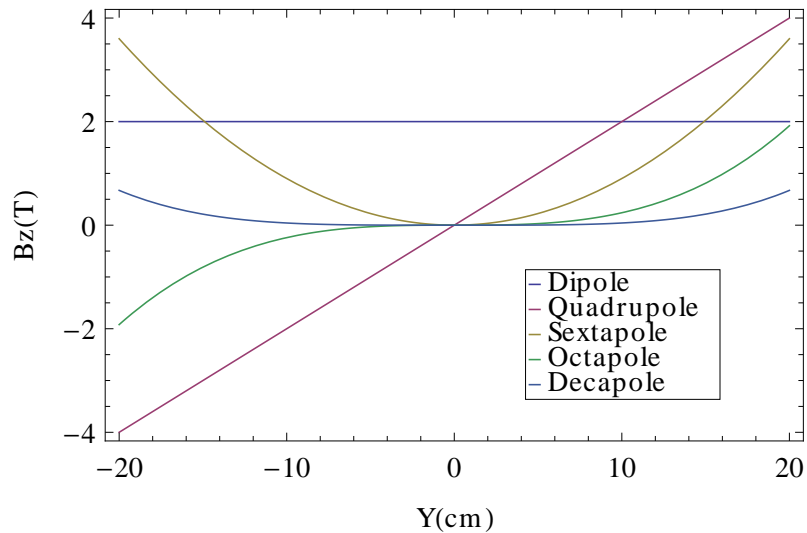


FIGURE 2.13: The first five multipole components which sum to make a scaling field.

## 2.6 Simulation Code

The tracking code used for all the studies is Zgoubi [43]. It is written in Fortran and takes input in the form of a text file with key words followed by lists of numbers. This form of input is impractical for large projects, so an addition has been written using Python to make the input more user friendly, called Pyzgoubi [50].

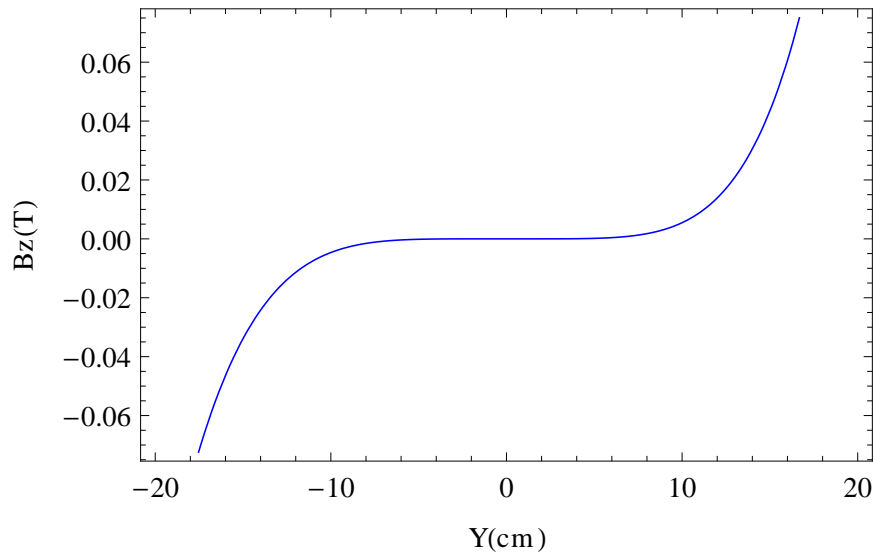


FIGURE 2.14: The difference between a scaling field and the sum of the first four terms of its Taylor expansion. Within  $\pm 20$ cm of  $y_0$ , they are very similar.

Zgoubi calculates the trajectories of charged particles in electric and magnetic fields [43, p.12]. It is particularly useful for FFAGs because it is able to calculate the trajectories of off orbit particles better than other packages considered like MAD-X [51].

The main geometry Zgoubi uses to model magnets is sections of arcs (see figure 2.15). The user defines a radius, then a total angle for the ‘map’ within which a number of magnets can be created. Reference positions for each magnet are specified as angles from the entrance to the map and the relative positions of its faces are specified as angles to the reference. The fields can be defined either by using the scaling law equation 2.27 or a Taylor expansion equation 2.30.

## 2.7 Parameter Searches and Downhill Fitting

When designing anything with a number of parameters that can be changed to not entirely obvious effect, it is often a good strategy to try a large number of different combinations of these parameters to find the most useful. This is called a parameter

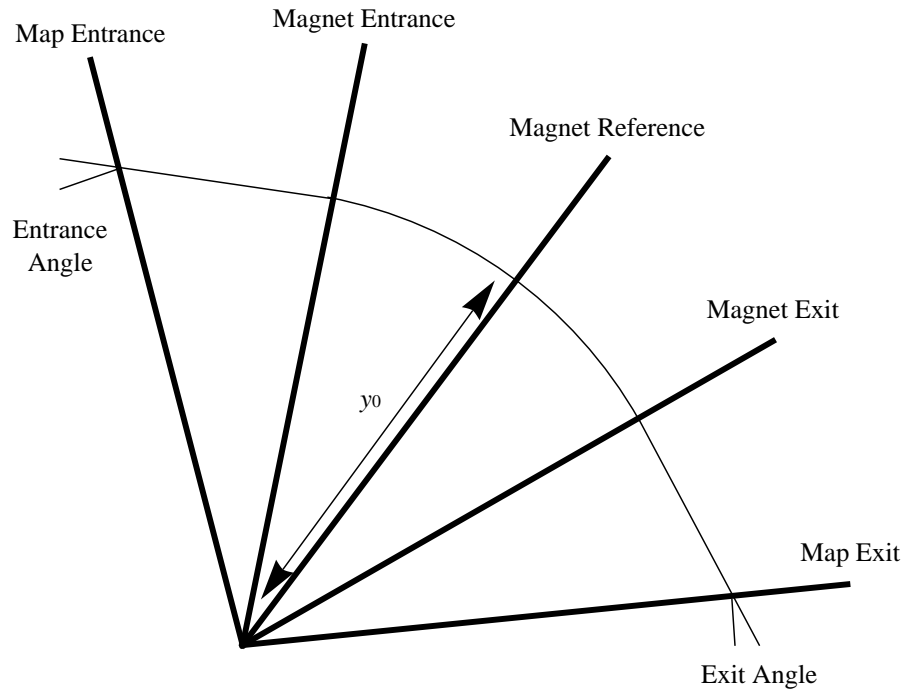


FIGURE 2.15: Zgoubi defines magnets along arcs. Angles are given to define the size of the ‘map’, the positions of the magnets and the magnet faces. The radius and the exit and entrance angles can also be defined.

search, or brute force fitting and is effective if the ranges the parameters are varied over are chosen carefully.

If all the combinations in a parameter search were set out in  $N$ -dimensional space, where  $N$  is the number of parameters, an ideal situation would be to search through all points in that space in very small small steps. However, processing time often limits the number of combinations which can be tried and the steps between points will usually be significantly larger than the precision required. For this reason, once a parameter search has found its best value, a different type of fitting is required that will find the best combination in a local area.

One method useful for this is called ‘downhill fitting’ [52, p.415]. Given a starting point ( $P_0$ ) and direction ( $u_0$ ) in the  $N$ -dimensional parameter space, a down hill fitting function will assess all the values over small distances in  $N$  different directions and find the best point ( $P_1$ ). It then starts again from  $P_1$  with direction pointing directly away from the

previous point (i.e.  $P_1 - P_0$ ). Eventually, when the distance between some point  $P_m$  and the next point  $P_{m+1}$  is small enough, it will stop and return the combination of parameters at that point.

The combined use of parameter search and downhill fitting function will be a major part of the design strategies for all of the design studies in this thesis.

## 2.8 Chapter Summary

This chapter explained the basic physics required to understand the major work in this thesis and demonstrated the author's grasp of the important concepts. It started with the motion of a particle in a uniform magnetic field (section 2.4), built up a picture of the behaviour of particles in alternating gradient fields (section 2.4.3) and explained the important points about non scaling Fixed Field Alternating Accelerators (section 2.5.4).

## Chapter 3

# Immediate Context

This chapter aims to put this thesis into context by giving an overview of the project that the gantry and transport line are designed to be a part of as well as gantries and transport lines for other purposes, both existing and proposed.

### 3.1 The CONFORM Project and EMMA

The CONFORM project (COstruction of a Non-scaling FFAG for Oncology, Research and Medicine) was set up in 2007 and includes three main projects: EMMA, the Electron Model With Many Applications; PAMELA, the Particle Accelerator for MEDical Applications; and a project to assess other potential applications for ns-FFAGs such as drivers for subcritical reactors [53].

EMMA is a test case for the principles of ns-FFAGs and has been successfully built at the Science and Technology Facilities Council (STFC) Daresbury Laboratory. This is a major achievement for all involved as it is the world's first working ns-FFAG, which will show that the principle of accelerating quickly using simple fixed field magnets is

a sound one. This may signal a much wider use of this technology in the future given the advantages of combining the high current and fixed fields of the cyclotron with the variable energy extraction of the synchrotron. It is also very important to the PAMELA project as it validates the concepts of ns-FFAGs as well as the simulation software.

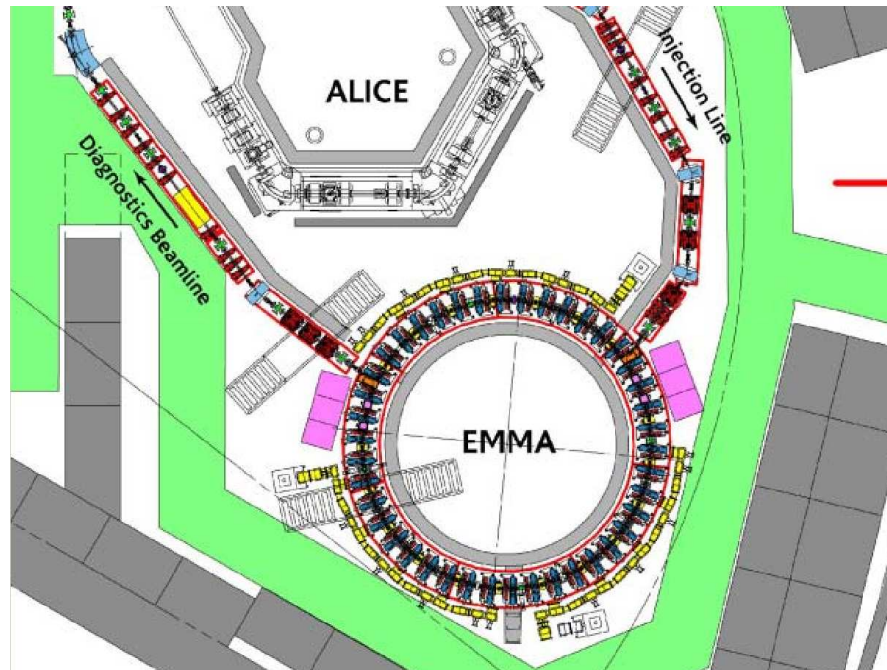


FIGURE 3.1: The EMMA accelerator at the Daresbury Laboratory [48].

Made up of 42 cells, EMMA (see figure 3.1 for a schematic) accelerates electrons from  $10 \rightarrow 20$  MeV. Each cell (figure 3.2) is made up of only a focusing and a defocusing quadrupole so, ingeniously, bending is achieved by the beam being slightly horizontally displaced from the magnet centres. There are 19 RF cavities in total, one in every other gap between cells, except where the beam is injected from another accelerator ALICE and where it is extracted to a diagnostic beam line [48].

The remarkable thing about EMMA is its linear fields. With scaling FFAGs, great lengths are gone to ensure that the effective gradient remains constant throughout acceleration, meaning the use of complicated non-linear fields and very wide (in the region of 1m) orbit excursions. This is done so that the accelerating particles do not cross

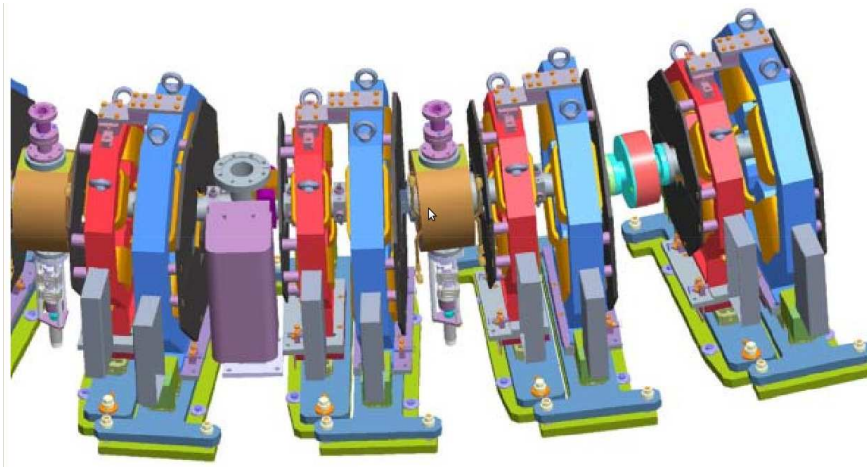


FIGURE 3.2: Four EMMA cells, each one consisting of a small red focusing magnet and larger blue defocusing magnet. Also shown are two RF cavities, an ion pump and a wall current monitor. [48].

resonances which destroy the beam. The principle with EMMA is that the particles can be accelerated through resonances so quickly that they do not have time to build up.

## 3.2 PAMELA

This section gives a brief overview of the PAMELA project, its various components and how this thesis fits into it.

According to the PAMELA design report [26], “the aim of the PAMELA project is to design a highly efficient CPT facility, using the features of ns-FFAG technology to improve performance over existing facilities”. Using fixed fields allows kHz acceleration rather than the Hz possible in a synchrotron, but the variable energy extraction is preserved. It is claimed that this will “result in a much improved patient experience, greater patient throughput due to shorter treatment durations and in the case of Carbon fewer treatment sessions”.

Figure 3.3 shows the layout of the proposed PAMELA accelerator. Carbon ions originate at the source in the bottom left of the figure and are shaped into bunches, ready for

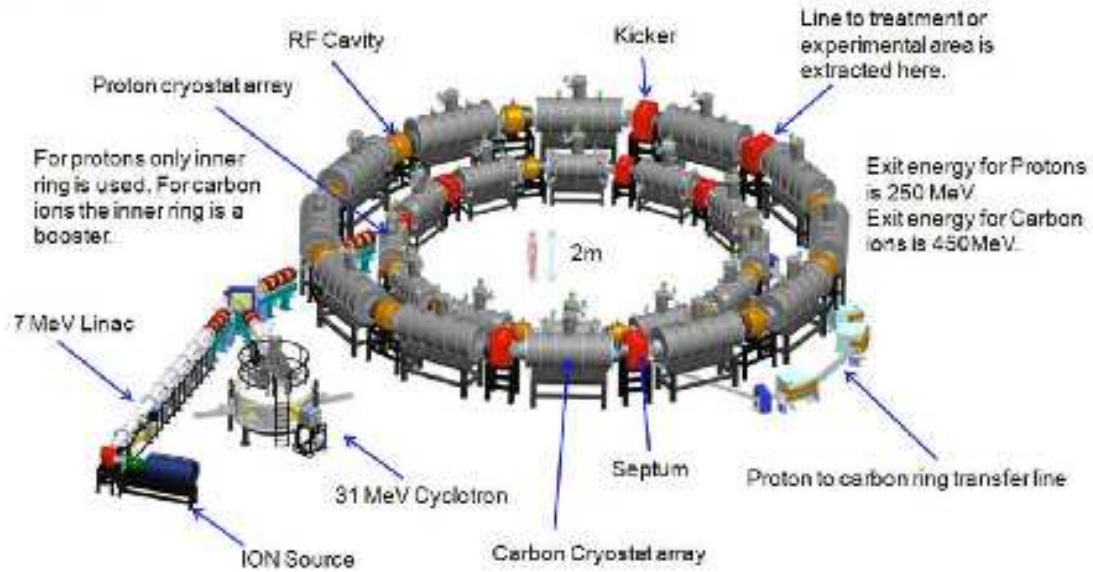


FIGURE 3.3: The layout of the PAMELA accelerator. The larger ring is the carbon accelerator and the proton ring sits inside. The transport line to take the beam to the treatment rooms will attach in the top right of the picture [26].

acceleration, then pre-accelerated with the 7MeV linac; whereas the protons originate from a source inside the cyclotron where they are also pre-accelerated and then shaped into bunches (see section 3.2.7). Both types of particle are matched into the same transport line with a switchable dipole, from where they are transported to the injection system, which injects them into the smaller proton accelerator. The PAMELA cells (section 3.2.3) are made up of three superconducting magnets each (section 3.2.4), which require the cryostat arrays visible in the figure. There is space in between each cell for the RF cavities (section 3.2.6, diagnostic devices and injection and extraction magnets (section 3.2.6). Protons can be extracted from the accelerator at any momentum up to a maximum of 0.729 GeV/c, but the carbon ions are accelerated up to 0.729 GeV/c in the smaller ring before being transported to the larger, outer ring with the proton to carbon transfer line. They are then accelerated to a maximum of 1.909 GeV/c before being extracted into the transport line to the treatment rooms.

TABLE 3.1: Summary of the clinical requirements of PAMELA. See [26] for a more complete version.

Parameter	Value	Units
Horizontal dose field size	$15 \times 15$	cm
Maximum SOBP width	13	cm
Maximum depth	25	cm
Energy range ( $p^+$ )	$70 \rightarrow 250$	MeV
Energy range ( $C^{6+}$ )	$110 \rightarrow 430$	MeV
Dose field uniformity	$< 2$	%
Dose field tolerance	$< 2$	%
Beam spot size (FWHM)	$4 \times 4 \rightarrow 10 \times 10$	mm
Scanning speed	$> 100$	Voxel/sec
Energy Step	$0.5 \rightarrow 2$	MeV
Single dose	$1 \rightarrow 7$	Gy
Intensity range	$0.05 \rightarrow 1.5$	nA
Bunch intensity	$2.5 \times 10^5 \rightarrow 6.5 \times 10^6$	ppp
Scanning speed	0.5	cm/msec

### 3.2.1 Clinical Requirements

The clinical requirements are meant to reflect an ‘oncologists’ wish-list’ which currently cannot be met due to the limitations of existing technology. These are summarised in table 3.1 [26, p.16] and the parameters that apply directly to the gantry and transport line are: the field size, the beam spot size and the energy range.

### 3.2.2 Spot Scanning Issues

One of the advantages of using charged particles is that, due to the low beam divergence as it passes through the patient, it is possible to deliver the dose in series of precise ‘pencil beams’. One of the goals of the PAMELA project was to be able to do this. It requires small active dipole magnets to control the transverse beam position as well as active quadrupole magnets to control the beam size. The design of this will be discussed further in chapter 4, but it was important for the design of PAMELA to know what kind of beam size would be useful and what errors could be tolerated.

There are two main considerations when delivering a dose of radiation to a target volume: ‘uniformity’ and ‘tolerance’. Uniformity is the maximum dose deviation from the average dose, which should be within 2%, and tolerance is the deviation of the average dose from the prescribed dose, which should be within 5% maximum, however 2% is desirable [26, p.8].

These requirements inform beam size requirements and the upper limit on beam positioning errors. Using information about the spread of beams in tissue and the minimum resolution of medical imaging technology, the required beam spot size was between  $4\times 4$  mm and  $10\times 10$ mm. A study of beam uniformity with beam positioning errors was carried out. This showed that to achieve the 2% requirement, a maximum of 0.2mm error can be tolerated, if the volume is rescanned five times or a 0.3mm error if a maximum overdose in the tumour of 10% is allowed.

### 3.2.3 The PAMELA Lattice

For obvious reasons, the success of EMMA would be a great moment for all involved, but was also very important for those working on PAMELA because it will show that ns-FFAGs are possible. However, the concept at the heart of PAMELA is different to that of EMMA. While linear magnets were suitable for electrons, it was found that the same type of design could not be used for protons or carbon ions as their extra inertia increases the time needed for them to accelerate to therapeutic energies, and crossing resonances will distort the beam significantly [54]. Instead, PAMELA had to develop a new type of lattice that is both non-scaling (to preserve the small momentum compaction) and non-linear (to avoid the tunes moving into resonances with acceleration) [49]. The type of cell that was developed is used as a starting point for the designs in this thesis.

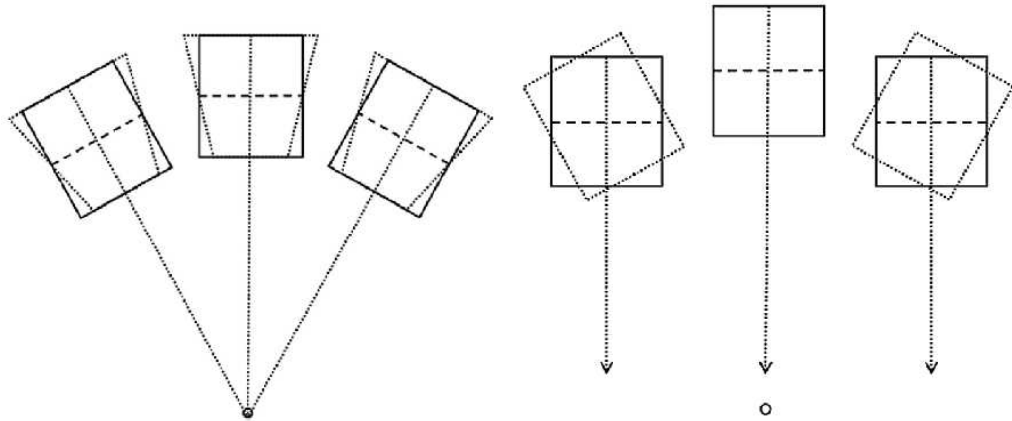


FIGURE 3.4: Conversion from FFAG sector shaped magnets to ns-FFAG rectangular magnets. [49].

The design strategy is to start with a scaling FFAG in an FDF configuration and with a very high  $k$  value, then break the scaling law by only using the dipole and the first few multipole components (see section 2.5.4). Also, the magnets, which in a scaling FFAGs are usually sector shaped, are straightened out into rectangles (figure 3.4(a)), made parallel (figure 3.4(b)) and allowed to reach superconducting strengths [55] [49] [26, p.42].

The proton ring uses 12 triplet cells of the type described above (see figure 3.5). The ratio of magnet length to accelerator circumference was set as a balance between the requirement for a compact design and the stability of the beam, which is improved by a lower ratio. Specific values of  $k$  and the DF ratio were then found by a parameter search and the magnet length within the cell increased slightly to reduce the peak magnetic field. Table 3.2 shows the parameters of the final proton ring design and the effect these parameters have are discussed again in section 5.4 where the design of the gantry is described.

An interesting characteristic of the PAMELA design is the use of the ‘second stability region’ in Hill’s Equation (equation 2.9). As discussed in section 2.4.6 if the tune in one cell reaches certain values the beam will resonate and blow up. A large resonance

<b>Parameter</b>	<b>Inj.</b>	<b>Ref.</b>	<b>Extr.</b>
Proton Kinetic Energy [MeV]	30.95	118.38	250
$C^{6+}$ Kinetic Energy [MeV/u]	7.84	30.98	68.36
$B\rho$ [Tm]	0.811	1.621	2.432
Cells		12	
$r_0$ [m]		6.251	
Magnet length [m]		0.3144	
Packing factor		0.48	
Field index, $k$		38	
Orbit excursion [m]		0.176	

TABLE 3.2: Lattice parameters for the PAMELA proton ring [26].

is at a  $\pi$  phase advance per cell, so if a magnet designer were to increase the  $k$  value, increasing the tune per cell, at some point close to  $\pi$ , the beam would blow up and be of no use. However, it is perhaps not widely known that there are usually further stable values of  $k$  beyond the  $\pi$  barrier, which have large values of  $k$  and so small momentum compaction. This is how the PAMELA lattice manages to keep the aperture low enough to be practicable for superconducting magnets.

Unfortunately, this concept cannot be used in the gantry and transport line, as there are sections of lattice that will need exactly a  $\pi$  phase advance to create points of dispersion suppression. These dispersion suppression points will be discussed in chapters 5 and 6, but from the explanation in section 2.4.10, it can be seen that anything greater than a  $\pi$  phase advance will not result in dispersion suppression. So, since the second stability region in Hill's Equation is defined by having a phase advance per cell greater than  $\pi$ , the first stability region must be used.

The carbon ring requires a scaling up in size of the proton lattice because of the increased rigidity of the carbon ions [56] [26]. The design process was similar to that of the proton ring and it proved, again, to be a careful balance between the desire to make as small an accelerator as possible the requirements imposed by beam stability, the limits of magnet

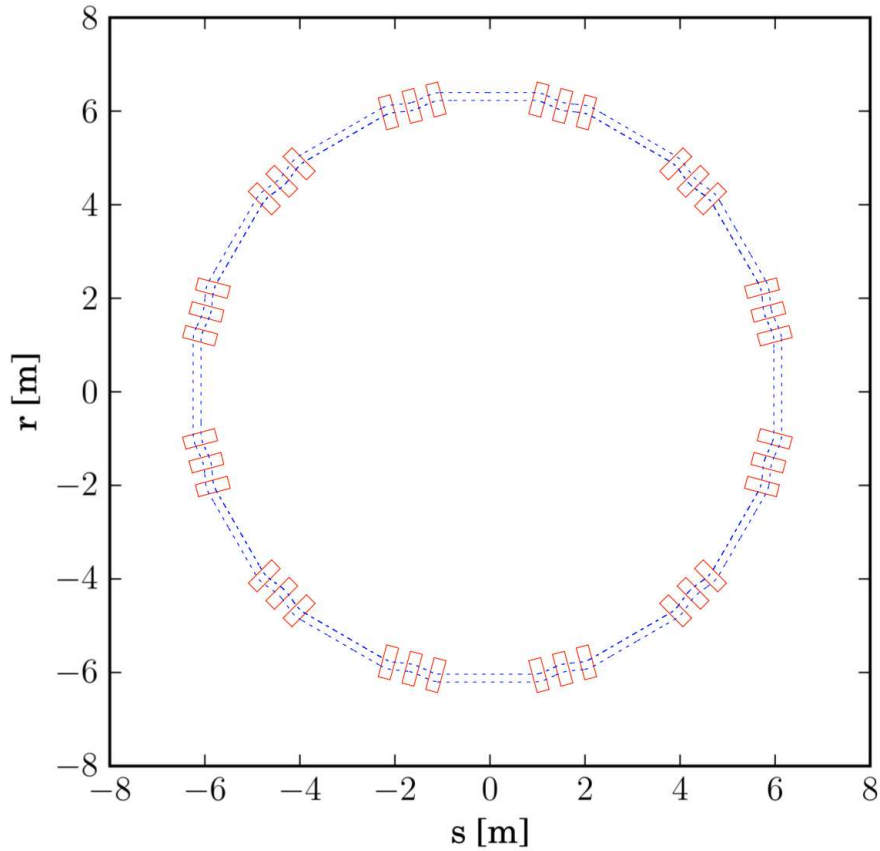


FIGURE 3.5: The PAMELA proton lattice with particle tracks at the injection (inner dotted line) and extractions energies (outer dotted line) [26].

technology and the need for space between cells to fit the RF units. The parameters of the carbon ring are shown in table 3.3.

Parameter	Value
Cells	12
$r_0$	9.3 m
Magnet length	0.6330 m
Packing factor	0.65
Field index, $k$	42
Orbit excursion	0.217 m

TABLE 3.3: Lattice parameters for the PAMELA carbon ring [26].

Both rings underwent rigorous testing in simulation for tune variation, dynamic aperture and sensitivity to positioning errors and in all of these were found to be successful.

### 3.2.4 Magnet Design

The high fields in both PAMELA rings coupled with their non-linear nature, presented a real challenge for magnet design [57]. This resulted in some unconventional magnets being designed using so called ‘tilted solenoid’ or ‘double helix’ technology [58]. Figure 3.6 shows a basic dipole design, with concentric helical coils made out of the same piece of superconducting, niobium-tin wire. Each coil creates a solenoid field and a dipole field, but since the current in each is flowing in an opposite direction, the solenoid fields cancel and only the dipole field remains. Further multipoles can be produced by adding further pairs of coils around the outside [26, p.62]. Depending on the aperture and number of multipoles required, field strengths of up to around 4T can be achieved.

Successful tests have been done in simulation to see if these magnets are indeed suitable for PAMELA [26, p.69] and figure 3.7 shows the result of a small test of the complicated winding procedure.

### 3.2.5 Extraction

Extraction from the accelerator into the transport line is done with the use of kicker and septum magnets (figure 3.8). The kicker gives a short pulsed field to the particles to be extracted, which is just enough to knock them vertically out of the aperture before they are bent further by the high field strength septum after the next cell.

The challenge in the kicker is the very fast rise times required of the magnet. Vertical extraction was a necessity because the fields required to overcome the large horizontal beam excursion would require a much slower magnet than would be suitable for PAMELA.

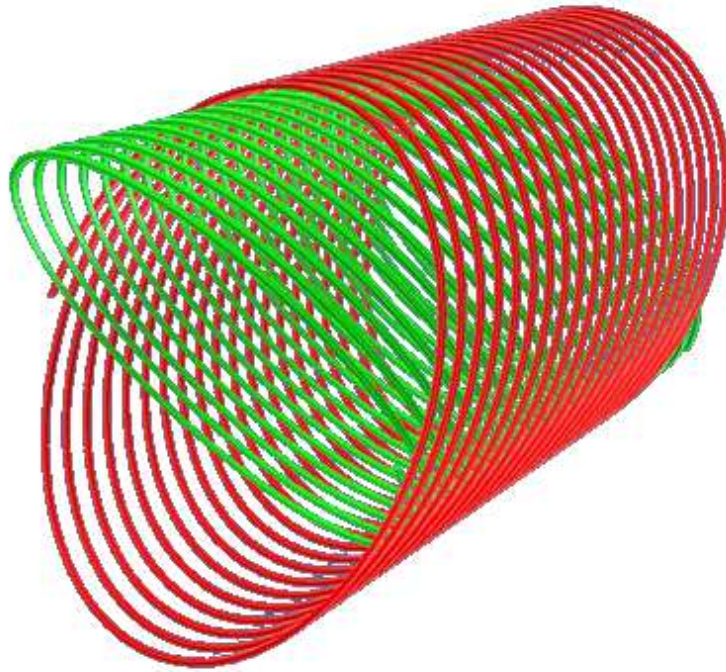


FIGURE 3.6: An example of the ‘tilted solenoid’ type of magnets used by PAMELA. This is just a simple dipole, whereas the PAMELA magnets would have more coil pairs around the outside.

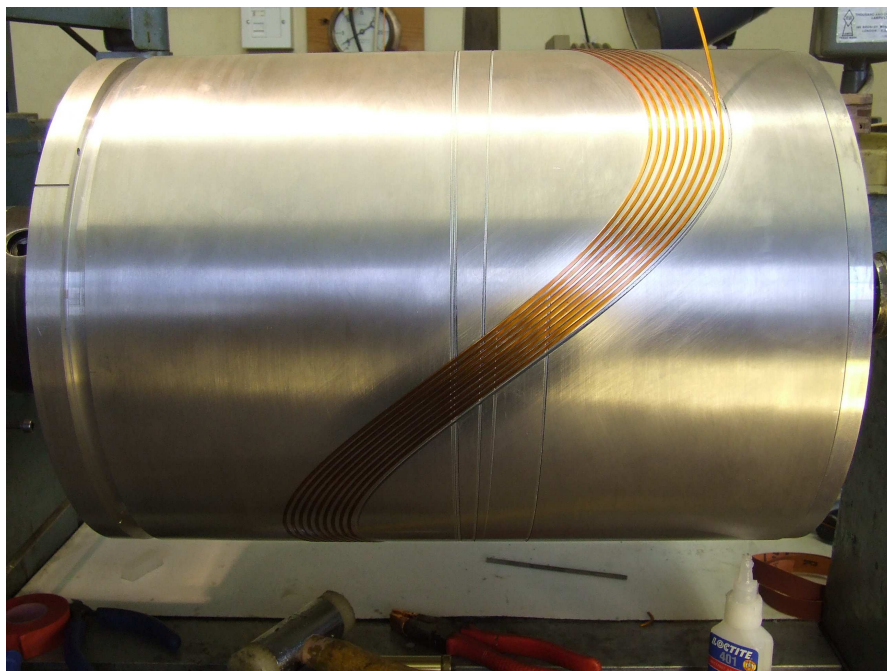


FIGURE 3.7: A trial to see if the complicated winding techniques required would be possible.

In the septum, the challenge was in varying such a high field ( $\approx 4\text{T}$ ) at the rate of a kHz with such a wide aperture. Superconducting magnets can easily reach such high fields, but would be far too slow to cope with PAMELA's repetition rate. The solution was to conceptually design a so called 'FFAG septum' which has a varied field along its aperture.

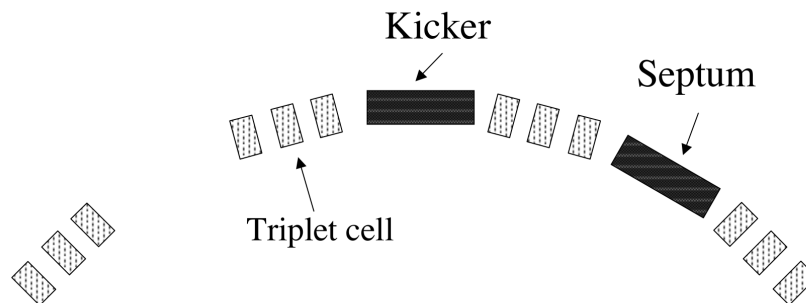


FIGURE 3.8: The extraction set-up in the PAMELA ring. The kicker knocks a particle vertically just out of the aperture, where it is collected by the septum, which with a much higher bending field, fully removes it from the ring.

### 3.2.6 Acceleration

PAMELA requires a repetition rate in the RF system of over an order of magnitude higher than anything achieved by existing rapid cycling proton synchrotrons [26, p.93]. The design that will be investigated further is the well established ferrite loaded rf cavity system, except with a type of ferrite not commonly used. The properties of this ferrite need to be tested to show that it can create the cavity performance required for PAMELA to be a realistic design.

### 3.2.7 Pre-Acceleration

PAMELA will employ a different pre-acceleration scheme for protons and carbon ions. Protons require a simple cyclotron, whereas the carbon ions require a more complicated

arrangement involving a source of four different carbon ions, selection of C4+ using a dipole, bunching with a chopper, pre accelerating and focusing with an quadrupole that pulses at radio-frequencies (called an RFQ), accelerating further with a linac and using a stripping foil to convert the C4+ to the C6+ required by PAMELA.

After pre-acceleration, the beams pass through a switching dipole and are matched into the main accelerator. A fuller explanation can be found at [26, p.18].

### 3.3 Existing Gantries

A gantry is a rotating structure, designed to deliver beam to the patient. These vary greatly in size, from  $\approx 3\text{m}$  high X-ray gantries which fit inside normal sized rooms and have electron linacs and X-ray producing targets mounted on them, to  $\approx 15\text{m}$  high carbon gantries which have treatment room built inside their turning radius so that the patients are not worried by the tonnes of equipment rotating around them. Figure 3.9 shows the end of the Heidelberg Gantry to give an impression of the size of the structure.

No FFAG transport lines or gantries exist, but variable field ones do, so it is worth looking at them. Table 3.4 gives an overview of the types and sizes of existing gantries that will be used as comparisons for the design in this thesis.

All but one of them are isocentric, which means they rotate around a fixed centre (the isocentre) where the patient lies. The other option is to have exocentric gantries, where the patient moves around a central point (figure 3.10). In the case of the ‘Riesenrad Gantry’ design [60] the bending magnets are at the central point and the patient rotates around it as if on a ferris wheel (in fact, this type of gantry is named after one such wheel

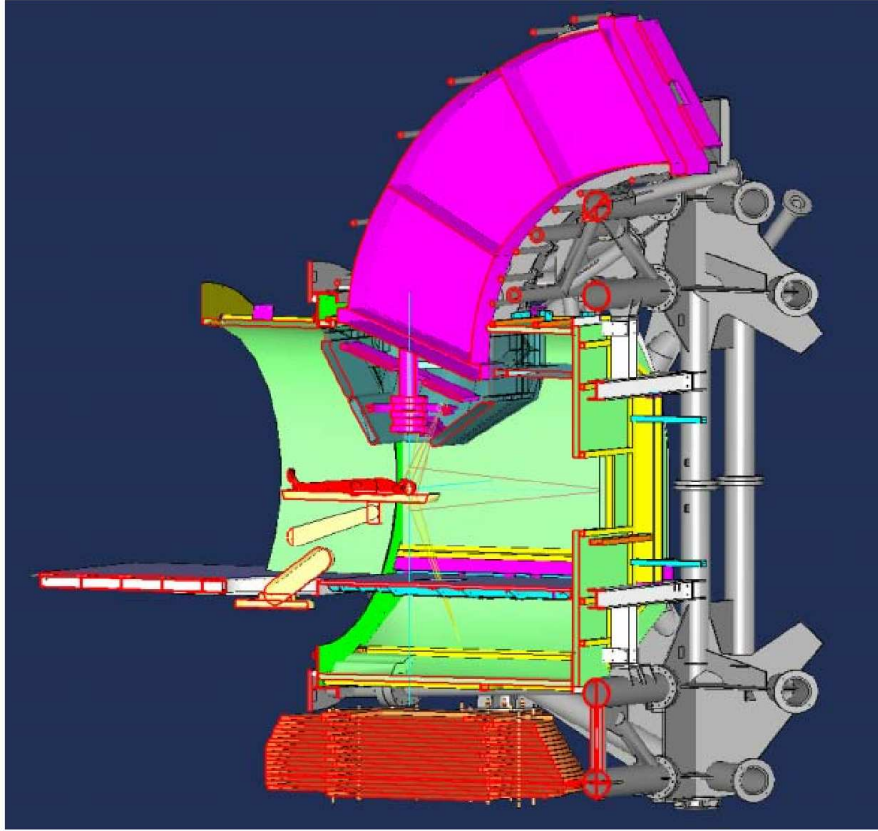


FIGURE 3.9: The last section of the Heidelberg gantry gives an impression of the scale of the structure. [59].

TABLE 3.4: Parameters of existing gantries. Key: a = assembly, o = in operation, c = commissioning, d = design, iso = isocentric rotation, exo = exocentric rotation. Information from [59].

Site	Munchen	PSI 1	PSI 2	Hyogo	Chiba	Shizuoka	Heidelberg	Chiba
Ion	H <sup>+</sup>	C	C					
Status	a	o	c	o	o	o	a	d
Type	iso	exo	iso	iso	iso	iso	iso	iso
Energy (MeV/u)	250	230	230	230	235	235	430	400
Length (m)	10.1	10.2	11.6	9.5	10.7	9.0	19.0	16.9
Radius (m)	5.0	1.4	3.2	4.8	5.0	4.8	5.6	7.1
Number of Dipoles	2	3	3	2	2	3	3	3
Number of Quads	7	7	7	7	9	4	8	7

in Vienna). However, exocentric schemes can also be a compromise between patient and magnet movement, as is the case in the very compact PSI 1 gantry [61].

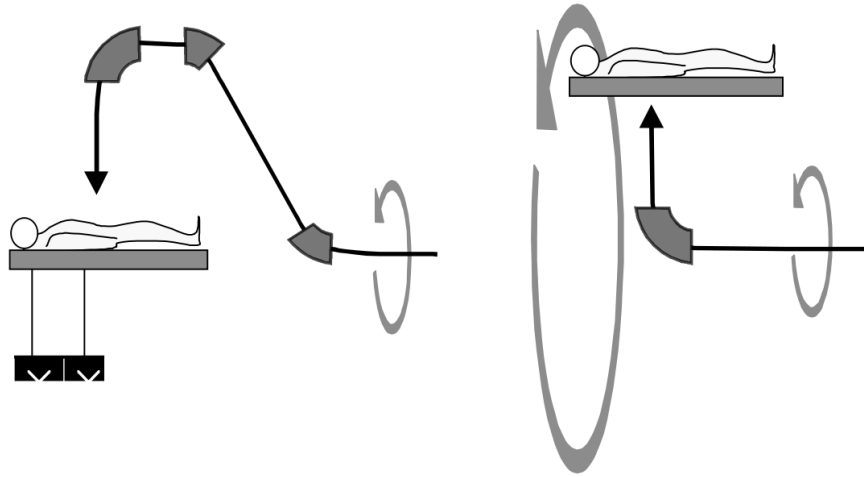


FIGURE 3.10: Examples of isocentric (left) and exocentric (right) gantries [62, part 2, p.151]. The patient stays at the fixed centre of an isocentric gantry, while they move around a circle in an exocentric gantry. Exocentric gantries can take the form shown here, or both the magnet and the patient can rotate around different circles, to make a more compact design.

Exocentric designs make perfect sense from the point of view of an engineer because of the vast weight difference between the bending magnets and the patient. However, isocentric designs predominate because of requests from clinicians to move the patient around as little as possible.

Figure 3.11 gives an idea of the main components of a typical gantry. A dipole field bends the beam upwards, to create height, then two more rotate it to the vertical so it can be directed at the patient. The scanning magnets are placed before the final dipole magnet to give a wider field and so that the beams at the patient are almost parallel. It also allows the height to be reduced, since the scanning magnets can be horizontal, rather than vertical. However, this does mean that a large aperture is required in the final magnet making it very bulky and requiring it to contain a large vacuum.

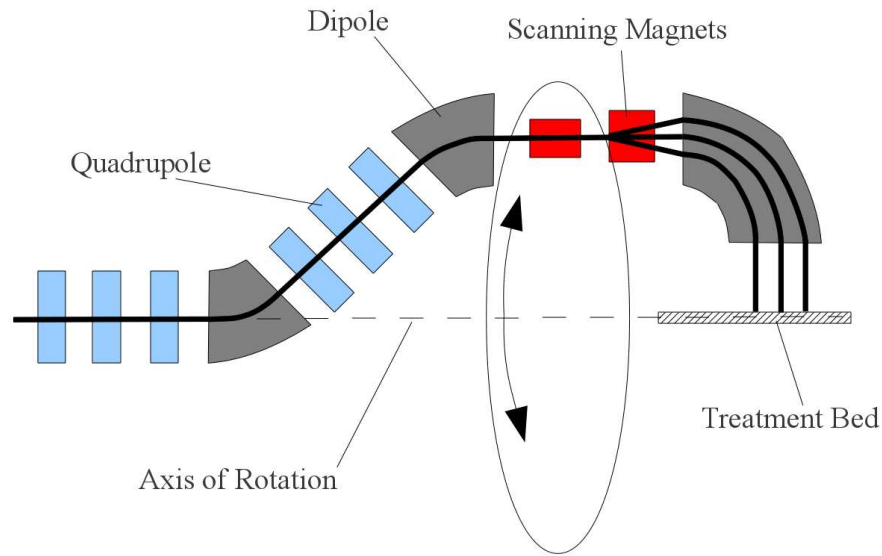


FIGURE 3.11: An example variable field gantry design which rotates  $360^\circ$ . The solid lines are particle tracks at three different energies [63].

### 3.3.1 Designs for Matching into a Rotating Gantry

The rotation of the gantry can cause problems with optics, especially when the beam from the accelerator is an unusual shape. In this case, complicated rotator magnet designs have to be devised [64], and time varying magnets are required. However it is likely that the beam into the PAMELA gantry will be more reliable and a rotationally invariant beam can be created.

There are three methods for matching into a rotation gantry and they are discussed in depth in [62, part 1, p.144]. These are called:

- Symmetric beam method
- Round beam method
- Rotator method

The symmetric and round beam methods are really requirements of how the optics are set up either side of the rotation point, whereas the rotator method uses an extra piece of matching lattice between the transport line and gantry that rotates to half the angle of the gantry.

The symmetric method is by far the easiest to understand. The idea is to create a rotationally invariant beam by having equal horizontal and vertical emittances, Twiss functions as well as zero dispersion. This design is very useful when the beam is a regular shape as it will be in PAMELA.

The round beam method is more relaxed about the shape of the beam at the start of the gantry:  $\sqrt{\varepsilon\beta}$  in the vertical and horizontal planes have to be equal and it is advised that the alpha functions both equal zero [62], presumably to simplify matching the  $\beta$  function by keeping it constant through the interface between transport line and gantry. However, it also requires that the phase advances over the length of the gantry are integer multiples of  $\pi$  and that allowances are made for the Twiss functions changing within the gantry as it rotates. This could cause a problem with scanning magnets, but if a point can be created before the end of the gantry where the phase advances in both planes are integer multiples of  $\pi$ , the optics in the lattice after this point will be invariant with rotation and the workings of the scanning system would be unaffected.

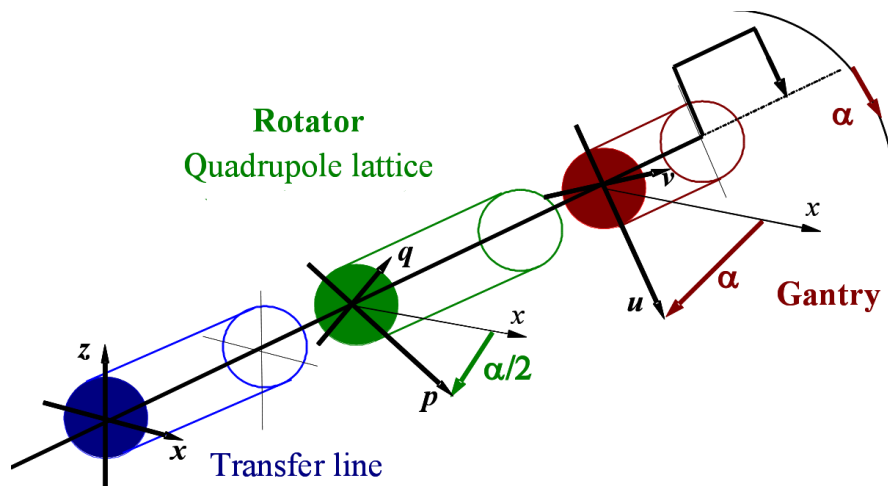


FIGURE 3.12: A schematic of a ‘rotator’ section used to map a beam from a transport line to a rotating gantry.  $\phi_y = 2\pi$  and  $\phi_z = \pi$  within the rotator quadrupoles. The rotator is rotated to half the angle of the gantry relative to the transport line [62].

The rotator method maps the Twiss functions from the end of the transport line into the rotating gantry. It makes no requirements of the beam, except that it must have zero

dispersion at the exit of the gantry, which makes it very useful in situations where the beam has a very irregular shape [64]. The principle is shown in figure 3.12. The rotator section of lattice has to have a  $2\pi$  horizontal phase advance, a  $\pi$  vertical phase advance and a rotation angle of exactly half of the gantry rotation. When the beam arrives at the gantry, it will have exactly the same Twiss functions, but be rotated by the same angle as the gantry. As this scheme will not be used in this thesis, the mathematics of how this works will not be reproduced here, however they are explained in [62, part 1, p.152].

### 3.4 FFAG History and Relevant Literature

The history of FFAG design can be seen as a history of trying to battle against the effects of tune variation. Some designs try to keep the tunes steady by changing gradient with horizontal position, some use the shape of the magnets, while others use the acceleration speed made possible by fixed fields in the magnets and fixed frequencies in the RFs to make resonance effects negligible.

This section deals with the existing literature on FFAGs and ns-FFAGs which could be useful to the design of the gantry and transport line. First there will be a discussion of the history of FFAGs and examples of different basic cell types designed for accelerators and their relative properties, followed by gantry and transport line designs more specifically.

#### 3.4.1 Early FFAGs

The concept of the FFAG follows so naturally on from the concept of alternating gradient focusing, that it was proposed independently four times in the early 1950s soon after alternate gradient focusing was invented. In the USA it was proposed by Haworth and

Snyder [65] as well as Symon [46]; in Japan it was proposed by T. Ohkawa [66]; and in the USSR by Kolomesky [67].

A 1956 paper by Symon et al. [46] summarises the different types of FFAG conceived of at the time. The two main types were the radial sector FFAGs and the more compact spiral sector FFAG. The radial sector type is most useful to this thesis and it is discussed in section 2.5.

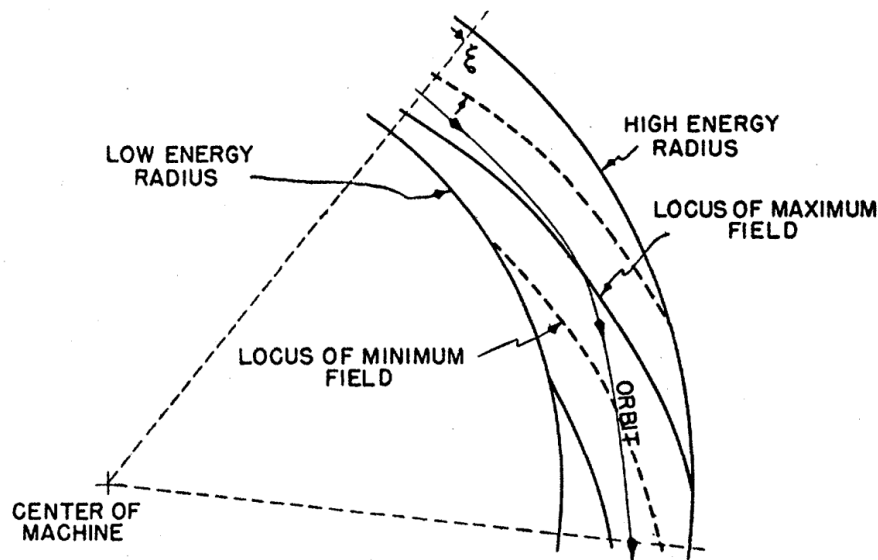


FIGURE 3.13: A section of a spiral sector FFAG as drawn in [46]. Alternate gradient focusing is provided by the particle travelling over the peaks and troughs in the field as they spiral outward.

The spiral sector FFAG uses more complicated magnets than the radial sector FFAG (figure 3.13). Like the radial type, the field increases with radius overall, but on the small scale, the gradient is alternating (figure 3.14). The peaks and troughs of the gradient actually spiral out, so that a particle experiences an alternating gradient as it travels around the orbit, which keeps the beam focused. The lack of the negatively bending defocusing magnets makes for a much more compact design, however complications arise with injection and extraction.

The benefits these designs had over the cyclotrons of the time was partly that the edges

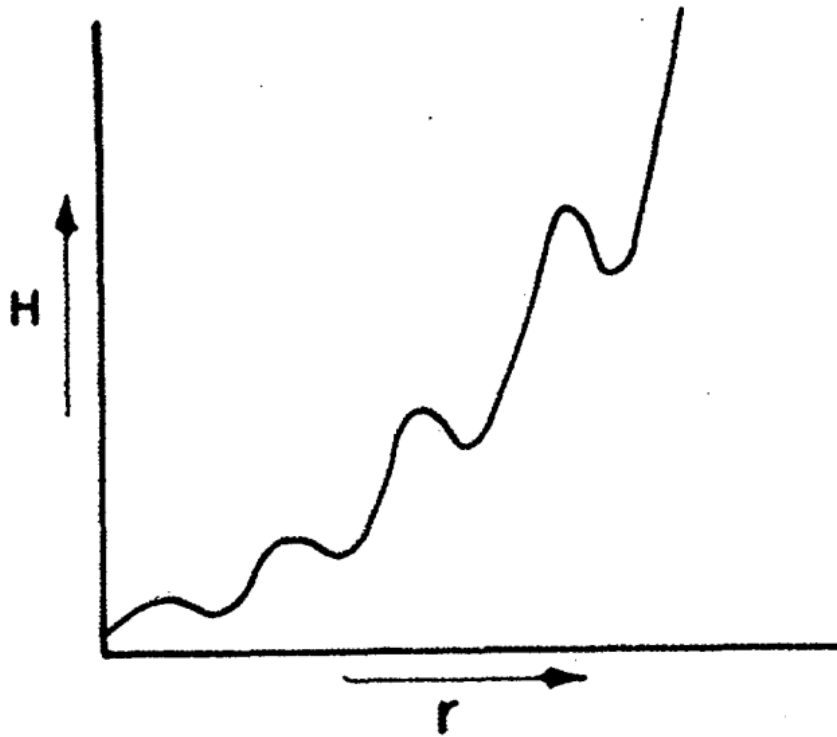


FIGURE 3.14: A radial slice through the field of a spiral sector FFAG as drawn in [46]. These peaks and troughs actually spiral outward so that a particle will experience alternate gradients in quick succession as it travels around the accelerator.

of the sector magnets create focusing quadrupole and sextupole fields, but also that the space between magnets could be used for RF cavities, leading to higher achievable energies. Also, compared to the large disk magnets in cyclotrons, FFAG magnets could be horizontally thinner, leading to much smaller and cheaper vacuum systems, as well as the reduced cost of the magnets themselves [65].

After over a decade of research into FFAGs by MURA (the Midwestern Universities Research Association) based in Chicago, they were abandoned as synchrotrons became the dominant accelerator type in high energy physics. Several innovations came from the study of the non-linear fields in these machines. One which is very relevant to this thesis is the tracking of particles by computer simulation [5, p.17].

After MURA ended its interest, the idea of FFAGs was not seriously entertained again

until the 1980s. Unfortunately, this interest was short lived, and proposals for spallation sources (where high  $Z$  materials are bombarded with high energy protons to produce neutrons [68]) were rejected in the US and Germany [65].

### 3.4.2 Revival of the Fixed Field Alternating Gradient Accelerator

In 2000 the first proton FFAG was switched on at KEK in Japan [69]. It had a maximum energy of 1MeV, eight radial sector triplet magnets in the DFD configuration and an orbit radius of  $0.8 \rightarrow 1.1\text{m}$ . Major innovations were introduced in magnets and RF design for this FFAG and it paved the way for nine more FFAGs to be built by 2008 with energies reaching 150MeV [65].

There are also many FFAGs in design or production, ranging from the tiny MEICo Laptop [70], which has a maximum radius of only 2.8 cm and maximum energy of only 1MeV, to the largest J-PARC Neutrino Factory Accelerator, which has a radius of 200m and will accelerate muons to 20,000 MeV [65, p.25].

Both of these are being developed in Japan, which has emerged as the main centre for this technology. However, there is also interest in France, where the RACCAM project aims to build a spiral sector FFAG for proton therapy [71]; as well as in the USA where there is, among other things, interest in using FFAGs for acceleration of high power beams for medicine and industry [72].

### 3.4.3 The First Non Scaling FFAG Design

A huge leap in the development of FFAGs came in 1997, when the study of rapid cycling rings for muon acceleration led to the realisation that if acceleration is fast enough, resonances do not have time to build up and the careful adherence to the scaling law

can be abandoned [65] [47]. This allows a number of useful advantages to be gained, like the use of linear magnets and a reduction in aperture due to a higher field gradient being possible.

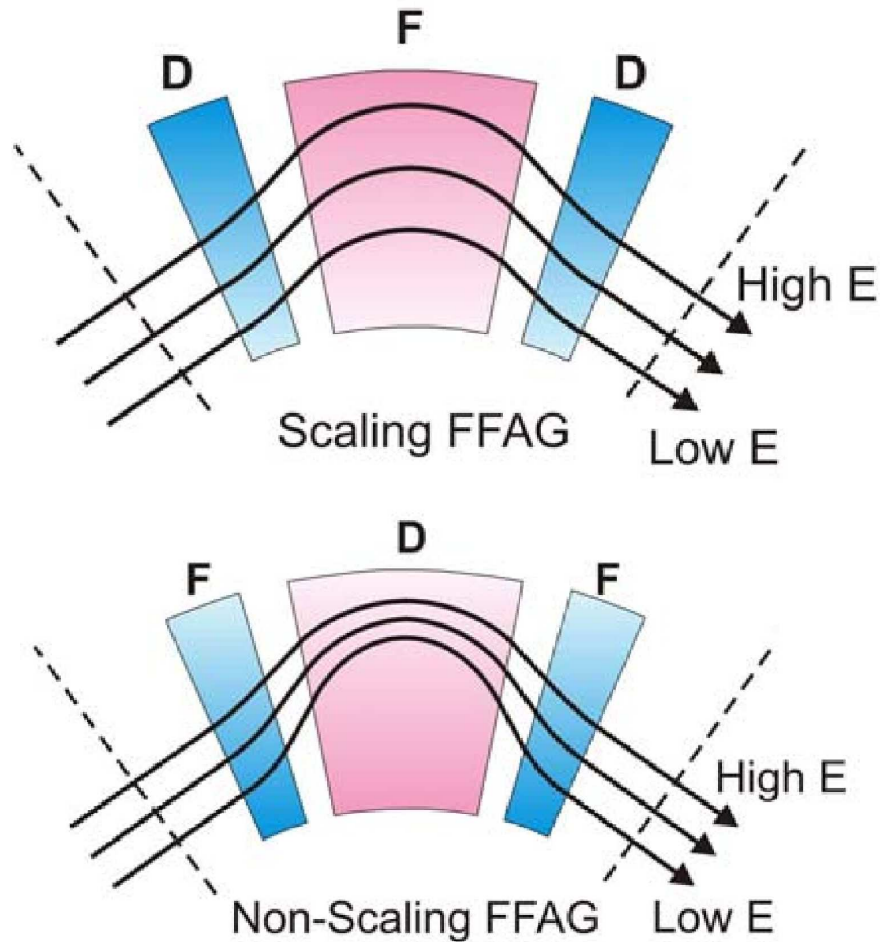


FIGURE 3.15: Comparison of FFAG and ns-FFAG orbit positions [65]. Shows the definition of ‘non-scaling’ because the orbits change shape with energy. In this example the field gradient is reversed in the ns-FFAG case to reduce the aperture in both F and D magnets, but this is not necessary, nor is the swapping from DFD to FDF.

The idea was developed into a full ring by 1999 [73], with magnets with a field gradient that reduces radially, rather than increases. Perhaps counter intuitively, this creates a smaller aperture in the F magnet and an even smaller one in the large D magnet. A number of designs followed and EMMA, as mentioned, has been successfully built.

There are three accelerator designs in particular that are of interest to the development of PAMELA and the designs in this thesis.

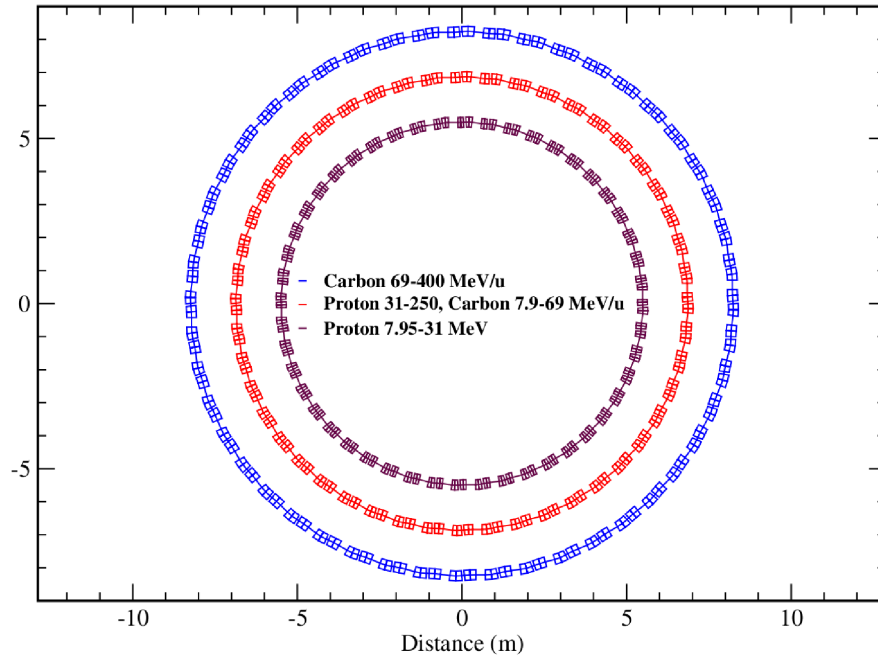


FIGURE 3.16: The three rings of the KST lattice [74].

### 3.4.4 The Keil, Sessler, Trbojevic Lattice

The linear non-scaling idea, was developed for accelerating protons and carbon ions and formed into a lattice design by Keil, Sessler and Trbojevic (called the KST lattice) [74]. The KST lattice uses three rings to accelerate protons to 250MeV and  $C^{6+}$  to 400MeV/u (figure 3.16). The central ring works as the extraction ring for protons as well as the injection ring for carbon, with the inner and outer rings taking only one species. Like EMMA, it uses a doublet cell, but the magnets are combined function, rather than the bending being caused by magnet offsets. Figure 3.17 shows one of these cells. The KST lattice is very compact, leaving only 8cm between magnets in the cell and 29cm between cells in the central ring. This helps to produce low beta functions and dispersion, but may be a problem with overlapping fields and fitting in RF units.

This design was critiqued from a PAMELA perspective in [75] and found to be too sensitive to positioning errors to accelerate a proton beam without inducing resonances. However, this does not automatically discount the basic design from use in the gantry

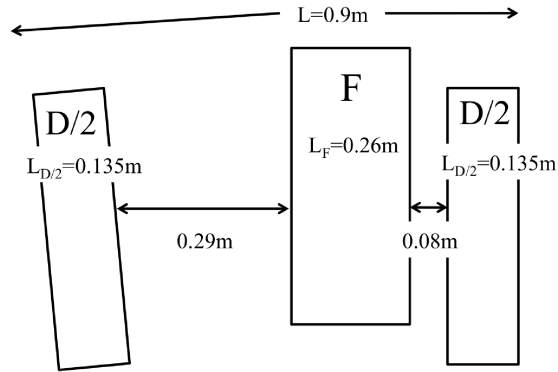


FIGURE 3.17: A KST lattice cell [75].

as single pass transport lines cannot build up resonances and a compact design will be desirable. D. Trbojevic has followed this line of inquiry in a number of papers, which will be discussed in section 3.4.7.

### 3.4.5 Edge Focusing ns-FFAG

How PAMELA got round the problem of resonances has been discussed in section 3.2, but another way of doing it has been investigated by Carol Johnstone and Shane Koscielniak [76]. While non-linearities are reintroduced to the fields in PAMELA to control tune variation, in this design, it is attempted with a combination of weak focusing (see section 2.4.3), a radial shaping of the pole tip, edge focusing and the linear focusing from the quadrupole gradient.

Edge focusing arises when a beam goes through the fringe field of a magnet at an angle. Different angles will give different strength focusing, so changing the angles of the magnet entrance with radius, keeps the tunes stable with acceleration.

In simulation, this produces some impressive results so far, however, it was rejected by the PAMELA project through fears that the magnets would be problematic to manufacture; especially if they are to be superconducting. This is also a valid reason to discount

it for the studies in this thesis.

### 3.4.6 Grahame Rees Pumplet Design

What all the slow cycling ns-FFAGs have in common is an increase in variable parameters to adjust compared to the original ns-FFAG concept. Johnstone and Koscielniak have extra modes of focusing, the PAMELA lattice has extra field components, while Grahame Rees has added extra magnets [77].

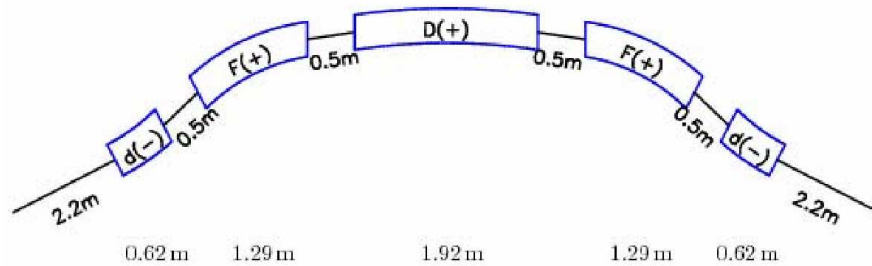


FIGURE 3.18: A ‘pumplet’ cell. The term derives from the Welsh for ‘five’.

Rees’s ‘pumplet’ (pronounced ‘pimplet’) cells, shown in figure 3.18, are flexible enough to match different types of cell together to allow for insertions with long drift lengths where needed. This design is being considered for use as a proton driver for a proposed neutrino factory and it has been adapted for medical applications [77], with a gantry proposal discussed below.

### 3.4.7 Gantry Design Developed from the KST Lattice

This design has developed out of the KST lattice [74]. The geometry is created by taking three quarters of a ring, then turning around the first quarter. Magnets can then be taken out either side of the point where the line has been switched, to lower the height [78–80].

Dispersion and beta functions are kept low with a very dense lattice, but the design proposes small permanent magnets, so the weight should be less than conventional gantries [80]. The height is only 2.61m and it uses scanning magnets at the end of the gantry (see figure 3.19). A variation on this gantry is also discussed in [80] using superconducting magnets and with the scanning magnets placed before the final triplet. This is also a very compact and dense design.

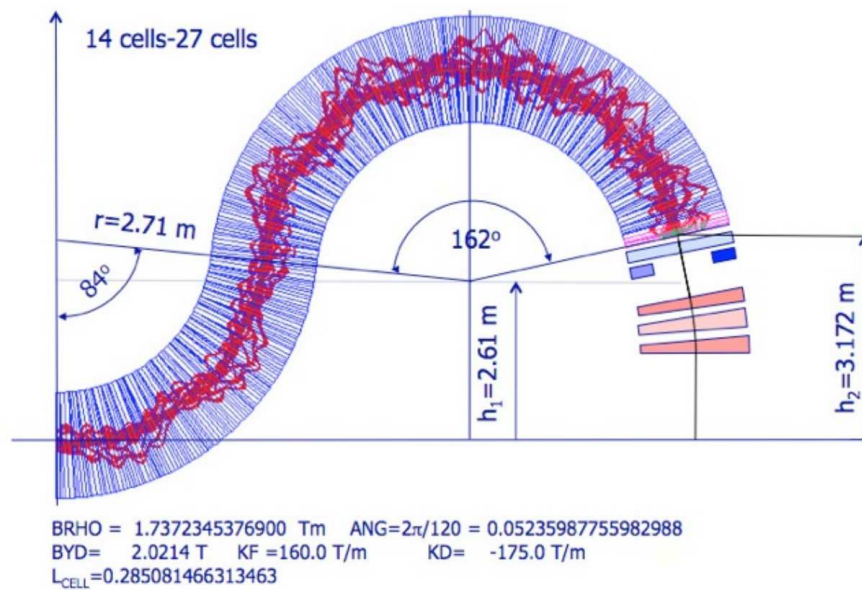


FIGURE 3.19: A gantry developed from the KST lattice [80].

This gantry has been proposed for use with the PAMELA lattice, however, it will not be pursued. This because the density of the magnets is too great. Although the gantry will not require any RF cavities, the magnet design here would be very challenging (for example, at the switch of the point of curvature, opposite bending magnets are placed immediately next to each other). The designers point out that permanent magnets are available that could overcome these problems [80], however, the PAMELA lattice is already using non-conventional magnets in its main ring, so further unconventional type magnets in the gantry would probably be too high a risk.

However, the overall geometry is a good place to start for the design of an FFAG gantry and will be used in this thesis.

### 3.4.8 Gantry Design by Grahame Rees

This is a proposal for a new geometry of a gantry that aims to overcome the problem of the reverse bend in conventional gantries and the idea can be seen clearly in figure 3.20. The  $270^\circ$  bending is done by large combined function (dipole and defocusing quadrupole) magnets with small focusing magnets between each cell. In the initial plans, it has a 10m diameter, which is about half the length of the Heidelberg gantry, but its circular shape means it also has a 10m radius — roughly double the height. Scanning is done in the nozzle above the patient, but there would also be a tracking dipole where the ions are injected below the patient platform.

The idea of an horizontally compact gantry design with no reverse bend and simple magnets that neither ramp over time or create complicated beam dynamics, is very appealing. However, the large bending magnet next to the patient may cause problems and it has a very high vertical radius compared to the other gantry designs. The reason it will probably always be higher than conventionally shaped gantries is that it has to do a complete  $270^\circ$  bend, whereas conventional gantries can flatten out by not bending an initial  $90^\circ$  before bending back.

### 3.4.9 Transport Line Design by Shinji Machida

As bending is tied to focusing in FFAG magnets, transporting a beam in a straight line is not entirely straight forward. The scaling law itself, assumes a curvature by defining a radius. The solution proposed by Shinji Machida in [82] is to make the curvature very

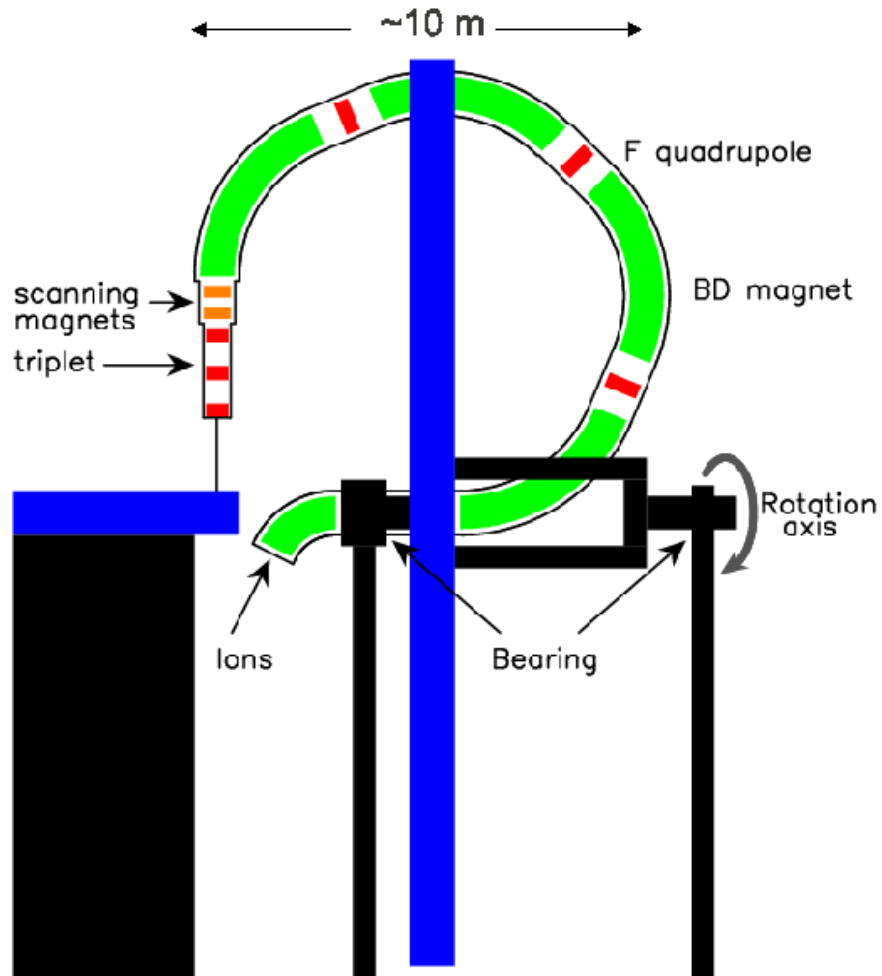


FIGURE 3.20: A proposed gantry layout without a reverse bend [81].

small by making the radius of curvature very large. The scaling law is rewritten as:

$$Bz = Bz_0 \left( \frac{y + y_0}{y_0} \right)^k \quad (3.1)$$

Where  $y_0 \gg y$ .

Machida uses a quadruplet cell, which can really be thought of as a doublet with the F and the D magnets split in half. A long straight can then be added between either F or D magnets because the deflections of the particles and the Twiss parameter alpha, will be zero at these points, as shown in figures 3.21 and 3.22.

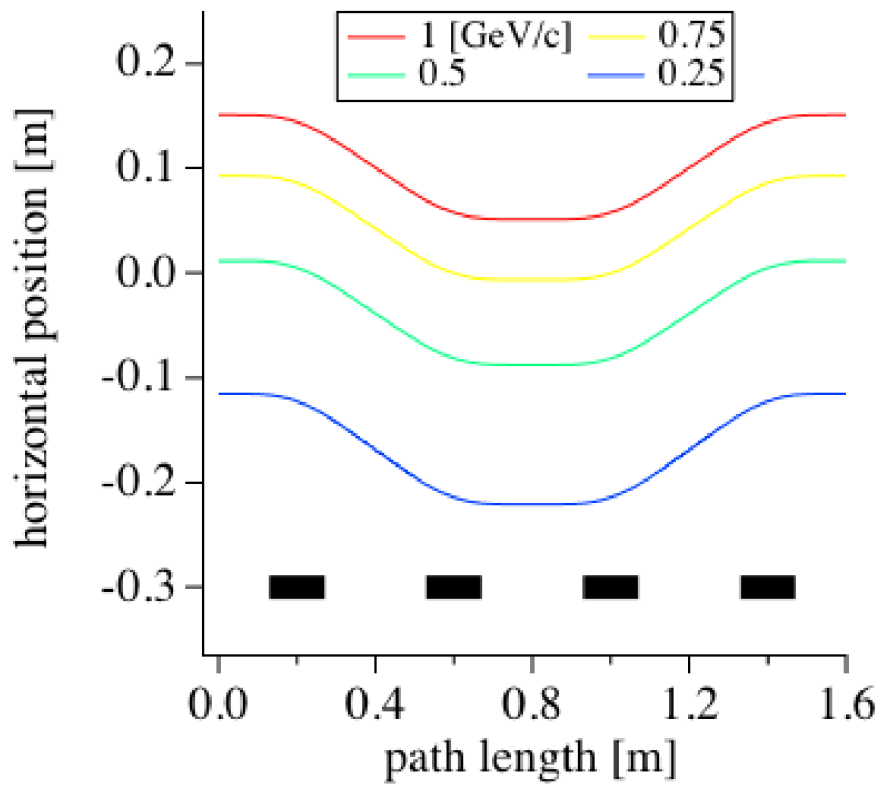


FIGURE 3.21: Tracks through a quadruplet straight transport line cell. [83].

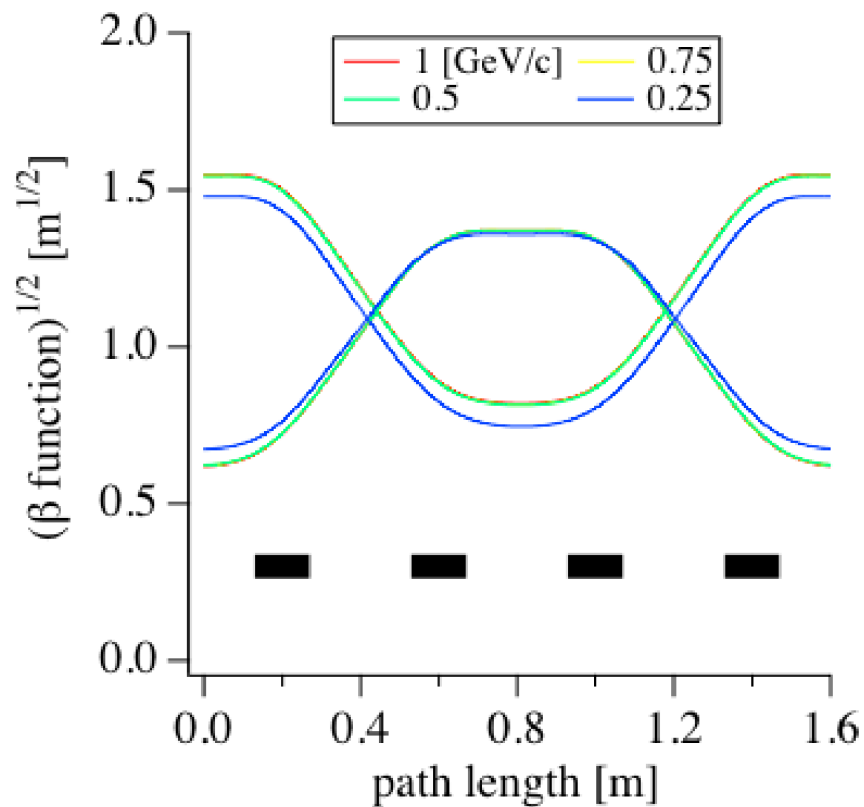


FIGURE 3.22: Beta functions through a quadruplet straight transport line cell. [83].

It is also shown in [82] how an FFAG dispersion suppressor can be designed by doubling the  $k$  value of the cells.

This paper is obviously a good base to build the transport line design on and it will be studied further, along with the dispersion suppression technique.

### 3.5 Motivation for a New Gantry and Transport Line

From this review of the existing literature, it can be seen that a new line of inquiry is desirable for the PAMELA gantry and transport line. Although the PAMELA accelerator would still be advantageous with a variable field gantry and transport line [26], its full potential would probably only be reached using fixed fields for the down stream elements because this will allow the fastest switching between energies and subsequently reduced treatment times.

For reasons already discussed above, of all the approaches to FFAG design, the one used in the main PAMELA ring seems the most practically appropriate.

### 3.6 Chapter Summary

This chapter gives an overview of the immediate context to the work in this thesis which shows the author's understanding of the specific field in which he is working. The PAMELA project was explained (section 3.2) because the work in this thesis is for that project. Existing gantries and rotator systems are discussed in sections 3.3 and 3.3.1 because a gantry is to be designed. A history of FFAGs is presented in section 3.4 which builds up to a review of the current literature on the subject.

## Chapter 4

# Specifications and Challenges

The broad aims of this thesis are to design a transport line and gantry for the PAMELA project using ns-FFAG magnets. This chapter will narrow down the exact specifics, give an overview of the challenges these create and identify possible starting points for the task ahead.

The statement of the aims of this thesis as ‘designing the transport line and gantry for PAMELA’ is a concise, but broad statement, which could include a wide range of areas of study I do not intend to go into. This thesis is really concerned with a *lattice design* for the main bending and focusing magnets. This means that, for example, it will not go into detail about how a particular magnet will be fabricated, or the engineering issues involved in rotating 5m high gantry holding 30 superconducting magnets and all the liquid nitrogen required to keep them cool. These are interesting and important problems, but beyond the scope of this thesis. I will also only be designing beyond the start of the bending magnets in the transport line and before the end of the bending bending magnets in the gantry, as a result the extraction system from PAMELA and the scanning system at the patient will not be tackled. The PAMELA project intends

to treat with protons and carbon. This thesis, however, will mainly design for proton therapy, since the principle needs to be shown with these, lighter, particles first, before the higher magnetic rigidity of the carbon ions can be tackled.

## 4.1 Specifications

There are three sets of requirements that the transport line and gantry must meet. Firstly, and most obviously, the magnets have to be engineerable; there may be solutions with 6T fields and 20cm long magnets, but they would only be useful to this study if a general proof of principle is required and could be refined into a reasonable design. Secondly, there are clinical requirements; this is a design which will be used for medical applications, hopefully within hospital buildings, so there are constraints on the beam that is delivered and the space that can be used in doing so. Thirdly, there are requirements specific to the PAMELA project; the transport line has to match to the extraction point of the PAMELA ring as well as be constructed at the same time.

The beam specifications are dictated by the clinical requirements [26]. Firstly the energy range has been chosen so that the beam can penetrate between 3cm to 25cm into the body, to reach the most deep seated tumours from any angle. The lower limit corresponds to the energy at which protons become useful [26]. This corresponds to an energy range in the transport line and gantry of 60 to 240 MeV or a momentum range of 0.369 to 0.729 GeV/c. From the point of view of the gantry and transport line, switching between these energies should be treated as instantaneous.

The voxel size should be between  $4 \times 4 \times 4$  mm and  $10 \times 10 \times 10$  mm (or  $64 \text{ mm}^3$  and  $1000 \text{ mm}^3$ ) [26], though only the transverse dimensions are important to this thesis. These

put a constraint on the beta functions at the end of the gantry, because it means the  $\sqrt{\varepsilon\beta}$  in both the horizontal and vertical planes should be between 4 and 10 mm.

The scanning system may take a slightly different form than that defined in [26]. All existing scanning systems have no variation of horizontal position with momentum, so a volume will be filled voxel by voxel, with a beam shape as regular as possible. However, as FFAGs have an inherent dispersion, a less conventional way of filling a volume could possibly be used. Assuming the intensity of the beam can be varied as quickly as the energy, it would be theoretically possible to fill a volume with an irregular shape like a curve. This would be a great aid to lattice design, but would put a burden on the treatment planning software [84].

The advantage of using an FFAG accelerator is that scanning through the energy range can be done very quickly; considerably reducing the time it takes to scan any given volume. In principle, the transport line and gantry should not slow this down by introducing variable field magnets, so FFAG magnets should be used throughout. However, as this thesis will show, there are reasons why this is not always possible, or even desirable, but it is an important goal in the first approximation.

Due to the non-linear nature of the type of magnets this thesis considers, scanning cannot be done before the final 90 degree bend as it is in most existing gantries [26, p.148]. The fact that scanning must be done after the bending places a constraint on the space between the last bending magnet and the centre of rotation. This length is determined by the maximum angle needed to be swept by the scanning magnets added to the space needed for the patient.

The PAMELA project requires an area  $20\text{cm} \times 20\text{cm}$  to be treated from any given rotational position of the gantry. This can be achieved with a 0.1 rad deflection and 2m

of drift. However, this will not be the upper limit because at least a metre is required for the patient to fit into without feeling claustrophobic and another 2 metres will be needed for the scanning dipoles and quadrupoles to control the beam size. Therefore there should be three metres between the end of the bending magnets and the isocentre (figure 4.1).

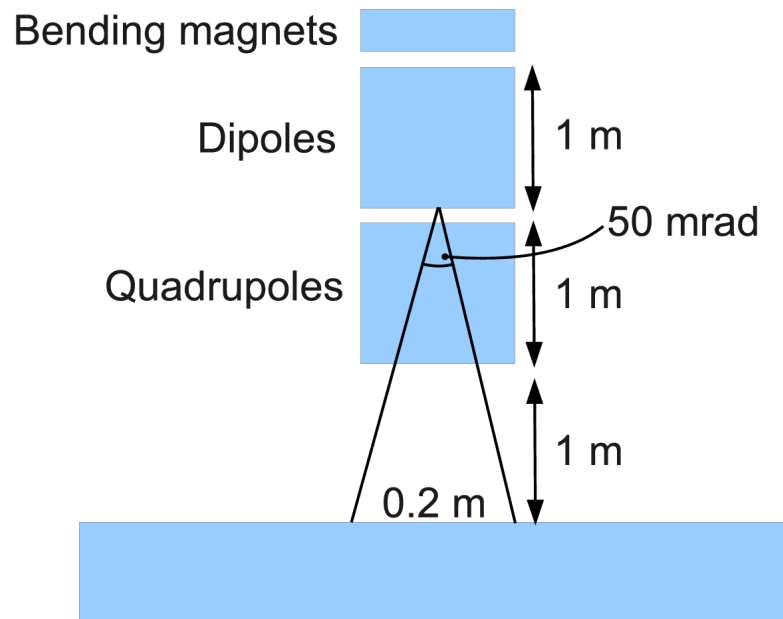


FIGURE 4.1: Schematic of the end of the gantry showing that 3m is needed between the last bending magnet and the isocentre.  $50\text{mrad} \approx 3^\circ$

To keep costs of the project down, it was suggested that the magnets used be similar to those used in the PAMELA main ring (section 3.2.4). Turning that requirement into concrete numbers is difficult as designing them is a complicated process. However, at the time of design, as a rule of thumb, the author was advised that the peak field should not exceed 3T and the length should be a minimum of about twice the aperture [85]. (Although, if a design can be made with fields less than 1T, it might be possible to use more conventional warm magnets, which would theoretically be cheaper than the PAMELA type magnets). Another constraint this imposes is that the magnets must be rectangular in the horizontal plane and be orientated parallel to the other magnets

within the same cell. The cost issue also means as few magnets as possible should be used.

The geometry of the gantry is constrained by the space it should fit in to and the distance needed between the end of the bending magnets and the patient. In hospitals, height is often more expensive than length, so the design should prioritise appropriately. The gantry at Heidelberg is the largest currently existing and requires 10m of height to do a  $360^\circ$  revolution; this is considered to be too large for anything comparable to be built again. The PAMELA design should be smaller.

#### 4.1.1 Summary of Specifications

Beam Specifications:

- Momentum range = 0.369 GeV to 0.729 GeV
- Switching between momentum at a rate of  $\approx 1\text{kHz}$
- Positional dispersion limited to 5cm at end of gantry.
- Angular dispersion limited to within around  $0.03^\circ$  (0.5 mrad) at the end of the gantry.
- No distortion of the beam due to rotation of gantry.
- $0.4\text{cm} < \sqrt{\varepsilon\beta} < 1.0\text{cm}$

Magnet specifications:

- Fixed fields throughout the transport line and gantry
- Rectangular in the horizontal plane
- Magnets parallel with in cells
- Aperture of the magnets around half the size of the length
- Fields no higher than 30T
- As few magnets as possible to be used

Space Specifications:

- 3m from bending magnets to patient
- Total height less than 10m
- Height more important than length

## 4.2 Design Challenges and Possible Solutions

The purpose of this section is to identify the main challenges involved in transporting the beam from the PAMELA ring to the patient, and propose possible solutions, before discussing the design studies that will be undertaken. There are three main challenges: the transport line, the gantry and matching between the different sections.

### 4.2.1 The Design of the Gantry

In [78] the elevation and rotation of the beam required in the gantry is created by taking three quarters of an FFAG ring and turning the bottom around. Fig.4.2 shows how this would look using the PAMELA ring. This is a good place to start the design because it fits the criteria of using the same magnets as PAMELA. However, there are a number of problems that need to be overcome to make this into a reasonable gantry design.

#### 4.2.1.1 Switch of Curvature

The most striking problem is that the curvature changes at point B in fig.4.2, meaning that a high energy particle travelling on the outside of the curve between A and B would have to either travel on the inside of the curve between B and C (negative dispersion), or switch sides at point B in fig.4.2.

As discussed in section 2.5.3, the scaling law offers the possibility of negative dispersion. However, the momentum compaction in a negative  $k$  field is different to that using a

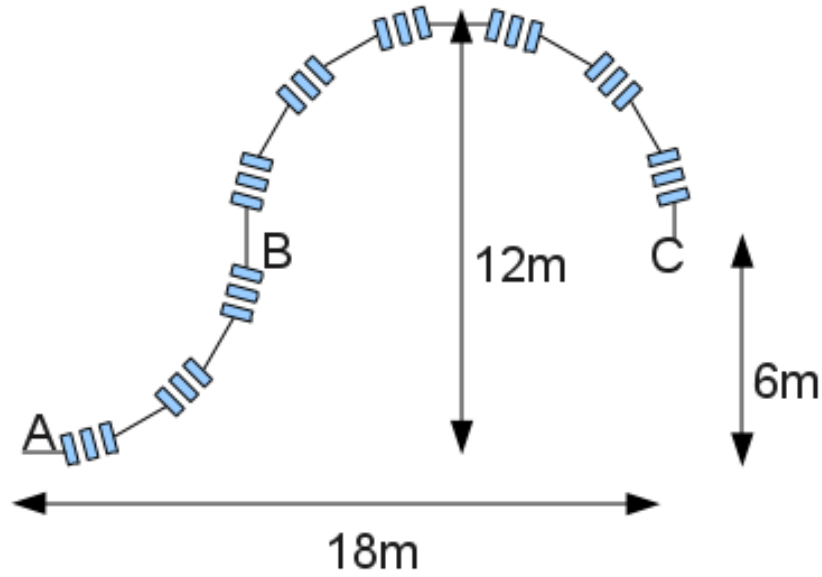


FIGURE 4.2: Schematic of the PAMELA lattice turned into a gantry by taking three quarters of the ring and flipping the bottom quarter. Points A, B and C are referred to in the main text.

positive  $k$ . This can be seen in equation 2.28, which rearranges to:

$$y = y_0 \left( \frac{p}{p_0} \right)^{\frac{1}{k+1}} \quad (4.1)$$

For any given  $p$ , the effect of swapping the sign of  $k$  is more than simply swapping the sign of  $y$ . This means that matching between the regions would be problematic.

The more appealing approach is to create a lattice that will switch the equilibrium orbit positions from one side to the other either side of point B. This involves the dispersion being reduced to zero and recreated afterwards.

#### 4.2.1.2 Rotation

As mentioned in section 3.3.1 all existing rotator systems rely on time varying magnets to match the beam to the rotating gantry. This clashes with the need for an entirely fixed field system, and it would be desirable to design a novel solution to this problem.

The major problem, however, is that every energy is necessarily travelling along the same path through the rotator, so it is very difficult to see how manipulating the Twiss functions of each energy independently would be done with fixed fields.

Of the existing solutions discussed in 3.3.1, only the symmetrical beam method would be appropriate. The rotator method is mainly useful for irregularly shaped beams and would add unwarranted complexity to the design. Whereas the round beam method requires some point within the gantry at which the phase advances are an integer multiple of  $\pi$  in both planes. As will become apparent in section 5.5, achieving this for all momenta with fixed fields would be very problematic due to the non-linear nature of suppressing dispersion with FFAG fields.

The symmetrical beam method works by making the beam rotationally symmetrical at the entrance to the gantry (point A in fig.4.2). This means that dispersion should be zero and the transverse shape of the beam should be circular. A circular beam requires  $\beta_y = \beta_z$  and  $\alpha_y = \alpha_z = 0$  and the transport line should be designed in a way that it delivers this with fixed field magnets if at all possible.

#### 4.2.1.3 The End of the Gantry

At the end of the gantry (point C), the beam will go into the scanning system. From discussions with the designer of this system [84], it was decided that the beam must have zero angular dispersion (to within  $0.03^\circ$  or  $0.5\text{mrad}$ ), and a reduced positional dispersion. As at points A and B in fig.4.2, dispersion suppression is required. This will be discussed in section 4.2.5.

### 4.2.2 Transport Line

The schematic in fig.4.3 shows a possible layout for the treatment rooms and the transport line. It contains the major challenges that any transport line design will have to overcome: transporting the beam in a straight line; bending the beam; and reverse-bending the beam into the treatment rooms with a switchable magnet.

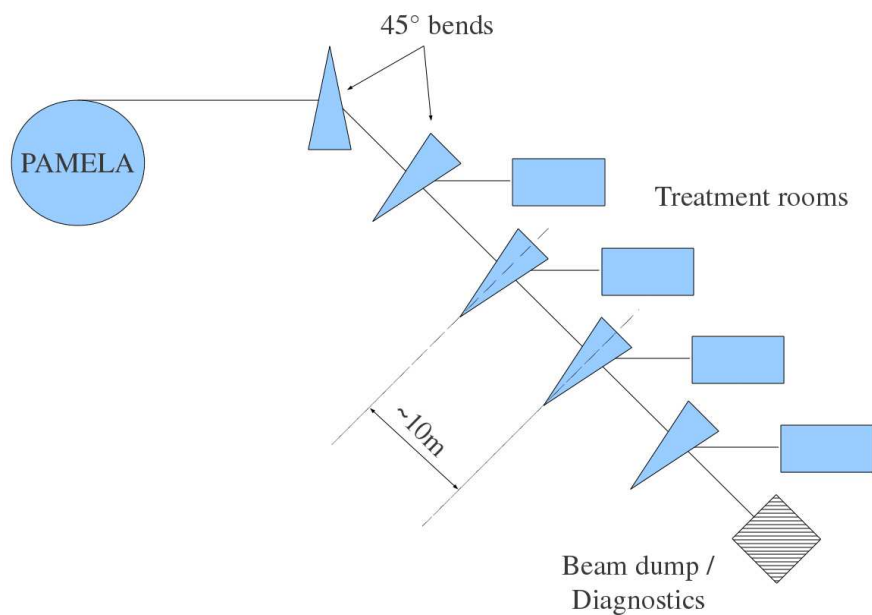


FIGURE 4.3: Schematic of the transport line and treatment rooms.

#### 4.2.2.1 Transporting the beam in a straight line

The problem of straight FFAGs has been discussed in section 3.4.9 with reference to [82]. This is the approach this thesis will use as a starting point.

#### 4.2.2.2 Bending

Once a straight design has been achieved, it will be another challenge to disrupt the periodicity of the lattice and introduce the matched bending section shown in fig.4.3.

This is a lattice design problem and involves creating a section of lattice which matches

to the equilibrium positions and the Twiss functions in the straight sections either side of the bend.

### **4.2.2.3 Switching into Treatment Rooms**

An even bigger challenge will be the extraction to the treatment rooms because these are reverse bends, which, as discussed already, will be problematic with FFAG magnets. Moreover, a switchable magnet will have to be used to redirect the beam to the treatment room.

The obvious solution for the switching magnet is to put a dipole somewhere in the long drift between cells. This has the advantage of using simple magnets to do the switching, but there will have to be matching to cope with the dispersion created by the dipole.

Another possible solution is to switch off one of the magnets in the main transport cell in a way that angles the beam away from the straight. This means that no new magnets need be manufactured and there will be no added dispersion, however if the magnets are superconducting, it may not be an easy thing to turn off a magnet within a cell.

As in the gantry, where a similar problem involving reverse bends is faced, a solution using dispersion suppression should be explored.

### **4.2.3 Matching to PAMELA**

At the time of writing, an extraction scheme has not been fully worked out for PAMELA, so any design will have to be flexible enough to add a matching section. As a guide, however, this thesis will use the characteristics of the beam at the centre of PAMELA's long drift.

#### 4.2.4 Matching from Transport line into the Gantry

The point at which the transport line and the gantry meet is very important because the gantry has to be able to rotate through 360 degrees without distortion of the beam. There are various ways of dealing with this (outlined in [62, p.143]), but none specifically proposed for FFAG gantries.

The simplest solution would be to create a perfectly round beam at this point with horizontal beta equal to the vertical beta and both alphas equal to zero (see section 3.3.1). Dispersion would also have to be zero here. This is especially challenging for an FFAG type machine because the gradient of the field effects both the equilibrium orbit positions (which have to be brought together to eliminate dispersion) and the beta functions.

#### 4.2.5 Dispersion Suppression with Scaling Magnets

As discussed in section 2.4.10, dispersion suppression can be achieved by creating a section of lattice which has half the closed orbit of the previous section and excites half of a betatron oscillation; a  $\pi$  phase advance. In a scaling field, the closed orbit positions can be halved by doubling  $k$  [82]. This is shown by taking the first term of the expansion of equation 4.1:

$$y = y_0 + \frac{y_0}{k+1} \frac{p}{p_0} \quad (4.2)$$

So for a given  $p$ ,  $y \propto \frac{1}{k+1}$ . As will be explained in sec 5.2,  $k \gg 1$ , so for all momenta:

$$y \propto \frac{1}{k} \quad (4.3)$$

and doubling  $k$  halves the equilibrium orbit position. This is the technique that will be used for all dispersion suppression points, however, because this only uses the first term of the expansion of the scaling law, it is not exact, so does not provide perfect dispersion suppression in all cases. This will be tackled in section [5.5](#).

### 4.3 Chapter Summary

This chapter sets up the two design chapters, demonstrating the author's clear idea of the project being undertaken. The specifications are set out in section [4.1.1](#) and the challenges which will be tackled are identified subsequently.

## Chapter 5

# Gantry Design Studies

### 5.1 Introduction

This chapter deals with the process of designing the FFAG gantry. It starts in sections 5.2 and 5.3 with a design of a circular FFAG lattice that is known to work. Three quarters of this ring is then taken and the bottom quarter turned around; as in [78] (see also figure 4.2). In section 5.4 the problems of dispersion described previously in section 4.2.1 are solved (5.5) and it is shown that a gantry design using these type of magnets is possible in principle (5.6). The author presents his own, novel work when describing the solution for the problem of perfect dispersion suppression in section 5.5 and the gantry design presented in section 5.6.

The author's own work is also presented in section 5.7 with a novel design, which reduces the overall height. This requires a complete re-design, which is split up into stages: The final 90° bend is tackled in section 5.7.2; with the preceding S shaped part of the lattice tackled in section 5.7.3; the whole gantry is tied together and its properties presented in 5.7.4. This design is novel and all the work towards achieving it is the author's.

The final section of this chapter (5.10) acknowledges that the final design is probably too large for the PAMELA project and discusses ideas for further work and new lines of inquiry.

Parts of this work are in [86] (section 5.5), [87] (section 5.7) and have been used for the PAMELA design report [26].

## 5.2 Basic Magnet Design

The magnets are modelled in the same way as in the main PAMELA lattice [49]. This starts with the radial sector magnet design described in [46], but for simplicity of manufacturing, the magnets are made rectangular. The field lines within the magnets are regular and parallel with the magnet faces.

The magnets in Zgoubi are defined on an arc (see sec.2.6) because they have to be made rectangular using a very large radius of curvature; making  $y_0 \gg y$  and using the version of the scaling law described in [82]: equation 3.1. The exact size of  $y_0$  is arbitrary, but for convenience of calculation,  $y_0 = 1\text{km}$  will be used. In a 1m magnet, this gives a curvature of  $0.6^\circ$ , which can be compensated for when specifying the exit angle in the definition of the magnet in Zgoubi.

To maintain the focusing strength,  $k$  has to increase by the same order of magnitude as  $y_0$ . So as  $y_0$  is going from  $\approx 1\text{m}$  to  $1\text{km}$ ,  $k$  should become  $k \times 1000$ . This can be seen by looking at the expansion of the scaling law (equation 2.30). Taking the quadrupole term:

$$Bz = B_0 \frac{k}{y_0} y \tag{5.1}$$

If  $k$  is not increased by the same factor as  $y_0$ , increasing  $y_0$  would have the effect of reducing the quadrupole strength to close to zero. This thesis will take the multiplication factor of  $k$  as implicit, so a  $k$  of 5000, for example, will be referred to as 5.

The shape of the field going through the magnet in the  $s$  dimension is not uniform. Each magnet has a fringe field that extends beyond the edges of the magnet and the field does not jump to its full strength immediately within the magnet. Because the magnets are rectangular, the shape of the field is actually defined along  $x$ , the dimension tangential to  $s$  (see figure 2.1). The shape of the field along  $x$  is defined using the Enge function  $F(x)$  [43, p74]:

$$F(x) = \frac{1}{1 + \exp\left[\sum_{i=0}^5 C_i \left(\frac{x}{g}\right)^i\right]} \quad (5.2)$$

Where  $C_i$  are the Enge coefficients and  $g$  is the extent of the fringe field beyond the edge of the magnet, as well as how far into the magnet the full field is reached. Figure 5.1 is an example of what an Enge function looks like using the same coefficients ( $C_i$ ) as the main PAMELA ring: (0.1455, 2.2670, -0.6395, 1.1558, 0, 0)[49] as well as the same value of  $g$ : 0.15m.

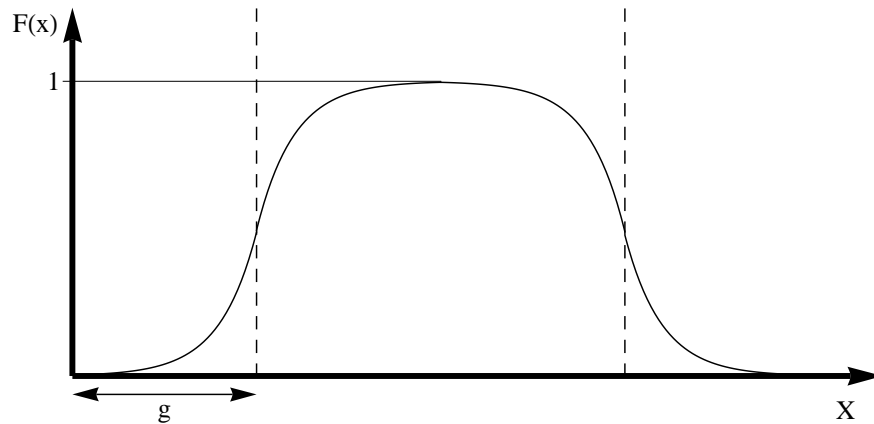


FIGURE 5.1: An example Enge function: used by Zgoubi to model the fringe fields.

The Enge function is combined with the scaling law 3.1, to give the field profile in the  $y$  and  $x$  dimensions:

$$Bz(y, x) = Bz_0 \left( \frac{y + y_0}{y_0} \right)^k F(x) \quad (5.3)$$

### 5.3 Basic Cell Design

There are two basic cell layouts that this thesis considers: the triplet (comprising three magnets) and the quadruplet (comprising four). The quadruplet will be used for the transport line and will be discussed in section 6.2.

#### Triplet

The triplet is used for all curved lattices and has the structure of two focusing magnets either side of a defocusing one (FDF). This ensures that the focusing magnets do the bending while the defocusing magnet adds vertical focusing. Figure 5.2 shows an example layout with three particle trajectories drawn through. The D magnet is offset to minimise the aperture.

### 5.4 Proof of Principle Gantry Design

#### Aims

The aim of this study is to show that an FFAG gantry with dispersion suppression points is at least possible in theory. The main thing to establish is that a lattice can be created with equilibrium orbits that start and finish with zero dispersion; the other requirements set out in section 4.1.1 are secondary in this section.

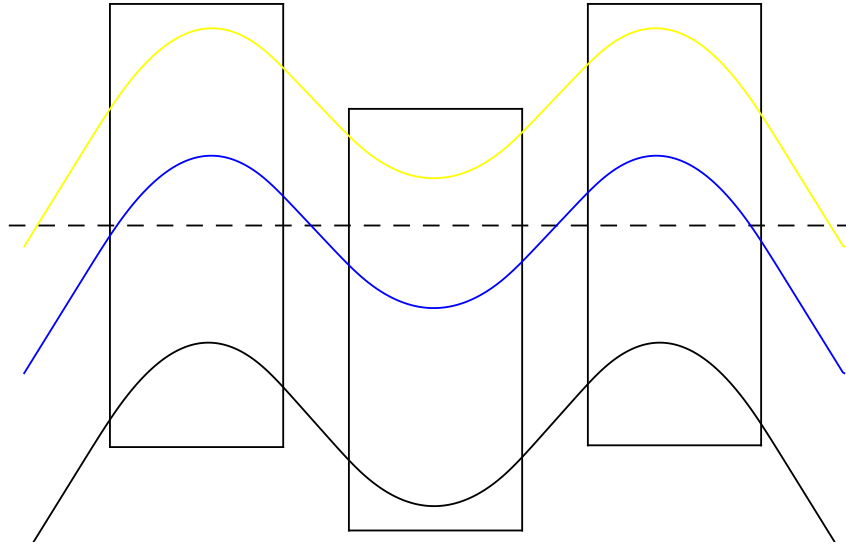


FIGURE 5.2: An example triplet cell (FDF) with three particle trajectories shown (yellow = 0.369 GeV/c, blue = 0.549 GeV/c, black = 0.729 GeV/c). The thick black lines give an idea of where the magnets are and the dotted line is the X dimension.

## Methods

For this gantry to work, dispersion suppression as described in section 4.2.5 has to be achieved, which requires stable orbits to be found for cells with  $k$  and  $2k$  field indexes. There also has to be a section of  $2k$  lattice which has a  $\pi$  phase advance. Theoretically, this could be achieved over any number of cells, however, a  $\pi$  phase advance in one cell would be difficult to design because it would create a resonance when stable orbits are being searched for, conversely, if too many cells are used, the gantry would be excessively large.

To find suitable cell designs, a parameter search of single cells was undertaken. Table 5.1 summarises which parameters were varied and the resulting effects.

From the working lattices available in the results of the parameter search, a cell design was then chosen which had a phase advance close to  $\frac{\pi}{4}$ . Because there were a number of candidates available with a suitable phase advance, the number of magnets required by

each one to bend the beam through  $270^\circ$  could also be considered in the hope it could be turned into a practical design.

TABLE 5.1: Summary of the parameters of a cell and their significant effects.

Parameter	Range	Description	Effects
$k$	$1 \rightarrow 17$	The field index.	Phase advance and momentum compaction.
D/F	$0.8 \rightarrow 1.8$	The ratio of the strength of the D magnet to the F magnet.	Phase advance and maximum field.
Bend angle	$12.875 \rightarrow 45$	Bend angle per cell	Number of cells in the gantry, the phase advance and maximum field.
Cell length	$75 \rightarrow 200$	The length of each cell	Size of the gantry, phase advance and maximum field.
Packing factor	$0.5 \rightarrow 0.9$	The ratio of magnet to drift space within the cell	Phase advance and maximum field.

The next step was to vary  $k$  and the D/F ratio to make the phase advance equal  $\frac{\pi}{4}$  exactly.  $y_0$  is then altered in both the normal and suppressor cells so that the equilibrium orbits of the central momentum were aligned.

A gantry was then simulated using scaling fields. It is summarised in table 5.2, while figure 5.3 shows a schematic of the layout. Zero dispersion was assumed at the entrance and a 3m drift was added to the end to give an idea of what the beam might look like at the distance a patient would be. Success is measured by the amount of dispersion after the last bending magnet and before the scanning system (point C in figure 5.3).

#### 5.4.1 Results and Discussion

At this point, the values of interest are the final positions of the particles: if these are not satisfactory, the gantry will not work. The required uniformity and range of the final positions are constrained by what compensation is possible in the design of the scanning

TABLE 5.2: Parameters of the scaling gantry design.

Parameter	Value	Units
$k$	1.982	
D/F	1.18	
Bend angle	22.5	degrees
Cell length	75	cm
Magnet length	15	cm
Peak Fields (F,D)	6.65, -6.05	T
Max aperture	36.8	cm
Total Cells	12	
Height	636	cm

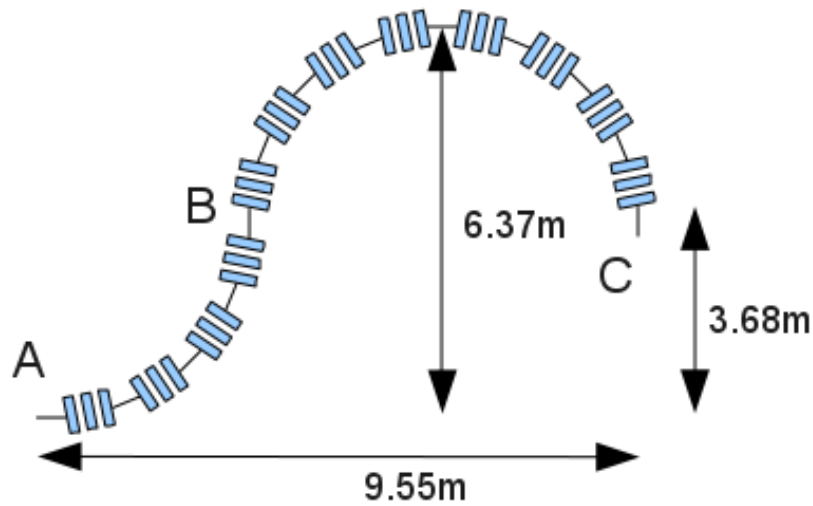


FIGURE 5.3: A schematic of the layout of the scaling FFAG gantry design summarised in Table 5.2. Points A, B and C are the points of zero dispersion suppression.

magnets at point C in figure 5.3 of the gantry and specified in 4.1.1. This states that the final positions across the energy range should be within 5cm and the angles should all be less than  $0.6^\circ$  (1mrad). The results of the simulation are summarised as the following series of three plots showing the tracks of particles travelling through the gantry and their final positions. Figure 5.4 shows the tracks of five particles over the entirety of the energy range. Figure 5.5 shows the final positions of the particles and figure 5.6 shows the final angles. The final positions and angles of the particles clearly show that this design is not good enough to use. The problem is that the dispersion suppression is not perfect at the swap point (point B in figure 4.2) and after the final bending magnet

(point C), so the next section looks at how to create near perfect dispersion suppression using FFAG magnets.

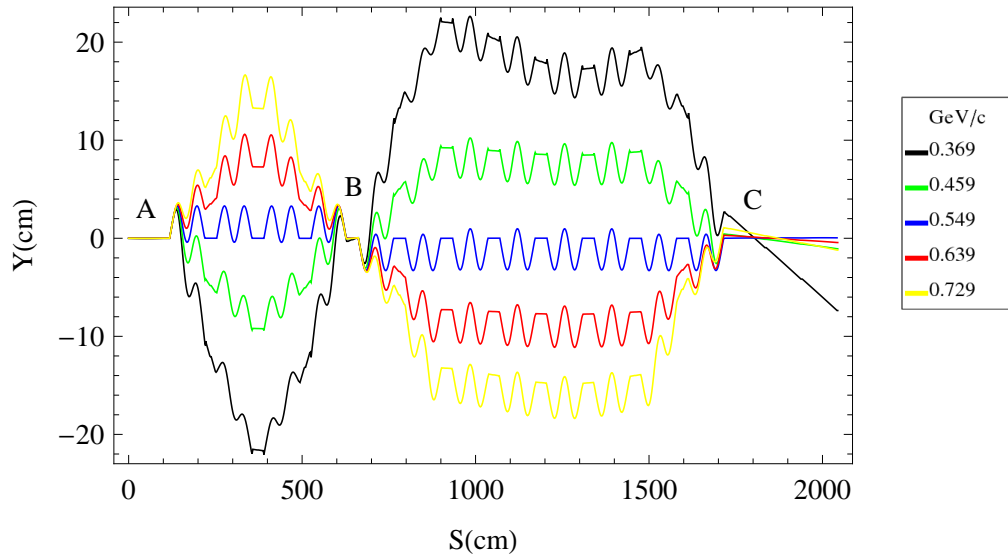


FIGURE 5.4: The particle tracks of five different momenta through the scaling gantry. Points A,B and C correspond to those in figure 5.3. The irregularity after point B is due to less than perfect dispersion suppression and excitation at points A, B and C.

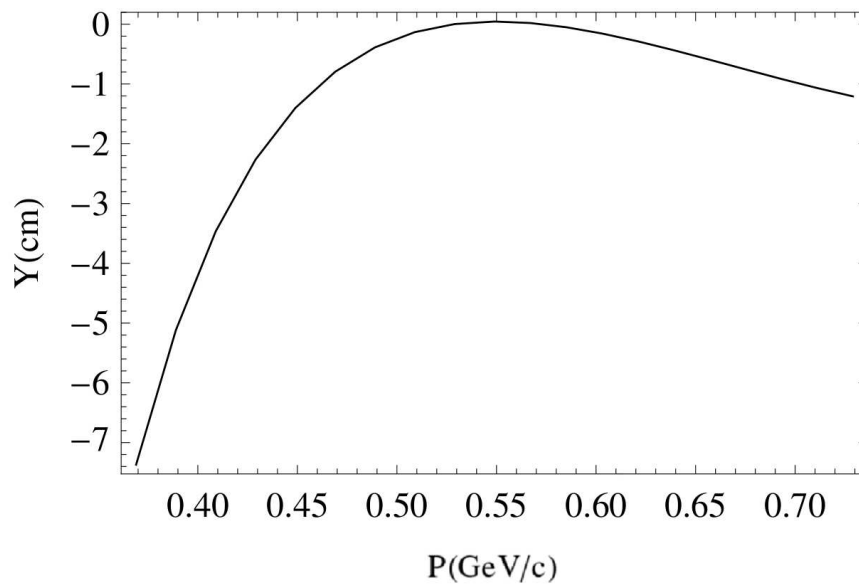


FIGURE 5.5: Final particle positions in the scaling gantry design. Zero dispersion was assumed at start.

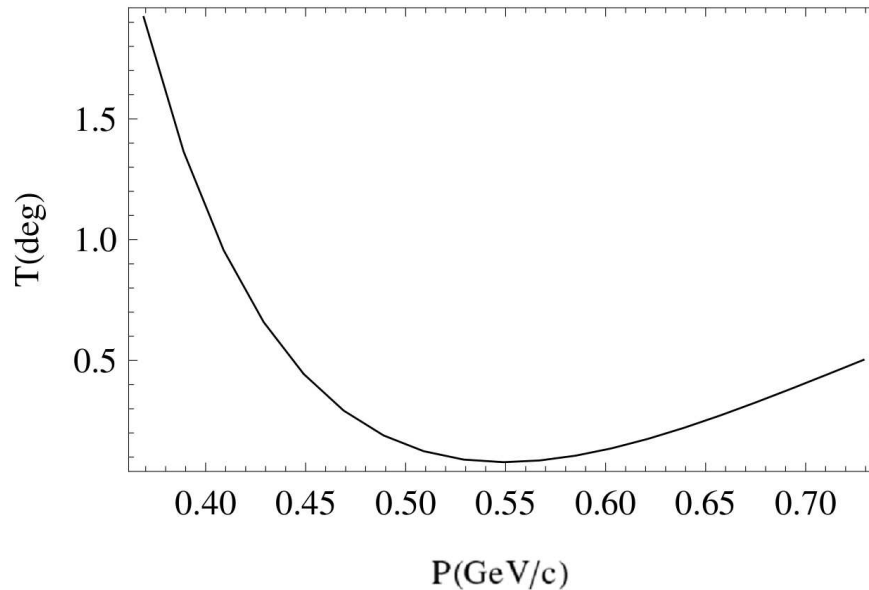


FIGURE 5.6: Final particle angles in the scaling gantry design. Zero dispersion was assumed at start.

## 5.5 Near Perfect Dispersion Suppression

FFAG dispersion suppression has been discussed in section 4.2.5 and [82], where it is noted that the energy range for perfect dispersion suppression is limited. This section presents a procedure to design a non-scaling FFAG dispersion suppressor that improves upon the equivalent scaling design in final horizontal position by around a factor of 30 and deflection by around a factor of ten.

### 5.5.1 Cell Description

The cell this section concerns uses rectangular magnets in an FDF configuration (see figure 5.7) and the  $k$  value and ratio of D to F magnet strengths were chosen so that the horizontal phase advance through the centre of the suppressor cells equals exactly  $\pi$  (see table 5.2).

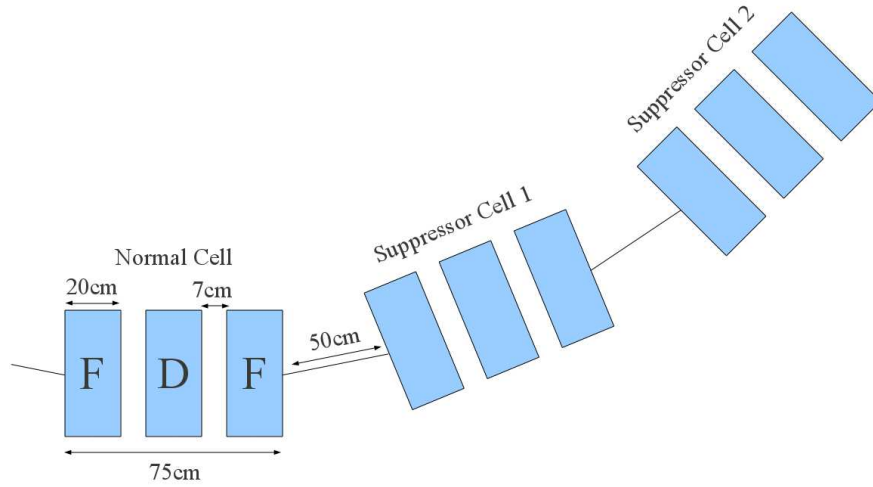


FIGURE 5.7: Schematic of the cell lay-out for the suppressor. There is  $22.5^\circ$  bending in each cell.

### 5.5.2 Non-Linearity

The scaling field in the FFAG is designed to keep the betatron oscillations of particles uniform, regardless of their rigidity, by varying the gradient. This works perfectly for small betatron oscillations because the field gradient over  $\delta y$  can be approximated to a quadrupole field. However, over large oscillations, the non-linearity of the field has an effect, and this causes problems for dispersion suppression.

In the linear case, dispersion suppression can be achieved when two conditions are met (see 2.4.10):

- (i) The closed orbit for each particle is half its horizontal position at entrance,
- (ii) The phase advance for all off-orbit particles is  $\pi$ .

As mentioned in section 4.2.5, to fulfil condition (i) in an FFAG, the closed orbit positions can be halved for all momenta by doubling the field index ‘ $k$ ’[82]. However, because equation 4.2 contains only the first term of the Taylor expansion of the scaling law, it is only an approximation and condition (i) will not be fulfilled exactly.

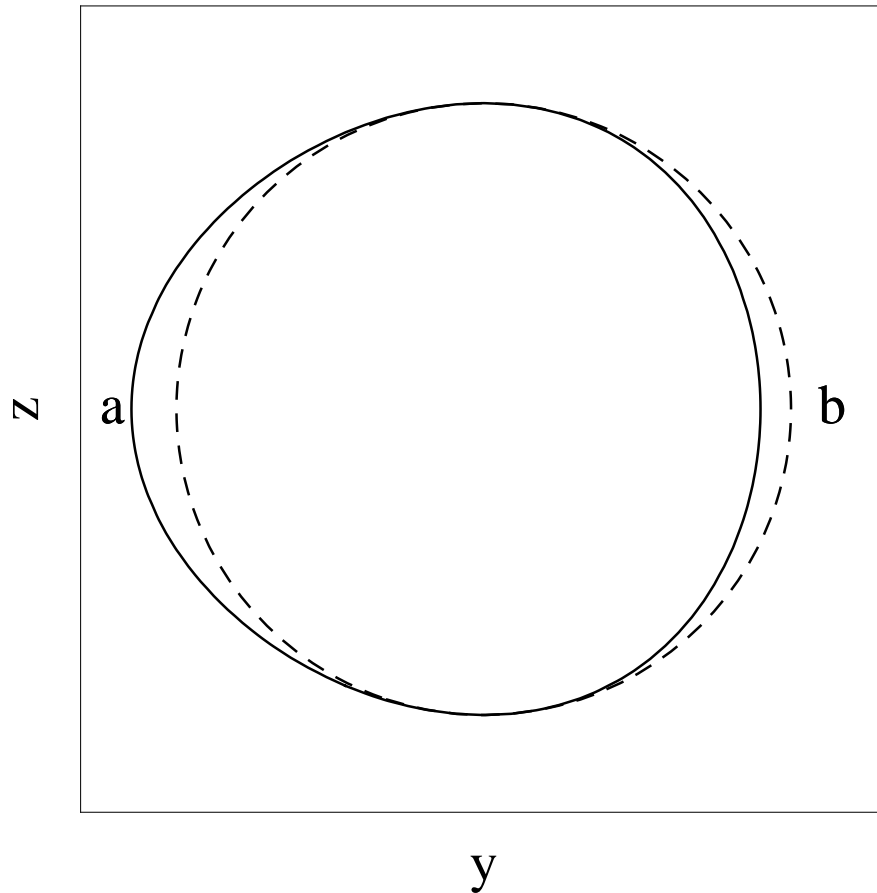


FIGURE 5.8: The equations of motion for a linear field (dotted line) and a scaling field (solid line). A  $\pi$  phase advance in the linear field would take a particle to the exact opposite  $y$  position, whereas in the scaling field it is more complicated.

To illustrate this, consider figure 5.8. This shows plots for the equations of motion of two particles around a shared closed orbit position at a fixed  $s$ . The dashed line shows the motion of a particle in a linear field, with only the quadrupole component of equation 2.30 present. The solid line shows what happens when the sextupole, octapole and decapole fields are added. In the linear case, the motion around the closed orbit is circular, while in the non-linear case, the motion is compressed at higher  $y$  positions and extended at lower ones. The relevance this has to dispersion suppression is that the  $\pi$  phase advance required will go either from  $a$  to  $b$  or vice versa. In the linear case, point  $a$  is exactly the same distance from the centre as point  $b$ , which is what is required for dispersion suppression. However, in the non linear case, a particle starting

at point  $a$  will undershoot the exact opposite position and a particle starting at point  $b$  will overshoot it.

Another illustration of the problem is given in figure 5.9. This shows the difference between the magnitude of the linear quadrupole field and the non-linear scaling field. If points  $a$  and  $b$  mark the extremities of a betatron oscillation in a linear field, you can see that at point  $a$  in the scaling field, the gradient is steeper and the particle will experience stronger focusing, which will cause a shorter amplitude to be described. Whereas at point  $b$ , the gradient is less and so the amplitude will be greater.

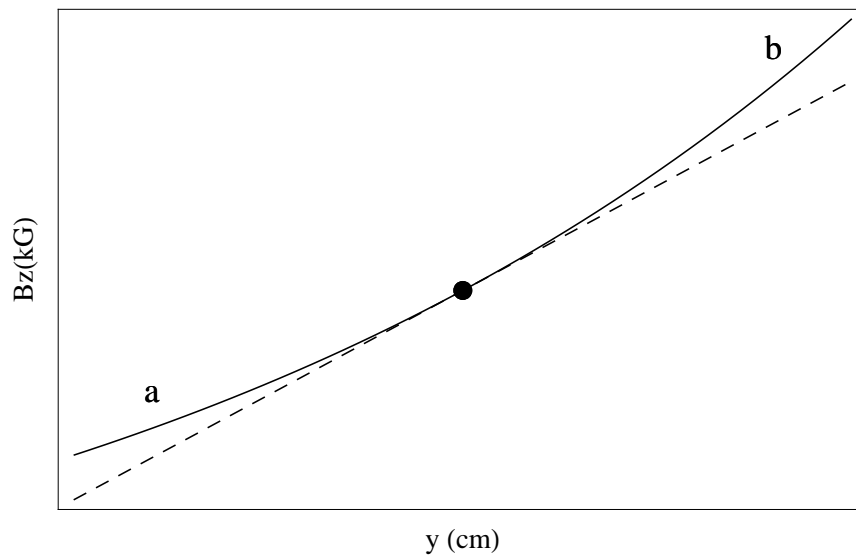


FIGURE 5.9: Comparison of linear (dotted line) and scaling (solid line) field profiles. Points  $a$  and  $b$  mark the extremities of a large amplitude betatron oscillation in the linear field. Notice the difference in gradient at these two points.

In the case of the dispersion suppressor under consideration, lower momentum particles are below the central orbit, so are likely to undershoot it as they complete a  $\pi$  phase advance, and higher momentum particles are above the central orbit, so will overshoot it. This will result in a final displacement below the central orbit dependant on momentum.

Additionally, when the idea of circular motion of a particle in an idealised field is replaced by the more realistic picture of a particle moving through a section of non-linear lattice, not all off-orbit particles will have a phase advance of exactly  $\pi$ . The particles that

travel the furthest in fields with gradients different from at their equilibrium orbit will be effected the most and have phase advances furthest from  $\pi$ .

So, if figure 2.9 is the path of a particle in a linear dispersion suppressor, then figure 5.10 is what the path might look like in a scaling field.

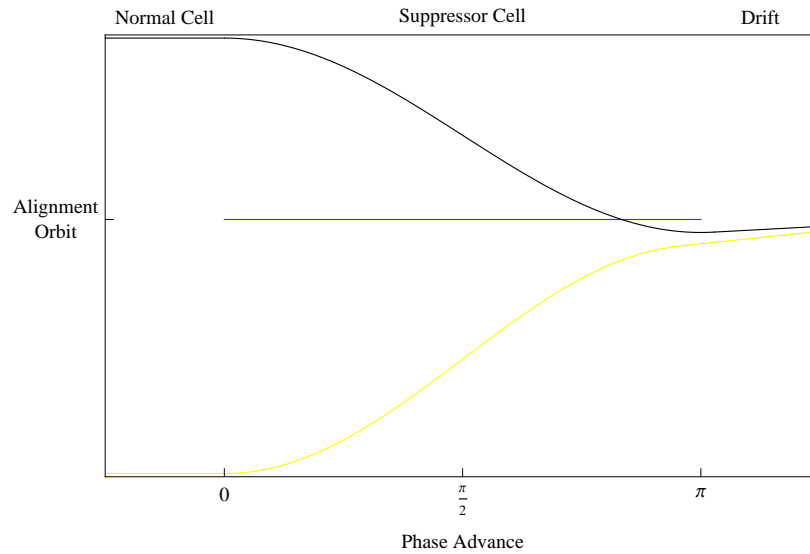


FIGURE 5.10: Sketch of dispersion suppression in a scaling field. Particles miss the alignment orbit and have phase advances  $\neq \pi$ .

Indeed, this is what is seen when the dispersion suppressor (figure 5.7) is simulated. Figure 5.11 shows the tracks through one normal cell and two suppressor cells of five different momenta covering the entire energy range; figure 5.12 shows how the final position depends on the momentum of the particle and figure 5.13 shows the final deflection.

### 5.5.3 Fitting Method

These displacements must be compensated for in some way if perfect dispersion suppression is to be achieved, however this cannot be done with purely scaling magnets. To understand why, consider compensating by changing the closed orbit positions in the suppressor cells. The lower momentum orbits would have to be compacted and shifted towards zero, while the orbits further out from the centre would have to be spread out.

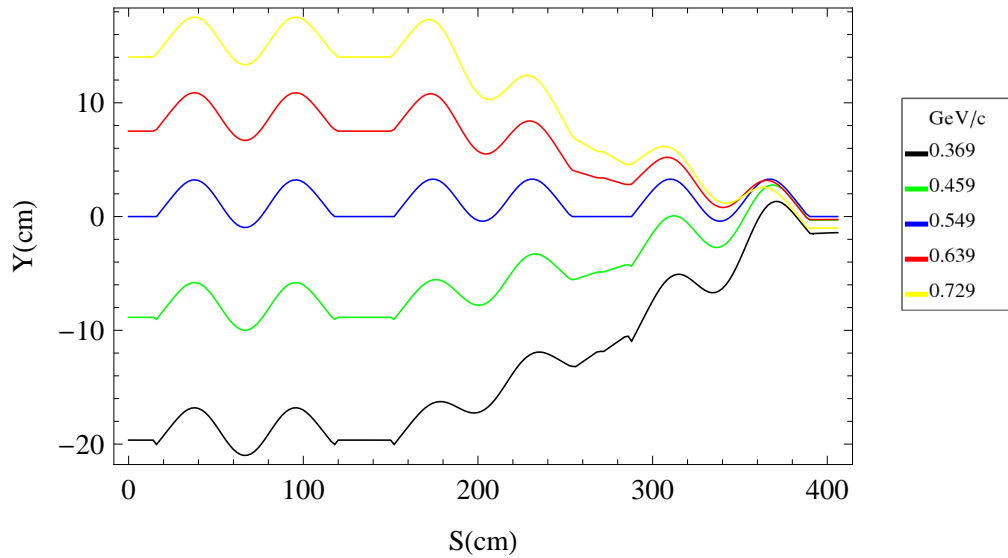


FIGURE 5.11: Tracks through a scaling dispersion suppressor for five different momenta. Significant dispersion is visible at around 400cm.

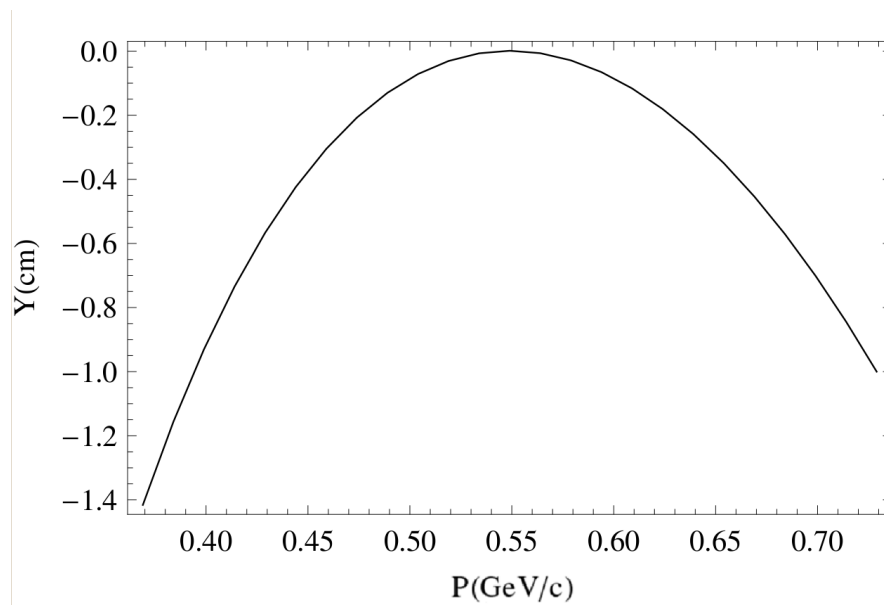


FIGURE 5.12: Horizontal position vs momentum at the end of a scaling dispersion suppressor. Notice how the non-linearity causes the particles above the orbit to overshoot and the particles below it to undershoot.

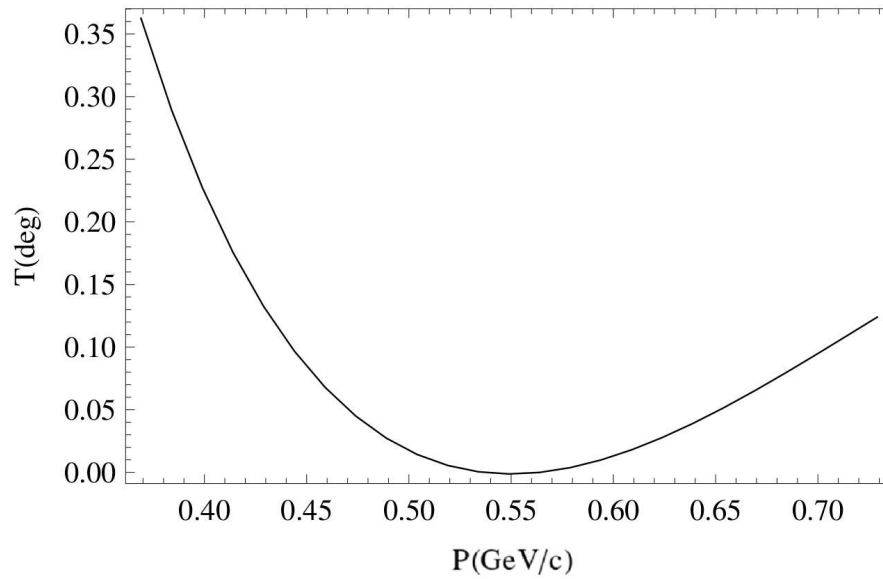


FIGURE 5.13: Horizontal deflection vs momentum at the end of a scaling dispersion suppressor. The deflections are different because most particles have not gone through exactly a  $\pi$  phase advance. The different phase advances are due to each particles different path through the non-linear field.

This rules out simply varying  $k$ , as it would result in *all* closed orbits being either closer together or further apart. The scaling law has to be broken.

To do this, a Taylor Expansion of the scaling law is truncated at the decapole term and the individual multipole components varied in each of the two suppressor cells as well as the normal cell.

For simplicity during the fitting process, the dispersion suppressor was considered ‘backwards’; i.e. the particles were started with zero horizontal position and angle at the end of suppressor cell 2 in figure 5.7 and passed through suppressor cell 1 and into the normal cell.

There is a choice whether to compensate by changing the closed orbits in the suppressor cells or in the normal cell. Because there is less overlap of particle positions within the magnets, it was found to be easier to fit the position of the closed orbits in the normal

cell to the amplitude of the betatron oscillations in the suppressor cells, rather than vice versa.

To correct for the variations in phase advance, the two suppressor cells were varied so that the exit angles were zero for all momenta. To avoid the fitting function arriving at a solution with zero field through all magnets, and because of the overlapping particle tracks in cell 2, only cell 1 was varied. The  $k$  value of suppressor cell 2 can be used to tweak the momentum compaction in the resulting normal cell, so for example, if the resulting aperture is too large, the  $k$  of suppressor cell 2 could be increased to reduce it. This can only be taken so far, however, as varying  $k$  has an effect on the phase advance. This is a summary of the procedure:

- (i) Fit the tune of the alignment orbit particle to  $\pi$  through both suppressor cells.
- (ii) Ensure  $\pi$  phase advance for all momenta by fitting the exit angles out of suppressor cells to zero by varying suppressor cell 2 only.
- (iii) Fit the closed orbit positions in the normal cell to the exit positions from the suppressor cells.

#### 5.5.4 Results

The resulting dispersion suppressor restricts the final dispersion to within 0.5mm and  $0.025^\circ$  (0.4 mrad), which can be seen in figures 5.15 and 5.16. Figure 5.14 shows the tracks through the fitted dispersion suppressor. Note that in comparison to figure 5.11 the closed orbits in the normal cell have been stretched in the  $y$  dimension below the central orbit and compressed above it. The values of the constants in equation 2.30 are summarised in Table 5.3.

TABLE 5.3: Values for the multipole constants ( $b_n$ ) in equation 2.30 for a non-scaling dispersion suppressor.

Cell	$y_0(\text{cm})$	$Bz_0(\text{T})$ [F,D]	$b_1 \times 10^3$	$b_2 \times 10^6$	$b_3 \times 10^9$	$b_4 \times 10^{10}$
1	100033.9	3.816, -4.507	1.907	2.405	2.733	0.1154
2	100012.6	3.371, -3.982	4.143	5.776	23.21	459.4
3	100013.2	3.388, -4.002	4.003	7.461	8.307	1164

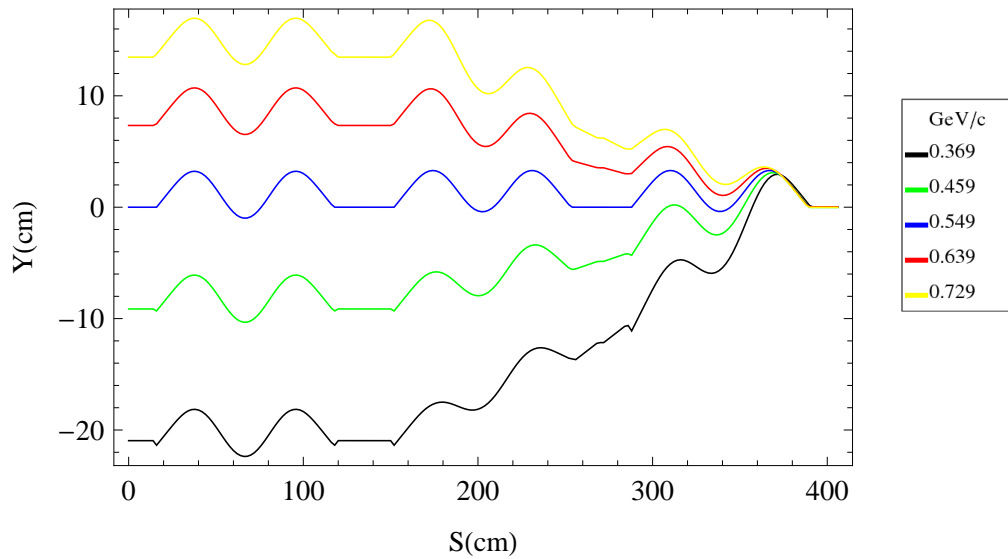


FIGURE 5.14: Tracks through a non-scaling FFAG dispersion suppressor with the multipole components varied to create zero dispersion at the end.

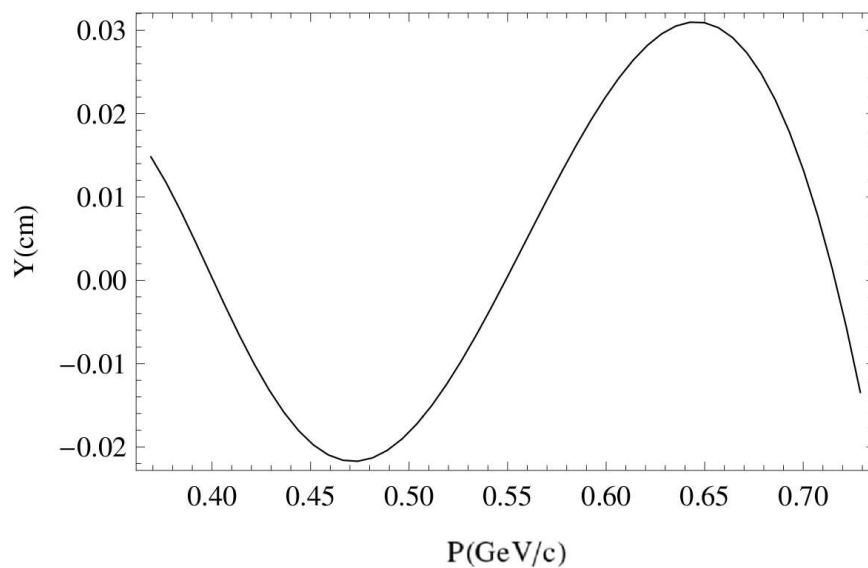


FIGURE 5.15: Horizontal position vs momentum at the end of a non-scaling dispersion suppressor. Notice the change in scale from figure 5.12.

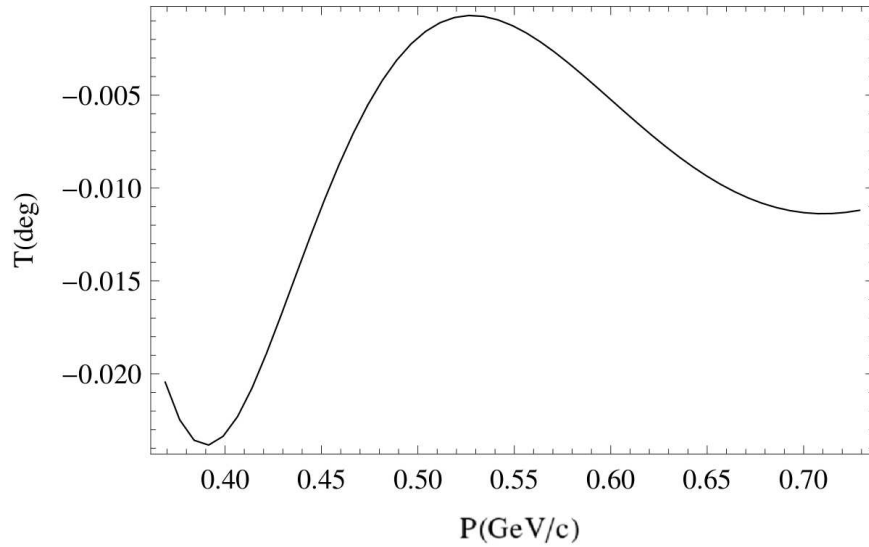


FIGURE 5.16: Horizontal deflection vs momentum at the end of a non-scaling dispersion suppressor. Notice the change in scale from figure 5.13.

The  $\beta$  functions through the dispersion are shown in figure 5.17 and the phase advance<sup>1</sup> in figure 5.18. Because of the different paths through the suppressor cells, there is a variation in all the Twiss functions and the phase advance dependent on momentum. This might result in periodic orbits not being available for all momenta because the variation in tune may excite a resonance. Other designs might be able to overcome this problem, but since the design considered here is for a single pass lattice, a periodic solution is not strictly necessary.

### 5.5.5 Error Study of A Dispersion Suppression Point

The purpose of this study is to assess how sensitive the dispersion suppression point is to transverse errors in magnet positions. The dispersion suppression point was chosen because it is likely to be the most sensitive type of lattice section in the transport line and gantry, so it will give a lower limit on the precision required. Also, this point is the

<sup>1</sup>Please note that this is the phase advance of the small amplitude betatron oscillations on top of the large amplitude oscillation excited by the dispersion suppressor.

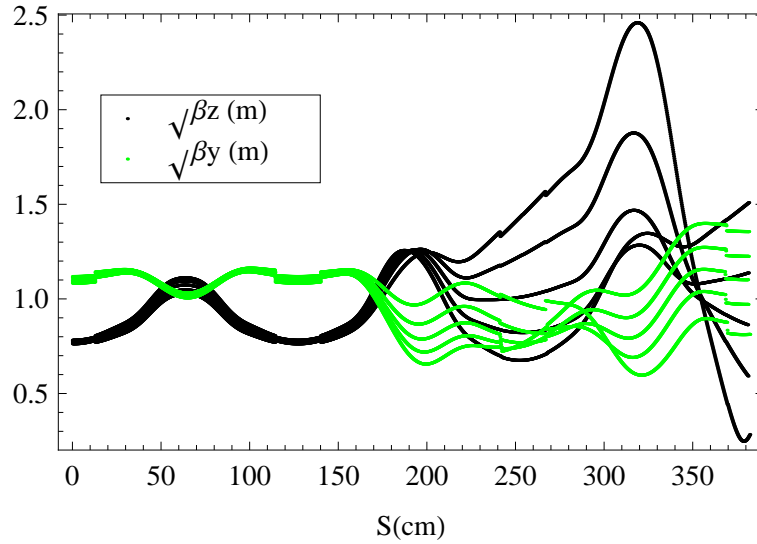


FIGURE 5.17: Beta functions through the non-scaling dispersion suppressor. Initial values are the periodic beta values for the normal cell. The discontinuities seen at around 0, 125, 250 and 370 cm are artefacts from how drift spaces are simulated in Zgoubi. They have no impact on the real values of the simulation.

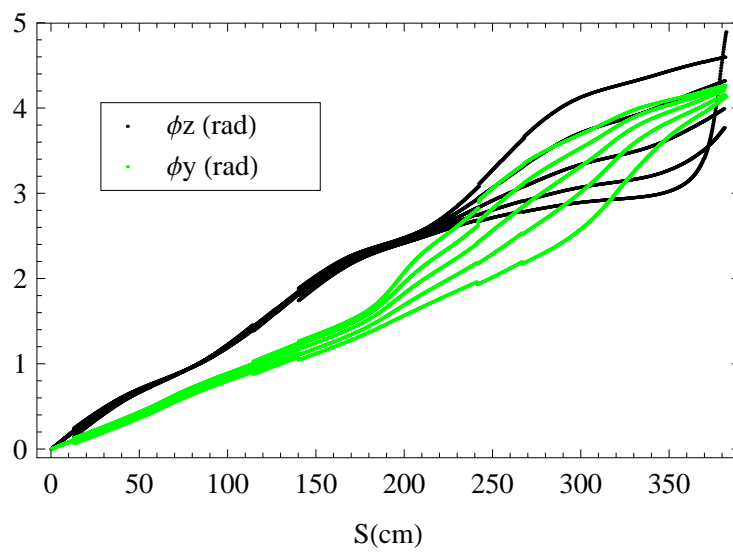


FIGURE 5.18: Phase advance through the non-scaling dispersion suppressor. As in figure 5.17 the discontinuities are artefacts and can be ignored.

most novel part of this thesis, in that the dispersion suppressor has not been studied elsewhere, so it is useful to investigate it further.

It was decided to add errors only to the horizontal transverse position of the magnets because these are the most straight forward to model in Zgoubi. It may be reasonable to assume that this will be the primary source of error in any case. Longitudinal errors can probably be discounted because a longitudinal positional error will manifest itself as a transverse error when the particle reaches the magnet face, but because the angle of incidence will typically be small, the error produced will be negligible compared to a transverse error of the same size.

To test the importance of vertical errors, the field experienced by a particle displaced by a small amount on the z axis was compared to a field experienced by a particle displaced by the same amount on the y axis. It was found that the ratio of the strength of a kick from a z displacement to a kick from a y displacement ranged from  $\approx 10^{-4}$  for a displacement of 50  $\mu\text{m}$  to  $\approx 0.1$  for a displacement of 1cm. However, by itself this does not show that a vertical error is unimportant. To do that, the relative sensitivities must be considered.

The relative importance of the vertical and horizontal errors can be calculated using the equation for the linear approximation of closed orbit response to dipole kicks [88, eq.1]:

$$\Delta\chi(s) = \frac{\sqrt{\beta_\chi(s)}}{2 \sin \pi\nu_\chi} \cdot \Delta\theta_\chi \cdot \sqrt{\beta_\chi(s_{kick})} \cdot \cos(|\phi_\chi(s) - \phi_\chi(s_{kick})| - \pi\nu_\chi) \quad (5.4)$$

Where  $\chi$  indicates either y or z, and  $\Delta\chi(s)$ ,  $\beta_\chi(s)$ ,  $\phi_\chi(s)$ ,  $\nu_\chi(s)$ ,  $\theta_\chi$ , and  $s_{kick}$  are the displacement of the closed orbit, the beta function, the phase advance, the tune, the kick angle, and the location of the kick along S, respectively [88].

This study will look at the four closest magnets to a dispersion suppression point, giving a  $2\pi$  horizontal phase advance between  $s_{kick}$  and  $s$ .  $\Delta\theta$  will be equal in both cases and all the other values were found from simulation.

For the central momentum, the closed orbit responses of a z axis kick was found to be  $\approx \frac{2}{5}$  of the response in the y axis. Combined with the relative kick strengths due to the fields experienced, it can be said that positional errors in the y direction will be the most important. However, due to the non-linear nature of the fields, it could only be said for certain with a full error study involving z displacement.

#### 5.5.5.1 Method and Results

The section of lattice selected to study was the four cells closest to the dispersion switching point in the final design of the gantry (see section 5.7.3). This covers a  $2\pi$  betatron oscillation and a switch in curvature.

The most straight forward way to model separate horizontal displacements in every magnet in Zgoubi is to use the dipole fields. An initial test was done to find how a closed orbit position changes due to the same change in the dipole fields of every magnet in a cell. The result of this was then used to calculate the required dipole field for a given error.

To simulate random positional errors, nine magnitudes of error were chosen, ranging from  $10\mu\text{m}$  to  $1\text{cm}$ . These were used as standard deviations on Gaussian distributions with means of zero. At every magnitude, each magnet was given a different error from the distribution and particles at five momenta were tracked with their final positions being recorded. This was repeated 500 times to improve the statistics.

Presented below are plots of the standard deviations of the resulting errors in position (figure 5.19) and angle (figure 5.20). The gradient of the fitted straight line is known as the amplification factor and is shown for each energy in the figures.

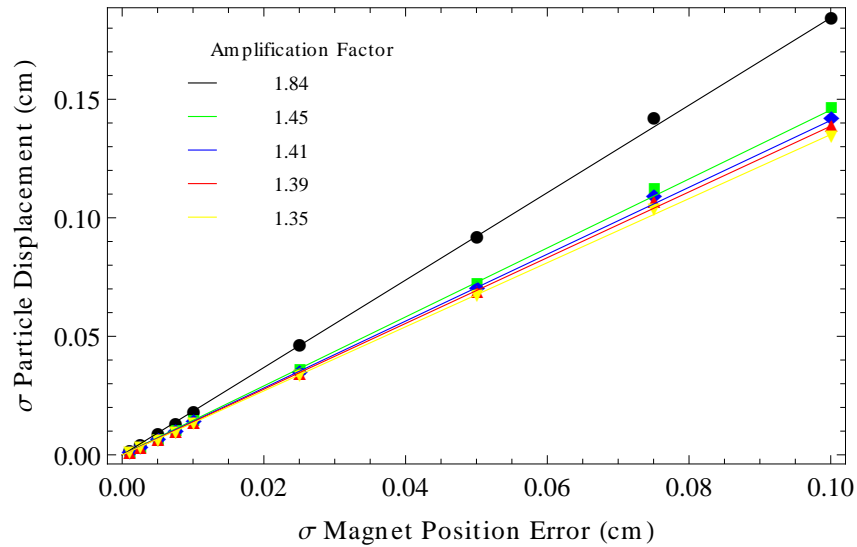


FIGURE 5.19: Sensitivity of particle position to errors in the magnet positions in an FFAG dispersion suppressor with the Amplification Factors shown in the legend. Both errors are the standard deviation of random distributions. Five momenta are shown in the range 0.369 (black)  $\rightarrow$  0.729 (yellow) GeV/c.

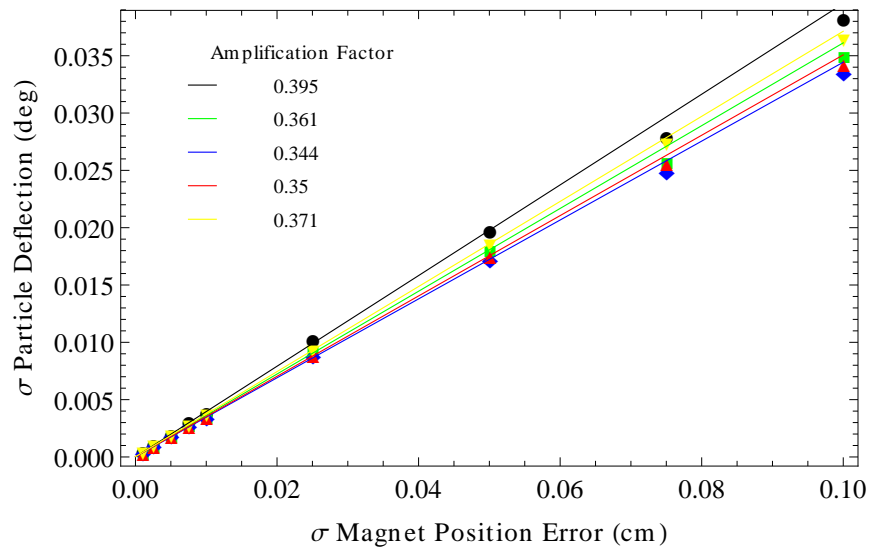


FIGURE 5.20: Sensitivity of particle deflection to errors in the magnet positions in an FFAG dispersion suppressor with the Amplification Factors shown in the legend. Both errors are the standard deviation of random distributions. Five momenta are shown in the range 0.369 (black)  $\rightarrow$  0.729 (yellow) GeV/c.

### 5.5.5.2 Discussion of the Results of the Error Study

Both position and angle errors increase fairly linearly with magnet displacement over the range, although the angle seems to deviate close to 1mm. The amplification factors are displayed as legends in figures 5.19 and 5.20.

As you can see, the worst case in both plots is the lowest momentum (0.365 GeV/c), which is almost 2:1 positionally and 4:10 degrees per cm angularly. This means that at 50 microns, around the limit for positional accuracy, the position will have an error of around 0.1mm, and an angular error of around  $0.002^\circ$ , or 0.03mrad.

A similar study was carried out in the main PAMELA ring [75, p.79], albeit over 1000 turns, and the displacement due to a  $50\mu\text{m}$  error was found to be  $\approx 0.2\text{mm}$ , so that this section of the lattice introduces half as much positional error as the whole of the main ring is not ideal. It is also comparable in size to the target positioning error in the PAMELA Design Report of 0.3mm [26, p.12].

To get the full picture of what this means, the study would have to be repeated for the whole gantry. Also, a fuller study would include rotational errors, errors in the field gradients of the magnets and errors in all the positional dimensions that were ignored in this study. Moreover, using the dipole field to simulate magnet displacement does not take into account the effect of how the magnet's fringe fields will change with particle position, but that kind of study would have to wait until field maps using more advanced designs of the magnets were created and will be left for further work.

### 5.5.6 Discussion of the Dispersion Suppression Study

Near perfect dispersion suppression in an FFAG has been achieved in simulation by compensating for the non linearity in the scaling field in the closed orbit positions in the normal cell. This successfully brings all equilibrium orbits to the same trajectory, however, the effect of the non-linear fields have on the the Twiss parameters, could be problematic (see figure 5.17). This technique is novel and was first presented by the author in [87]. Sensitivity to random errors in the magnet positions was explored and found to be comparable to that of the main PAMELA ring, as well as to the target accuracy for the gantry. This means it would be a significant factor in any design which included it and a full error study of the whole system will be required to assess its effect.

## 5.6 Properties of the Non-Scaling Gantry

The next step is to apply the dispersion suppression technique to the gantry design in section 5.4. Figure 5.21 shows tracks through the gantry assuming zero dispersion at the entrance. Figures 5.22 and 5.23 show how the final positions and angles of the particles vary with momentum  $3m$  after the end of the bending magnets.

The  $\beta$  functions through the bending sections of the gantry look like figure 5.24. These are unruly, but as the PAMELA design report shows, not unreasonable for the scanning system to cope with [26, p.150].

### 5.6.1 Discussion

The equilibrium orbit positions of this design meet the requirements set out in section 4.1.1, so from that point of view it is a success and shows that, in principle, this approach

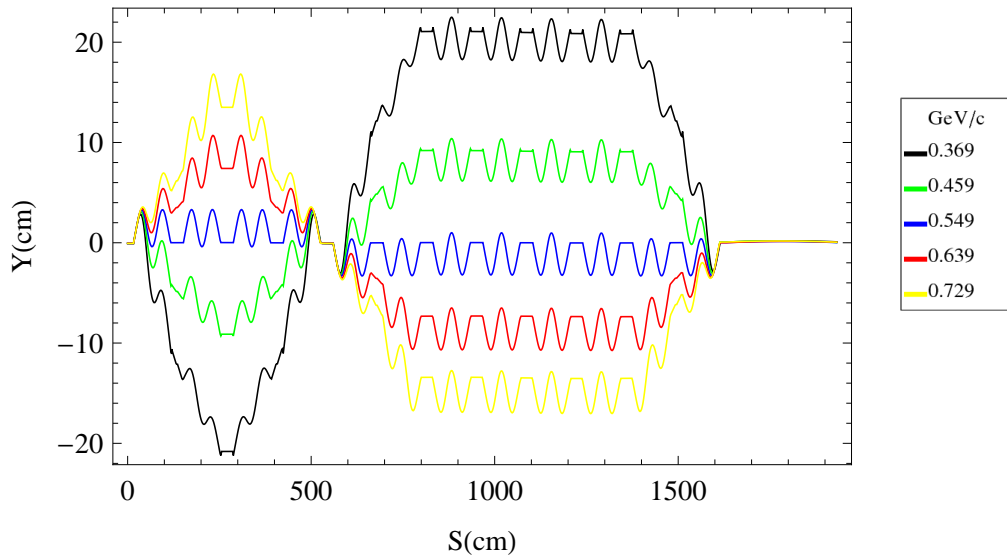


FIGURE 5.21: Tracks through a non scaling FFAG gantry using the dispersion suppression technique outlined in the previous section.

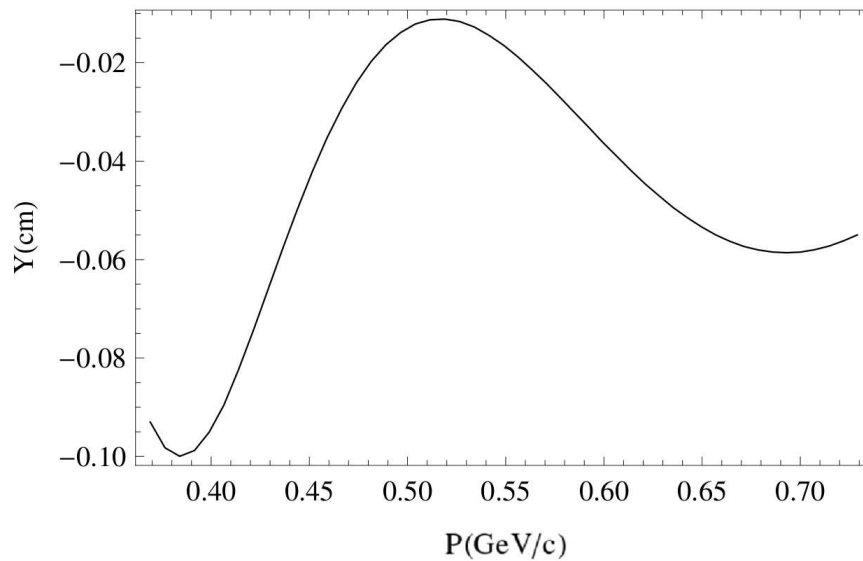


FIGURE 5.22: Horizontal position vs momentum at the end of a non-scaling gantry.

to the gantry has promise. However, no attention has been paid to the other requirements in section 4.1.1. There are many things wrong with this design.

Firstly, it is too tall needing around 13m to be rotated through  $360^\circ$ , which is 3m larger than that of the gantry at Heidelberg. This is a big problem, because the magnets are also too short for the aperture, which means that the gantry will only get bigger as they are extended to a more realistic length. The other problem is that, because the

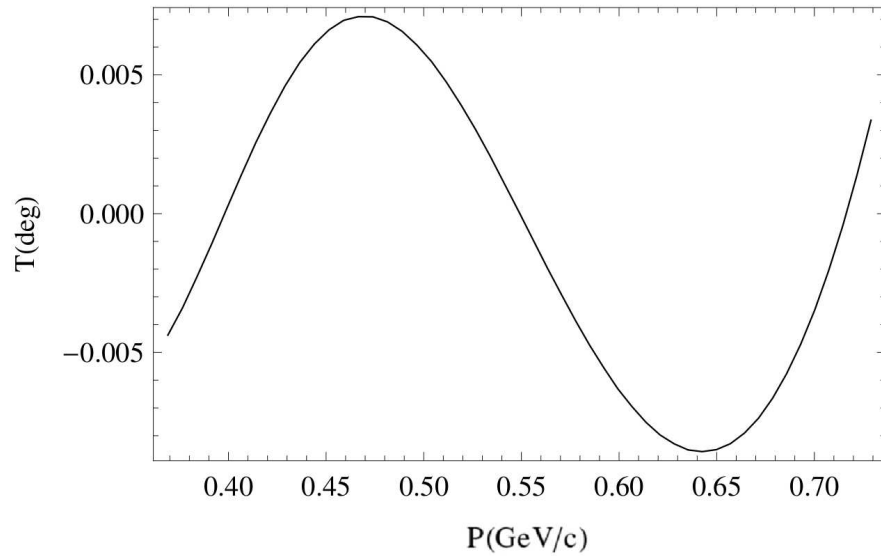


FIGURE 5.23: Horizontal deflection vs momentum at the end of the non-scaling gantry combination

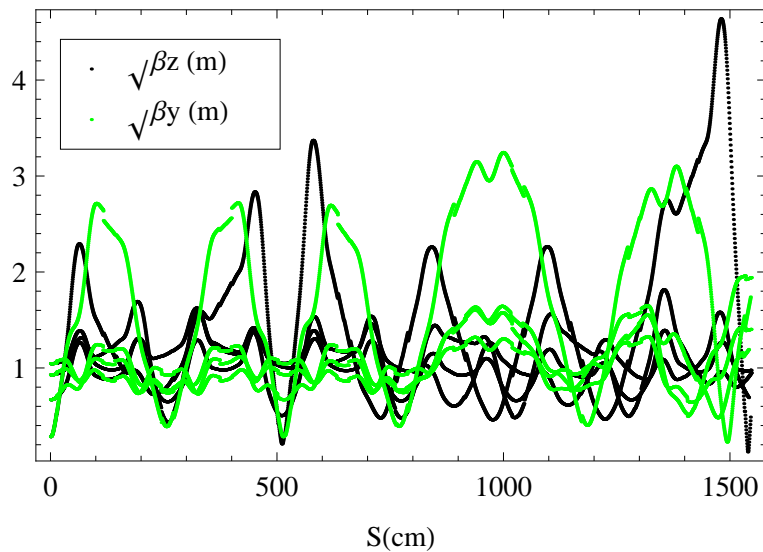


FIGURE 5.24: Beta functions through the bending sections of the gantry. The drift at the end has been ignored, because the beam size will be manipulated by the scanning system.

dispersion suppression makes use of fields with high ‘k’ and wide amplitude betatron oscillations, the peak field can become too high. However, this might be solved by increasing the magnet length. The next section describes an attempt to create a gantry design with more realistic magnets and overall size.

## 5.7 Flattened Gantry Design

A major problem with the gantry in section 5.6 is its height. The following section is an attempt to reduce the height, while paying attention to all the other requirements. The height could be reduced by taking out cells either side of point B in figure 4.2, reducing the total bend angle between the entrance and the swap point, as well as the bend angle between the swap point and the top of the gantry. In fact, only the final bend needs to be  $90^\circ$ , which means the height is constrained by the 3m clearance plus the height of the final bend. This also helps reduce the field in the dispersion suppressors of the first section as well as the bending, which could have a beneficial effect on the beta functions.

### 5.7.1 Design strategy

To make things simpler, the gantry can be split up into four different sections marked on figure 5.25: The section from the entrance to the swap in curvature (section 1), from the swap in curvature to the top of the magnet (section 2), a large bending section (section 3), and a dispersion suppression section at the end (section 4). Splitting the final  $90^\circ$  bend into two sections was done because bending and suppressing the dispersion at the same time will increase the peak field.

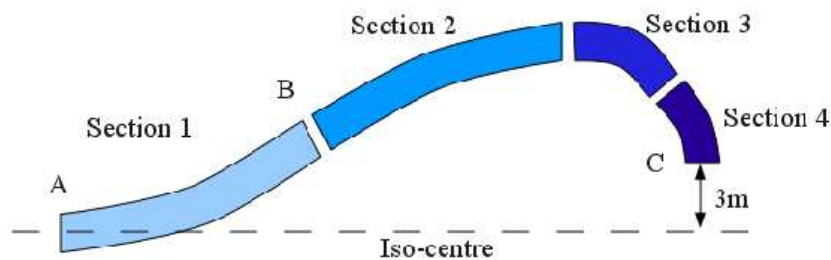


FIGURE 5.25: The gantry split up into four sections. A, B and C are the dispersion suppression points.

The design of this gantry has to begin with the final  $90^\circ$  bend (section 3 in figure 5.25). How it is achieved determines the overall height of the gantry and constrains the characteristics of all other sections. So the starting point has to be an FFAG cell with the largest bend possible in the smallest space. After that is set, the cell that makes up what is left of the  $90^\circ$  bend (section 4) should also act as a dispersion suppressor for point C. Thankfully, this does not have to be as good as at points A and B and can be done in a single cell.

Next, a scheme has to be worked out to go from zero dispersion at point B to the closed orbit positions in the large bending magnet (section 2 in figure 5.25). Then, the entrance section can be designed with the opposite total bend, a height to make sure the clearance at C is 3m and dispersion suppressors at either end (section 1). Finally, because creating perfect dispersion suppression involves fitting the equilibrium orbit positions in the normal  $k$  cells, sections 3 and 4 will have to be tweaked to match to section 2.

### 5.7.2 The $90^\circ$ Bending Section

Although sections 3 and 4 of the gantry have different requirements, they can be designed together. Figure 5.26 shows a schematic of these sections. Preliminary tests for a parameter search found that the aperture would probably be somewhere in the region of 30cm. Given the rule of thumb in sec.4.1.1 that the magnet length should be no less than twice its aperture, the range of magnet lengths was set around 60cm.

Immediately there is a problem, however. If the magnets will be around 60cm and if 20cm is left between magnets to avoid the overlap of fringe fields [85], the total length of a cell is around 220cm. Assuming a 30cm drift between cells, figure 5.27 shows how

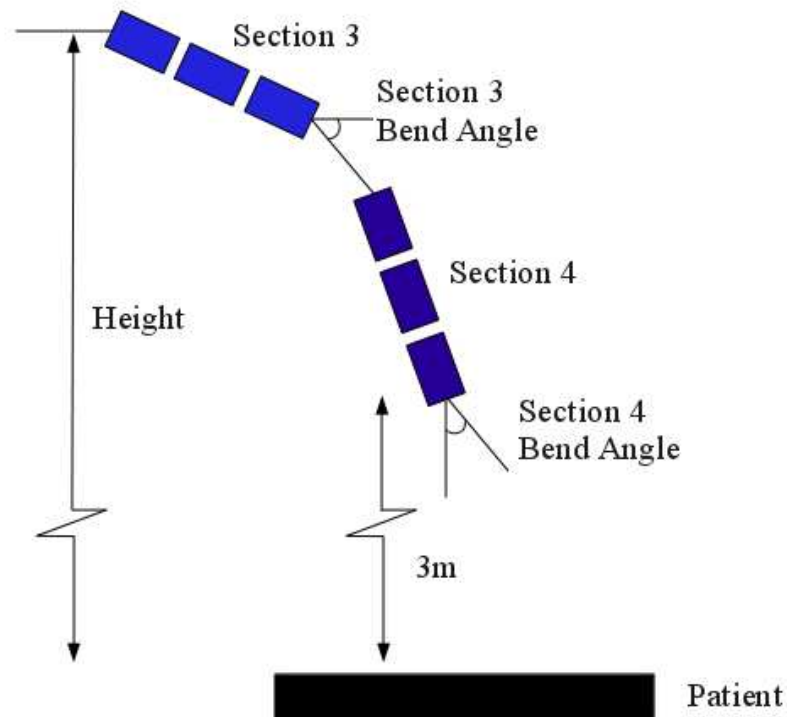


FIGURE 5.26: A schematic of the last two sections of the gantry.

the height of the gantry depends on the bend angle of the first cell. 500cm represents a total gantry height of 10m which is the upper limit set out in section 4.1.1. As figure 5.27 clearly shows, if section 3 has a bend angle of  $45^\circ$ , which is the minimum one would expect, the gantry will be close to 600cm high, which results in a total height of 12m if the gantry is to rotate around  $360^\circ$ .

This seems an intractable problem if two triplets are to be used, but it will be useful to design a gantry in this way to show the smallest possibility with this set-up, then explore possible ways to shorten it.

### 5.7.2.1 Parameter Search

Both magnets are single pass magnets, so in the design, I abandoned any hope of finding closed orbits or periodic Twiss functions. It helps that the dispersion suppression does not have to be perfect at point C in figure 5.25, because the phase advance does not have

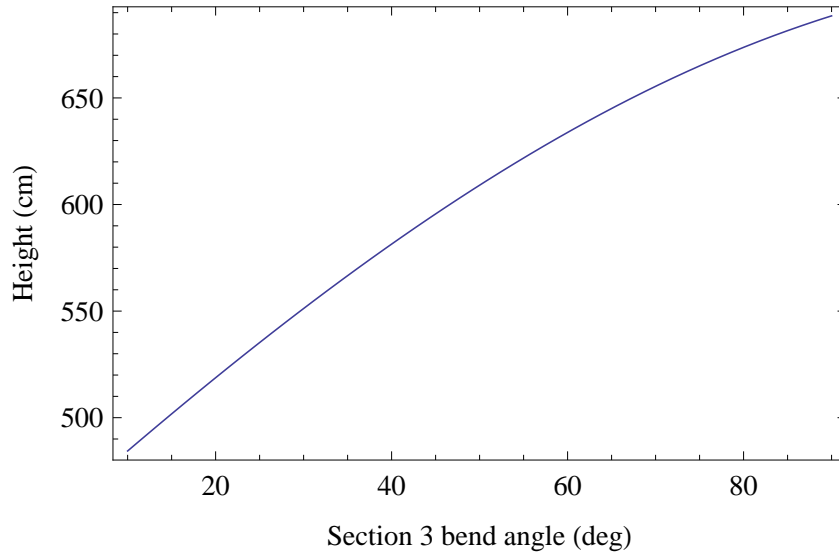


FIGURE 5.27: How the total height of the gantry depends on the bend angle of the section 3 triplet.

to be exactly  $\frac{\pi}{2}$ . Instead, various values of  $k$  can be tried in section 4 to find a suitable value. This is a less precise method than that used in section 5.5, but good enough for this purpose. The parameters varied are summarised in table 5.4. The magnet length was assumed to be the same in all cells for ease of calculation (cells next to dispersion suppression points could be made shorter as they will have a smaller aperture, but that is a consideration for later in the design process).

TABLE 5.4: Parameters varied in the two triplet design of the final  $90^\circ$  bend.

Parameter	Range
Magnet Length	50 $\rightarrow$ 70 cm
Section 3 Bend Angle	$46^\circ \rightarrow 60^\circ$
Section 3 D/F	0.2 $\rightarrow$ 1
Section 4 D/F	0.2 $\rightarrow$ 1
Section 3 $k$	2 $\rightarrow$ 5
Section 4 $k$ multiple	1.3 $\rightarrow$ 1.7

The values the lattices were tested for were aperture, peak field and final beta value. The particle positions on the entrance to the lattice were assumed to be on the equilibrium orbit of the section 3 triplet and the initial beta values in horizontal and vertical were arbitrarily chosen as 5m; which initial tests showed are approximately what can be expected from the first two sections of the gantry.

### 5.7.2.2 Parameter Search Results

Out of the valid configurations found by the parameter search, lattices with apertures less than 30cm and peak fields less than 30T were considered. The parameters of the gantry were then tweaked by small amounts for local optimisation. Table 5.5 has the specifications of these magnets, figure 5.28 shows the tracks through the two triplets, figure 5.29 shows the fields and figure 5.30 shows the beta functions.

TABLE 5.5: Characteristics of the best lattice from the parameter search.

Parameter	Section 1	Section 2	Units
$k$	3.5	4.55	
D/F	0.7	0.7	
Bend angle per cell	46	44	degrees
Cell length	220	220	cm
Magnet length	60	60	cm
Peak Fields (F,D)	2.466, -1.397	2.528, -1.283	T
Max aperture	29.7	28.0	cm
Height	307		cm

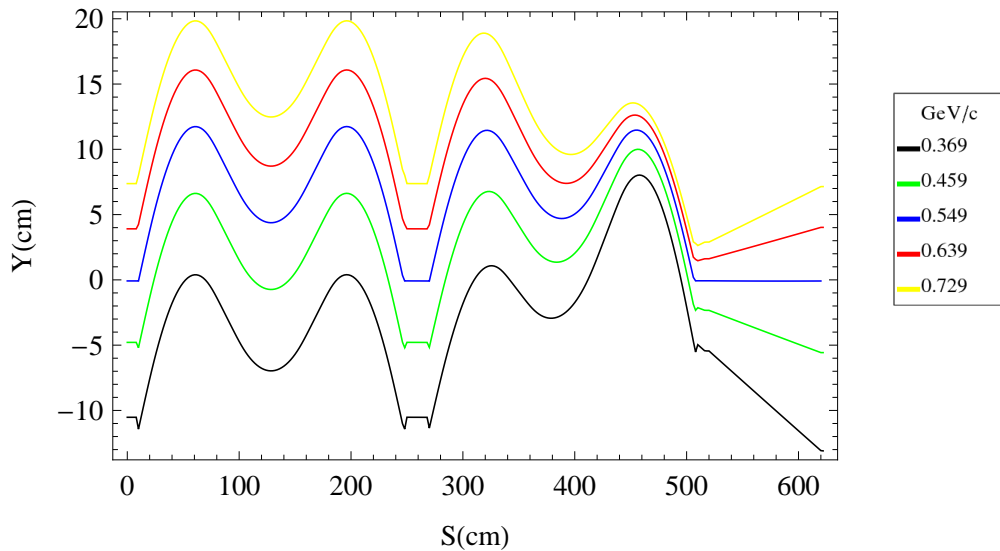


FIGURE 5.28: Tracks through the best lattice from the parameter search.

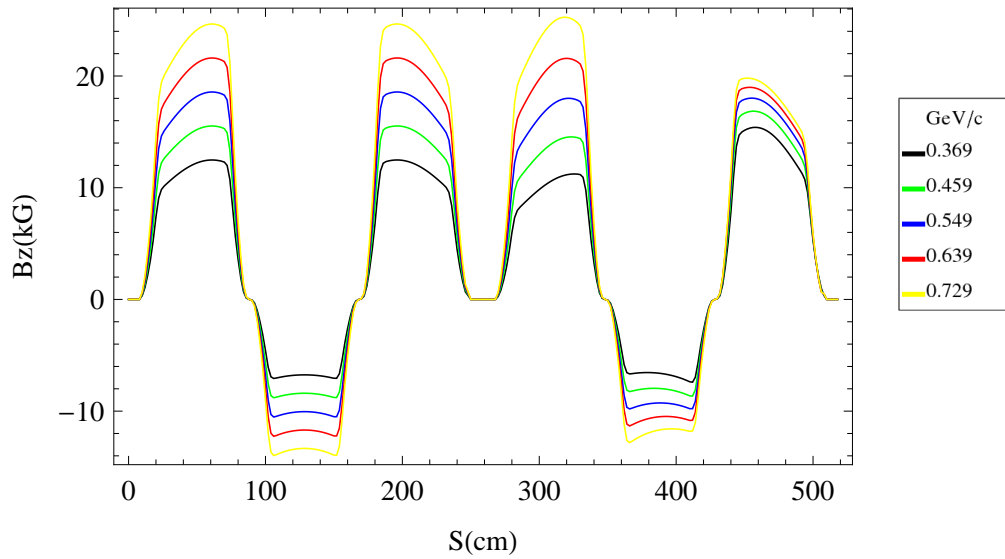


FIGURE 5.29: Fields experienced by five particles with different momenta travelling through the best lattice found by the parameter search.

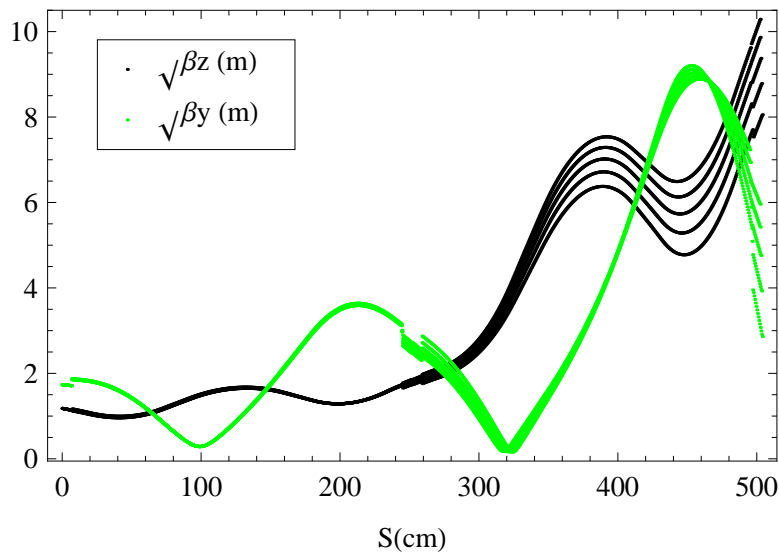


FIGURE 5.30: Beta functions through the best lattice from the parameter search.

### 5.7.2.3 Optimisation

The dispersion suppression in section 4 does not produce small enough positional (within 5cm) or angular (within  $0.3^\circ$ ) dispersion. This can be addressed by varying the  $k$  value and the DF ratio in section 4. In trying to optimise for final position and angle using an automatic minimising programme, however, the results tend towards  $DF \rightarrow 0$ , meaning a very low defocusing field. Figure 5.31 shows the resulting tracks. Obviously, this has a

very detrimental effect on the vertical beta function (figure 5.32), which is very difficult to remedy using triplets.

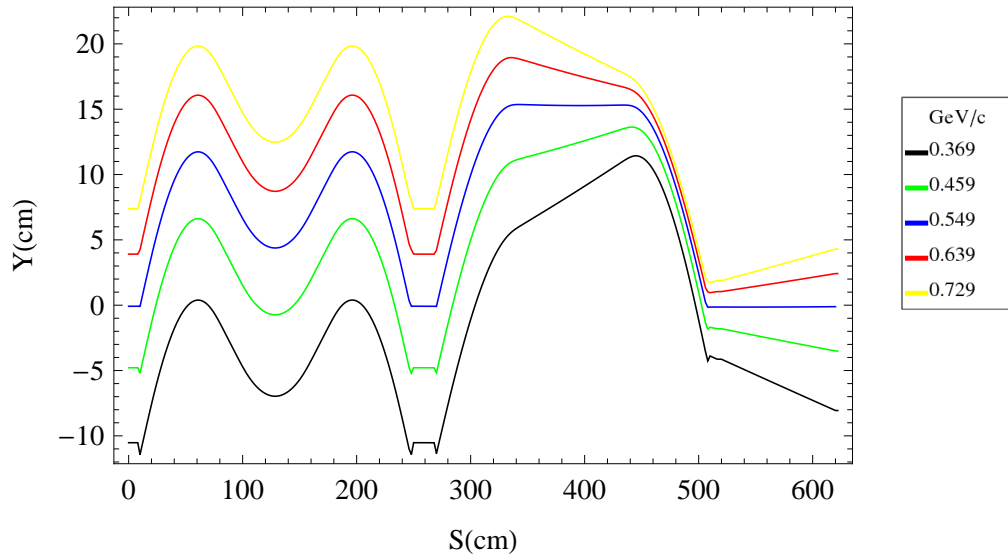


FIGURE 5.31: Particle tracks through the lattice created by automatically optimising the results of the parameter search using exit dispersion as the only criteria.

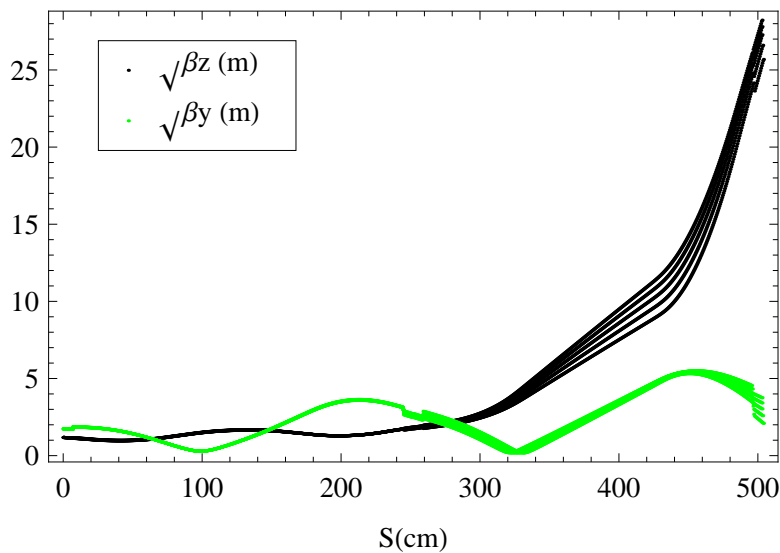


FIGURE 5.32: Beta functions through the optimised triplet cell in section 4.

From examining, figure 5.30, the reason this has a lower maximum  $\beta$  than other configurations in the parameter search can be attributed to the uniform way the vertical  $\beta$  function goes through section 3 and the low  $\alpha$  at its end. They both then go awry through Section 4.

From this observation, as well as the difficulty in creating decent dispersion suppression, and because of the height issue, it was decided to look at abandoning the idea of using a triplet in section 4.

#### 5.7.2.4 Triplet alternative in section 4

The final section will clearly need both focusing and defocusing magnets, but one question to consider is the order in which they should go. Figure 5.30 might suggest that the defocusing magnet should follow the last focusing magnet in section 3. However, a single dispersion suppressing focusing magnet will act like a focusing lens in converging all the particle paths towards each other (the non-linearity prevents a single focal point however), so a defocusing magnet will be required at the end to straighten the paths. Figure 5.33 shows the proposed layout.

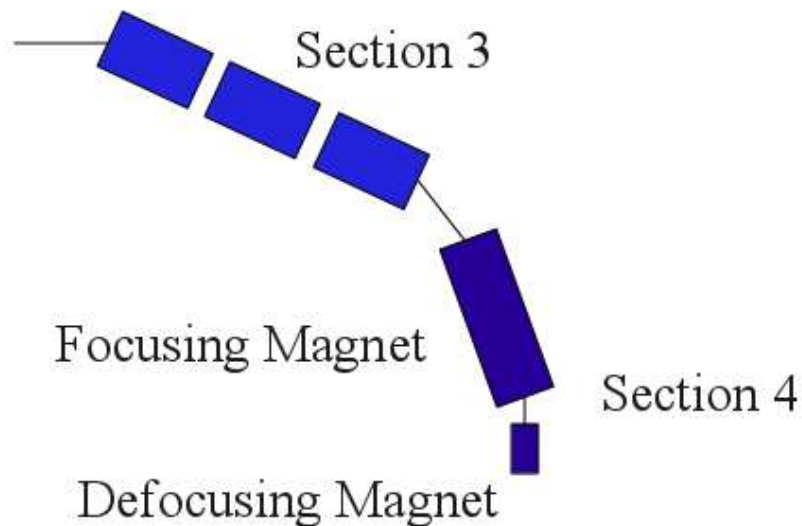


FIGURE 5.33: Alternative scheme for the end of the gantry. The triplet in section 4 is replaced with a large focusing ns-FFAG magnet and a small non-bending defocusing multipole magnet.

The advantage of this scheme, is that the defocusing magnet can have a reduced aperture and does not even have to be a bending magnet, which means it can be a small multipole that does not add too much to the height. Also, because there is no reverse bend, the focusing magnet will then not have to bend as much as the combined positive bending in the triplet design, which may help reduce the peak field and the total length of the section. It may even turn out that this magnet can do the majority of the  $90^\circ$  bend. To find out, another parameter search was undertaken.

### 5.7.2.5 Parameter Search for Alternative Design to the End of the Gantry

The small defocusing magnet will be designed to fit with the requirements of the large focusing magnet, so there is no need to include it in the parameter search. This parameter search is the same as in section 5.7.2.1 except there is no range of DF ratios for section 4.

Preliminary tests showed that the focusing magnet could be 1m long and create a  $45^\circ$  bend with a reasonable peak field and aperture, so this was taken as a starting point for the parameter search. Table 5.6 summarises the parameters which were varied and the ranges that were covered.

TABLE 5.6: Parameters varied in the alternative design of the final  $90^\circ$  bend.

Parameter	Range
Triplet Magnet Length	50 $\rightarrow$ 70 cm
Single Magnet Length	75 $\rightarrow$ 125 cm
Section 3 Bend Angle	$46^\circ \rightarrow 60^\circ$
Section 3 D/F	0.5 $\rightarrow$ 1
Section 3 $k$	2 $\rightarrow$ 5
Section 4 $k$ multiple	1.3 $\rightarrow$ 1.8

### 5.7.2.6 Alternative parameter search results

The results of the parameter search were filtered down to four lattices that had maximum fields less than 30T and apertures less than 30cm. Of these, the lattice was chosen which had the lowest maximum beta value in the hope of keeping the beta functions small in the final version. The chosen configuration is summarised in table 5.7 and figures 5.34, 5.35 and 5.36 show the tracks, fields and beta functions through the lattice. The height in table 5.7 is the height of the triplet and the large focusing magnet only; the height of the whole gantry will be calculated during the design of the small defocusing magnet.

TABLE 5.7: Characteristics of the best lattice from the parameter search.

Parameter	Section 1	Section 2	Units
$k$	4	1.4	
D/F	1	n/a	
Bend angle per cell	50	40	degrees
Cell length	220	n/a	cm
Magnet length	60	75	cm
Peak Fields (F,D)	2.989, -2.056	2.701	T
Max aperture	27.39	23.11	cm
Height	203.86		cm

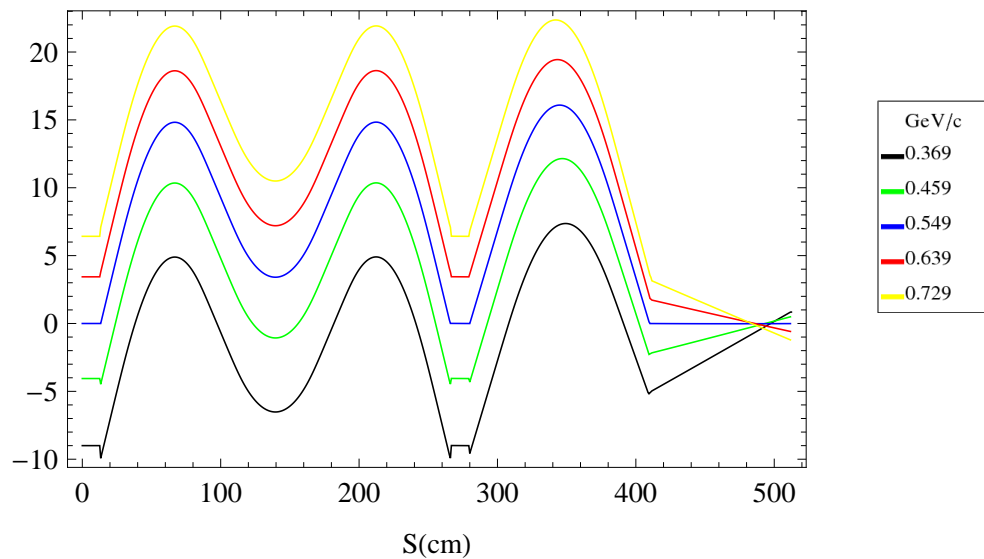


FIGURE 5.34: Particle tracks through the result of the parameter search for a gantry end consisting of one triplet and one large focusing magnet.

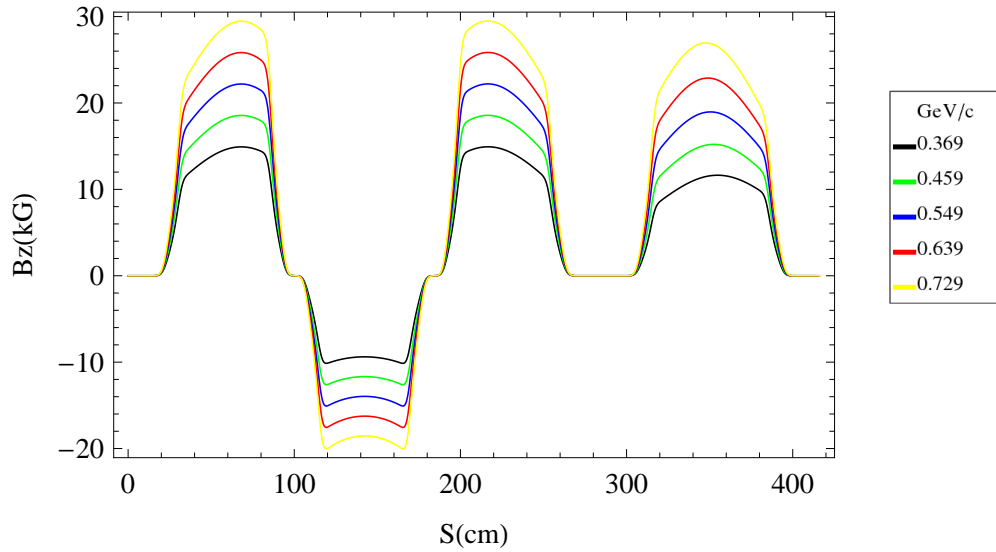


FIGURE 5.35: Fields experienced by particles travelling through the result of the parameter search summarised in table 5.7.

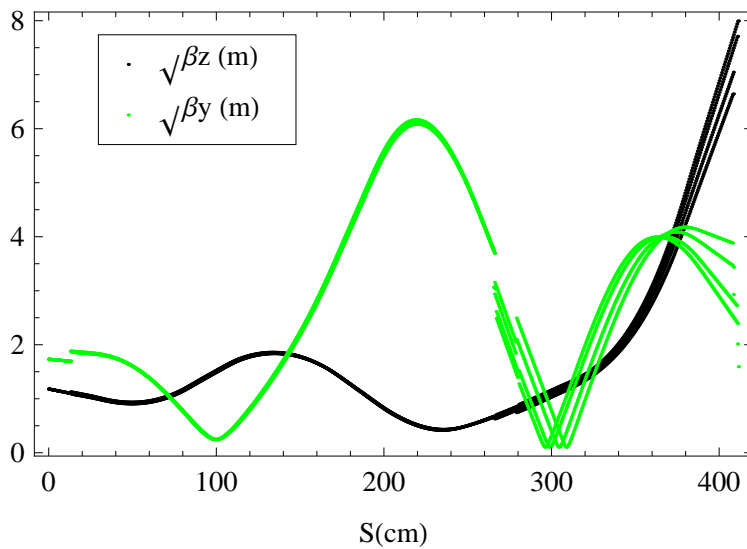


FIGURE 5.36: Beta functions through the result of the parameter search summarised in table 5.5. The discontinuity at  $S = 275\text{cm}$  is an artefact of the way drift spaces are dealt with in the simulation code and does not effect the accuracy of the plot.

### 5.7.2.7 The Defocusing Magnet

This will have to be redesigned when section 3 and the focusing magnet are tweaked after sections 1 and 2 have been completed, but an initial design needs to be made so that a height can be set.

The defocusing magnet will have no bending, but will need one or more of the higher

order multipole fields to compensate for the non-linearity in the particle positions caused by the FFAG magnets. The drift space after the large focusing magnet can be used as a free parameter to control the spread in horizontal position at the end, although obviously the shorter the distance the better, so the  $k$  of the final magnet could also be used.

Figure 5.37 shows that such a scheme can be designed and figure 5.38 shows that the fields experienced by the different momenta particles will be relatively small in the defocusing magnet. However, this is not a finalised design, but it shows that the length of the magnet can be reasonably set at 20cm and the drift at around 30cm. This makes the total height of the gantry around 550cm (that is 204cm for section 3 and the large defocusing magnet, 300cm for the scanning magnets and around 500cm for the defocusing magnet).

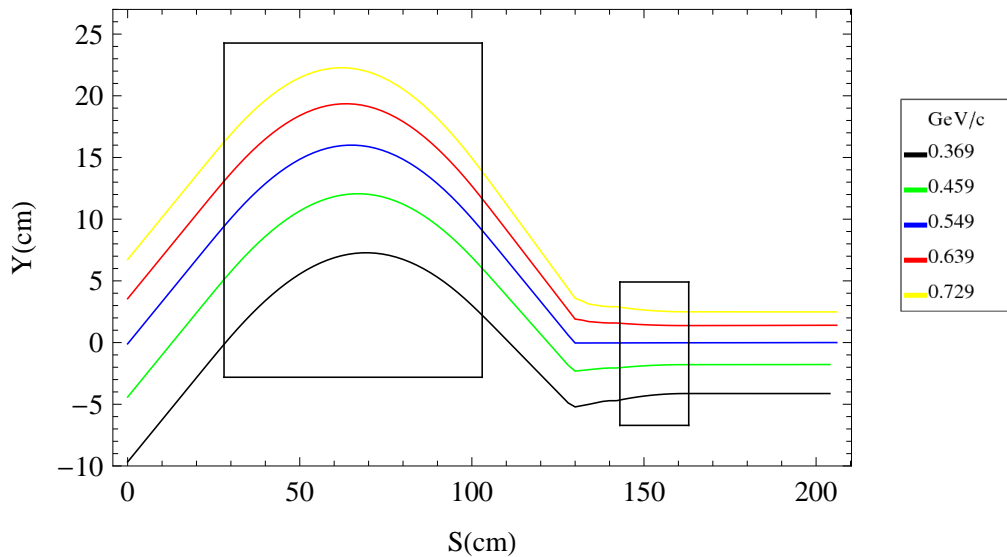


FIGURE 5.37: Tracks through initial design of final focusing and defocusing magnets. Magnet shapes are drawn for clarity.

### 5.7.3 The Design of Gantry Sections 1 and 2

Section 1 is probably the most flexible section as its two zero dispersion ends make it relatively self contained. For this reason it can be left to last to make up whatever height

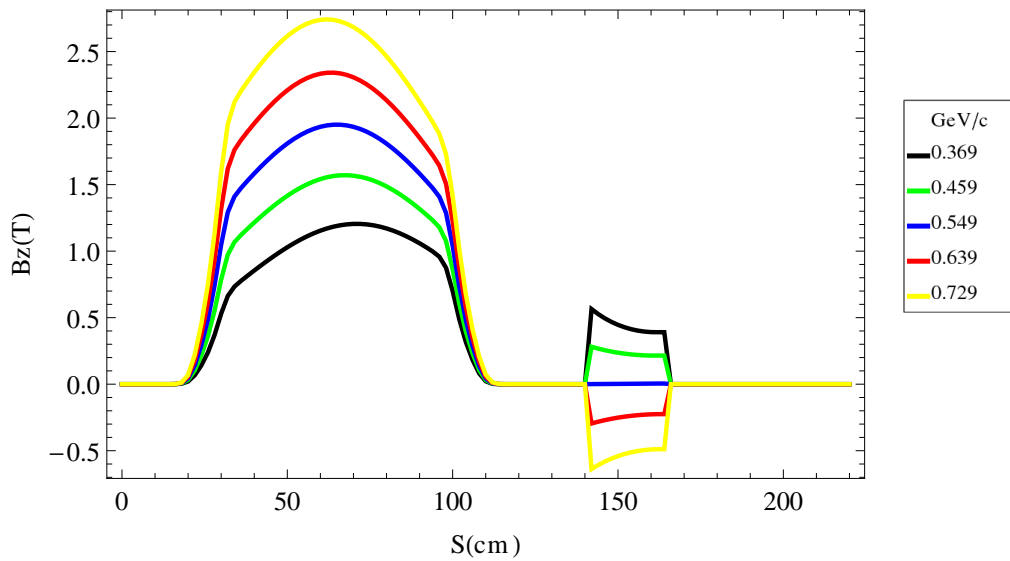


FIGURE 5.38: Fields through initial design of final focusing and defocusing magnets. The defocusing magnet has peak fields five times smaller than the main FFAG magnets.

is left over after section 2 is designed. However, both sections have to have the same bend angle, so the question is how to create a  $2\pi$  phase advance in section 1 and a  $\pi$  phase advance in section 2 with the same bend angle in each section.

One way is to give all cells the same size and bend angle. The different dispersion suppression requirements could then be met by having differing phase advance per cell in each section, and/or different numbers of suppressor cells per section. For example, a design with four cells in each section, could split the  $\pi$  phase advance over two cells in section 1 and 4 cells in section 2 or it could split the  $\pi$  phase advance over two cells in both sections and make up the rest of the bending in section 2 with normal  $k$  cells.

The phase advance can be changed by varying:

- Magnet length.
- Ratio of drift space to magnet within the cell (called the packing factor).
- Length of the long drifts between cells.
- Bend angle.
- $k$ .
- DF ratio.

However, in this design, a lot of those will be fixed. The magnet length should be as low as possible to reduce weight and size of the overall gantry. Given that the aperture in section 3 is around 30cm, means the length should be around 60cm. Similarly the short drifts between magnets should be around 20cm to avoid the fringe fields overlapping, so the packing factor is more or less fixed. Again the lengths of the long drift should be as small as possible while leaving ample room between cells for maintenance. For the purposes of this study, this was estimated at 500cm, which is a high estimate because any reduction can only be beneficial. The bend angle is fixed by the height of the gantry and the length of the cells and long drifts; however, it can be varied indirectly by the total number of cells used. This leaves only the  $k$  values and the FD ratio which can be used to achieve the right tune; although the  $k$  value can only be varied in section 1 as it is fixed to  $k = 4$  for normal cells and  $k = 8$  for suppressor cells in section 2, so that the equilibrium orbit positions match to section 3.

### 5.7.3.1 Parameter Search

As mentioned, the total number of cells is a variable which must be considered. Obviously, the fewer cells the better, however, given the constraints, the correct tune may not be available in every configuration. Figures 5.39 → 5.42 show the working points for 4, 6, 8 and 10 cell configurations respectively. These were created by finding the bend angle which made a lattice of the required height, then varying the DF ratio and the  $k$  value and finding the tune using the alignment orbit (0.549 GeV/c). The dots show all the configurations that were stable enough to produce a tune and any point with  $k = 8$  (the required  $k$  for the suppressor cells so the normal cells, with  $k = 4$ , match to section 3) is coloured red. The size of each point is a representation of the DF ratio just to give an idea of how changing it effects the tune.

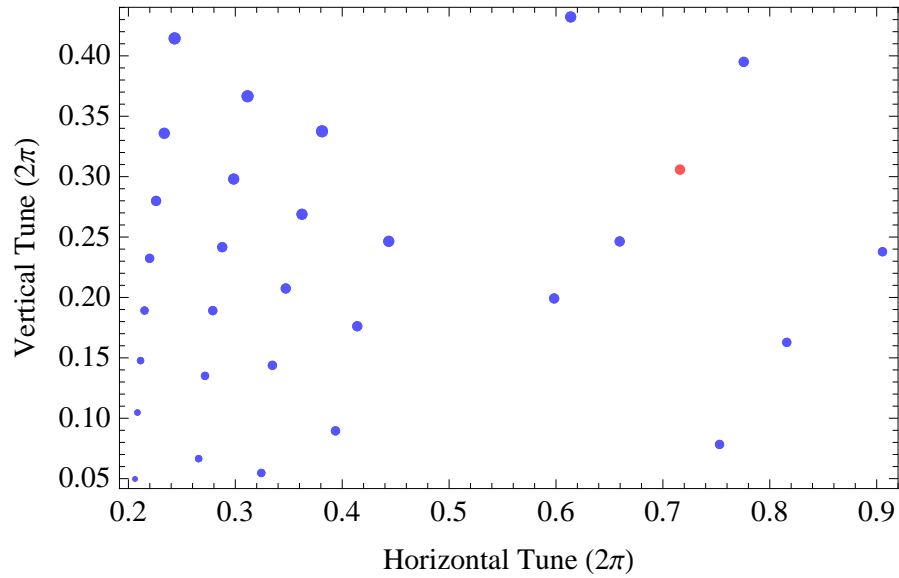


FIGURE 5.39: Tunes for a 4 cell solution to sections 1 and 2. The dots represent all the combinations of DF and  $k$  which give stable tunes. The tunes are represented as fractions of  $2\pi$ , so a cell with a  $\frac{\pi}{2}$  phase advance would be on the line  $= 0.25$ . The red dots are working points where  $k = 8$ , which is desirable to match to section 3.

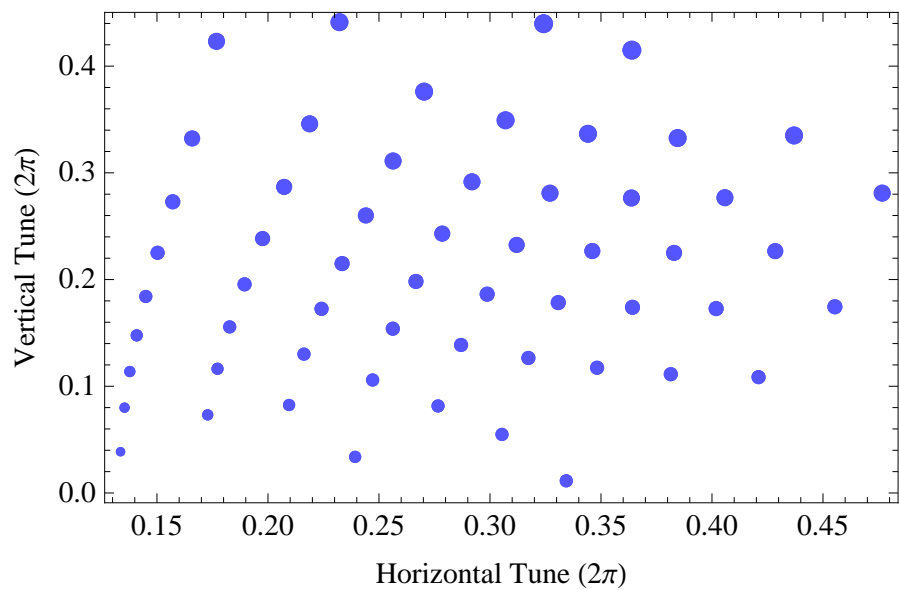


FIGURE 5.40: Tunes for a 6 cell solution to sections 1 and 2. The size of the blue dots is proportional to the value of the DF ratio to give an idea of how it effects the tune. A red dot indicates a working point where  $k = 8$ , which is desirable to match to section 3.

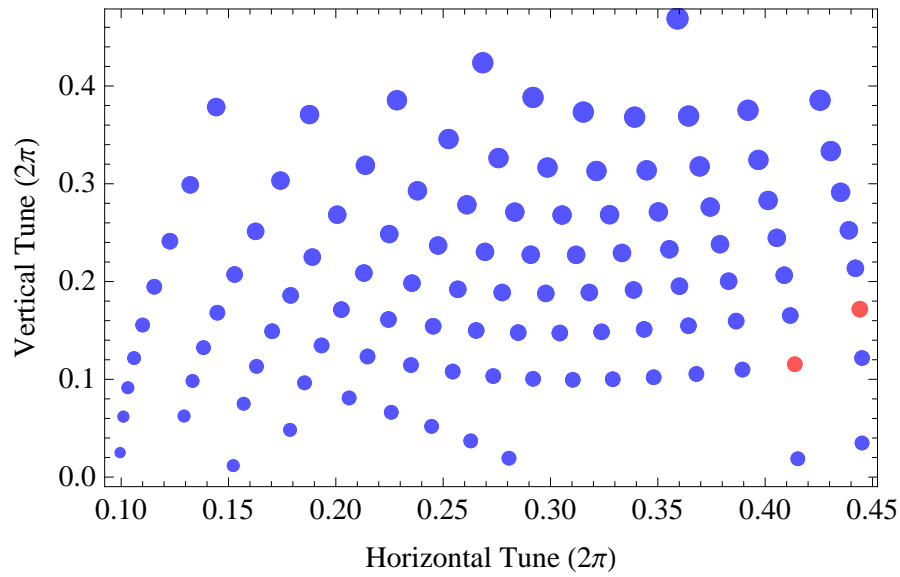


FIGURE 5.41: Tunes for an 8 cell solution to sections 1 and 2. A red dot indicates a working point where  $k = 8$ , which is desirable to match to section 3.

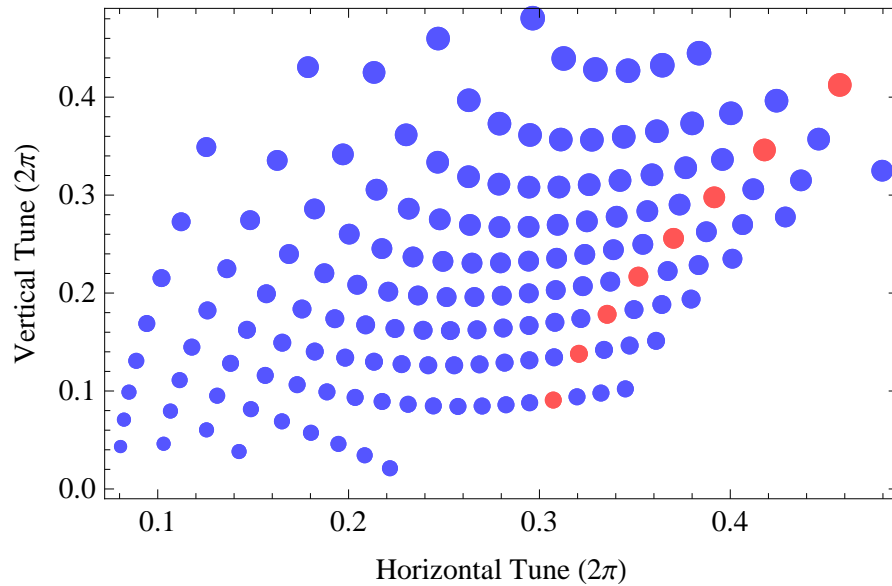


FIGURE 5.42: Tunes for a 10 cell solution to sections 1 and 2. A red dot indicates a working point where  $k = 8$ , which is desirable to match to section 3.

The four cell lattice, was probably always going to be unrealistic in section 1 as creating a cell with a  $\pi$  phase advance is very difficult due to resonances, but the fact that there are no working points with  $k = 8$  anywhere near a  $\pi$  phase advance underlines that it is not worth pursuing.

The six cell lattice has working points with a phase advance of  $\frac{2\pi}{3}$ , so the  $2\pi$  phase

advance required in section 1 could be achieved here. However, section 2 would either have to consist of 3 suppressor cells of phase advance  $\frac{\pi}{3}$ , or 2 suppressor cells with phase advance  $\frac{\pi}{2}$  and a normal  $k$  cell, and there are no working points available at all with a  $k$  of 8.

The 8 cell lattice could consist of four suppressor cells in section 1 and two in section 2, with all suppression cells having a phase advance of  $\frac{\pi}{2}$ . However, looking at figure 5.41, there are no working points available with  $k = 8$  and the correct phase advance.

Similarly, the 10 cell lattice would have four suppressor cells in section 1 and two in section 2, but there would also be an extra normal cell in each section. Again there are no ideal working points, for section 2, however, the length of this gantry would be 26m, which is already prohibitively long, so trying a gantry with 12 cells would be pointless.

### 5.7.3.2 Matching Sections 2 and 3 using intermediate $k$ values

One solution to this problem is to decrease  $k$  in section 4 of figure 5.25. One of the working points with a phase advance of  $\frac{\pi}{2}$  has a  $k = 6$ , which would correspond to  $k = 3$  in the normal cell and section 3. The problem is that this would increase the aperture in section 3, and although it would only be by a few centimetres, the fields are so high in that magnet, it is important to keep the aperture as low as possible.

Another possible solution is to use a value of  $k$  intermediate between the normal cell in section 3 and section 4. Figure 5.43 gives an idea of how this works. There is a  $\pi$  phase advance through a field with the highest  $k$  possible ( $k_1$ ), which takes the particle to the equilibrium orbit position of a  $\frac{k_1}{2}$  cell. Then, to take the particle to the closed orbit position of a  $k_2$  cell, another  $\pi$  phase advance is taken through a field with  $k$  half way between  $\frac{k_1}{2}$  and  $k_2$ . This shares the problem with the previous solution of increasing the

aperture, however, because the bending is less, the fields are lower in section 2 and an increased aperture will be less of a problem.

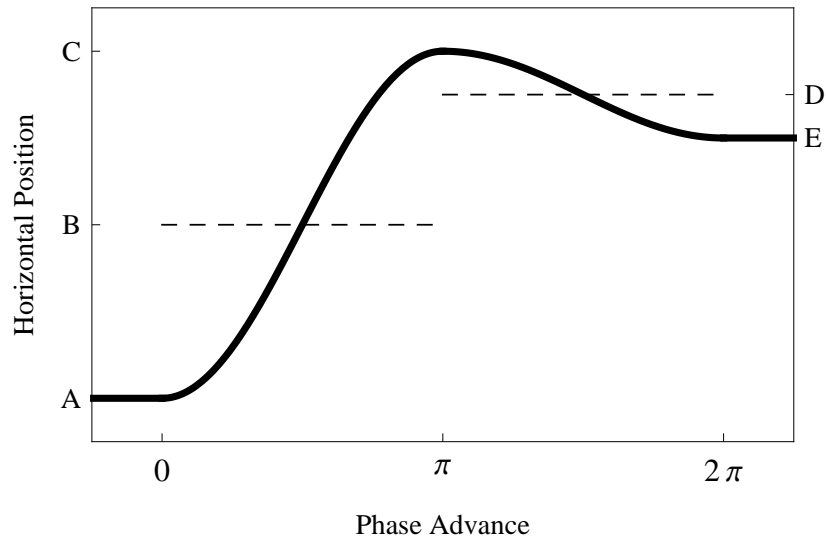


FIGURE 5.43: A particle is at a zero dispersion point A does a  $\pi$  phase advance through a field with an equilibrium orbit at B taking it to a horizontal position C. Another  $\pi$  phase advance through a field with an equilibrium orbit at D takes the particle to point E.

Figure 5.44 shows the  $k$  values of all the working points with horizontal tunes close to  $\frac{\pi}{2}$ . In this case, the highest  $k$  possible with the correct phase advance is 4. This will take the particles to the equilibrium orbits of a cell with  $k = 2$ . A  $k$  of 3 would then be required to bring them to the equilibrium orbits of section 3 where  $k = 4$ . There are working points with  $k = 3$  and phase advance close to  $\frac{\pi}{2}$ , so the next step will be to create this lattice.

#### 5.7.4 Joining Up the Whole Gantry

After designing sections 1 and 2 and fitting the multipoles as described in section 5.5, sections 3 and 4 were tweaked so that all closed orbits were aligned and the dispersion at the end was correct.

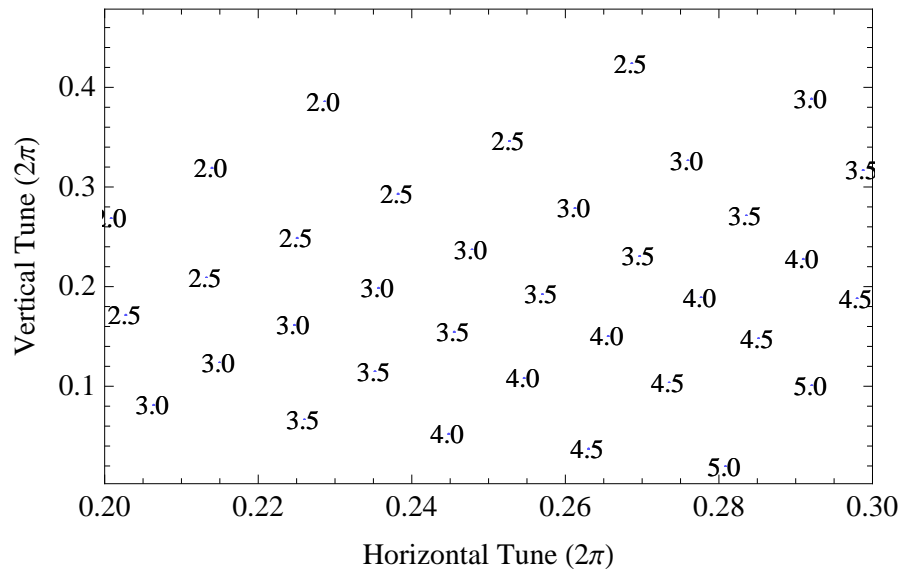


FIGURE 5.44: A selection of tunes for the 8 cell solution to sections 1 and 2. The numbers are the  $k$  value at each working point.

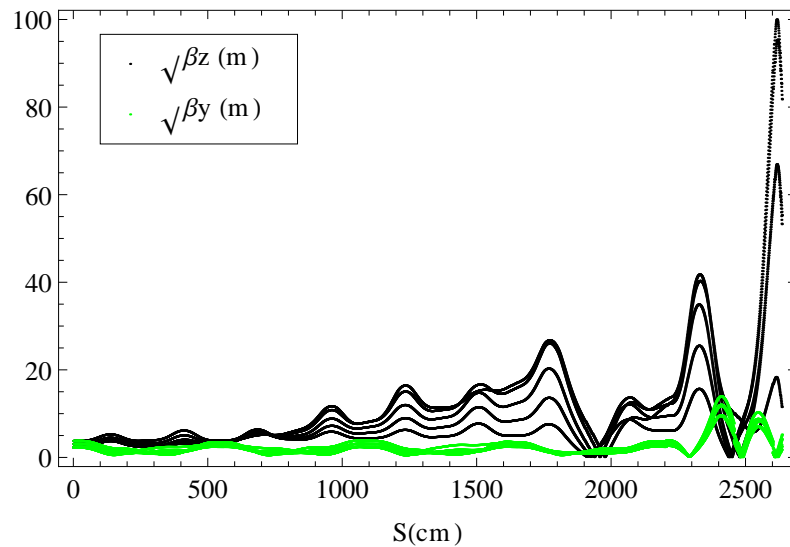


FIGURE 5.45: Beta functions through the whole gantry. The price paid for varying the multipole components of the different cells is wayward beta functions.

As figure 5.45 illustrates, the price paid for moving away from the scaling field is non-uniform beta functions. Controlling the size of the beam will be a challenge for the scanning system following the bending magnets, however, the task can be made easier by adding a small defocusing quadrupole placed at the point of zero dispersion between sections 1 and 2. This is a desirable place for it because it will not affect the closed orbit positions of the particles, but will affect the beta functions.

A parameter search was undertaken to find the optimal strength of the quadrupole to create the smallest value of beta at the end of the bending magnets. The length was chosen as 20cm, which raises the height by 7.6cm. This is only a few cm larger than the amount the gantry height was rounded down by when at the start of the section 1 and 2 design. This makes the height of the gantry 557.6cm.

## 5.8 Characteristics of the Whole Gantry

The characteristics of the final gantry design are summarised in table 5.8 and table 5.9 shows the multipole coefficients for equation 2.30. Figure 5.46 shows the particle tracks through the gantry. On this plot the three dispersion suppression points can clearly be seen and the bulge in dispersion at the seventh cell from the left is where sections two and three have been matched with an intermediate  $k$  value (section 5.7.3.2). Figure 5.47 shows the fields, which are kept within reasonable limits, and figure 5.48 shows the beta functions. Table 5.10 shows the optimal initial beta values, which were used to create 5.48. As described in section 4.2.1.2, the horizontal and vertical Twiss values have to be equal at the point where the gantry rotates. This ensures a circular beam which is the same no matter the rotation of the gantry. After initial tests, it was decided to add the extra constraint that the alpha values equal zero, because the downhill fitting function tended towards unstable solutions, especially at high momenta, when allowed to vary. The beta functions have been significantly reduced with the addition of the quadrupole (SQ in table 5.8), but they still remain very high at the end. This will require further work to correct.

TABLE 5.8: Parameters of the flattened gantry design. SM stands for the small multipole at the end of the gantry and SQ stands for the small quadrupole in the middle.

Parameter	Section 1	SQ	Section 2	Section 3	Section 4	SM	Units
$k$	2.20	n/a	2.20, 1.47	4	6	n/a	
D/F	1.58	n/a	1.58, 2.05	1	n/a	n/a	
Bend angle per cell	7.46	0	7.46	50	40	0	degrees
Number of Cells	4	1	4	1	1	1	
Cell length	220	20	220	220	70	25	cm
Magnet length	60	20	60	60	70	20	cm
Peak Fields (D,F)	-1.102, 0.976	0.0011	-1.889, 1.320	-2.007, 3.016	2.742	- 0.643	T
Max aperture	32.75	0.035	33.21	25.85	21.45	4.45	cm
Height	557.6						cm
Length	2346						cm

TABLE 5.9: Values of the  $b_n$  constants to go into equation 2.30 for the final gantry design. SQ and SM are the small multipoles. \* denotes where the actual value is used rather than that divided by the number at the top of the column.

Section	$b_1 \times 10^3$	$b_2 \times 10^6$	$b_3 \times 10^9$	$b_4 \times 10^{12}$	Bz0 (T)	$y_0$ +100,000 (cm)
1 <sub>1</sub>	3.881	9.745	8.612	6.188	0.5493, -0.8682	-33.29
1 <sub>2</sub>	4.400	9.678	14.19	15.59	0.5271, -0.8332	-30.30
SQ	-3.249*	0	0	0	0	0
2 <sub>1</sub>	3.881	9.745	8.612	6.188	0.5493, -0.8682	-33.29
2 <sub>2</sub>	4.400	9.678	14.19	15.59	0.5271, -0.8332	-30.30
2 <sub>3</sub>	2.720	4.347	3.983	1.592	0.8923, -1.831	-29.66
2 <sub>4</sub>	2.937	4.590	4.169	-0.1278	0.8559, -1.756	-28.90
3	4.302	11.39	12.10	7.268	1.166, -1.165	-12.54
4 <sub>1</sub>	9.948	27.12	30.60	65.11	0.5565	-12.86
SM	-24.45*	-7.600*	-52.97*	0	0	0

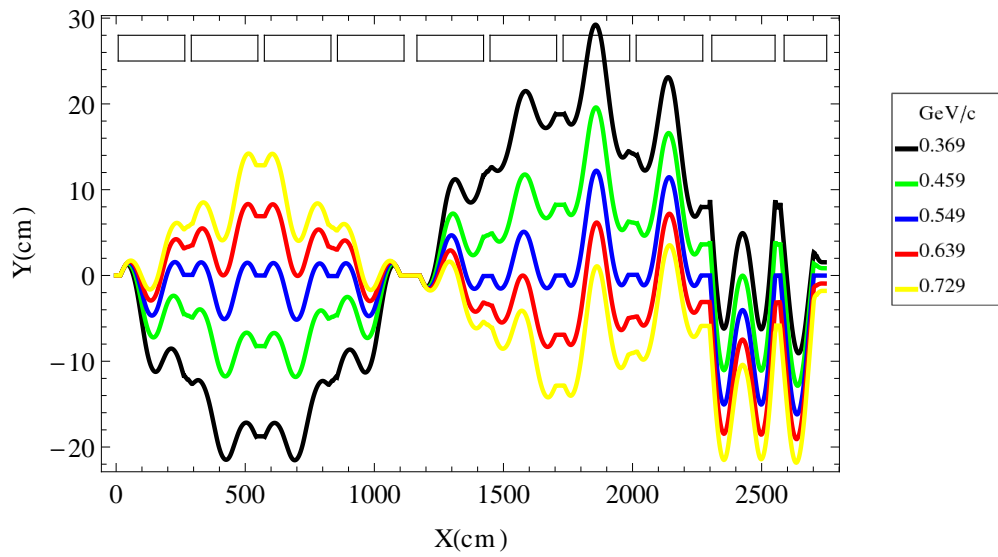


FIGURE 5.46: Particle tracks through the whole gantry. The boxes indicate the positions of whole cells.

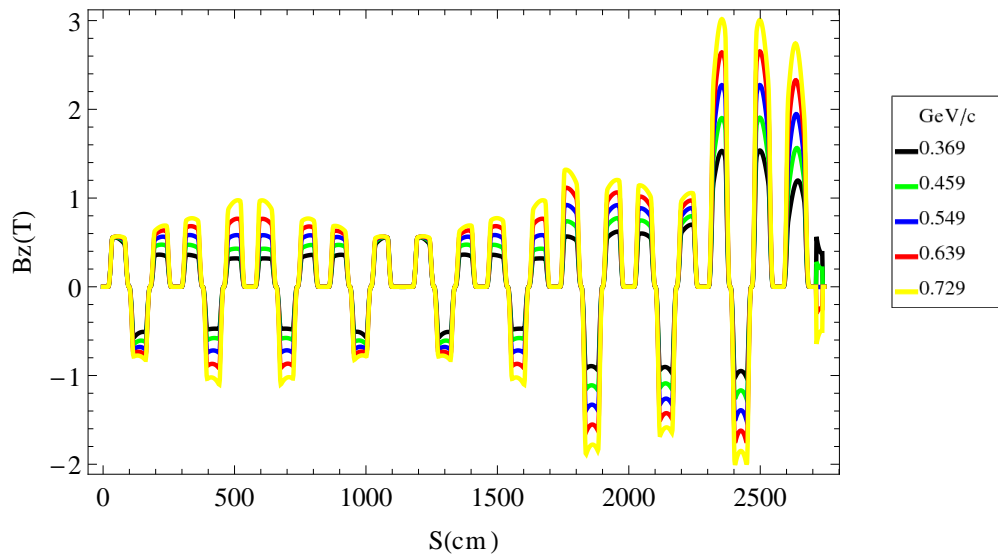


FIGURE 5.47: Fields experienced by particles through the whole gantry. Note that they do not exceed 3T.

TABLE 5.10: Optimal initial beta values for the gantry. This is only a small summary of a larger table in appendix A.

Momentum (GeV/c)	Beta (m)
0.369	4.92
0.459	5.47
0.549	5.90
0.639	9.58
0.729	14.22

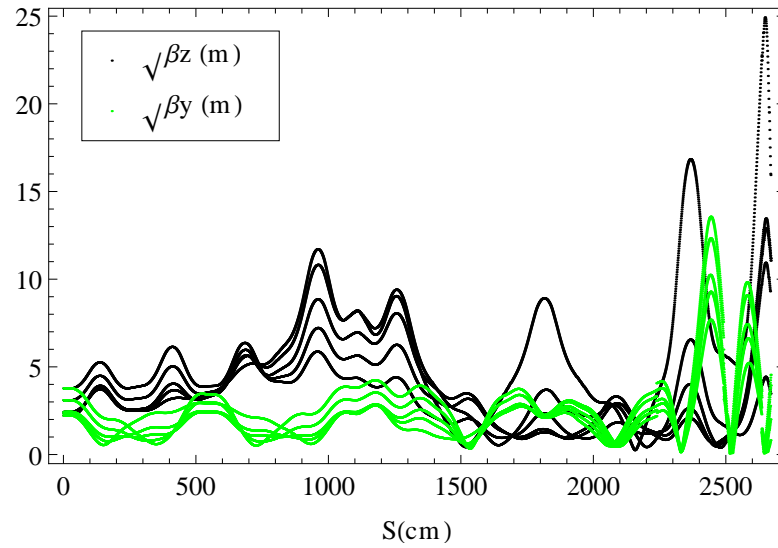


FIGURE 5.48: Beta functions through the whole gantry. These are the optimum functions assuming that horizontal and vertical betas are equal at the start for each momentum.

## 5.9 Testing Rotation of the Gantry and Tolerance of Positional Errors at the Entrance

So far, it has been assumed that particles would enter the gantry exactly on axis and with zero deflection, meaning the rotational position of the gantry was irrelevant. This section aims to test what happens when particles are introduced off axis with non-zero deflections over  $360^\circ$  of gantry rotation. This is important, because it will inform section 6.6 where matching to the treatment room from the transport line will be attempted.

The rotation of the gantry was simulated by entering particles with non-zero  $y$  and  $z$  coordinates at the entrance. This was done for five displacements (0.001, 0.01, 0.1 and 1 cm),  $180^\circ$  rotation (as the error will be symmetrical at this point) and three momenta (0.369, 0.549, 0.729 GeV/c).

Figures 5.49 → 5.51 show the resulting deflections for 0.369, 0.549 and 0.729 GeV/c respectively and figures 5.52 → 5.54 show the positional errors for the same momenta.

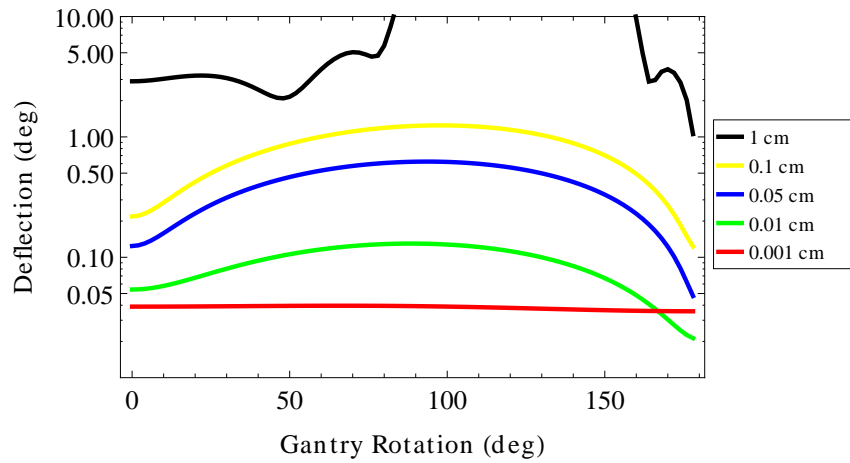


FIGURE 5.49: Gantry rotation deflection errors with 0.369 GeV/c particles. The key refers to the particles' initial distance from the gantry rotation axis and 'deflection' refers to the final angle the particle's direction makes with 'S'. A log scale is used purely for clarity. Where the black line disappears indicates particles being lost before reaching the end.

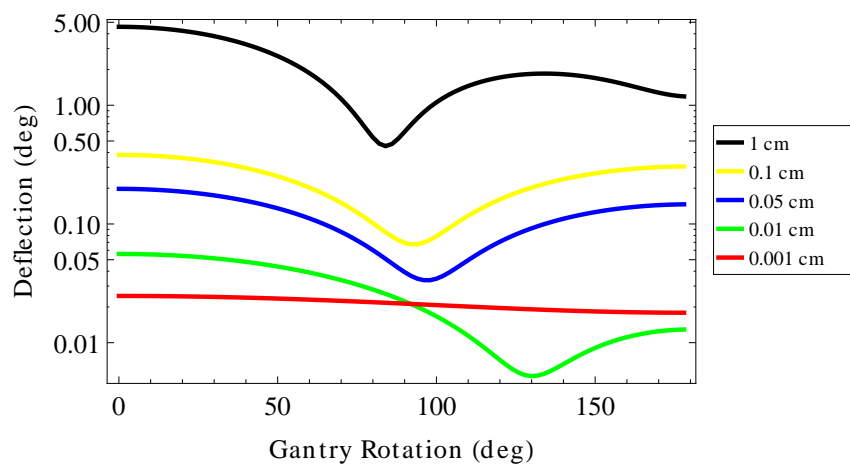


FIGURE 5.50: Gantry rotation deflection errors with 0.549 GeV/c particles. The key refers to the particles' initial distance from the gantry rotation axis and 'deflection' refers to the final angle the particle's direction makes with 'S'. A log scale is used purely for clarity.

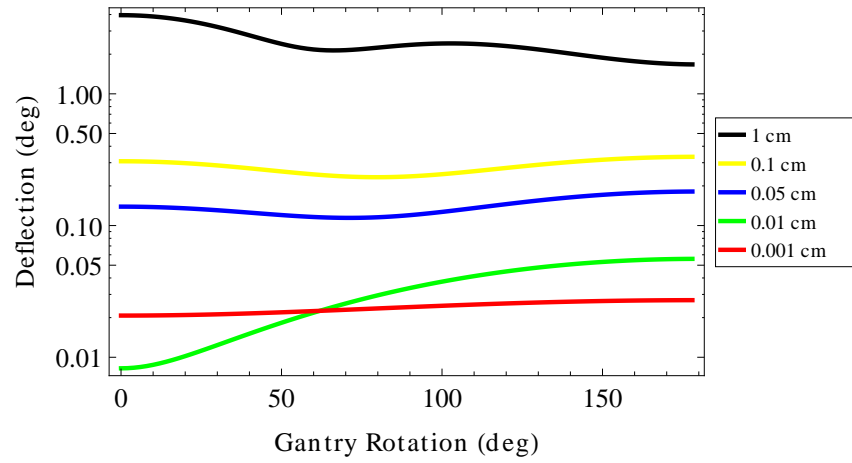


FIGURE 5.51: Gantry rotation deflection errors with 0.729 GeV/c particles. The key refers to the particles' initial distance from the gantry rotation axis and 'deflection' refers to the final angle the particle's direction makes with 'S'. A log scale is used purely for clarity.

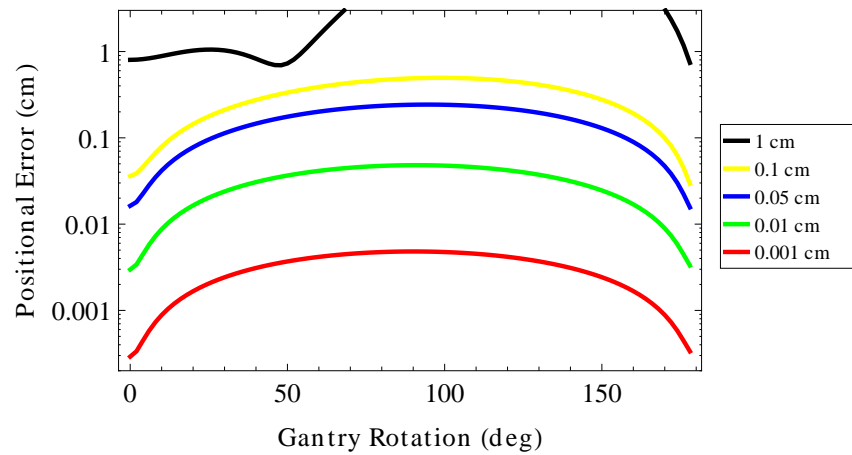


FIGURE 5.52: Gantry position errors with 0.369 GeV/c particles. The key refers to the particles' initial distance from the gantry rotation axis and 'position error' refers to a particle's final distance from its equilibrium orbit. A log scale is used purely for clarity. Where the black line disappears indicates particles being lost before reaching the end.

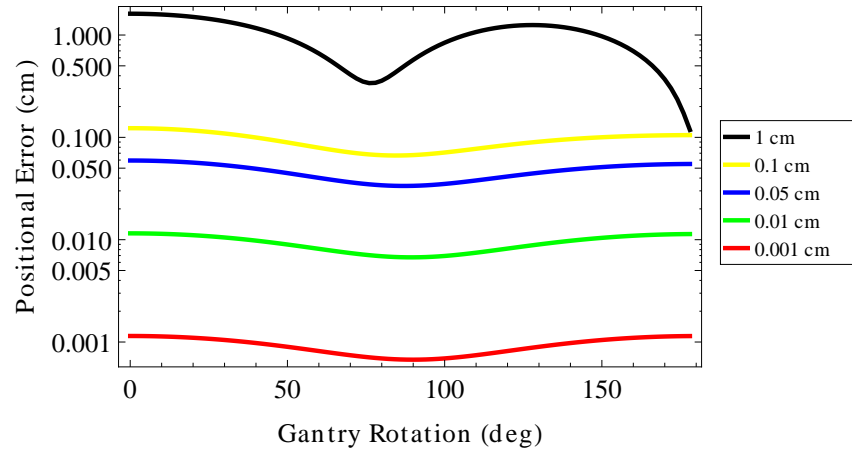


FIGURE 5.53: Gantry position errors with 0.549 GeV/c particles. The key refers to the particles' initial distance from the gantry rotation axis and 'position error' refers to a particle's final distance from its equilibrium orbit. A log scale is used purely for clarity.

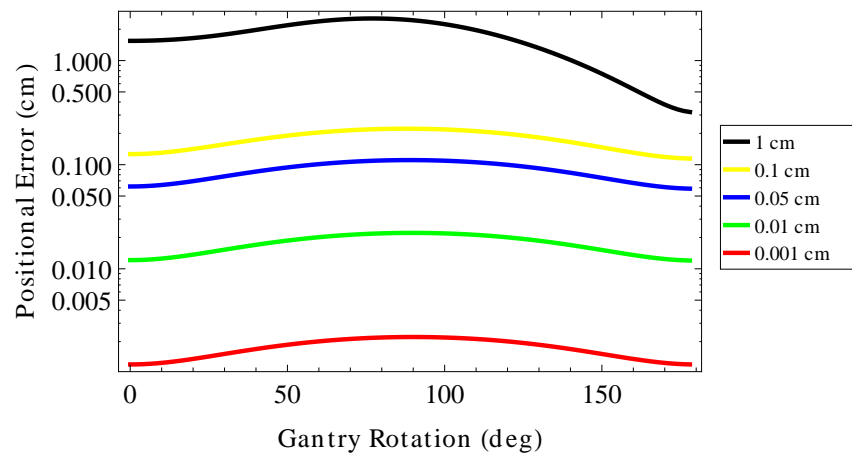


FIGURE 5.54: Gantry position errors with 0.729 GeV/c particles. The key refers to the particles' initial distance from the gantry rotation axis and 'position error' refers to a particle's final distance from its equilibrium orbit. A log scale is used purely for clarity.

If you ignore the, almost certainly, unrealistic initial error of 1cm, the final positional errors in the worst case 0.369 GeV/c tend to go about an order of magnitude higher than the initial error. At 0.549 and 0.729 GeV/c, the errors tend to stay roughly the same as the original error.

In terms of final deflection, the worst case (again 0.369 GeV/c) shows about  $1^\circ$  deflection with a 0.1cm original error. Apart from the high and low limit, the final error seems to approximately scale with initial error, so a 0.05cm original error gives  $\approx 0.5^\circ$  final deflection.

The scanning system at the end of the gantry is required to produce an accuracy of 0.02cm [26, p.116]. This means that with no other error in the system and considering only position, the positional error at the start of the gantry would have to be limited to  $\approx 0.002\text{cm}$ . Moreover, given that there is 3m between the end of the bending magnets and the patient, the maximum angular error would have to be  $\approx 0.004^\circ$ , which is too small to be achieved with this lattice. This could be achieved, however, with an active scanning system before the entrance to the gantry. That proposal is made in the PAMELA design report [26] and will be discussed again in section 6.7.3.

## 5.10 Ideas for Further Study

At around 11m high and 25m long, the current gantry design is too large to be competitive with existing gantries (although, obviously, the energy can be changed much faster).

One possible solution to the height problem is to integrate the scanning magnets with the final 90 degree bend. This would result in a complicated system where control of

the beam size and horizontal position would be coupled, however it is an idea worth pursuing because the beam behaviour, although complicated, would be predictable and could be characterised and taken into account by the control systems. Assuming the scanning section remains roughly the same height, the total height might then be around 3m, giving the gantry a height of about 6m.

This means that in figure 5.25, there would need to be zero dispersion at the exit from section 2, avoiding any need for varying  $k$  in the way described in sec.5.7.3.2 and so hopefully avoiding the problems with the Twiss functions. Figure 5.55 shows the tracks through an initial design of sections 1 and 2 in such a layout and figure 5.56 shows the beta functions with horizontal and vertical betas arbitrarily defined as 7m for all momenta. The height of this design is 3m and the magnet lengths are around 55cm each.

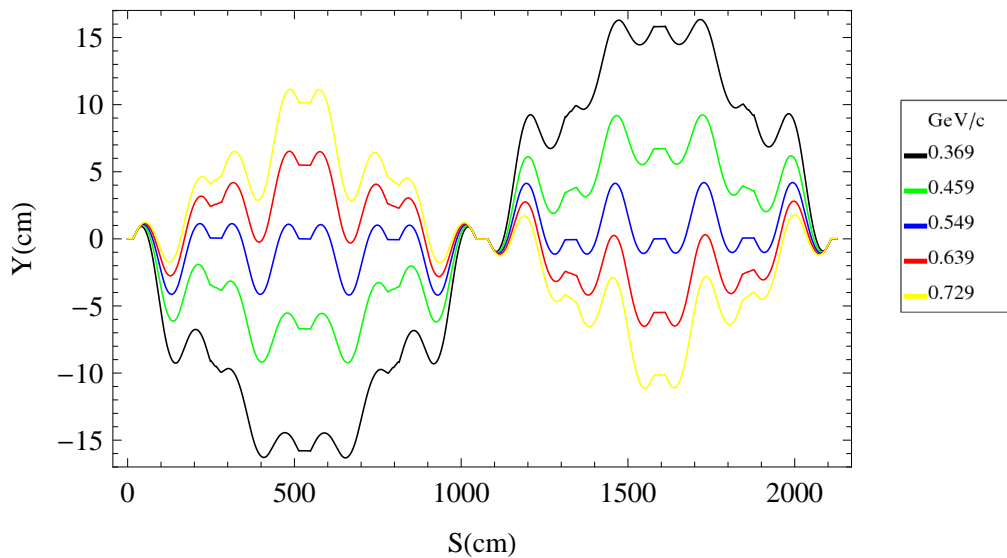


FIGURE 5.55: Tracks through sections 1 and 2 if scanning is integrated into sections 3 and 4.

The problem of length still remains, however. With reasonable magnet lengths and four cells per section, the length is roughly 20m. To be competitive, the gantry would need to be closer to 10m which would not be possible even if 3 cells were used per section.

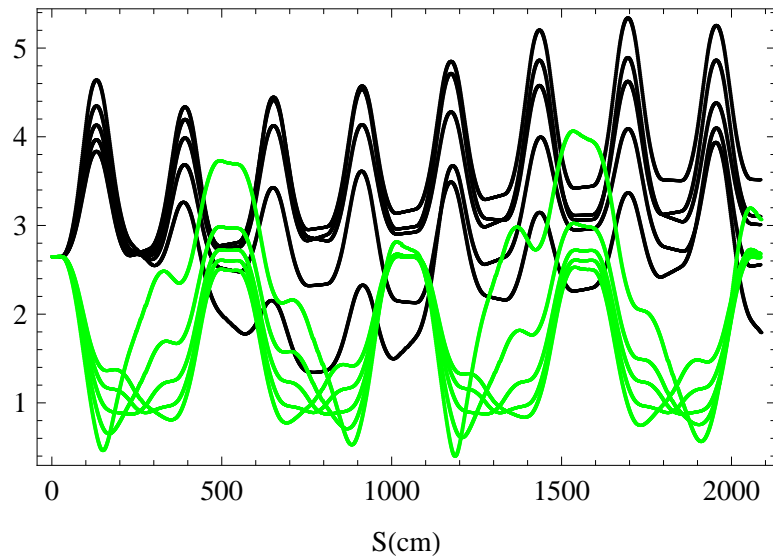


FIGURE 5.56: Beta functions through sections 1 and 2 if scanning is integrated into sections 3 and 4. All betas are assumed to be 7m at start and all alphas assumed to be zero. The black lines represent the square root of the vertical beta functions and the green the horizontal.

To achieve this, an alternative approach will be needed to the design of sections 1 and 2. The PAMELA project needs to switch energies very quickly, but perhaps it does not need to do so over the entire energy range. A tumour of 15cm, for example, will not need the entire energy range. A system could be envisioned, then, where the magnets in the gantry have a number of strength settings which can be switched between in the time it takes for the gantry to rotate to the next treatment position.

If this is possible, one idea is to abandon the PAMELA style triplet all together and use just dipoles and quadrupoles over a limited energy range. A very straight forward system is shown in figure 5.57. A zero dispersion beam is deflected upwards with a dipole, exciting dispersion within the beam. A focusing magnet then makes the particle beams parallel and a long drift takes the particles to the necessary height. The process is reversed at the other end, with a focusing magnet and a dipole removing the dispersion. The energy range is limited by the aperture in the focusing magnet and the following study looks briefly at the feasibility of such an idea.

It is assumed that the energy range required to be changed very rapidly (that is between gantry rotations) at any time is plus or minus 45MeV (which is plus or minus 275MeV/c in momentum), and that 3m of elevation is required in a length of 8m; giving a deflection of  $\approx 20^\circ$  to the median energy particle. The largest positional spread will be at lower momenta, so a range of momenta between 0.369GeV/c and 0.645GeV/c were considered

A simulation was carried out of the set-up described above, but over a shorter distance than would be required in a gantry. The focusing magnets used quadrupole, sextapole and decapole fields to achieve the desired bending. Figure 5.58 shows the particle tracks through the proposed layout; there is very little dispersion at the end, so this shows, the idea could work. The problem comes from the beta functions because there are only focusing magnets in the lattice. Further study could look at adding defocusing magnets to remedy this, which may also make it possible to extend the system to the required length, but the length of the presented lattice could also be extended by placing sections in series.

## 5.11 Chapter Summary

In this chapter a design for a gantry was developed (section 5.6) using the main PAMELA ring as a starting point (sections 3.2.4 and 5.3). This involved a novel method of creating near-perfect dispersion suppression using ns-FFAG magnets (5.5) which was the author's work. The final gantry design (section 5.7.4) and the intermediate designs (sections 5.4 and 5.6) are also novel and all the author's work. The final section of this chapter discusses ideas for further work.

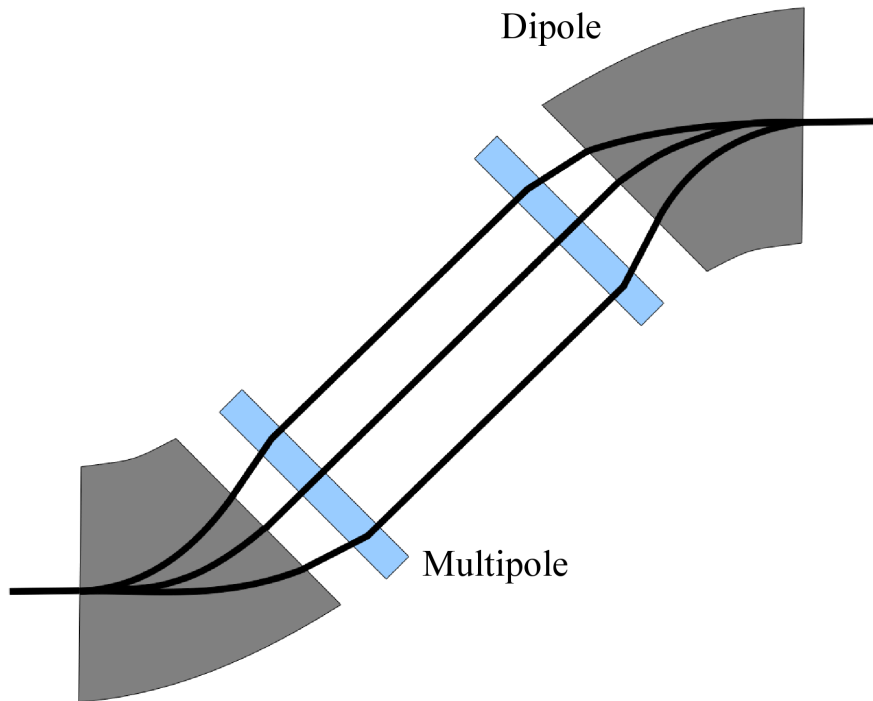


FIGURE 5.57: Initial schematic design for a lattice to create elevation in the gantry. Further multipoles would be added in between the existing multipoles to control the Twiss parameters.

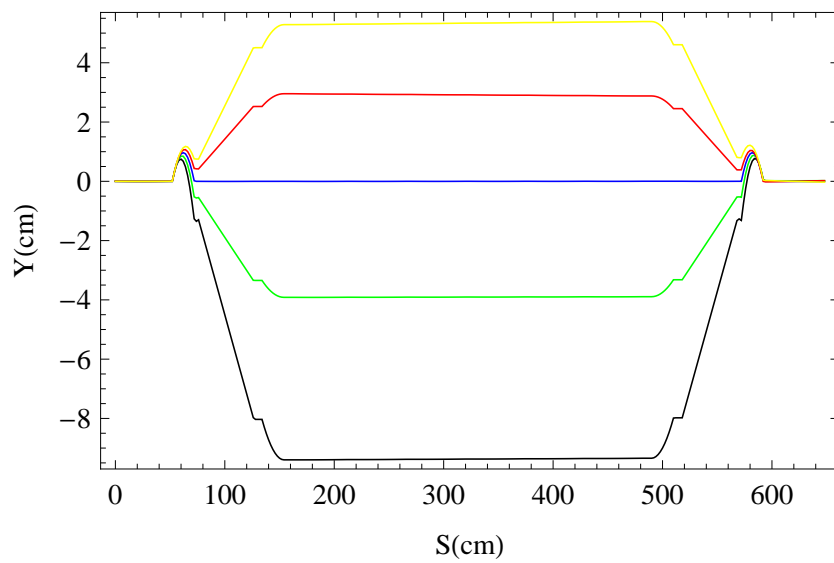


FIGURE 5.58: Tracks through initial design for a simple lattice to create elevation in the gantry. This is a reduced energy range chosen to cover a 15cm tumour: 0.369 GeV/c (black)  $\rightarrow$  0.645 GeV/c (yellow)

## Chapter 6

# Transport Line Design Studies

### 6.1 Introduction

This chapter deals with the design of the transport line which takes the beam from the main accelerator to the treatment room. It starts with an optimisation of a straight transport line design [82], then presents a design for a  $45^\circ$  bending section. A scheme for extracting the beam from the main transport line to the treatment rooms is then presented and discussed. Apart from the original straight transport line design, all of this chapter is novel and the author's own work. Some of the work on optimising the transport line (section 6.3) was presented in [89] and has been used in the PAMELA design report [26].

### 6.2 Basic Cell Design

The basic design of the magnets is the same as in section 5.2 (meaning all  $k$  values should be taken as multiplied by 1000), however, this section will consider an additional

cell layout, the quadruplet, because of the need to transport the beam in a straight line (see section 3.4.9). This is used for the straight lattice [82]. The structure can either be FDDF or DFFD depending on the position of the long drift, as it is a straight lattice and the total bending should be roughly equal in both transverse dimensions. The example in figure 6.1 is the latter and both F magnets are offset in this case.

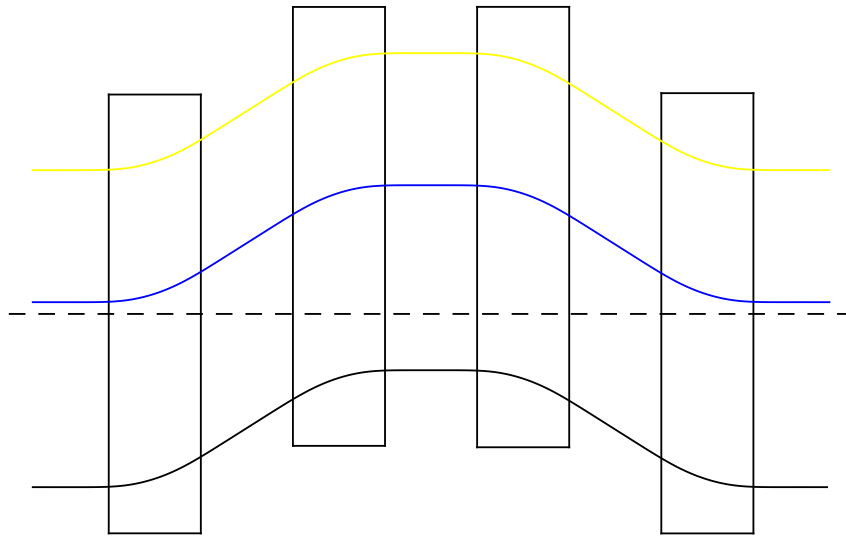


FIGURE 6.1: An example quadruplet cell (DFFD). The boxes give an indication of where the magnets are.

### 6.3 Optimisation of Straight FFAG Beam Transport Line

This is a study to find the optimal DF ratio,  $k$  value and placing of the long drift within the cell described in section 6.2 for the straight transport line described in [82] and compare the results using scaling fields with the non-scaling fields found using a truncated Taylor Expansion (section 2.5.4). The qualities considered were: acceptance, aperture, field strengths and dispersion at the centre of the long drift where extraction to the treatment rooms is likely to take place. The only measure which has an exact figure attached is acceptance. The guidance from design of the RFQ at the start of the PAMELA complex and the medical requirements at the end of the gantry, is that the

emittance should be around  $10\pi$ mm mrad; therefore, the acceptance of this transport line should exceed that value. The other qualities are such that the lowest value is desirable.

These studies will help our understanding of this novel transport line design as well as serving as a starting point for the design for the PAMELA project.

### 6.3.1 Parameters of Study and Method of Optimisation

It was decided to test a transport line with a length of 30m because this is the proposed length of the main straight section running from the first treatment room to the last (see figure 4.3). In order to keep the transport as sparse as possible, the ideal would be to have one cell per 10m, however, initial simulations showed that this was impossible with the existing cell design. Instead, a set up with one cell per 5m was settled on, which keeps the transport line fairly sparse, and maintains the 10m periodicity. The geometry of this layout is summarised in table 6.1.

TABLE 6.1: Geometry of the transport line cell to be considered.

Magnets	4
Magnet length	20 cm
Short drift length	20 cm
Cell length	160 cm
Long drift length	340 cm
Periodicity	500 cm

Closed orbits were found for the highest, lowest and an intermediate momenta (0.369, 0.549 and 0.729 GeV/c respectively) and groups of particles were then tracked through the lattice with larger and larger initial emittances until the smear exceeded the 0.1 limit. The acceptance was found for each momenta by approaching the limit in smaller and smaller emittance steps until the smear = 0.1 to an adequate precision. The lowest

acceptance was taken to be representative of the working point, however very little variation with momentum was observed.

The aperture was taken as the largest  $y$  value within a magnet, minus the lowest. The dispersion was found in the same way, but in the long drift sections and the field strengths were simply the largest encountered by each particle through the lattice.

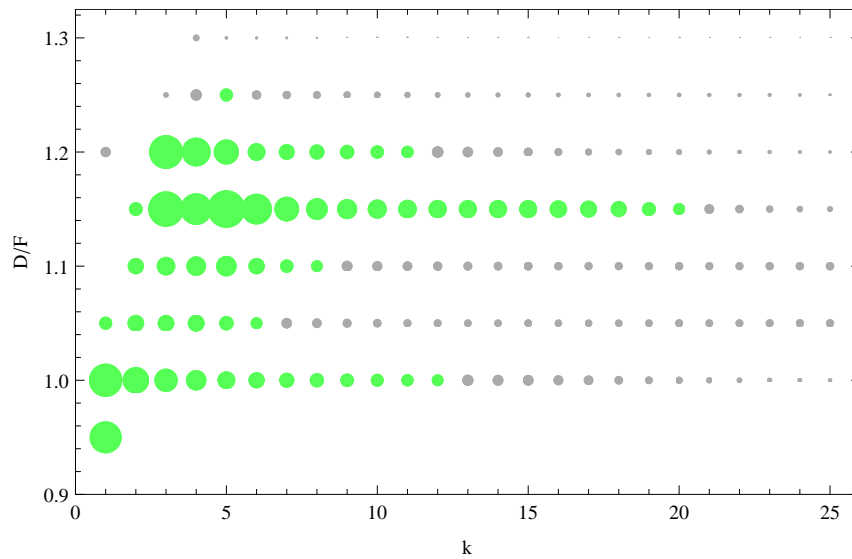


FIGURE 6.2: The acceptances for 30m of transport line using cells with non-scaling magnets in a DFFD configuration. The size of the dots are proportional to the square root of the acceptance in units of  $\pi\text{mm mrad}$ . Green dots represent acceptances  $> 10\pi\text{mm mrad}$  and grey dots represent lower acceptances. For scale: the largest acceptance (at  $k = 5$  and  $D/F = 1.15$ ) is  $101.75\pi\text{mm mrad}$  and the smallest (at  $k = 20$  and  $D/F = 1.3$ ) is  $0.028\pi\text{mm mrad}$ .

### 6.3.2 Straight Transport Line Optimisation Results

As might be expected, the working points all have DF ratios close to 1, but perhaps surprisingly, the  $k$  values reach as high as 260. Useful acceptances only cover a small fraction of that however. The difference between using scaling and non-scaling fields was marginal, so the non-scaling results are displayed ( $k$  refers to the scaling field the Taylor expansion was taken from). Figures 6.2 and 6.3 show the acceptances of the working points of the two cell configurations.

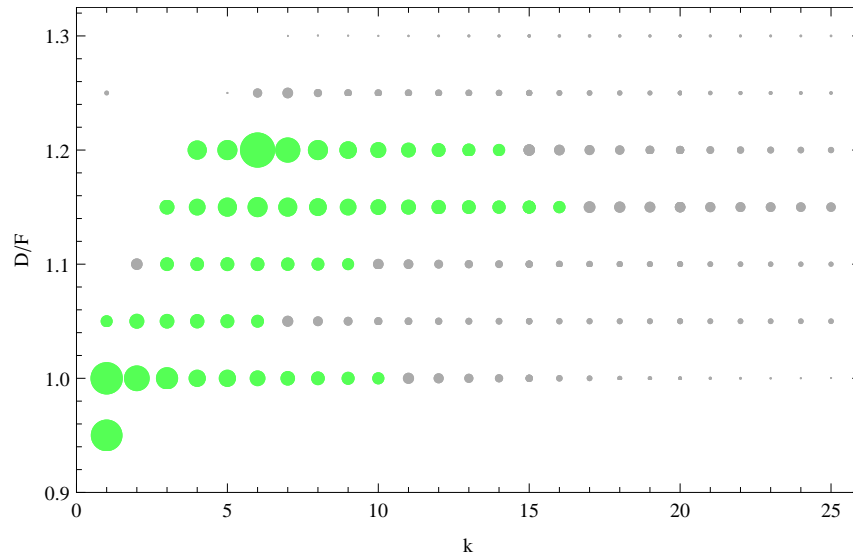


FIGURE 6.3: The acceptances for 30m of transport line using cells with non-scaling magnets in a FDDF configuration. See figure 6.2 for description of dot size and colour.

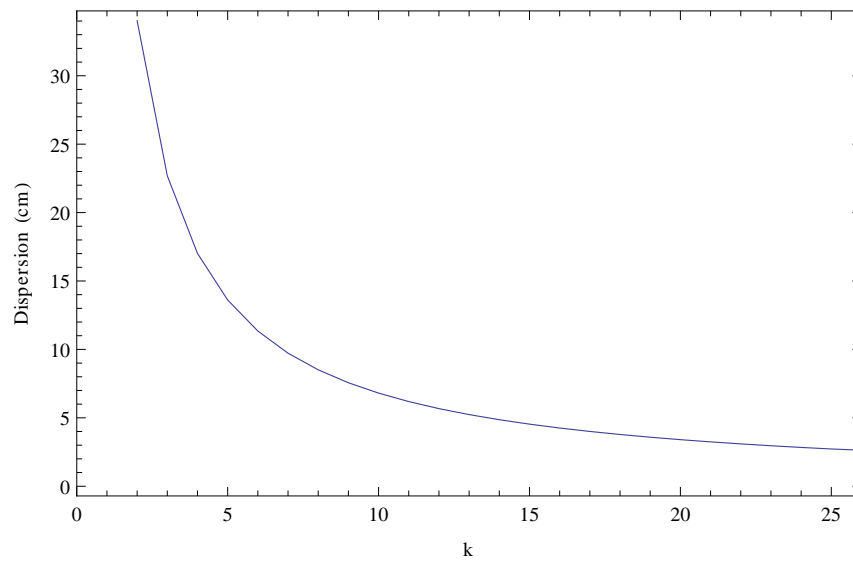


FIGURE 6.4: The dispersion in the long drift of a transport cell. This only depends on  $k$ .

Figure 6.4 shows how the dispersion at the centre of the long drift varies with  $k$ . The dispersion was chosen for display instead of aperture because it is more useful to future studies, where the beam will be extracted from the long drift. The DF ratio was set at 1 and left out of the plot because it has little effect. The peak fields of the working points with acceptances and dispersions likely to be useful were not so large to present problems for magnet designers, so will only be discussed for individual designs of interest.

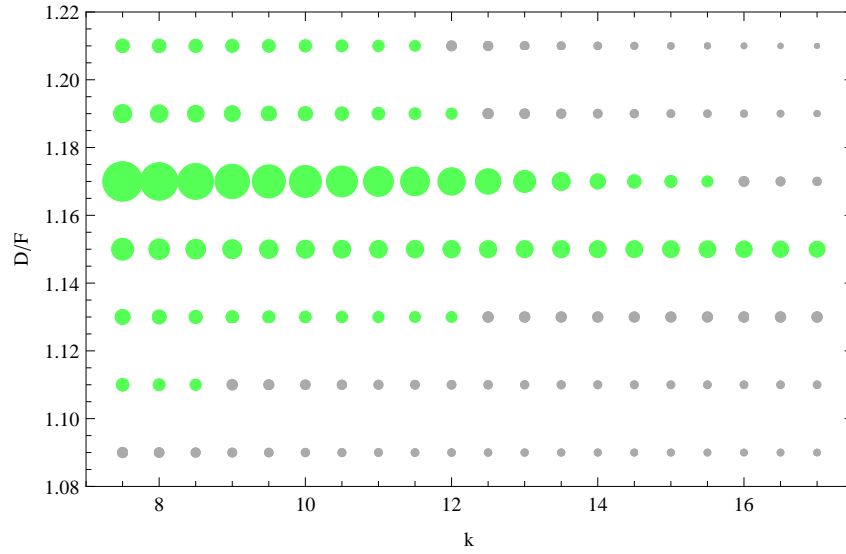


FIGURE 6.5: The acceptances for 30m of transport line using cells with non-scaling magnets in a DFFD configuration,  $k$  close to 12 and  $D/F$  close to 1.15. For scale, the largest dot at  $k = 7.5$  and  $D/F = 1.17$  represents an acceptance of  $122.03\pi\text{mm mrad}$ .

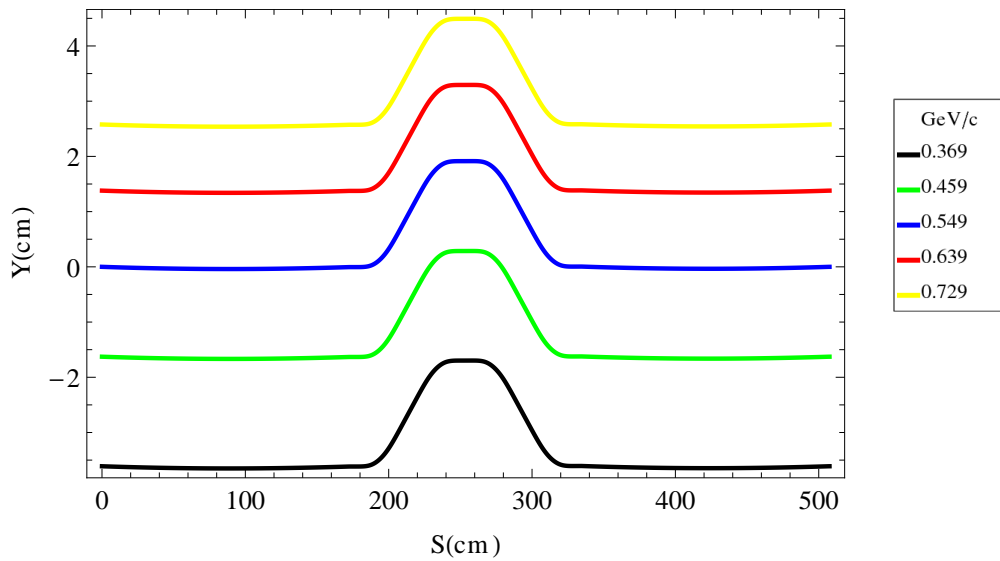
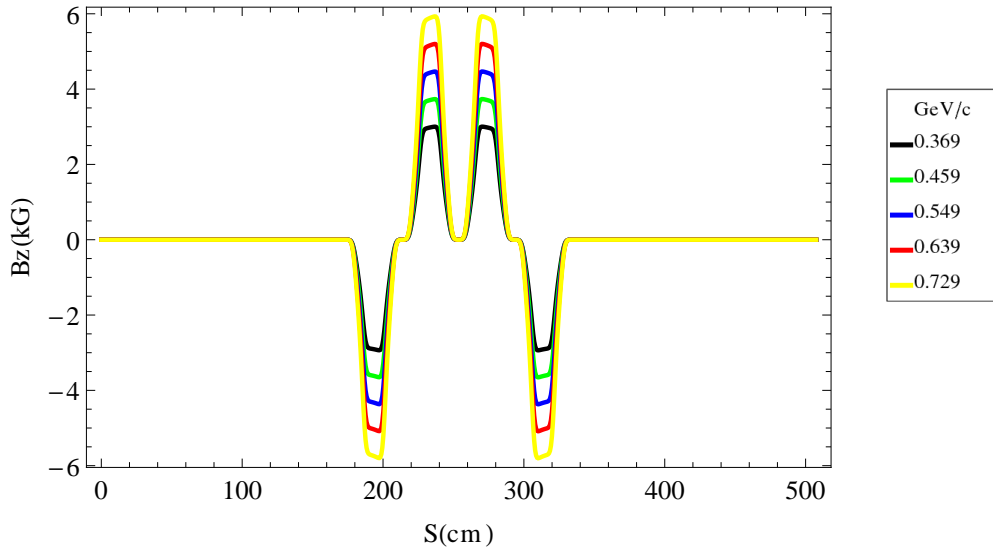
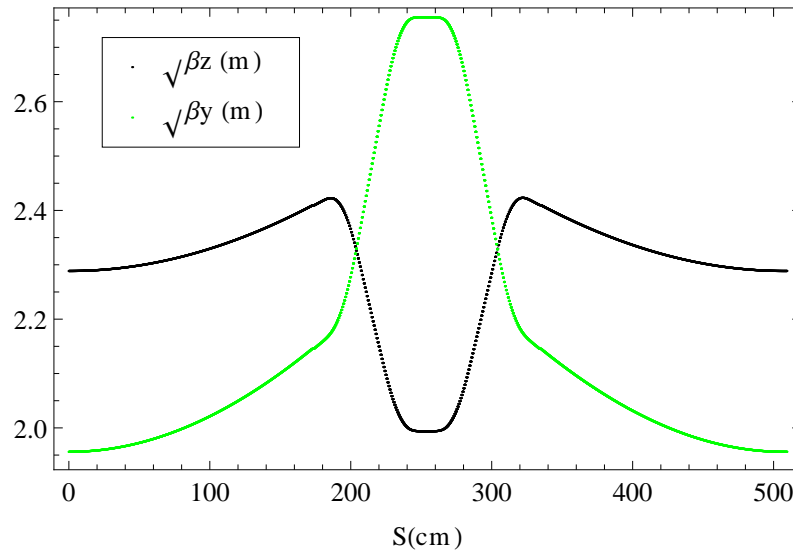


FIGURE 6.6: Tracks through cell with  $k = 11$  and a DF ratio of 1.17.

There are working points available for use as an FFAG beam transport line in both DFFD and FDDF cell configurations, however, the DFFD has more with higher acceptances. There is a conflict between using higher  $k$  values to reduce the dispersion at the centre of the long drift and using lower  $k$  values to increase the acceptance, but from inspection it seems that there are good compromises available around  $k = 12$  with a cell configuration of DFFD. Figure 6.5 shows the acceptances and long drift dispersions close to  $k = 12$

FIGURE 6.7: Fields through cell with  $k = 11$  and a DF ratio of 1.17.FIGURE 6.8: Beta functions through cell with  $k = 11$  and a DF ratio of 1.17.

and  $D/F = 1.15$ .

A good point to base further studies on is DF ratio of 1.17 and (the Taylor expansion of)  $k = 11$ . Figures 6.6 → 6.8 show the tracks, fields and betas through one cell of that design. Figure 6.9 shows the horizontal phase space of a group of particles with a  $10\pi$  mm mrad emittance before and after travelling through 30m of the transport line and figure 6.10 shows the vertical phase space. Both ellipses rotate, however the smear is a measure of the distortion of the shape, which does not change a great deal in either

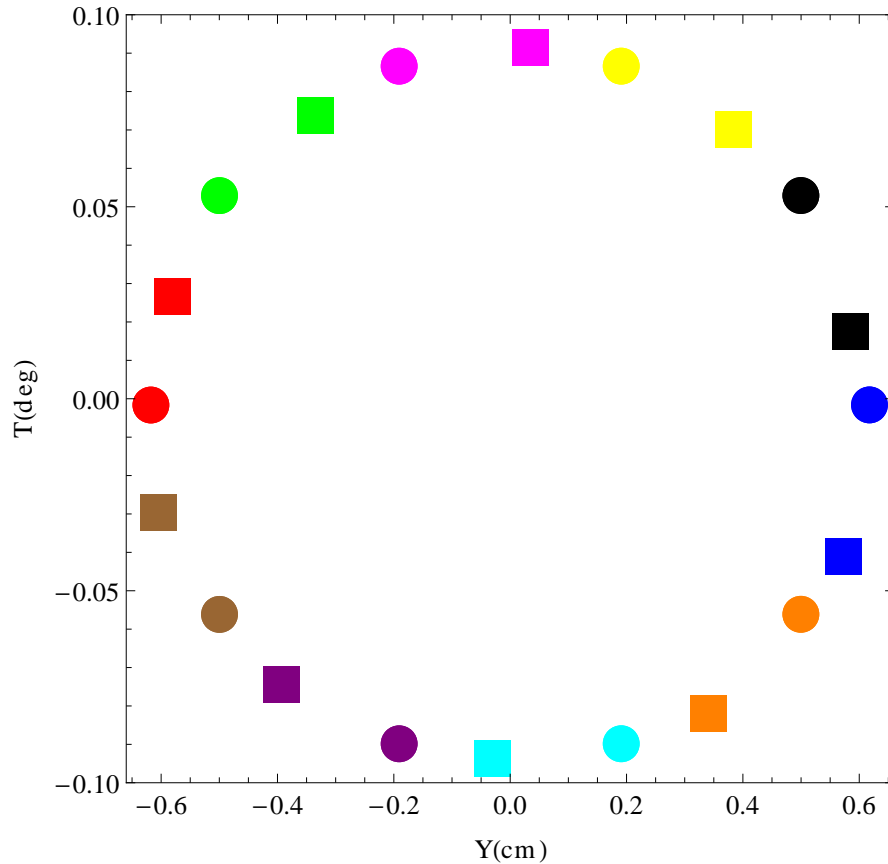


FIGURE 6.9: Horizontal phase space ellipses through 6 cells with  $k = 11$  and a DF ratio of 1.17. Circles show where the particles started and rectangles show where they finished. Each particle is a different colour.

case. The largest smear is in the horizontal phase space and it is 0.064. Please note that this is not the finalised design of the straight cells. This can be found at the end of the next section, where a bending section is added, in table 6.5.

## 6.4 Transport Cell for Carbon

This is a study to see if the optimal straight transport design can be adapted for use with the carbon beam that PAMELA will produce. The carbon beam will have a momentum range of  $0.729 \rightarrow 1.909$  GeV/c per nucleon, so either the field strength or the magnet length would need to be increased. Although the fields strengths are low in the transport line, a design was tried with 50% more magnet length and cell length (so

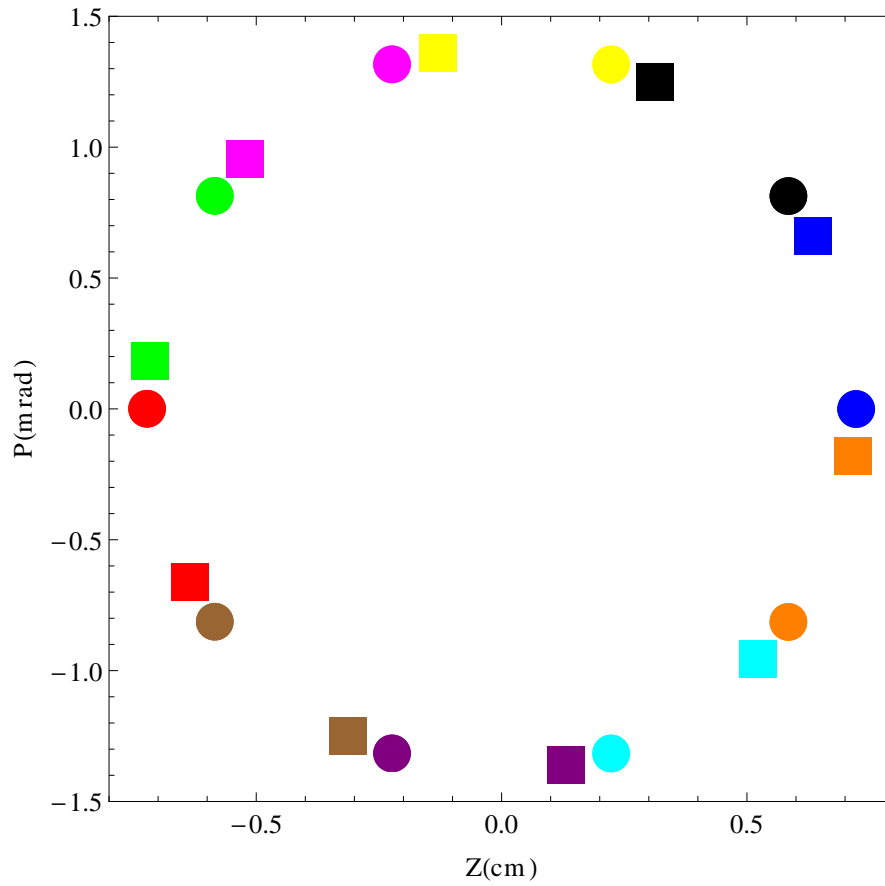


FIGURE 6.10: Vertical phase space ellipses through 6 cells with  $k = 11$  and a DF ratio of 1.17. Circles show where the particles started and rectangles show where they finished. Each particle is a different colour.

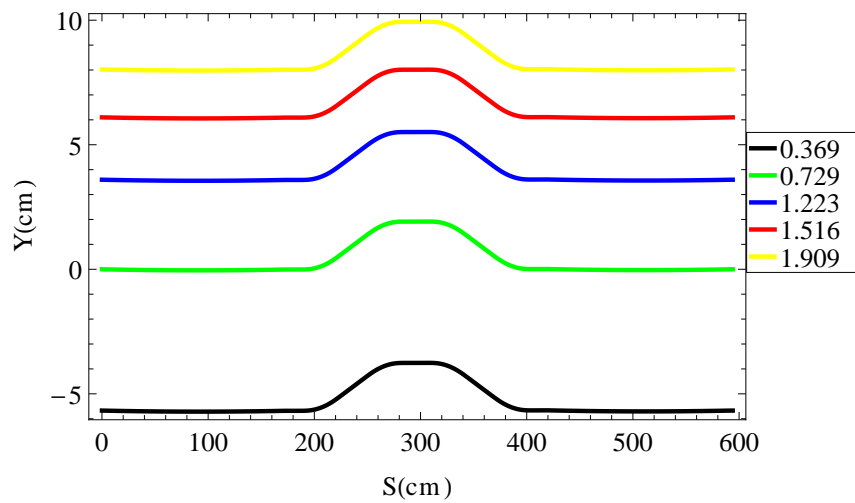


FIGURE 6.11: Tracks through a possible straight transport line for both protons and carbon. The units for the key are GeV/c.

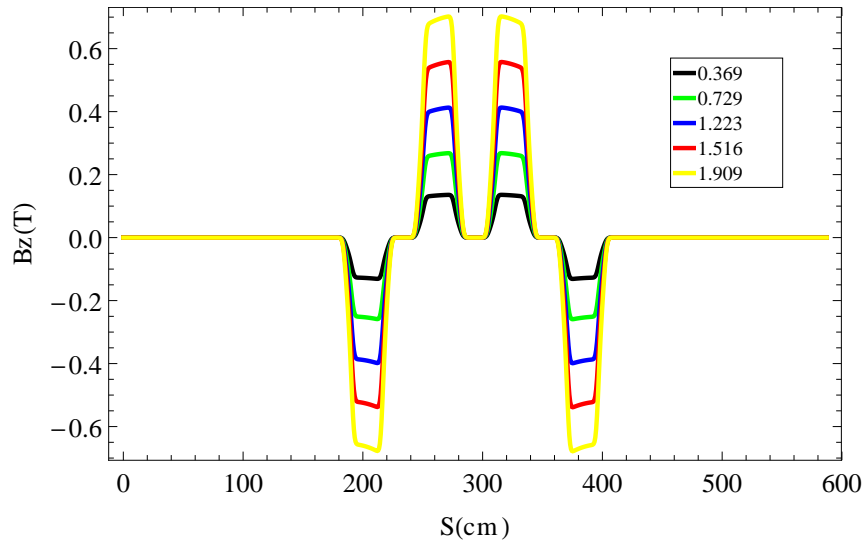


FIGURE 6.12: Fields through a possible straight transport line for both protons and carbon. Notice that by increasing the length of the magnets by a half, the required fields have remained roughly the same as in the proton only cell.

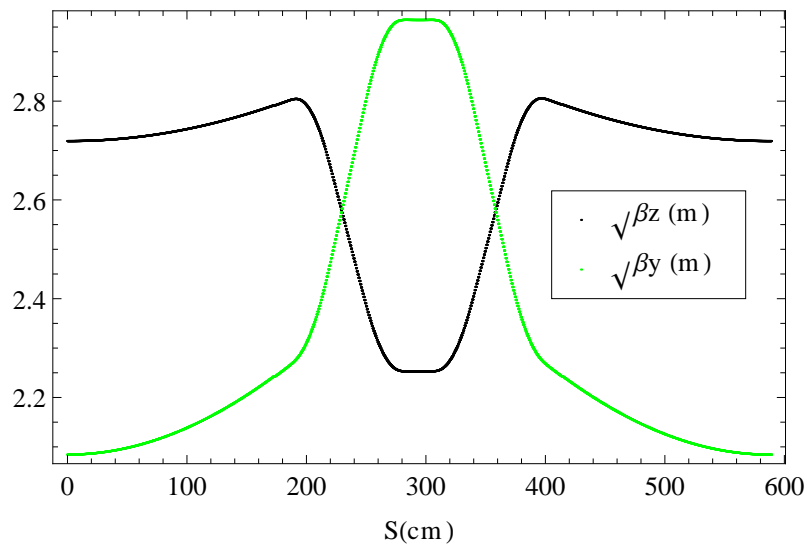


FIGURE 6.13: Beta functions through a possible straight transport line for both protons and carbon  $6+$ . The momentum range is from 0.369 to 1.909 GeV/c per nucleon.

the same packing factor). After a slight adjustment of the  $k$  value, a configuration was found that not only takes the carbon momenta, but takes the proton momenta too: a combined range of 0.369 GeV/c to 1.909 GeV/c. This raises the possibility of the same transport line being used for both types of particle.

Figure 6.11 shows the tracks of five momenta over the full range. Although the aperture has dramatically increased it is still within the bounds of possibility for a magnet

aperture (the orbit excursion in the main PAMELA ring is 17cm [26, p.17]), especially with these low fields. Figure 6.12 shows that the field strengths required are similar to the proton only design and 6.13 shows that the periodic beta functions remain stable across the whole energy range. Table 6.2 summarises the parameters of this design.

TABLE 6.2: Transport Line Straight Cell for Carbon and Protons Specifications.

Parameter	Value	Units
Momentum range	0.369 $\rightarrow$ 0.729	(GeV/c)/u
Magnets per cell	4	
Magnet length	30	cm
Short drift length	30	cm
Cell length	240	cm
Long drift length	340	cm
DF ratio	1.17	
$k$	12	
Field strength (max,min)	0.702, -0.678	T
Aperture	14.39	cm

To get a full appreciation of the possibilities of this design a full parameter search similar to the one in section 6.3 would have to be undertaken. However, that will be left for further work as this thesis is concerned with creating a working proton design first to show that it is possible, before a full carbon design is attempted.

## 6.5 Adding a Bending Section to the Transport Line

The next step is to add a 45° bend in between straight sections (see figure 4.3). The basic requirements for this section are:

- To bend the beam through 45°.
- To match equilibrium orbits to the straight lattice.
- To match beta functions to the straight lattice.

So, an ideal design for the bending section would be a single cell with a  $k$  of 11 to match the optimal straight lattice design and a bend angle of 45° to keep the number

of magnets used to a minimum. Triplet cells are more appropriate for bending sections than quadruplet cells because a net bending needs to occur and an imbalance of focusing to defocusing is desirable. For this reason, the basic cell geometry will be the same as that used for the gantry (figure 5.2).

Unfortunately, there are no such ideal cell designs with stable orbits. Of course, the  $45^\circ$  can be made up of more than one magnet; and there are cell designs with stable orbits that have bend angles of  $22.5^\circ$ ,  $15^\circ$  and  $11.25^\circ$ . However, the configurations with the same  $k$  as the optimal straight lattice are not close to matching its beta functions.

This means that the optimal straight lattice as defined in the previous section will have to be abandoned and a new optimum found with the requirement that it matches to a  $45^\circ$  bending section. To do this, a new parameter search was undertaken involving both the bending and straight sections.

To reduce the complexity, only the  $k$  value was changed in the straight section, with the rest of the parameters being those of the optimal lattice found in the previous section. This can be justified by considering figure 6.5. The acceptances of lattices with a DF ratio close to 1.17 remain valid over a wide range of  $k$  values, so the optimal  $k$  for the bending section will probably not have a  $k$  that makes the acceptance of the straight section too low. This means that when attempting to match the straight and bending sections, it is reasonable, in the first attempt at least, to only vary  $k$ .

### 6.5.1 Parameter Search for the Bending Section

The parameters changed in the bending section were: bend angle per cell,  $k$ , DF ratio, long drift and packing factor. For each configuration, the closed orbit positions and beta

functions were found and tested against those of the straight lattice with the same  $k$ .

This is summarised in table 6.3.

TABLE 6.3: Bending Section Parameter Search. Magnet length was kept constant at 60cm and the short drift 20cm.

Parameter	Range
$k$	$2 \rightarrow 20$
Packing factor	$0.5 \rightarrow 0.8$
Long drift length	$50 \rightarrow 350$ cm
Bend angle per cell	$11.25^\circ \rightarrow 45^\circ$
DF ratio	$0.8 \rightarrow 1.8$

When the closest match was identified, a more precise match was found using a downhill fitting function (see section 2.7). All parameters used in the parameter search were varied for this, except for the bend angle. Also allowed to vary slightly, was the DF ratio and long drift of the straight section.

After this fitting process was finished, the field profiles of both section were made non-scaling by using the Taylor expansions and the coefficients of the curved section were varied so that the equilibrium orbits matched perfectly.

### 6.5.2 Bending Section Result and Final Straight Cell Design

The specifications of the resulting bending cell are shown in table 6.4 and figures 6.14 and 6.15 show the tracks and beta functions through a  $45^\circ$  bend between two straight cells.

### 6.5.3 Discussion of the Matched Bending Section

The ability to match a bending section to the straight transport line design is very useful to this design for the PAMELA project. However, it could also be the start of a design for a ‘race-track’ style FFAG ring, as is currently done with synchrotrons. This is a

TABLE 6.4: Transport Line Bending Cell Specifications. The  $b_n$  values are those in equation 2.31

Magnets per cell	3
Magnet length	60 cm
Short drift length	10 cm
Cell length	200 cm
Long drift length	98.2 cm
Bend angle per cell	15°
DF ratio	1.416
$b_1$	4971.5
$b_2$	12236891.7
$b_3$	20438752621.9
$b_4$	26368787187869.9

TABLE 6.5: Transport Line Straight Cell Specifications. The  $b_n$  values are those in equation 2.31

Magnets per cell	4
Magnet length	20 cm
Short drift length	20 cm
Cell length	160 cm
Long drift length	340 cm
Periodicity	500 cm
DF ratio	1.220
$b_1$	5000.0
$b_2$	12497500.0
$b_3$	20820835000.0
$b_4$	26010428123750.0

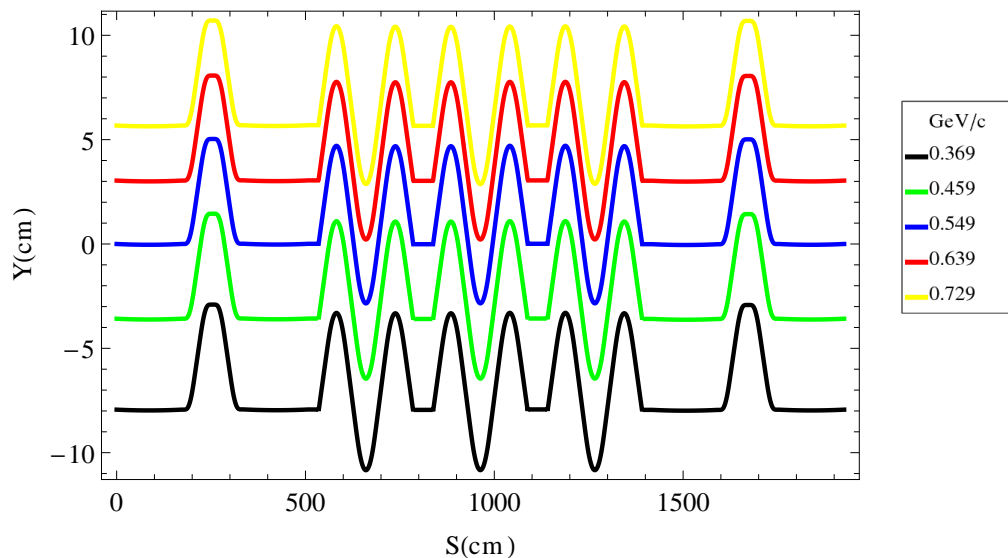


FIGURE 6.14: Tracks through a 45° bending section between two straight transport cells.

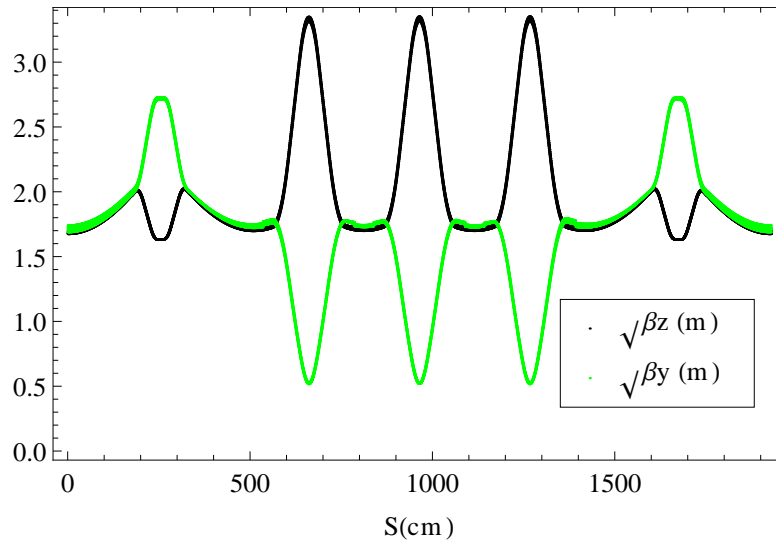


FIGURE 6.15: Beta functions through a  $45^\circ$  bending section between two straight transport cells.

ring with straight sections where space can be made for beam extraction, acceleration or experiments that would not normally be possible in a circular ring. Designs for FFAG racetracks have been proposed [90] [91] [92], but as yet, none have been built. Adapting this particular design to make an FFAG racetrack may be an interesting idea for a future study.

## 6.6 Extraction from the Transport Line

### 6.6.1 Purpose of Study

The purpose of this section is to find a way to switch the beam into the treatment room out of the straight transport line using switchable magnets. It will be shown that this is prohibitively complex to achieve using binary, on/off, magnets and a solution with variable field dipoles will necessarily be introduced. This will be justified at the end of the section not only due to the difficulties in doing it any other way but as a way of

introducing energy selection into the design of the transport line, which is beneficial to patient safety.

## 6.6.2 Ideas for Fixed Field Extraction from the Transport Line

The following sections go through all the possibilities that were considered that do not use variable field magnets. They will each be briefly described and their suitability discussed as a way of justifying the use of variable field dipoles in section 6.6.3. Although none of them were successful in this particular context, they include some interesting ideas for FFAAG transport design.

### 6.6.2.1 Switching One Magnet Off

Deflection of the beam out of the straight quadruplet transport cells could be achieved, in principle, by switching off one of the constituent magnets. The design of the straight transport line includes an overall balance in bending strength between the F and the D magnets, so when one is switched off, overall bending will occur. Figures 6.16, 6.17, 6.18 and 6.19 show the effects of switching off each of the four magnets individually. Switching off the F magnets is most interesting to us because it creates the reverse bending this design requires; and from comparing figs 6.18 and 6.17, it appears that switching the second focusing magnet off is the most desirable as it keeps the required aperture to a minimum. Figure 6.20 shows that while this obviously disrupts the periodicity of the beta functions, they are not disastrously affected and there may be some way to correct them.

This particular configuration would probably produce enough of a kick to give all of the energies enough elevation before the next cell. In the current design, the drifts between

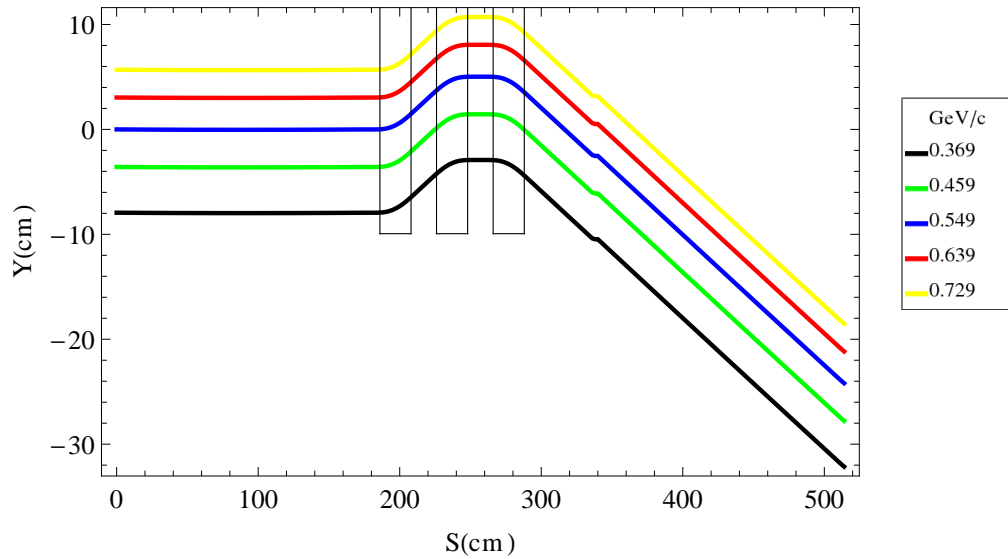


FIGURE 6.16: Tracks through a straight transport cell with the second D magnet switched off. This creates approximately  $8^\circ$  positive deflection in all momenta. The boxes show where the switched on magnets are and their height gives an approximation of the aperture required.

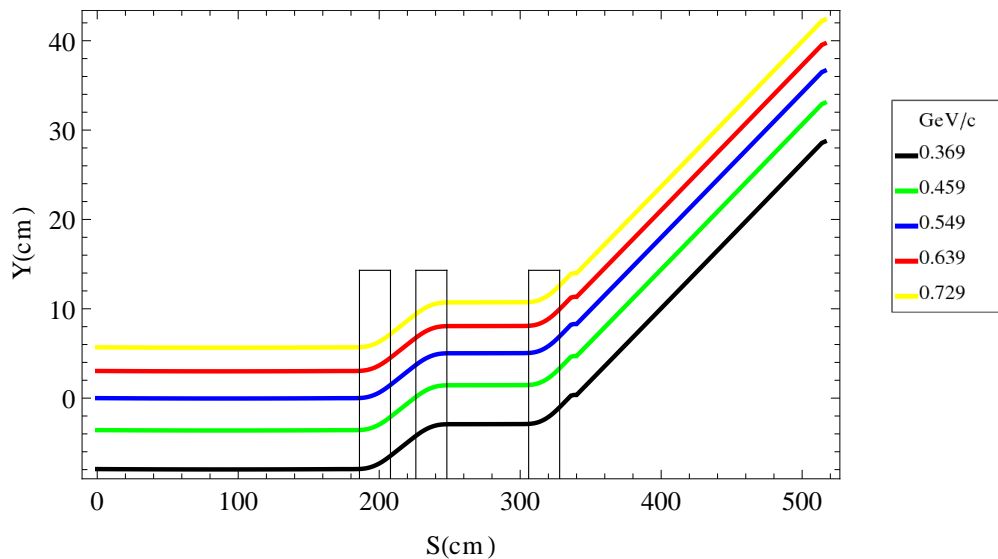


FIGURE 6.17: Tracks through a straight transport cell with the second F magnet switched off. This creates approximately  $10^\circ$  negative deflection in all momenta. The boxes show where the switched on magnets are and their height gives an approximation of the aperture required.

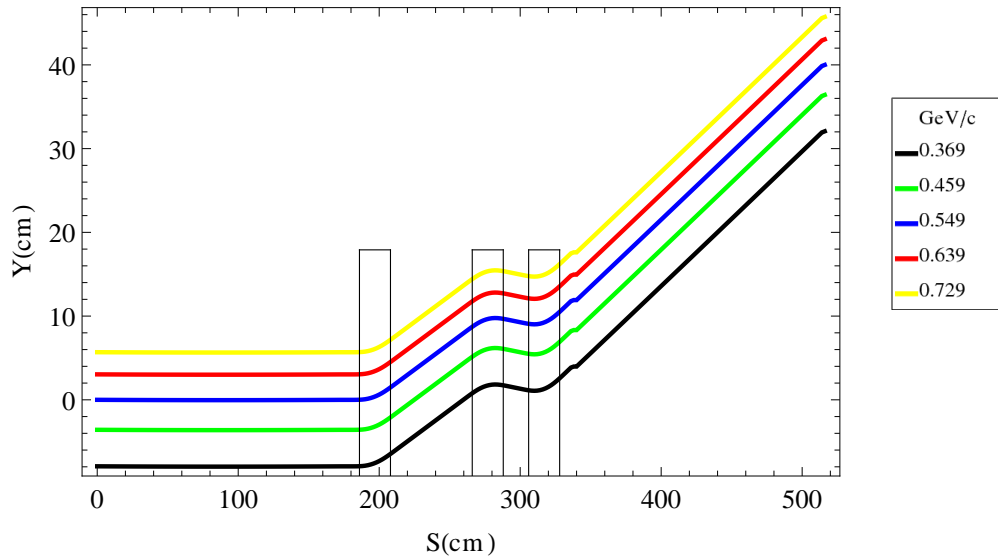


FIGURE 6.18: Tracks through a straight transport cell with the first F magnet switched off. This creates approximately  $10^\circ$  negative deflection in all momenta. The boxes show where the switched on magnets are and height length gives an approximation of the aperture required.

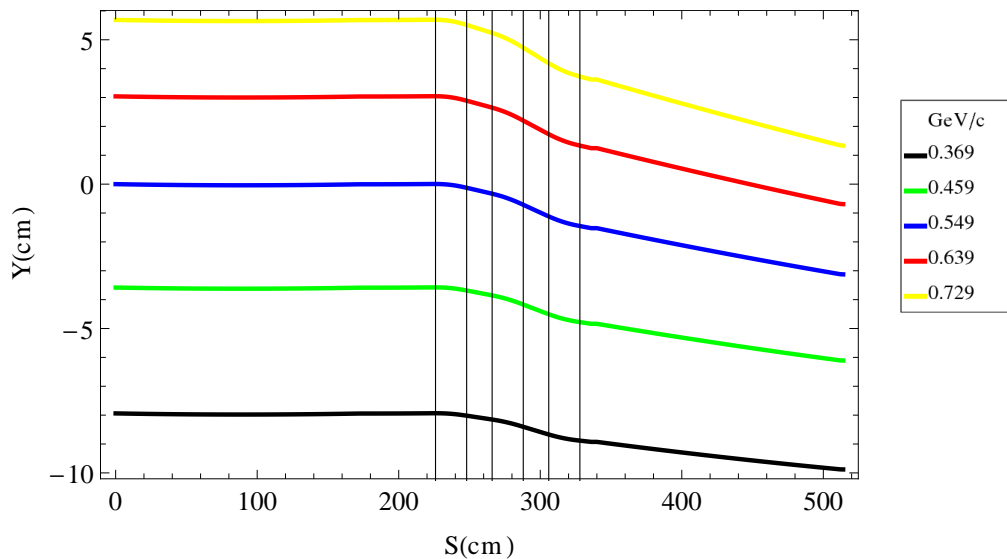


FIGURE 6.19: Tracks through a straight transport cell with the first D magnet switched off. This creates small negative deflections in all momenta. The boxes show where the switched on magnets are and their height gives an approximation of the aperture required.

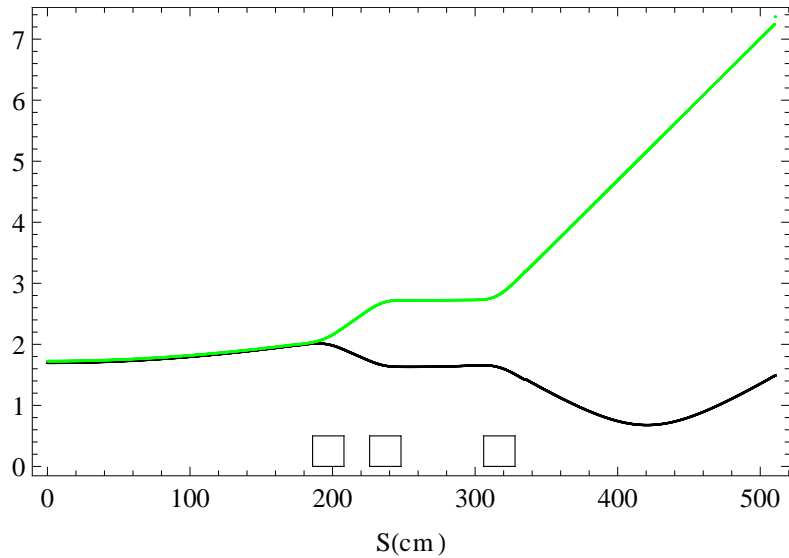


FIGURE 6.20: Beta functions through a straight transport cell with the second F magnet switched off. The boxes show where the switched on magnets are. The green line is the horizontal ( $y$ ) beta functions for all momenta in the range  $0.365\text{GeV} \rightarrow 0.729\text{GeV}$  and the black line shows the vertical ( $z$ ) beta functions.

cells is 340 cm and the deflection produced by turning F2 off is around  $10^\circ$ ; so by the end of the drift, when the particles reach the start of the next cell, each particle will have shifted about 60cm in the Y direction. This means that the lowest energy, which starts at around -10cm will be  $\sim 40\text{cm}$  above the top of the aperture (+10cm) in the transport cell below. This is probably enough space for the magnets and casing of the transport cell. If it is not enough for both the transport cell casing and whatever magnet is required to take the ejected beam, then the ejected beam could be allowed to drift until there is.

This is an elegant solution as it does not require any extra magnets to produce the extraction kick, however it will not be considered further for this design. There may be some practical problems in turning off one of the magnets in a cell, but there is also the problem that the beam will have to be bent by a further  $35^\circ$  with the lowest energy on the outside of the bend and the highest energy on the inside. As discussed in the gantry design chapter, this is not feasible and it is better to look for a design which switches

the positions of the particles as well as ejects them.

### 6.6.2.2 Switchable Dipoles

This is an obvious idea, using the most basic magnets available. At each ejection point, a switchable dipole would be placed deflecting the beam out of the transport line. Another dipole, with the exact opposite field strength would then cancel out the bend - and, importantly, the dispersion - before an FFAG bending section would take the beam to the treatment room. The distance the beam is taken away from the main transport line is controlled by the strength of the dipoles. An example of tracks through the dipoles in this scheme is shown in figure 6.21. One advantage of this idea is that dipoles appear as drifts to the beta functions because there is no field gradient.

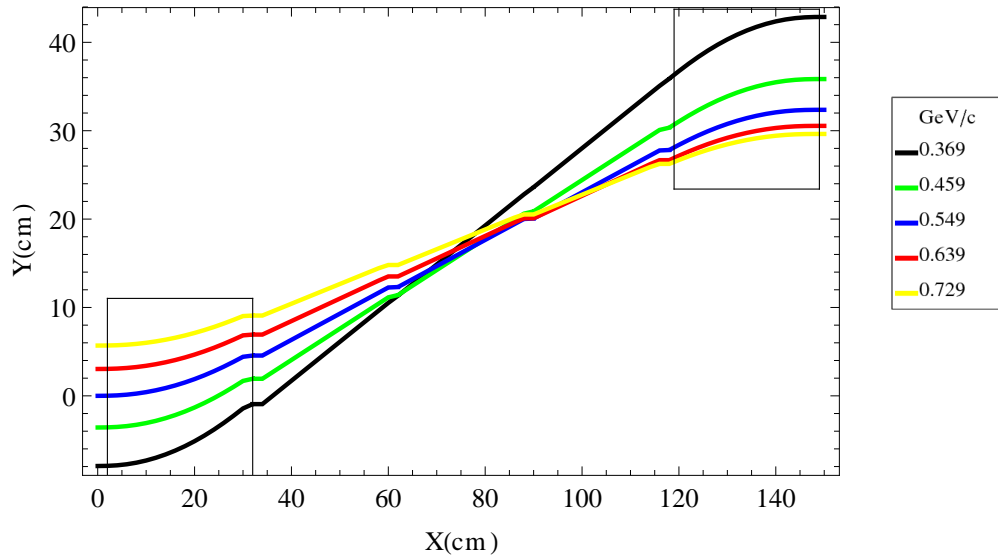


FIGURE 6.21: Example of ejection system using two dipoles of opposite strength. The discontinuities in the lines are due to glitches in display, rather than any real effect.

While this is appealing in its simplicity, it would be impossible to match to the beam after the second dipole to the field profile in an FFAG. Figure 6.22 shows how the difference in relative position vs momentum is quite large for most of the momentum range. This is too big a difference for the type of ns-FFAGs that this thesis deals with

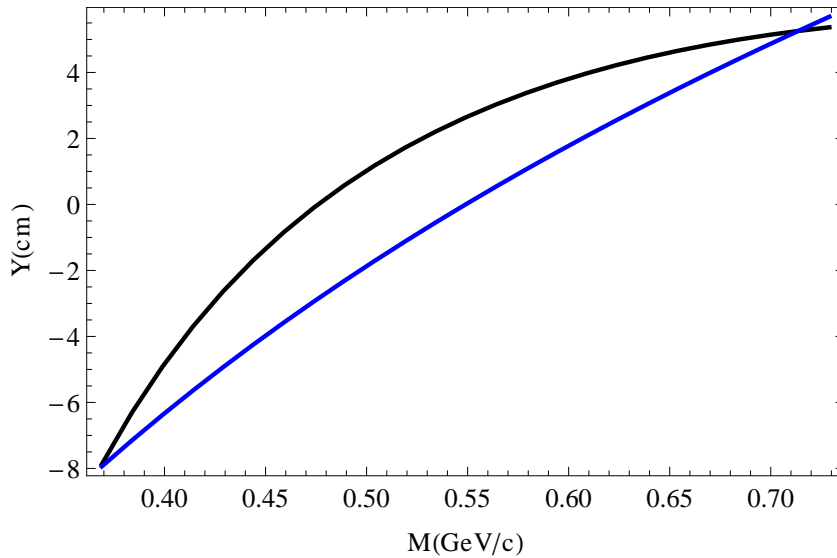


FIGURE 6.22: Comparison of particle positions at the exit of the fixed dipole ejection system and the equilibrium positions in a scaling FFAG cell.

to cope with, and would only get worse, if beam were deflected to a greater distance from the transport line.

### 6.6.2.3 Dispersion Suppression

After designing the matched bending section for the transport line, an obvious thought would be to extract using a bending FFAG cell which could be switched on and off. However, such a bend would have to have negative dispersion - with the lowest energy on the outside of the bend and the highest on the inside - and as in the gantry, dispersion suppression would be required to achieve it. This would mean that in the proposed layout described in figure 4.3, a  $2\pi$  phase advance would have to occur in the 10 meters between every switching point, which would require at least three cells to do so stably. This would defeat the object of having a sparse transport line somewhat but a test of the principle was carried out. It was found difficult to achieve perfect dispersion suppression with the straight cells however and the attempt abandoned. It is not obvious why this

would be the case, because in theory, all that is required is a  $\pi$  phase advance, but in practice, so far, it could not be done.

#### 6.6.2.4 Curved Transport Line

This is a much more radical idea than the others as it requires an entirely new transport layout which would use triplet cells in a curved transport line. The idea of this is to have sections of  $2\pi$  phase advances, with dispersion suppression points every three cells. Depending on whether a switching cell is turned on or off, the beam will go one of two ways (figure 6.23). The layout can either be circular (perhaps with PAMELA at the centre) or in a ‘snake’ type layout with treatment rooms on either side (figure 6.24). This idea is fairly appealing as it could make extraction easier and the requirement for the transport line to bend through  $45^\circ$  one way, then the other, would be met as a part of the design, rather than as additions to it.

Tests were done and various possible lattices found using parameter searches and the dispersion suppression design process. These resulted in some promising lattices. Figure 6.25 shows the tracks through a design similar to the ‘snake’ layout in figure 6.24, except there are four cells between each dispersion suppression point, rather than three. In this case the beam will have gone all the way to the end, switching curvature at every dispersion suppression point; three times in total. It seems promising and the beta functions in figure 6.26 are not as smooth as they could be, but remain low enough over this distance to avoid dismissing the idea completely.

However, this idea was not pursued any further because the idea of switching on and off a whole cell would not be practical. Also, lattices with low beta functions tend to have more cells between dispersion suppression points, which means this type of

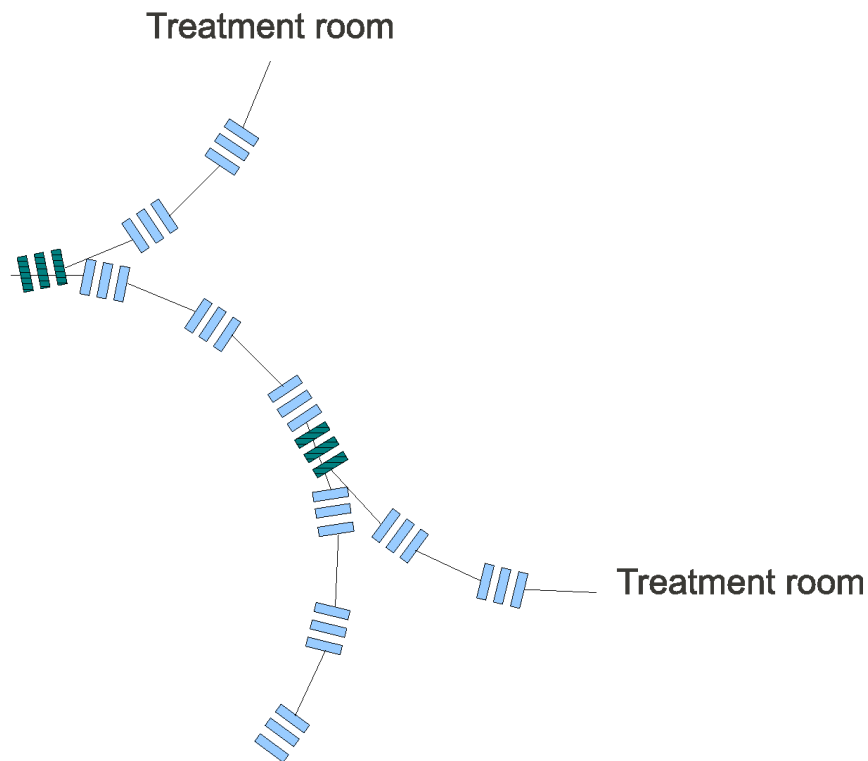


FIGURE 6.23: How a curved transport line might switch into treatment rooms. Every three cells would have a  $2\pi$  phase advance. At the dispersion suppression points, the darker cells would switch on to take the beam to a treatment room, or off to let the beam continue.

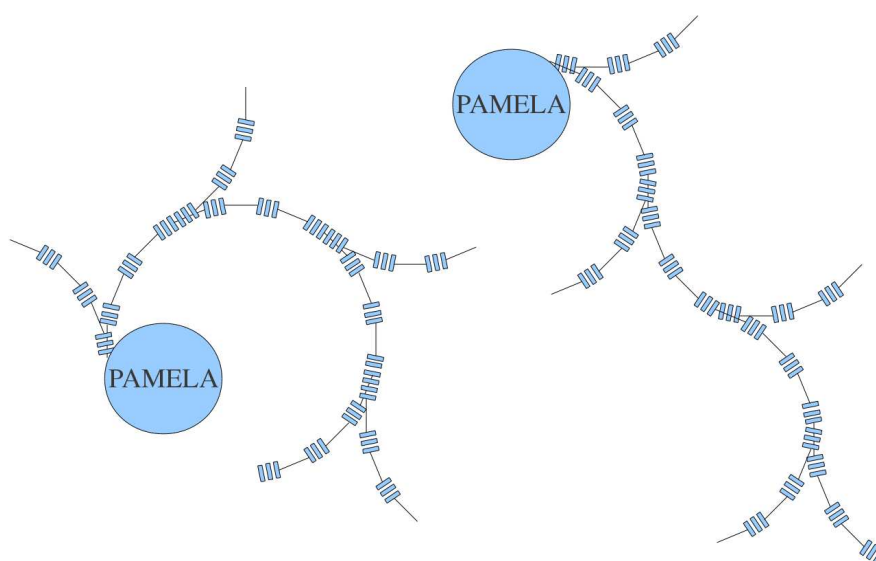


FIGURE 6.24: Two possible new layouts for curved BTL using triplet cells. This attempts to solve the problems of bending out from a straight transport line, by having curves as part of the main section. The layout on the left is a circular design and the one on the right a 'snake' type.

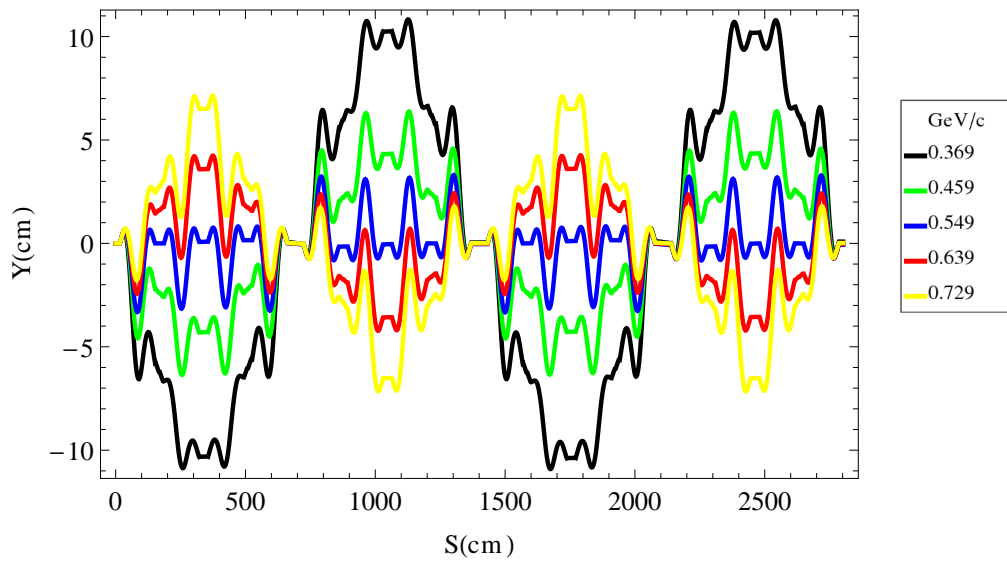


FIGURE 6.25: Tracks through a ‘snake’ type curved transport line. There are four cells between each dispersion suppression point and it switches curvature three times.

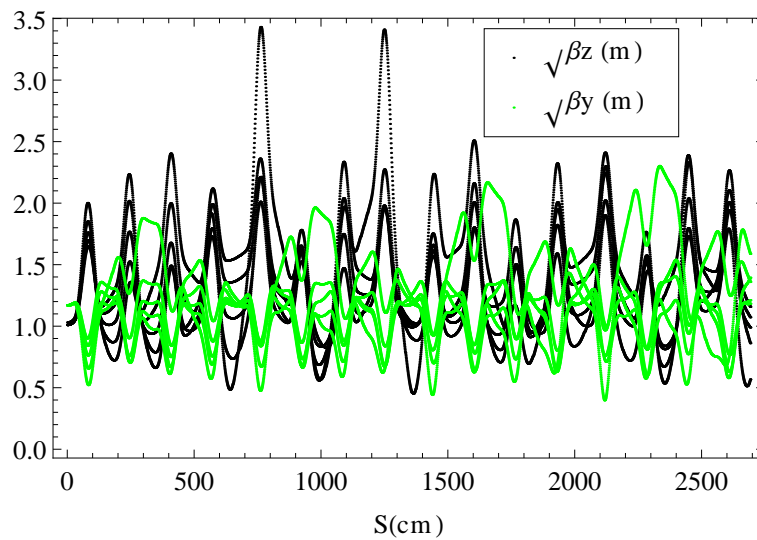


FIGURE 6.26: Beta functions through the curved transport line. The initial beta values to make this plot were chosen arbitrarily, but within reason.

transport requires many more magnets than the straight design discussed previously. For example, in the design discussed in section 6.3 has two cells and eight magnets between each extraction point, whereas the curved design shown in figure 6.25 would have four cells and 12 magnets.

### 6.6.3 Justification for a Variable Field Switching Dipole

Rather than switching a whole cell off and on, it would be much more practical to use an arrangement with a simple dipole. As shown in section 6.6.2.2, a dipole arrangement with fixed fields is very difficult to achieve as matching between the dispersion caused by the dipole and the field profile of an FFAG magnet is prohibitively problematic. Partly for this reason it is worth considering moving away from an entirely fixed field design and use a variable strength dipole to extract the beam at this point.

There is an obvious objection to doing so: why spend all the effort designing the rest of the PAMELA complex using ns-FFAG magnets only to slow the whole thing down with a variable magnet? The answer comes in two parts:

Firstly; sweeping this one small dipole should be a more trivial and much faster operation than sweeping the many magnets used in conventional gantry and transport lines. This means that there is still a clear speed advantage to making the complex predominantly fixed field. It does prevent PAMELA from switching between two arbitrarily chosen energies instantaneously, as would be possible in a totally fixed field machine, but there is no clinical reason that a treatment volume must be filled in this ‘random access’ way as normally the treatment volume would be filled in a series of small steps.

The second reason a variable dipole would be useful at this point, is to do with the safety of the machine. In variable field machines, a particle with an incorrect energy would be kicked off orbit by any of the dipoles it passes through and be lost before getting anywhere near the patient. In a totally fixed field machine, however, there is nothing to stop a particle with an erroneous energy travelling right from start to finish. This is clearly a safety risk because it could cause dose to be delivered to places outside of the treatment area.

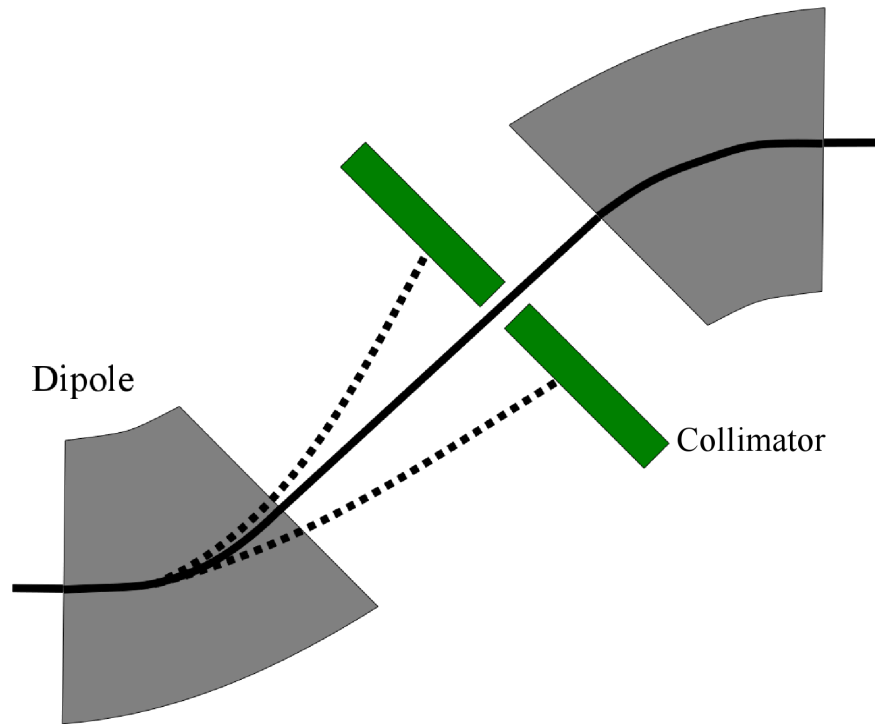


FIGURE 6.27: Schematic of an energy selecting ejection system for the transport line, using variable field dipoles and movable collimator. The continuous black line is the track of the desired momentum, whereas the dotted lines are the tracks of particles with erroneous momentum.

Using a variable field dipole for the switching mechanism gives us the opportunity to block any particles which do not have the correct energy. A system of a dipole and a collimator will deflect the beam away from the transport line as well as block any particle with the wrong energy; a second dipole will cancel any dispersion caused by the first and FFAG bending magnets can then take the beam to the treatment room (figure 6.27). This, along with the complications in designing a fixed field solution described in section 6.6.2, is the best justification for introducing variable dipole fields into the design.

The design of these two dipoles will be relatively straightforward. A fitting algorithm can be used to match the particle positions at the end of the transport line to the bending FFAG magnets using the field strength of the dipoles. However, the exact design for the variable field switching dipoles can only really be made once the matching into the

treatment room has been considered, since the design for the  $45^\circ$  bend and dispersion suppressor required to prepare the beam for the rotator is more complicated and less flexible than the design of the dipoles.

## 6.7 Design for $45^\circ$ bend and Matching into Treatment Room

This section deals with the design of the  $45^\circ$  bend away from the straight transport line and matching both equilibrium orbits and beta functions into the gantry. The problem here is similar to some of those faced in the gantry design: a section of lattice must bend the beam through  $45^\circ$  and simultaneously suppress the dispersion to zero. It is perhaps more flexible than anything in the gantry because there is no restriction on  $k$  and bend angle per cell can be any factor of 45 (although, of course it should be as high as possible).

There is the added challenge here, though, that was not faced in the gantry: the beta functions at the point of entry to the treatment room, where the gantry rotates, must match the specific values for the optimal beta functions found in the design of the gantry (see figure 5.48), shown in appendix A and summarised in table 5.10. The horizontal and vertical beta functions must be equal to each other to create a completely circular beam which is invariant during the rotation of the gantry.

To summarise, in addition to the usual constrictions on maximum field, aperture and drift spaces, the specifications of this section are:

- Must bend the beam through  $45^\circ$ .
- Must have a zero dispersion point at the end.
- Horizontal and vertical beta functions must be equal to each other for each energy and match those in appendix A.

These three requirements can almost be split up into different sections of lattice: a section of lattice that will do most of the bending; a section that does the dispersion suppression (and the rest of the bending); a section that matches the beta functions to the gantry. However, the first two sections have to be designed together because they have to match beta functions, equilibrium orbit positions and their bend angles have to add up to  $45^\circ$ .

The matching of the beta functions will be done in section 6.7.3. Because of the disruption to the beta functions caused by the dispersion suppression magnets, it will be impossible to exactly match them to the start of the gantry only using fixed fields. But, since time varying dipoles have been introduced into the design, it will also be possible to introduce time varying quadrupoles here to control the beta functions.

### 6.7.1 Dispersion Suppression and bending

The dispersion suppression and bending sections were attempted with only two magnets doing both functions at the same time. However, it proved to be impossible to achieve with sensible field strengths and beta functions, so a parameter search was undertaken for each section, then possible matches were found and the best refined into a design.

The parameters varied are summarised in table 6.6 and the criteria considered when finding matches were:

- The sum of the bend angles must be  $45^\circ$ .
- The  $k$  of the dispersion suppressor magnets must be twice the  $k$  of the bending magnets.
- The beta functions need to match roughly with each other and with the straight transport line so that they will not be unreasonable at the end.
- Also, the phase advance in the dispersion suppression cells had to add up to  $\pi$ .

TABLE 6.6: Parameter Search for 45° Bend and Dispersion Suppression into Treatment Room. The magnet length was held at 60cm throughout.

Parameter	Range	
	Dispersion Suppression	Bend
$k$	4 → 11	2 → 5.5
Packing factor	0.5 → 0.9	0.5 → 0.9
Long drift length	50 → 300 cm	50 → 300 cm
Number of Cells	2 → 3	1 → 2
Bend angle total	0° → 10°	45° → 35°
DF ratio	1.6 → 2.1	0.8 → 1.5

### 6.7.1.1 Results

This parameter search only turned up a small number of candidates that matched all of the criteria; all of these had  $k$  values of 4.5 for the bend and 9 for the dispersion suppression cells. The match with the total bend angle closest to 45° had a total bend of only 41°, but it was found that the bending section could easily be adjusted to make up the difference. These lattices were refined using the dispersion suppression process and adjustments made to reduce the size of the resulting beta functions. The resulting designs are summarised in table 6.7 and the tracks (figure 6.28) and final positions (figures 6.30 and 6.31) show that near perfect dispersion suppression matched to a 45° bend has been achieved. A big achievement is that the beta functions (figure 6.29) are relatively controlled given the inherent non-linearities of the dispersion suppressor. However, the exact Twiss parameters of the beam at the start of this plot were taken from the end of a cell of the straight transport line, so the exact beta functions will not be known until the extracting dipoles are designed and the beta functions of the whole transport line simulated.

TABLE 6.7: Designs of 45° Bend and Dispersion Suppression into Treatment Room.  
 \*Only the dispersion suppression cell 1 (i.e. the one nearest the the dispersion suppression point) has a  $k$  value, because all other cells were adjusted using the Taylor Expansion.

Parameter	Dispersion Suppression	Bend	Units
Bend angle per cell	3	19.5	degrees
Packing factor	0.9	0.8	
Cell length	200	225	cm
Magnet length	60	60	cm
Long drift length	50	300	cm
Number of Cells	2	2	cells
DF ratio	1.93	1.47	
$k^*$	8.94	n/a	
b1	9065.763	3538.359	
b2	39271200	6538764	
b3	11549640000	20563200000	
b4	9087254000000	24700290000000	
Max aperture	16.55	21.24	cm
Field strength (max, min)	0.595, -0.758	1.514, -1.549	T

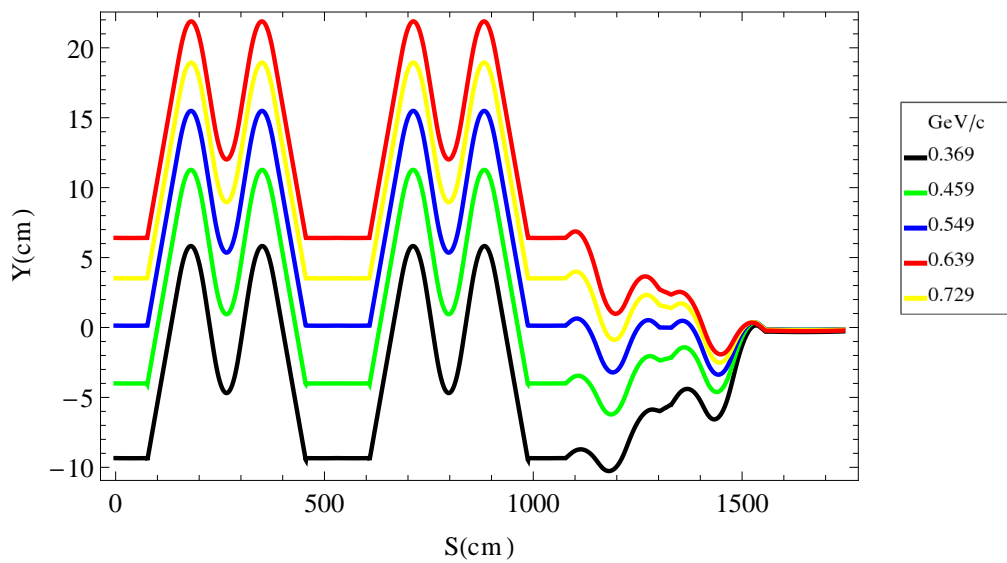


FIGURE 6.28: Tracks through best design of 45° extraction bend and dispersion suppressor of particles with five different momenta.

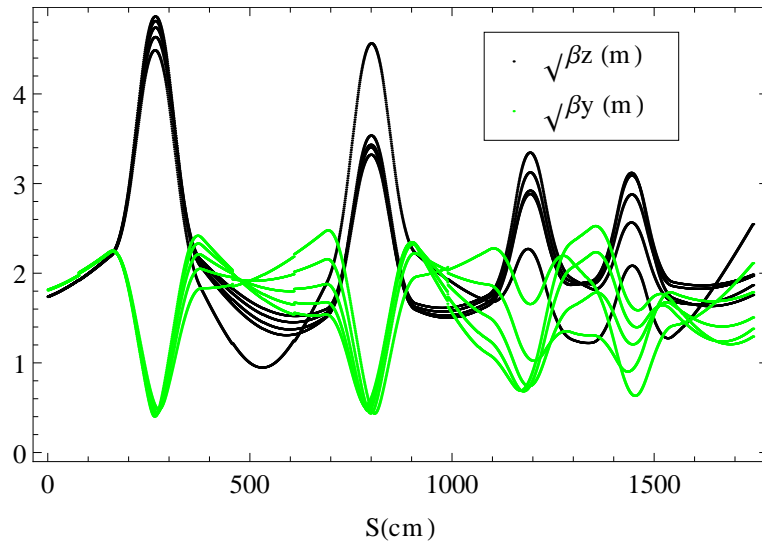


FIGURE 6.29: Beta functions through best design of  $45^\circ$  extraction bend and dispersion suppressor for momenta from  $0.369\text{GeV} \rightarrow 0.729\text{GeV}$ .

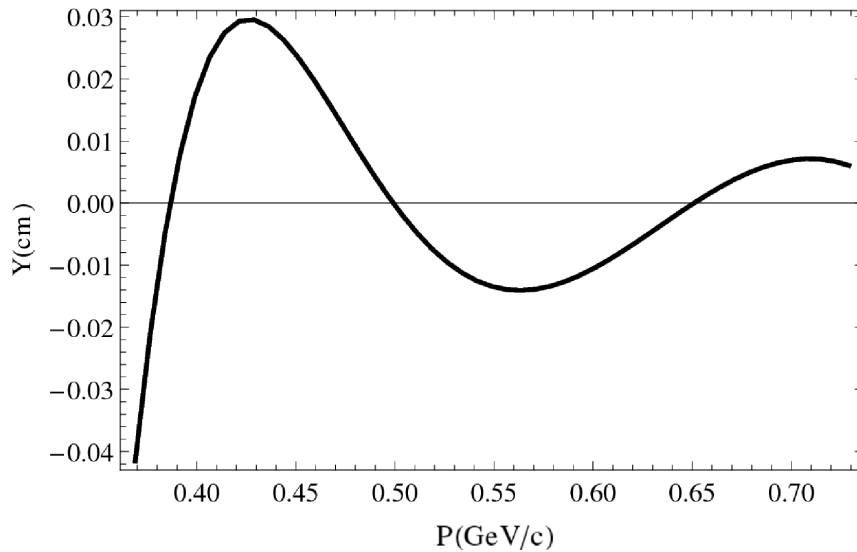


FIGURE 6.30: Final positions of particles through the  $45^\circ$  extraction bend and dispersion suppressor with ideal initial positions.

### 6.7.1.2 Discussion of The $45^\circ$ Bend and Matched Dispersion Suppressor

These are the best possible final positions as they do not take into account any of the transport line before the  $45^\circ$  bend, let alone positional and field gradient errors. From inspection of the plots in section 5.9 it looks like just these final positions alone would produce a  $0.5^\circ$  deflection error and around a  $0.05\text{cm}$  position error at the end of the gantry with the lowest (worst case) momentum. This further strengthens the case made

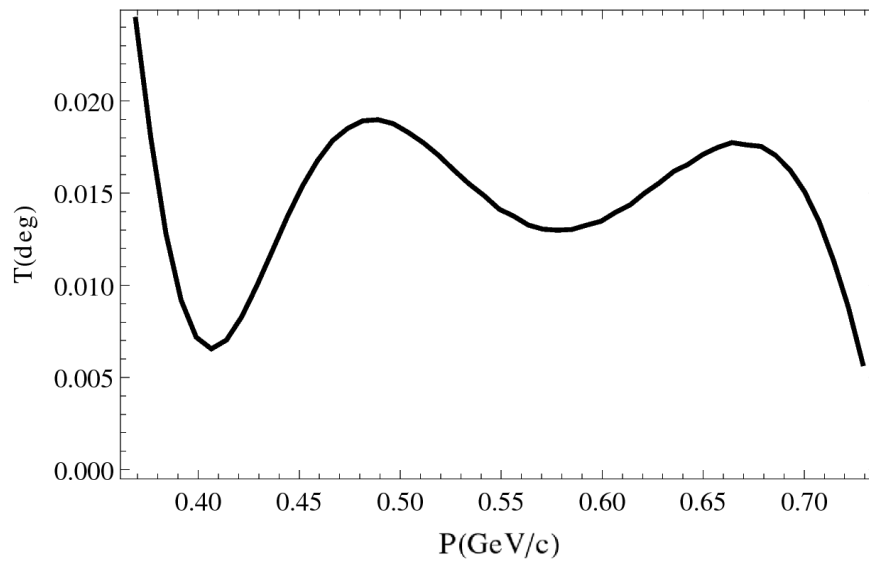


FIGURE 6.31: Final angles of particles through the  $45^\circ$  extraction bend and dispersion suppressor with ideal initial positions.

in [26] for having an active scanning system at the entrance to the gantry as well as at the end of the gantry. In fact, it may be worth investigating the value of a scanning system at the dispersion suppression point a third of the way through the gantry (at point B in figure 5.25) as well, since magnet positioning and field gradient errors can only add to these errors and real-time correction may be essential.

### 6.7.2 Design for a Variable Field Switching Dipole

With the  $45^\circ$  bend designed, the switching dipoles can now be designed. This is a straight forward procedure: a reasonable, but arbitrary magnet length was chosen (30cm) and a field strength found for each energy to take the beam from the equilibrium orbit in the straight transport line to the correct position in the  $45^\circ$  bending magnets. It was decided to take the beam 1m away from the orbit of the central momentum particle in the straight transport, to give ample room for the magnets and casing of both the straight transport cells and the  $45^\circ$  bend cells.

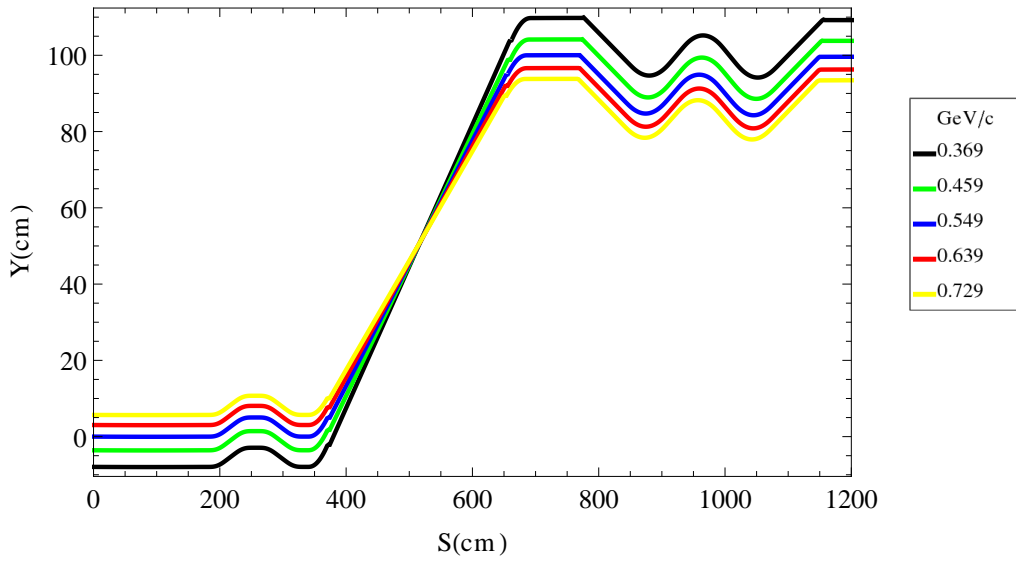


FIGURE 6.32: Tracks through the variable field transport extraction dipoles, with a straight cell downstream and a curved cell upstream.

Table 6.8 shows a selection of the field strengths required over the energy range (a more complete version can be found in appendix A). The field strength is the opposite in each magnet, so only the strength of the first dipole is shown. Figure 6.32 shows tracks through the dipoles and that they match the equilibrium orbits of the two sections of transport line.

TABLE 6.8: Field strengths for variable field switching dipole. This is only a small summary of a larger table in appendix A.

Momentum (GeV/c)	Field Strength (T)
0.369	-1.6870
0.459	-1.9413
0.549	-2.1727
0.639	-2.3813
0.729	-2.5704

### 6.7.3 Matching of Beta Functions

Since there are variable field dipoles in use, and the beta functions at the end of the dispersion suppressor are irregular, an unavoidable consequence of FFAG dispersion suppressors, it is probably justified to propose a series of variable field quadrupoles to

match the beta functions into the gantry. Also, as discussed in [26] and mentioned in the previous section of this thesis, an active system may be required to match the beam positions into the gantry, so variable field quadrupoles could be a part of that.

To show that it is possible to match the beta functions, the following study was carried out using a number of quadrupoles between the end of the transport line and the beginning of the gantry. For each energy, four values have to be matched: the horizontal and vertical beta functions have to equal the optimal values at the start of the gantry (table 5.10) and the alpha functions have to equal zero. This means there has to be at least four degrees of freedom for a solution to be possible. The only freedoms there are between energy changes are the strengths of each dipole, so an initial layout of four quadrupoles of length 20cm and with 20cm between them was decided on.

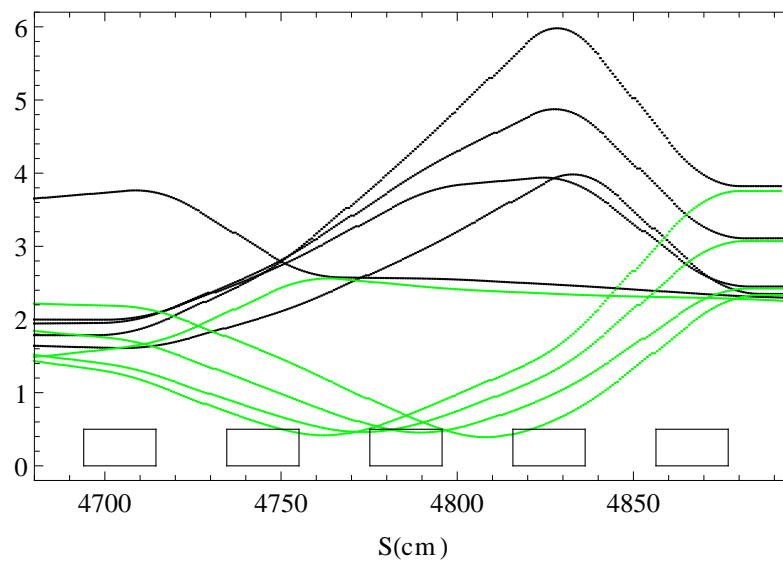


FIGURE 6.33: Beta functions through the five matching quadrupoles at the end of the transport line with boxes show their position. All beta final functions match to the optimal values at the start of the gantry.

After a parameter search, it was found difficult to complete the task with four quadrupoles, especially at the lowest energy, so an extra magnet was added to the design. The values in table 6.9 are results of parameter searches and a down-hill fitting procedure for five momenta. They match to the optimal beta values to within 0.1m and all the alpha

values match to zero to within 0.01 except for the problematic lowest momentum, which could only be matched to within 0.5. Figure 6.33 shows the beta functions through the five quadrupoles.

TABLE 6.9: Quadrupole strengths for matching Twiss functions from the transport line to the gantry.

Momentum (GeV/c)	Quadrupole k vales ( $\text{m}^{-2}$ )				
	Q1	Q2	Q3	Q4	Q5
0.369	-4.73	5.54	-0.437	-9.34	0.319
0.459	4.41	1.78	0.855	-1.43	8.99
0.549	4.50	1.31	-2.95	-5.58	7.41
0.639	4.87	2.04	-1.00	-7.57	7.40
0.729	5.98	3.38	0.63	-9.19	7.56

The effective gradients of the quadrupoles are all well within the range of the other PAMELA quadrupoles. However, in every case there is a large jump between 0.459 GeV/c and 0.369 GeV/c, so further investigation would have to be done to see if this is possible in a reasonable time.

#### 6.7.4 The Whole Transport Line

The plots in this section show all of the different parts of the transport line together. The tracks are shown in 6.34 and the final positions and angles are shown in 6.36 and 6.37 respectively. The beta functions are shown in figure 6.35. This shows that it is, in principle, possible to take particles over such a large distance of straight FFAG transport line, bend it positively, extract it, bend it negatively and create a zero dispersion point at the end. Although the accuracy in the final positions is not sufficient to match straight into the gantry, it is still a design which could be improved into a fully working design.

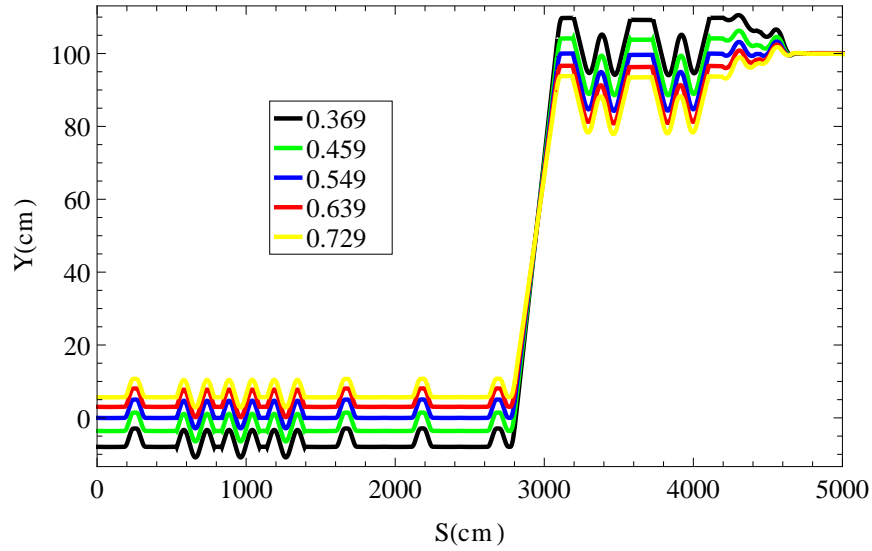


FIGURE 6.34: Tracks through the entire transport line. The order of cells is: two straight transport cells (table 6.5), three bending cells with a total bend of  $45^\circ$  (table 6.4), four more straight cells, the variable field dipoles (table 6.8), two negatively bending cells and two dispersion suppression cells, all with a total bend of  $-45^\circ$  (table 6.7).

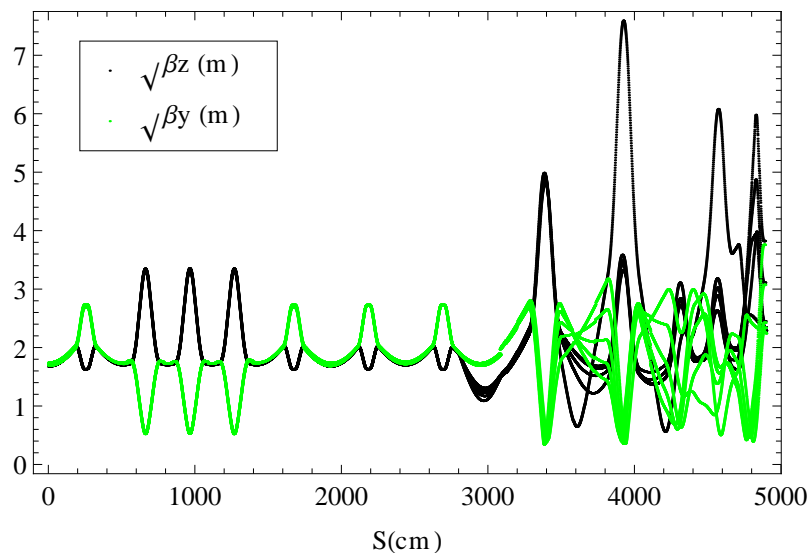


FIGURE 6.35: Beta functions through the whole transport line.

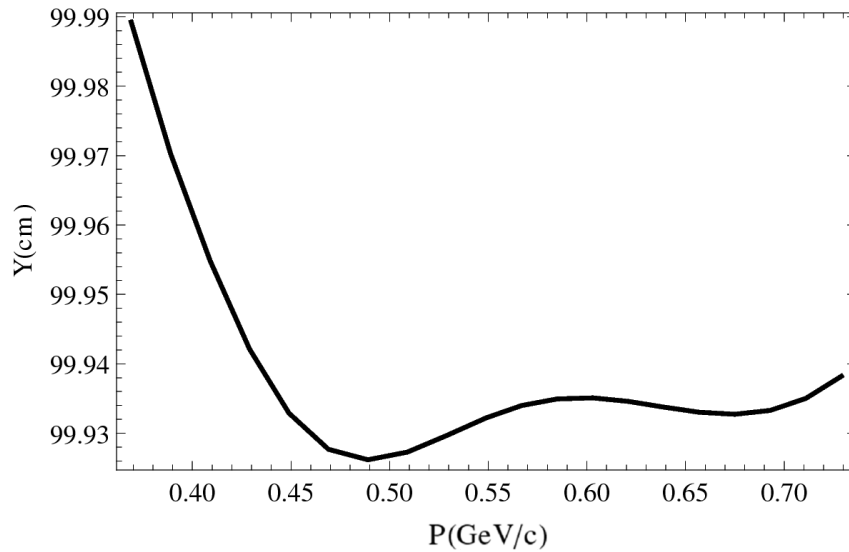


FIGURE 6.36: Final positions at the end of the transport line.

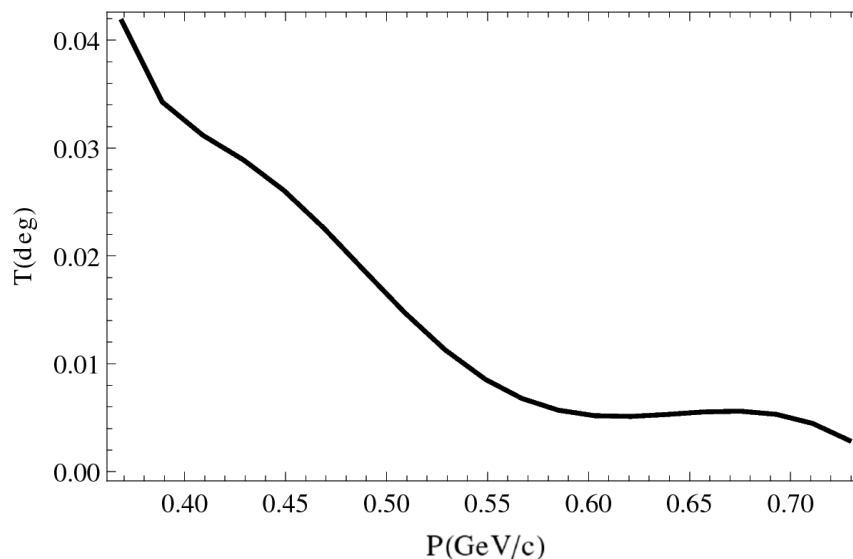


FIGURE 6.37: Final deflections at the end of the transport line.

## 6.8 Conclusion

This chapter showed the design of an ns-FFAG transport line. To do this, it was necessary to optimise an existing design for straight transport cells (section 6.3) and match bending cells to it (section 6.5). (This match may be an interesting result because it could form the basis of a race track style accelerator, currently only seen with synchrotrons). The design also required a section of lattice to bend the beam  $45^\circ$  away from the transport line and use a dispersion suppressor to match as best as possible into

the gantry (section 6.7). In order to extract from the straight transport line, it was necessary (section 6.6.3) to move away from a completely fixed field design and introduce variable field dipoles (section 6.7.2). Variable fields were also used to match the beta functions into the gantry (section 6.7.3).

## Chapter 7

# Conclusion

There are three main novel pieces work in this thesis: the discovery and development of the near perfect FFAG dispersion suppression design process in section 5.5, the gantry design in chapter 5 and the transport line design in chapter 6. Within this thesis, the author has also demonstrated an understanding of its context in the wider history of particle accelerator design (section 1.1); while in section 3.4 an understanding of its context in both the history and contemporary literature of FFAG accelerators was shown. The underlying physical principles required for the design of FFAG lattices were discussed in chapter 2; as were the relative benefits and ideas behind charged particle therapy in section 1.2.

In this chapter, I will assess how well the challenges set out in chapter 4 were met, as well as summarise the areas that require further work.

### 7.1 Assessment of Final Designs

The challenges to be met were set out in section 4.1.1 and are reproduced here.

Beam Specifications:

- Momentum range = 0.369 GeV to 0.729 GeV
- Switching between momentum at a rate of  $\approx 1\text{kHz}$
- Positional dispersion limited to 5cm at end of gantry.
- Angular dispersion limited to within around half an mrad at the end of the gantry.
- No distortion of the beam due to rotation of gantry.
- $0.4\text{cm} < \sqrt{\varepsilon\beta} < 1.0\text{cm}$

Magnet specifications:

- Fixed Fields
- Rectangular in the horizontal plane
- Magnets parallel with in cells
- Aperture around half the size as the length
- Fields no higher than 3T
- As few magnets as possible to be used

Space Specifications:

- 3m from bending magnets to patient
- Total height less than 10m
- Height more important than length

Largely the beam specifications have been met, however, none can be said to have done so without qualification. The transport line and the gantry have both been designed for the full momentum range and both dispersions are as required (section 5.8). However, to meet the last two items, an active scanning system will have to be introduced at the entrance to the gantry, which may make switching between energies slower than 1kHz, especially at low energies, and further work will have to be done to reduce the beta values at the end of the gantry.

The magnet specifications were all met except for the desire to use only fixed fields. However, using a small number of variable fields has been justified in sections 6.6.3 and 6.7.3. This is justified not only as a way to avoid apparently intractable complications in extracting the beam from the transport line and matching to the gantry, but also for safety reasons because erroneous energies can be prevented from reaching the patient.

Of the space specifications, only the first was met. This was the most important, because the scanning system has to fit in this space, however, it made it very problematic to keep the height below 10m with a full 360° rotation. It is not clear how this can be overcome using these types of magnets with the clearance restriction of 3m after the bending magnets. Due to this, and the problems with the beam, ideas for avenues of further study into a more compact design were discussed in section 5.10.

Although these challenges were not completely met, this thesis has presented the first design for a near perfect FFAG dispersion suppressor (section 5.5) and assessed its susceptibility to positional errors (section 5.5.5). It has also optimised the first design for a straight transport line (section 6.3), shown that it can take the the full proton and carbon energy ranges required for CPT (section 6.4) and matched a bending section to it (section 6.5). Showing that PAMELA type magnets may not be the best starting point for a gantry is also a worthwhile achievement.

## 7.2 Further Study

The most further study is required in the gantry design: The main concern is that the dimensions need to be reduced in order to be competitive with existing conventional gantries. So both a length and full height of  $< 10\text{m}$  should be the goal.

If this design were to be taken any further, however, the horizontal and vertical betatron functions at the end of the gantry should be reduced in order to be compatible with scanning magnet requirements.

In the current study there was no time to create field maps for any of the FFAG magnets. This would need to be done to check the fields can be generated with existing magnet technology. Also, the possibility of mounting them on a moving gantry would have to be explored as this could cause problems with positional errors caused by magnet movement and, as superconducting technology is likely to be needed, with the cryogenic system.

The scanning system at the start of the gantry needs to be designed. This would involve variable field dipoles for position and quadrupoles for the beta functions, both linked to upstream diagnostics to eliminate errors.

A full error study of the dispersion suppressor is required which would involve all three positional dimensions, all three rotational dimensions and errors in the field gradients. This study then would need to be extended to the whole gantry and transport line.

A scheme needs to be developed to match from the main PAMELA ring to the start of the transport line. One idea for this is to use a dispersion suppression point straight after extraction probably with some variable field quadrupoles to match the beta functions.

Since the aim of the PAMELA project is to design a complex for both protons and carbon ions, a design for a carbon transport line and gantry should be attempted. An initial step was taken in section 6.4, with a design for a straight carbon transport line, but the bending sections would most likely prove more problematic. Carbon ions at therapeutic energies have a higher magnetic rigidity than protons, so any design would either require higher fields, longer magnets, a greater radius or a combination of the three.

---

One possible area of study that might follow from this thesis is the design of an FFAG racetrack. The bending section matched to the straight transport line in section 6.5 could form the basis of such a design. However, another idea would be to use the bend into the gantry and the dispersion suppression cells in section 6.6. This would be interesting to pursue, because RF cavities could be placed at the dispersion suppression points, reducing the problems for RF designers caused by the large dispersion in conventional FFAGs.

# Appendix A

## Miscellaneous Tables

TABLE A.1: Optimal initial betas values for the gantry: long version. See section 5.8

Momentum (GeV/c)	Beta (m)	Momentum (GeV/c)	Beta (m)
0.369	4.92431641	0.5562	6.27687836
0.3765	5.03625488	0.5634	6.65138245
0.384	5.20043945	0.5706	7.01745605
0.3915	4.33807373	0.5778	7.371521
0.399	4.28771973	0.585	7.70999908
0.4065	4.22601318	0.5922	8.02990723
0.414	4.56195068	0.5994	8.3289032
0.4215	5.33868408	0.6066	8.60540771
0.429	5.36376953	0.6138	8.85888672
0.4365	5.39074707	0.621	9.0899353
0.444	5.41619873	0.6282	9.30013275
0.4515	5.44195557	0.6354	9.49232483
0.459	5.46807861	0.6426	9.67042542
0.4665	5.49456787	0.6498	9.8394165
0.474	5.52166748	0.657	10.00665283
0.4815	5.54931641	0.6642	10.17883301
0.489	5.57769775	0.6714	10.36463928
0.4965	5.60687256	0.6786	10.57542419
0.504	5.52392578	0.6858	10.82572937
0.5115	5.29577637	0.693	11.13540649
0.519	5.0916748	0.7002	11.53314209
0.5265	4.9083252	0.7074	12.06355286
0.534	5.10915375	0.7146	12.80221558
0.5415	5.50180054	0.7218	13.89251709
0.549	5.89772034	0.729	14.21984863

TABLE A.2: Field strengths for the dipole transport line extraction scheme. See section [6.7.2](#)

Momentum (GeV/c)	Field Strength (T)
0.369	-1.687
0.389	-1.745
0.409	-1.803
0.429	-1.859
0.449	-1.914
0.469	-1.968
0.489	-2.021
0.509	-2.073
0.529	-2.123
0.549	-2.173
0.567	-2.216
0.585	-2.259
0.603	-2.300
0.621	-2.341
0.639	-2.381
0.657	-2.421
0.675	-2.459
0.693	-2.497
0.711	-2.534
0.729	-2.570

# Bibliography

- [1] L. Ward. William crookes in vanity fair, May 1903.
- [2] William crookes, June 2011. URL [http://en.wikipedia.org/wiki/William\\_Crookes](http://en.wikipedia.org/wiki/William_Crookes).
- [3] J. J. Thomson. Cathode rays. *The Electrician*, 39(104), 1897.
- [4] W. Röntgen. On a new kind of rays. *Nature*, 53(1396):274–275, 1896.
- [5] Edmund Wilson. *An Introduction to Particle Accelerators*. Oxford University Press, 2001.
- [6] M. Conte and W. Mackay. *An Introduction to the Physics of Particle Accelerators*. World Scientific, 2nd edition, 2008.
- [7] W. Henning and C. Shank. Accelerators for america’s future. Technical report, U.S. Department of Energy, 2010.
- [8] Jai website. <http://www.adams-institute.ac.uk/accelerators.php>, December 2009.
- [9] Z. Chuang. Particle accelerators: An introduction. In A. Chao, H. Moser, and Z. Zhao, editors, *Accelerator Physics, technology and applications: selected lectures of OPCA International Accelerator School*. World Scientific, 2002.
- [10] J. Cockroft and E. Walton. Experiments with high velocity ions. *Proceedings of the Royal Society*, A136(619), 1932.

- 
- [11] Science museum / science in society picture library, Accessed 2011. URL [www.scienceandsociety.co.uk/](http://www.scienceandsociety.co.uk/).
- [12] R. van der Graaff. A 1 500 000 volt electrostatic generator. *Physical Review*, 38: 1919–20, 1931.
- [13] S. Y. Lee. *Accelerator Physics*. World Scientific, 2nd edition, 2004.
- [14] G. Ising. Prinzip einer methode zur herstellung von kanalstrahlen hoher voltzahl. *Arkiv for matematik o. fysik*, 18:1–4, 1924.
- [15] E. Lawrence and N. Edelfsen. On the production of high speed protons. *Science*, 72:376–7, 1930.
- [16] A.W. Chao and M. Tigner, editors. *Handbook of Accelerator Physics and Engineering*, volume 2. World Scientific, Singapore, 1999.
- [17] M. Reiser. *Theory and Design of Particle Accelerators*. Wiley-VCH, 2nd edition, 2008.
- [18] M. Oliphant. The genesis of the nuffield cyclotron and the proton synchrotron. Department of Physics, University of Birmingham, 1967.
- [19] N. Christofilos. Unpublished report and us patent no. 2.736,799. filed 1950, issued 1956, 1950.
- [20] E. Courant, M. Livingston, and H. Snyder. The strong-focusing synchrotron: a new high-energy accelerator. *Physical Review*, 88:1190–6, 1952.
- [21] Diamond light source: Frequently asked questions, Accessed 2011. URL <http://www.diamond.ac.uk/Home/About/FAQs/Science.html#8>.

- [22] L. Bonolis and G. Pancheri. Bruno touschek: particle physicist and father of the  $e^+e^-$  collider. *European Physical Journal H*, March 2011.
- [23] Why the lhc: A few unanswered questions, Accessed 2011. URL <http://public.web.cern.ch/public/en/lhc/WhyLHC-en.html>.
- [24] Y. Mori. Ffag proton driver for muon source. *Nuclear Instruments and Methods In Physics Research A*, 451:300–303, August 2000.
- [25] D. Trbojevic, E. Courant, and A. Garren. Ffag lattice without opposite bends. In *AIP Conf. Proc.*, 2000.
- [26] K. Peach et al. Pamela design report. Technical report, CONFORM, 2011.
- [27] A. Assmus. Early history of x-rays, Accessed 2011. URL <http://www.slac.stanford.edu/pubs/beamline/25/2/25-2-assmus.pdf>.
- [28] R. Wilson. Radiological uses of fast protons. *Radiology*, 47(487), 1946.
- [29] IAEA. *Radiation Biology: A Handbook for Teachers and Students*. Training Course Series 42. International Atomic Energy Agency, Vienna, March 2010.
- [30] G. Barnet, C. West, A. Dunning, et al. Normal tissue reactions to radiotherapy: Towards tailoring treatment dose by genotype. *Nature Reviews Cancer*, 9:134–142, Feb 2009.
- [31] Psi proton therapy website, Accessed 2011. URL [http://p\\_therapie.web.psi.ch/images/Pr\\_Ph\\_depth2.png](http://p_therapie.web.psi.ch/images/Pr_Ph_depth2.png).
- [32] Tony Lomax. personal communication, 2010.
- [33] B. Slotman. *Shaped-Beam Radiosurgery: State of the Art*, chapter 2, page 14. Springer, 2011.

- 
- [34] G. Jiang, S. Tucker, et al. Radiation induced injury to the visual pathway. *Radiotherapy and Oncology*, 30(1):17–25, 1994.
- [35] A. M. Sessler. An introduction to cancer therapy with hadron radiation, May 2008. URL [www.pitt.edu/~super7/32011-33001/32751.ppt](http://www.pitt.edu/~super7/32011-33001/32751.ppt).
- [36] IAEA and ICRUM. Relative biological effectiveness in ion beam therapy. Technical report, International Atomic Energy Agency, Vienna, 2008.
- [37] NHS Supply Chain, personal communication, 2011.
- [38] Suzanne Amador Kane. *Introduction to Physics in Modern Medicine*. CRC Press, 2nd edition, 2009.
- [39] E. Pedroni. Lecture at oxford university, 2010.
- [40] T. Bortfeld and R. Jeraj. The physical basis and future of radiation therapy. *British Journal of Radiology*, 84:485–498, 2011.
- [41] T. Trikalions, T. Terasawa, S. Ip, G. Raman, and J. Lau. Particle beam radiation therapies for cancer. Technical report, Agency for Healthcare Research and Quality, 2009.
- [42] Helmut Wiedemann. *Particle Accelerator Physics*. Springer, 3rd edition, 2007.
- [43] F. Meot and S. Valero. *Zgoubi User's Guide*, 4.3 edition, March 2008.
- [44] Michael Craddock. The rebirth of the ftag. *CERN Courier*, Jul 2004.
- [45] Richard Feynman, Robert Leighton, and Matthew Sands. *The Feynman Lectures on Physics: The Definitive Edition*, volume 2. Addison-Wesley, 2006.

- [46] K. R. Symon, D. W. Kerst, L. W. Jones, L. J. Laslett, and K. M. Terwilliger. Fixed-field alternating-gradient particle accelerators. *Physical Review*, 103(6):1837–1859, 1956.
- [47] C. Johnstone and F. E. Mills. In *Proc. 4th Int. Conf. Physics Potential and Development of  $\mu^+$   $\mu^-$  Colliders*, pages 698–698, 1997.
- [48] R. Edgecock et al. Emma the worlds first non-scaling fflag. In *Proceedings of EPAC*, page 3380, 2008.
- [49] S. L. Sheehy, K. Peach, H. Witte, D. Kelliher, and S. Machida. Fixed field alternating gradient accelerator with small orbit shift and tune excursion. *Phys. Rev. ST Accel. Beams*, 13, 2010.
- [50] S. Tygier and D. Kelliher. Pyzgoubi interface to zgoubi. URL <http://sourceforge.net/projects/pyzgoubi/>.
- [51] Mad-x. URL <http://mad.web.cern.ch/mad/>.
- [52] W. Press, B. Flannery, S. Teukolsky, and W. Vetterling. *Numerical Recipes in C: the Art of Scientific Computing*. Cambridge University Press, 1992.
- [53] Conform website, Jun 2011. URL <http://www.conform.ac.uk/>.
- [54] S. Machida. Resonance crossing and dynamic aperture in nonscaling fixed field alternating gradient accelerators. *Phys. Rev. ST Accel. Beams*, 2008. ISSN 094003.
- [55] S. Machida. Ffags for proton acceleration. In *FFAG08 workshop*, 2008. URL <http://www.cockcroft.ac.uk/events/FFAG08/programme.htm>.
- [56] S. L. Sheehy, K. Peach, H. Witte, T. Yokoi, D. J. Kelliher, and S. Machida. Pamela: Lattice solution for a medical c6+ therapy facility. In *Proceedings of IPAC10*, 2010.

- 
- [57] H. Witte and et al et al. Pamela magnets - design and performance. In *PAC09*, 2009.
- [58] C. Goodzeit, R. Meinke, and M. Ball. Combined function magnets using double-helix coils. In *IEEE Particle Accelerator Conference (PAC)*, 2007.
- [59] U. Weinrich. Gantry design for proton and carbon hadrontherapy facilities. In *Proceedings of EPAC*, 2006.
- [60] S. A. Reimoser. *Development and Engineering Design of a Novel Exocentric Carbon-Ion Gantry for Cancer Therapy (The "Riesenrad" Gantry)*. PhD thesis, Europöeischen Laboratorium f00fcr Teilchenphysik CERN, 2000.
- [61] E. Pedroni, , et al. The psi gantry 2: a second generation proton scanning gantry. *Z. Med. Phys.*, 14:25–34, 2004.
- [62] P. Bryant, L. Badano, M. Benedikt, M. Crescenti, P. Holy, A. Maier, M. Pullia, S. Rossi, and P. Knaus. Proton-ion medical machine study (pimms) part 1. Technical report, CERN, Geneva, Switzerland, January 1999.
- [63] Petr Holy. *Ion gantry design and scanning techniques in hadron therapy*. PhD thesis, Zapadoceska Univerzita, 1999.
- [64] M. Pullia. *Dynamique de l'ejection lente et son influence sur les lignes de transfert*. PhD thesis, l' Universite Claude Bernard, 1999.
- [65] M. K. Craddock and K. R. Symon. Cyclotrons and fixed-field alternating-gradient accelerators. *Rev. Acc. Sci. Tech.*, 1:65–97, 2008.
- [66] T. Ohkawa. Ffag electron cyclotron. *Pys. Rev.*, 1955.
- [67] A. A. Kolomensky, V. Petukhov, and M. Rabinovic. Theory of cyclic accelerators. *Lebdev Phys. Inst. Report (Moskow)*, 1953.

- 
- [68] D. Filges and F. Goldenbaum. *Handbook of Spallation Research: Theory, Experiments and Applications*. Wiley-VCH, 2009.
- [69] Y. Mori, S. Machida, T. Yokoi, et al. Development of a fflag proton synchrotron. In *Proceedings of EPAC*, 2000.
- [70] H. Tanaka and T. Nakanishi. Hybrid accelerator using and fflag injection scheme. In *Proc. 17th Int. Conf. Cyclotrons*, 2004.
- [71] J. Pasternak, F. Meot, J. Fourrier, T. Planche, et al. Spiral fflag for hadron therapy. In *Cyclotrons and Their Applications, Eighteenth International Conference*, 2007.
- [72] C. Johnstone, M. Berz, K. Makino, S. Koscielniak, and P. Snopok. Advances in non-linear non-scaling fflags. *International Journal of Modern Physics A*, 26:1690–1712, 2011.
- [73] C. Johnstone, W. Wan, and A. Garren. Fixed field circular accelerator designs. In *Proceedings of Particle Accelerator Conference, New York*, page 3068, 1999.
- [74] E. Keil, A. M. Sessler, and D. Trbojevic. Hadron cancer therapy complex using nonscaling fixed field alternating gradient accelerator and gantry design. *Phys. Rev. ST Accel. Beams*, 10(054701), 2007.
- [75] S. L. Sheehy. *Design of a non-scaling fixed field alternating gradient accelerator for charged particle therapy*. PhD thesis, Lady Margaret Hall, University of Oxford, 2010.
- [76] C. Johnstone and S. Koscielniak. New nonscaling fflag for medical applications. In *Proceedings of PAC07*, 2007.
- [77] G. Rees. Non-isochronous & isochronous, non-scaling fflag designs. In *Cyclotrons and Their Applications, Eighteenth International Conference*, 2007.

- 
- [78] D. Trbojevic, B. Parker, E. Keil, and A. M. Sessler. Carbon/proton therapy: A novel gantry design. *Phys. Rev. ST Accel. Beams*, 2008.
- [79] D. Trbojevic, R. Gupta, B. Parker, E. Keil, and A. M. Sessler. Superconducting non-scaling ftag gantry for carbon/proton cancer therapy. In *Proceedings of PAC07*, 2007.
- [80] D. Trbojevic. Update on the innovative carbon/proton non-scaling ftag isocentric gantries for cancer therapy. In *Proceedings of IPAC10*, 2010.
- [81] G. Rees. New gantry idea for  $h^+/c6^+$  therapy, September 2008. Presentation.
- [82] Shinji Machida and Richard Fenning. Beam transport line with scaling fixed field alternating gradient type magnets. *Phys. Rev. ST Accel. Beams*, 13(8):084001, Aug 2010. doi: 10.1103/PhysRevSTAB.13.084001.
- [83] S. Machida. Beam transport line with a scaling type ftag magnet. In *Proceedings of PAC09*, 2009.
- [84] T. Yokoi. personal communication, 2010.
- [85] Holger Witte. personal communication, 2010.
- [86] *A Non-Scaling FFAG Gantry Design for the PAMELA Project*, 2010. IPAC.
- [87] R. Fenning, S. Machida, A. Khan, and R. Edgecock. A non-scaling ftag dispersion suppressor. *International Journal of Modern Physics A*, 2009. Awaiting Publication.
- [88] A. Morita, H. Koiso, Y. Ohnishi, and K. Oide. Recent progress of optics measurement and correction at kekb. In *Proceedings of EPAC*, 2006.
- [89] *An FFAG Transport Line for the PAMELA Project*, 2009. PAC.

- 
- [90] JB. Lagrange, T. Planche, E. Yamakawa, Y. Ishi, Y. Kuriyama, Y. Mori, K. Okabe, and T. Uesugi. Applications of advanced scaling fflag accelerator. In *Proceedings of the 7th Annual Meeting of Particle Accelerator Society of Japan*, August 2010.
- [91] D. Trbojevic. Muon acceleration with racetrack fflag. In *Proceedings of PAC07*, 2007.
- [92] S. Machida. Neutrino factory design based on fflag. *Nuclear Instruments and Methods In Physics Research A*, 2003.